Time-Dependent Stochastic Approaches for Strong-Field Spectroscopy of Correlated Models

Orthodoxou, Chris

Awarding institution:
King's College London

King's College London

Doctoral Thesis

Time-Dependent Stochastic Approaches for Strong-Field Spectroscopy of Correlated Models

---

Author:
Chris A. Orthodoxou

Supervisor:
Dr. George H. Booth

A thesis submitted for the degree of
Doctor of Philosophy
in the
Department of Physics

May, 2022

Abstract

Time-Dependent Stochastic Approaches for Strong-Field Spectroscopy of Correlated Models

The work in this thesis aims to extend our simulation capabilities and understanding of the optical response of two-dimensional Mott insulators subject to strong-field laser pulses. These correlated systems are modelled using the Fermi-Hubbard Hamiltonian, and their real-time evolution is performed using a combination of stochastic, exact and mean-field methods. This enables their high harmonic emission to be calculated, from which we can resolve the attosecond charge dynamics of electrons in both the frequency and time domains.

The research is split into two overlapping threads, the first of which seeks to characterise the emission and understand its microscopic origins. High harmonic generation (HHG) in one-dimensional and infinite-dimensional Mott insulators has previously been investigated using a variety of techniques, but their two-dimensional analogues are almost entirely absent from the literature due to a scarcity of appropriate numerical methods. This problem is approached using the versatile time-dependent variational Monte Carlo (tVMC) algorithm, supplemented by exact diagonalisation (ED), along with mean-field methods in the metallic limit. These are combined to describe and explain the effects of correlation, dimensionality and simulation parameters on the high harmonic emission. The analysis is performed across correlation regimes, from non-interacting conductors to heavily Mott-insulating systems, with a focus on transitions between these two limits via the photo-induced breakdown of the insulating ground state.

The second research thread moves away from analysing the optical response induced by laser fields, and instead explores ways that the fields can be designed to control the response. This is achieved using so-called current tracking, for which a protocol is derived that provides a prescription for the driving pulse required to generate any predetermined current in any Fermi-Hubbard system. This is implemented using the same combination of tVMC, ED and mean-field methods, along with further techniques that simplify the pulses to within existing experimental capabilities. These are then used to demonstrate near-arbitrary control over the HHG, including directional resolution of Mott transitions along perpendicular directions of the lattice.

Acknowledgements

Firstly, I have to thank my supervisor, George Booth, for his help and support throughout, especially at several key points. I also appreciate his patience during the first year or so while I found my feet, and am thankful for his choice of research topic out of the possibilities that we discussed early on, as it's allowed me to develop a strong interest in a field that I had previously known nothing about. I'd also like to thank Amelle, Gerard and Denys for our productive and interesting collaborations, and extra thanks to Gerard for proof-reading Chapter 5 and offering his useful suggestions. Finally, I'm grateful to Rob and Yannic for introducing me to various tools that have now become indispensable.

Of course I have to thank Jess, and I'm excited for whatever we choose to do next. Most of all though I'd like to express my gratitude to my parents, without whom it's certain I wouldn't have reached this point. If I have children then I will try my best to emulate your parenting and its constant love and support.

Chris A. Orthodoxou
May, 2022

Contents

List of Figures

List of Tables

List of Abbreviations

1D ..... One-Dimensional
2D ..... Two-Dimensional
3D ..... Three-Dimensional
3SM ..... Three Step Model
AFM ..... Antiferromagnetic
BOs ..... Bloch Oscillations
CB ..... Conduction Band
CBM ..... Correlated Bandstructure Model
DHPs ..... Doublon-Hole Pairs
DM ..... Density Matrix
DMFT ..... Dynamical Mean-Field Theory
DOS ..... Density of States
ED ..... Exact Diagonalisation
GS ..... Ground State
HHG ..... High Harmonic Generation
infinite-D ..... Infinite-Dimensional
iTEBD ..... Infinite Time-Evolving Block Decimation
LHB ..... Lower Hubbard Band
mid-IR ..... mid-Infrared
MIs ..... Mott Insulators
MPS ..... Matrix Product States
PWF ..... Pfaffian Wavefunction
QNPs ..... Quantum Number Projectors

RK4 ..... Fourth Order Runge-Kutta
SBE ..... Semiconductor Bloch Equations
SD ..... Slater Determinant
SR ..... Stochastic Reconfiguration
td-DMRG ..... Time-Dependent Density-Matrix Renormalization Group
TDSE ..... Time-Dependent Schrödinger Equation
TDVP ..... Time-Dependent Variational Principle
tVMC ..... Time-Dependent Variational Monte Carlo
UHB ..... Upper Hubbard Band
VB ..... Valence Band
VMC ..... Variational Monte Carlo
XUV ..... Extreme Ultraviolet

Diese Doktorarbeit ist meinen Eltern gewidmet

Αυτή η πτυχιακή εργασία είναι αφιερωμένη στους γονείς μου

1

Introduction

The work presented in this thesis exists at the intersection of two research fields that have typically been pursued independently of each other. The first is strongly-correlated systems, which concerns materials whose properties are critically and qualitatively dependent upon the details of the interactions between their constituent electrons. They have long been the topic of intense research due to their potential to unlock a deeper understanding of various elusive and important phenomena, including superconducting and Mott insulating materials. The latter are materials that are incorrectly predicted to be conductors by conventional band theory descriptions that do not account for the effects of electron correlation. The second field is high harmonic generation (HHG) in solids. This is a highly non-equilibrium effect that occurs when a solid-state system is exposed to an intense laser field, resulting in a strong nonlinear electronic response that induces the emission of large multiples (harmonics) of the incident frequency. Most investigations to date have focused on systems that can be well-approximated by single-particle models in which consideration of electron correlation is either excluded entirely or relegated to the inclusion of phenomenological dephasing terms.

Combining them both to study HHG in strongly-correlated solid-state systems is a challenging problem because it requires calculating the full dynamics of exponentially-scaling systems, and as a result there is a relative scarcity of appropriate numerical methods. The methods that are available have meant that research has been focused on one-dimensional (1D) and infinite-dimensional (infinite-D) lattices, with an almost complete absence of two-dimensional (2D) studies in the literature. The work in this thesis applies a combination of exact, mean-field and stochastic methods to the analysis of HHG in 2D Mott insulating systems, as described by the Fermi-Hubbard

model. This was split into two overlapping research threads that are presented here in Chapters 4 and 5, the first of which uses this full array of methods to study the effects of dimensionality and correlation on the frequency and time-resolved emission, from the metallic through to heavily-insulating limits, but with a focus on the regime in which photo-induced breakdown of the Mott insulating states can occur. The core of these results was recently published in Ref. [1]. Chapter 5 then introduces a protocol for current tracking within these same correlated systems, as first described in Refs. [2, 3]. This provides essentially arbitrary control over their optical response by enabling us to dynamically calculate the so-called control field required to induce any predetermined current in any system. Conclusions and the developed/benchmarked methods from the previous chapter are used to inform understanding of these control fields, which are ultimately used to generate 'directional' phase transitions across the two axes of a square lattice.

1.1 Outline of this Thesis

In Chapter 2, the background and overarching themes of the thesis are discussed. This starts with strongly-correlated systems, where the difficulty of their simulation is explained and the Hubbard model is introduced as a simple but effective way of approximating some aspects of their underlying physics. This is followed by a general discussion of HHG, starting with its origin in atomic gas-phase systems, and moving to its fairly recent demonstration in solids. In both cases, the three-step model (3SM) is defined and explored as a model for the origin of the HHG. A summary is given of the most common numerical methods used to simulate solid-state HHG. This leads on to a discussion of HHG in correlated systems, and a modified Fermi-Hubbard model and current operator are introduced, where the effects of the electric field are accounted for by the Peierls phase. A literature review is then given, which summarises previous approaches to HHG in correlated systems and the main conclusions of their investigations. Finally, some important results concerning photo-induced dielectric breakdown in Mott insulators are summarised.

Chapter 3 details the numerical methods that were developed and applied in this work. This starts with parameterised correlated wavefunctions, where the general

form of the chosen trial wavefunction is stated and its component parts are defined and explained. The stochastic reconfiguration (SR) and variational Monte Carlo (VMC) algorithms are subsequently introduced as ways of optimising a trial wavefunction and using the result to estimate expectation values. This is followed by a discussion of the two methods that were implemented for real-time evolution: time-dependent Variational Monte Carlo (tVMC) and exact diagonalisation (ED), along with the fourth order Runge-Kutta (RK4) method that was used in both cases to perform the time integration. The correlated bandstructure model (CBM) is then introduced and the ideas behind it are explained in detail, followed by a description of its implementation. This includes an analysis of the model's bandstructure, which attempts to mimic that of the full correlated ground state and will be important in future chapters. Finally, it is explained how the expectation of the current operator is used to calculate HHG, including the use of wavelet analysis to time-resolve the emission.

In Chapter 4, the theory and methods discussed so far are applied to the calculation and analysis of HHG in strongly-correlated systems. Firstly, ED is used to generate the evolution of various system observables, which demonstrate the existence of photo-induced Mott transitions. This is followed by an analysis of results that were calculated using a combination of ED, tVMC and mean-field methods, with the general aim of describing and explaining the effects of dimensionality and correlation on the emission in 1D and 2D. The HHG spectra are investigated first, followed by their time resolution in the form of spectrograms. In each case, the discussion is split between the metallic, transition and insulating regimes, i.e. the respective regimes in which Mott breakdowns cannot occur due to an absence of interactions (the systems are already conducting); in which breakdowns can and do occur; and in which they cannot occur because the interactions are too strong to be overcome by the laser field. HHG in the CBM is then presented and analysed, and its comparison with correlated systems is used to draw conclusions about the insulating limit. The final section looks at how the HHG changes as pulse and lattice parameters are varied, starting with the laser's peak field amplitude and frequency, and followed by the hopping and lattice constants. Finally, the chapter is summarised, limitations of the numerical methods are considered and possible improvements are proposed, along with several potential

avenues for future research.

Chapter 5 introduces the concept of current tracking, starting with separate explanations and derivations of the tracking protocols in 1D and 2D, and followed by a discussion of the constraints under which tracking must be done in order to ensure the results are physically reasonable. An ED implementation of tracking is used to demonstrate spectral mimicry using linearly-polarised control fields, where the HHG spectra of two systems are 'swapped' such that a conducting system is made to generate the emission of an insulator and vice versa. This is followed by a general discussion of the control fields that are required in different cases. The experimental feasibility of these driving pulses is then addressed, and fitting models are defined in order to simplify them, which is demonstrated with two examples that show how control fields can be constructed that are experimentally viable while still able to reproduce the main HHG features we are trying to mimic. tVMC is then reintroduced, and the protocol is generalised to include arbitrarily-polarised control fields that are allowed to vary freely in either dimension, thereby enabling the simultaneous tracking of a different current in each direction. This is used to demonstrate so-called directional Mott transitions, which is reproduced with a simpler fitted pulse that is within experimental capabilities. The stability of these results is shown, justifying the use of tVMC for tracking. Finally, tracking is used to demonstrate harmonic enhancement, where the emission intensity of selected harmonics is boosted. The chapter is concluded by an outlook section, where a few of the many potential directions for future research are considered.

The thesis finishes with two appendices. Appendix A is used to benchmark tVMC: firstly, some important aspects of the simulation setup are discussed; this is followed by comparisons between ED and tVMC for 12-site systems, and a discussion of the limitations and applicability of the method; and lastly, convergence of the results with respect to lattice size is checked and discussed. Finally, Appendix B introduces a simple 'harmonic selection' method that is used to recreate a complex case of directional Mott breakdown by easing the restrictions imposed by existing experimental capabilities.

2

Background

2.1 Strongly-Correlated Systems

In general, our aim is to describe, explain and predict the properties of condensed matter systems. Ideally, we would work directly with the full molecular Hamiltonian, which can be written in the form [4]

$$\begin{aligned}\hat{\mathcal{H}} = &-\frac{1}{2}\sum_i \nabla_i^2 - \sum_{i,I}\frac{Z_I}{|\mathbf{r}_i - \mathbf{R}_I|} + \frac{1}{2}\sum_{i\neq j}\frac{1}{|\mathbf{r}_i - \mathbf{r}_j|} \\ &-\sum_I \frac{1}{2M_I}\nabla_I^2 + \frac{1}{2}\sum_{I\neq J}\frac{Z_I Z_J}{|\mathbf{R}_I - \mathbf{R}_J|}\end{aligned} \tag{2.1}$$

where atomic units are used and lowercase denotes electrons and uppercase the nuclei. We could then add terms for e.g. electric and magnetic fields, and evolve the wavefunction in time using the Schrödinger equation[1], thereby generating all knowable information about the system. However, this is infeasible for realistic cases due to reasons that are intrinsic to the formulation of quantum mechanics. The calculation requires accounting for the simultaneous interactions of each part with every other, resulting in a Hilbert space of configurations that scales exponentially with the system size.

This notorious 'curse of dimensionality' necessitates the introduction of approximations. A common and extremely successful method is to consider an independent-particle picture in which the full N_e-electron problem is replaced with N_e separate one-electron problems, where each electron experiences an effective potential that at-

[1]Because this is a non-relativistic setting. The leading order relativistic contribution to the Hamiltonian is the spin-orbit coupling correction.

tempts to mimic the Coulomb interactions of all the other particles. This framework has made significant contributions to our understanding of materials, including the conventional band theory that classifies solids into metals, semiconductors and insulators. However, materials in which electron correlations are strong can give rise to interesting and exotic properties that cannot be explained by a single-particle picture and instead require working in a many-body basis. A famous case is high-temperature superconductivity [5–9], but other examples include colossal magneto-resistance [5] and, most importantly for this thesis, Mott insulators (MIs) [10].

MIs are materials that are predicted to be conductors according to band theory but actually exhibit insulating behaviour as a result of electron-electron interactions. Within the standard single-particle bandstructure picture, status as a conductor or insulator is determined by the occupation of energy levels, i.e. by whether or not there is a gap between the largest occupied and smallest unoccupied states. This description neglects quantum many-body effects and thus fails to accurately model materials such as the transition-metal compounds, which are insulators not due to their mean-field band filling but because of the localisation caused by Coulomb repulsion. Localisation in real space occurs because strong interactions have a large associated energy cost, which makes electron hopping energetically unfavourable. This occurs in conflict with the tendency of electrons to minimise their kinetic energy by delocalising over the lattice, and in fact this competition between kinetic and Coulombic contributions will be an important guiding principle in our description of MIs, as we will see very shortly.

It is clear that we require models that go beyond independent-particle approximations and attempt to include many-body effects. In fact, this need is encapsulated in the historical definition of correlation in which it is described as the difference between the expectation values of the Hartree-Fock and exact wavefunctions [4]. However, any such model will encounter the same problems of dimensionality, and so will inevitably require (often aggressive) approximations and simplifications. The intention is to capture important aspects of the underlying physics that contribute significantly to the quantities of interest. To that end, the famous Fermi-Hubbard model is used throughout this thesis.

2.1.1 The Hubbard Model

The Hubbard model [11–17] has become a paradigmatic framework for correlated systems. Its physical basis is the tussle between competing tendencies that exists in some solids. On the one hand, there is a delocalisation effect due to electron hopping, described in the model by a term $\hat{\mathcal{K}}$, that pushes the system towards a metallic state. On the other hand, repulsive Coulomb interactions, encoded via a term $\hat{\mathcal{U}}$, act as a driver towards localisation, forcing electrons onto different sites and encouraging the formation of an insulating state. The single-band Hubbard model is given by

$$\begin{aligned}\hat{\mathcal{H}} &= \hat{\mathcal{K}} + \hat{\mathcal{U}} \\ &= -t_0 \sum_{\langle ij\rangle\sigma} \hat{c}^\dagger_{i\sigma}\hat{c}_{j\sigma} + U\sum_j \hat{n}_{j\uparrow}\hat{n}_{j\downarrow},\end{aligned} \tag{2.2}$$

This describes itinerant electrons of spin σ that can tunnel between nearest-neighbour sites, denoted $\langle ij\rangle$, thereby gaining an energy given by the hopping constant t_0. They can also interact on a given site with another electron of opposite spin, costing an energy U. These processes are controlled by the creation (annihilation) operators $\hat{c}^\dagger_{j\sigma}$ ($\hat{c}_{j\sigma}$), which obey the canonical commutation relations $\{\hat{c}_{i\sigma}, \hat{c}^\dagger_{j\sigma'}\} = \delta_{ij}\delta_{\sigma\sigma'}$ and $\{\hat{c}_{i\sigma}, \hat{c}_{j\sigma'}\} = \{\hat{c}^\dagger_{i\sigma}, \hat{c}^\dagger_{j\sigma'}\} = 0$. The operators are defined on a basis of Wannier orbitals, such that applying $\hat{c}^\dagger_{j\sigma}$ to the vacuum state creates an electron in a Wannier state centered around site j. The number operator $\hat{n}_{j\sigma} = \hat{c}^\dagger_{j\sigma}\hat{c}_{j\sigma}$ counts the spin-σ electrons on j, and since the model assumes there is only one orbital per site it follows that $\langle \hat{n}_{j\sigma}\rangle \in [0, 2]$, corresponding to an empty, singly or doubly-occupied site.

The full many-body basis is composed of configurations $|x\rangle$ that specify the occupation of the lattice. Given that each site can be in one of 4 states, an L-site system has 4^L possible configurations. However, in this thesis half filling is always used, where $\langle \hat{n}_{j\uparrow}\rangle + \langle \hat{n}_{j\downarrow}\rangle = 1$, and we restrict to the $S_z = 0$ subspace. A general configuration is then constructed as follows

$$|x\rangle = \prod_{n,m=1}^{L/2} c^\dagger_{x_n\uparrow} c^\dagger_{x_m\downarrow} |\underline{0}\rangle \tag{2.3}$$

This reduces the dimension of the Hilbert space to $\binom{L}{L/2}^2$, which is still exponentially

scaling and clearly an impending issue.

Throughout this work, $e = \hbar = m_e = 4\pi\epsilon_0 = 1$ and so factors of these constants are excluded. The energy unit is normalised to the hopping constant, such that $t_0 = 1$ and U therefore represents the ratio U/t_0. The unit of time is then $[t_0^{-1}]$, although it will be presented in plots as cycles of the input pulse. The ratio U/t_0 is an important factor in determining the physics of a system, and there are two clear limiting cases. The first is the non-interacting $U = 0$ regime, which is just the tight-binding model $\hat{\mathcal{K}}$ and represents a metallic state of free electrons given by the Fermi sea of single-particle states. The second is the $U \to \infty$ so-called atomic limit, where the system is an insulator of singly-occupied sites with no charge fluctuations. The existence of these two regimes implies a transition between them for some U_c, and this critical value depends on the spin frustration, dimension and filling. In 1D the system is a metal for all U, with the exception of half filling where it is an insulator for all $U > 0$ [4, 18]. In the infinite-D limit, the critical value at half filling has been shown to exist at $U_c \approx 5.8$ [19].

The model owes its simplicity to a number of approximations [20]. Firstly, it is assumed that on-site interactions are large compared to those between sites, so that $U_{iiii} \to U$ and all other terms are set to zero. This is believed to be true for transition and rare earth metals [18]. Furthermore, hopping is restricted to nearest-neighbour sites and is taken as isotropic, $t_{\langle ij \rangle} \to t_0$. Finally, the Hamiltonian is limited to a single band, which is justified under the assumption that the Fermi surface lies inside a single conduction band (CB). Even with these simplifications, the model can only be solved analytically in the 1D thermodynamic limit using the Bethe ansatz [18, 21–24], and is exactly solvable with DMFT in the limit of infinite-D [25]. No known exact solution exists in any other dimension.

Despite being essentially the simplest possible correlated model, it can still make contact with real physical systems. Depending on geometry and filling, the Hubbard model has been shown to exhibit qualitative trends and phase transitions in strongly correlated materials, including the existence of spin liquids [26] and topological phases, a variety of magnetic orders, phase separation and charge ordering [27]. Simple *sp*-band systems can be approximately mapped to the Hubbard Hamiltonian, for example graphene with weak effective on-site interaction in the region of $U \approx 1.3$

[28] to $U \approx 1.6$ [29], while the experimentally obtained energy gaps of benzene were found to be well-reproduced by $U \approx 1.2$ [28]. It can also model the 2D planes of layered materials such as cuprates and organic charge-transfer salts, materials that can give rise to exotic correlated phases [30, 31], with strongly-correlated cuprate parent materials of high-temperature superconductivity being modelled with $U \sim 8$ [32, 33]. Finally, MIs and their metal-insulator transitions are an important physical realisation of the Hubbard model, for example the transition-metal oxides such as NiO and V_2O_3. These materials have an odd number of electrons per unit cell and therefore a partially filled CB, which causes band theory to incorrectly predict that they are conductors.

2.2 High Harmonic Generation

2.2.1 HHG in Atomic Systems

When an atomic gas is subjected to radiation of sufficiently large laser intensities it can have a nonlinear polarisation response, giving rise to optical effects such as second harmonic generation [34]. This can be described by treating the laser field as a perturbation of the atomic Hamiltonian. Valence electrons are excited to higher-energy states through the stimulated absorption of (often multiple) photons, and ultimately return to the ground state (GS) via emission. The transition rate of an n-photon process for field intensity I is proportional to I^n, so that the probability of an excitation decreases rapidly with the number of required photons, thereby limiting the harmonic orders that can be produced [35, 36].

However, if the electric field strength approaches the order of the atomic bonding strength then perturbation theory becomes inapplicable and new highly nonlinear phenomena can emerge. One such example is HHG, in which an intense incident field of frequency ω_L causes the emission of large odd harmonics of the input frequency. This process was first observed in gases in the 1980s [37], and can produce radiation spanning from the optical into the extreme ultraviolet (XUV).

Gas-phase high harmonic spectra have some general characteristics. The emission intensity can be divided into three regimes, starting with a perturbative region at

low harmonics where the yield decreases exponentially with increasing frequency of the emitted light. There is then a broad plateau of approximately-uniform intensity where the spectrum extends far past the ionisation potential I_p of the parent atom, before dropping suddenly at the cutoff frequency. This cutoff energy is given by $I_p + 3.17U_P$ [38, 39], where $U_P = \frac{E_0^2}{4\omega_L^2}$ is the cycle-averaged kinetic energy of the accelerated electron, known as the ponderomotive energy. The cutoff therefore scales quadratically with the laser's peak field strength, E_0.

These features can be understood through the 3SM [40, 41], in terms of either a semiclassical description [38] or the fully quantum Lewenstein model [42]. This offers an intuitive explanation of the process leading to emission through the following steps

1. **Tunneling:** the laser field distorts the atomic Coulomb potential enough that an electron can tunnel-ionise through the barrier into the continuum.

2. **Acceleration:** the electron is accelerated away from its parent atom and then back towards it as the field direction reverses. The strong-field approximation is used, where it is assumed that the laser field dominates over the ionic potential.

3. **Recombination:** the returning electron recombines with its parent atom and emits radiation with energy given by its kinetic energy plus the ionisation potential. The electron's kinetic energy depends on the ionisation time and it is predicted that the maximum possible value is $3.17U_P$, hence the stated cutoff energy.

Ionisation can be caused by tunneling or multi-photon absorption. The pulse and material parameters in which each of these processes dominate are determined by the dimensionless Keldysh parameter [43]

$$\gamma = \sqrt{\frac{I_p}{2U_P}} \tag{2.4}$$

When $\gamma \ll 1$ the system is in the tunneling regime, whereas when $\gamma \gg 1$ multi-photon ionisation is dominant.

HHG in gas-phase systems is a fundamental tool of attosecond science [44–46]. The high harmonics produced from a laser's interaction with an atom or molecule

carry information about their electronic structure that can be used to image atomic and molecular orbitals, both tomographically [47–50] and with laser-induced electron diffraction [51, 52]. A further development has been the use of HHG to generate attosecond pulses, as either isolated pulses or trains of them, with a wide range of applications relating to the control and time-resolution of attosecond processes [53–57].

2.2.2 HHG in Solids

HHG in bulk periodic solids is a new field, having only been demonstrated for the first time in 2011 in experiments that generated high harmonics by irradiating a ZnO crystal with a mid-infrared (mid-IR) laser [58]. Since then there have been a wealth of interesting results, with HHG studied in a diverse range of systems such as semiconductors [59–64], wide-gap dielectrics [65, 66], graphene [67–71], metamaterials [72], topological materials [73, 74], spin systems [75], thin films [76–78], amorphous materials [79] and rare-gas solids [80]. Furthermore, there is a great deal of interest in the use of HHG as a spectroscopic tool [46, 55, 56, 81, 82], including in the reconstruction of bandstructures [76, 83–85], the probing of crystal lattices and potentials [66, 86–89], and the real-time observation of quantum dynamics [61, 90, 91]. Finally, there are potential technological applications, with hope that solid-state HHG could lead to the development of highly compact XUV sources [46, 81, 92–94] and petahertz electronics [60, 90, 95–99].

2.2.2.1 Origins of HHG in Solids

The experimental studies of solid-state HHG conducted so far have focused on materials whose main properties are not determined by strong electron interactions, which has led to mean-field descriptions in which many-body effects are not considered. The starting point is the single-particle bandstructure, in which a valence band (VB) is separated from an empty CB by a gap, E_g. Only two bands are included here for simplicity, although of course real materials have more complicated structures. Furthermore, this general picture applies to both semiconductors and insulators, as both have their Fermi energy lying between the bands. Intense efforts have been

made to understand how such a system can produce HHG following irradiation by a high-strength laser, and the result is a picture with clear similarities to the atomic 3SM. The process can be summarised as follows [100–107]

1. **Tunneling:** an electron tunnels from the VB to the CB, creating a positively-charged hole in the VB.

2. **Acceleration:** the field accelerates the electron and hole in opposite directions in their respective bands.

3. **Recombination:** the electron returns to the VB by recombining with a hole, emitting a photon with energy given by the instantaneous band separation.

This is depicted in fig.2.1, which shows that there are two mechanisms responsible for emission: interband polarisation and intraband current. The former develops when electron-hole pairs are created and culminates during the recombination step, and is directly analogous to the recollision mechanism that causes HHG in atomic systems. Excitation happens preferentially at the minimum band gap point, as the tunneling probability between states in different bands decays with increasing separation. Electrons are delocalised, so recombination can happen with holes at nearby sites and can take place at any time, as opposed to the atomic case where it only happens if the electron's return trajectory coincides with its parent ion. The interband polarisation has been experimentally observed using attosecond pulses [108–111].

The second source process is the intraband current. It occurs during the acceleration phase, where electrons and holes exhibit highly nonlinear oscillations within their bands, causing emission. Furthermore, if an accelerating electron is driven past the edge of the first Brillouin zone then its quasi-momentum will suddenly reverse sign, causing charge oscillations and therefore emission. These have no equivalent in atomic HHG and are known as Bloch oscillations (BOs), or Bragg scattering in real space, and can happen multiple times per cycle if the field strength is sufficiently large. BOs have been the subject of much theoretical and numerical research [58, 61, 92, 100, 103, 113–115], and have now been directly observed in the lab [65, 76, 116, 117].

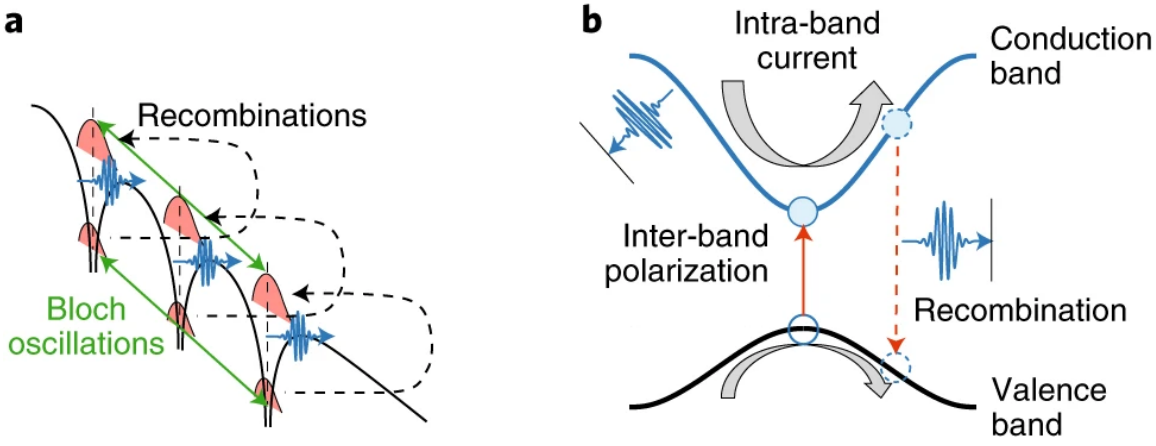

Figure 2.1: **The origin of HHG in solid-state systems.** In periodic solids there are two main emission mechanisms: interband polarisation and intraband current, shown here in real and momentum space. **a)** In real space, an excited electron can recombine with its source hole or a hole in an adjacent site, or can undergo Bragg scattering, which causes rapid oscillation between sites. **b)** In momentum space, polarisation builds between CB electrons and VB holes, leading to recombination. They can also be accelerated within their respective bands, or can wrap back around it through BOs due to the non-parabolic bandstructure. This image was adapted from Ref. [112].

These emission mechanisms are not independent, but are in fact intricately interdependent. After all, intraband currents can only form if interband polarisation exists, as in order for an electron to oscillate in the CB it must have first tunneled there from the VB, leaving behind a hole with which it forms a dipole. Similarly, intraband motion is an important determiner of the recombination energy by shifting the electron to a higher or lower energy state than the one it initially tunneled to. This complex interplay is sometimes explicitly encoded into the models. For example, in the semiconductor Bloch equations, which will be discussed more later, the equations of motion for the intra and interband processes are coupled differential equations which intimately depend upon each other.

The relative contribution and importance of inter and intraband processes is an unresolved problem, and there is research claiming the dominance of each. However, it is important to remember that the emission mechanisms will depend greatly on the pulse parameters and material being studied. In Ref. [118], ZnO was studied in the mid-IR regime and interband polarisation was found to be the dominant process. On

the other hand, intraband currents were the main contribution in the far-IR regime in GaSe [65], and in the near-IR regime in SiO_2 [76] and GaAs [119]. Numerical results in Refs. [101, 102] reproduced this wavelength dependency, finding that interband HHG is dominant in the mid-IR regime and intraband HHG in the far-IR. This could provide a method of experimentally distinguishing and comparing the two contributions. Similarly, Ref. [103] found that the time-frequency signatures of the two mechanisms were extremely different, which again could be used to experimentally distinguish between them to determine their relative importance.

The periodic structure and high density of solids make the microscopic origins of HHG intrinsically different than in gases. The periodic potential challenges the validity of the strong-field approximation, and the system now demonstrates a collective response in which excited electrons can migrate to nearby sites for recombination and scatter off of the potential through BOs. A detailed discussion of the differences between the HHG of solids and gases can be found in Refs. [80, 112, 118, 120], but two particularly important ones are worth mentioning here.

The harmonic spectra of condensed matter systems exhibit a similar plateau structure as found in gases. However, a vital difference is the cutoff energy, which in solids has been found to scale linearly with peak field strength [58, 65, 76, 80], as opposed to the quadratic dependence found in gases and discussed earlier, which immediately suggests differences in the generation mechanisms. Its origin is a matter of debate, but both inter and intraband processes are consistent with a linear dependency in certain cases. The cutoffs observed in Refs. [58, 76] were explained by BOs and were found to be proportional to the Bloch frequency, which is linear in field strength. The same scaling was observed due to interband processes in e.g. Refs. [83, 102, 103], where the cutoff is determined by the band separation induced at the peak field strength. The cutoff is then found to increase linearly with the peak field until the band separation reaches its maximum possible value, given by the distance between the VB and the Brillouin zone edge of the CB. At this point the cutoff does not increase further with field strength [101, 102, 118], unless the model includes multiple bands, in which case a larger peak field generates additional plateaus [80]. This can be understood as the electrons being excited to higher-lying CBs, with each extra plateau having a maximum cutoff determined by the gap between the VB and the edge of the higher

CB [103, 121, 122]. However, it has also been predicted that a higher plateau can arise from BOs, for example Ref. [115] where they used a two-band model in which the primary plateau emerged from interband recollisions but the second plateau from BOs.

2.2.2.2 Modelling HHG in Solids

The following briefly summarises some of the main models that have been developed so far to describe HHG in solids, and is partly based on the more thorough accounts in Refs. [35, 123, 124], where details of the derivations and applications can be found.

Semiclassical Model: In the first observation of solid-state HHG [58] and in later work [76, 125], a simple semiclassical two-step model was proposed in which interband contributions are ignored and emission originates solely from the intraband current within the lowest CB. An electron wavepacket centered at $k = 0$ is driven by a field with peak strength E_0 in a simple 1D band

$$\varepsilon(k) = \sum_n c_n \cos(nka) \tag{2.5}$$

where n is the spatial harmonic, k the quasi-momentum and a the lattice constant. The group velocity is $v_g(k) = d\varepsilon(k)/dk$, resulting in oscillatory movement with amplitude $\alpha = naE_0/\omega_L = n\omega_B/\omega_L$, where ω_B is the Bloch frequency. This anharmonic motion within the bands produces HHG, but if $\alpha > \pi$ then BOs also occur, increasing the harmonic output and demonstrating how the non-parabolic shape of solids' bandstructure causes BOs. The nonlinear current J generates an emission spectrum given by $\mathcal{S}(\omega) = |\mathcal{FT}\{dJ/dt\}|^2$. This has a cutoff proportional to α, which is the correct linear scaling. Despite the simplicity of the model, it showed good agreement with the experimentally-measured cutoff and spectrum of thin-film SiO_2 [76].

Time-Dependent Schrödinger Equation: The Schrödinger equation has been used extensively to study solid-state HHG by neglecting interactions between electrons and treating the solid as a single electron in an effective periodic potential [80, 103, 105, 121, 126]. The one-electron 1D time-dependent Schrödinger equation

(TDSE) describing a laser-solid interaction in the velocity gauge is given by

$$i\partial_t |\psi(t)\rangle = \left[\hat{\mathcal{H}}_0 + \hat{\mathcal{H}}_I(t)\right] |\psi(t)\rangle \tag{2.6}$$

$$= \left[\frac{\hat{p}^2}{2m} + \hat{U}(x) + \frac{1}{m}A(t)\hat{p}\right] |\psi(t)\rangle \tag{2.7}$$

where $\hat{U}(x)$ is the periodic potential and the dipole approximation has been assumed, $A(x,t) \approx A(t)$, as the wavelengths being considered are much larger than the lattice constant. This can be solved using the Bloch basis, which is composed of states $|\phi_{\lambda k}\rangle$, where λ is a band index and $\hat{\mathcal{H}}_0 |\phi_{\lambda k}\rangle = \varepsilon_n(k) |\phi_{\lambda k}\rangle$. The wavefunction for some quasi-momentum, $|\psi_k(t)\rangle$, can then be written in terms of these Bloch states, ultimately permitting the calculation of the laser-induced current for each k channel [103]

$$J_k(t) = -\frac{1}{m}\left[\mathrm{Re}\{\langle\psi_k(t)|\,\hat{p}\,|\psi_k(t)\rangle\} + A(t)\right] \tag{2.8}$$

A common alternative basis is the Houston basis, related to the Bloch basis by $|\tilde{\phi}_{\lambda k_0}(t)\rangle = e^{-iA(t)\hat{x}} |\phi_{\lambda k(t)}(t)\rangle$, where k_0 is the quasi-momentum in the field-free system [124]. The advantage of this formulation is that the current can be separated into explicit intra and interband terms, allowing their individual contributions to be compared (see Refs. [35, 124] for the details).

Semiconductor Bloch Equations: The semiconductor Bloch equations (SBE) [127] are another common approach, and have found widespread application to the description of HHG in solids [61, 100, 115, 127]. The starting point is actually the full many-body Hamiltonian within the second quantisation formalism, including terms for electron Couloumb interactions and the coupling of the system to lattice vibrations [124]. However, these are considered to have only minor effects and are often neglected. In particular, the electron-electron interactions are typically on the order of the exciton binding energy, which makes them very small compared to the light-matter interaction. The SBE are then derived from the Heisenberg equation of motion, and are a system of coupled time-dependent differential equations for the interband polarisation $p_k(t)$ and band occupations $n_k^{e(h)}(t)$ of electrons (holes) in the CB (VB), where we consider here only the 1D two-band version of the model. Electrons are initially filled in the VB, and can then undergo inter and intraband excitations,

producing a macroscopic intraband current $J(t)$ and interband polarisation $P(t)$

$$J(t) = \sum_{\lambda,k} v_k^\lambda n_k^\lambda(t) \tag{2.9}$$

$$P(t) = \sum_k \left(d_k p_k(t) + \text{c.c.}\right) \tag{2.10}$$

where v_k^λ is the group velocity and d_k is the interband dipole matrix element. This is then used to calculate the high harmonic spectrum

$$\mathcal{S}(\omega) \propto |\omega^2 P(\omega) + i\omega J(\omega)|^2 \tag{2.11}$$

This has two distinct contributions from the interband $|\omega^2 P(\omega)|^2$ and intraband $|\omega J(\omega)|^2$ terms, but also includes interference between these terms, reenforcing the fact that they are intrinsically coupled and also somewhat complicating the debate over which process contributes more to the HHG.

A related technique is the two-band density matrix equations [101, 102, 113, 118]. This is the same as the SBE in the single-electron limit and differs from it mostly by a frame transformation. In this model the HHG is calculated from the intraband $\mathbf{J}_{ra}$ and interband $\mathbf{J}_{er}$ current contributions [101]

$$\mathbf{J}_{ra}(t) = \sum_\lambda \int_{\overline{\text{BZ}}} \mathbf{v}_\lambda[\mathbf{K} + \mathbf{A}(t)] n_\lambda(\mathbf{K}, t) d^3\mathbf{K} \tag{2.12}$$

$$\mathbf{J}_{er}(t) = \frac{d}{dt} \int_{\overline{\text{BZ}}} \mathbf{p}(\mathbf{K}, t) d^3\mathbf{K} \tag{2.13}$$

where the quasi-momentum has been transformed to a frame moving with the vector potential $\mathbf{K} = \mathbf{k} - \mathbf{A}(t)$, which also shifts the Brillouin zone $\overline{\text{BZ}} = \text{BZ} - \mathbf{A}(t)$. This model was used in a widely-cited paper analysing HHG in ZnO [101], where it was concluded that the minimum band gap divides the spectrum into perturbative and non-perturbative sectors, with the former dominated by the interband current.

Time-Dependent Density Functional Theory: Ab initio methods based on density functional theory [128] have made important contributions to the study of HHG [107, 122, 129, 130]. These methods include an empirical exchange-correlation functional which approximates the effects of Pauli exchange and electron correlations.

By solving the time-dependent Kohn-Sham equation it is possible to calculate the microscopic current density [124]

$$\mathbf{j}(\mathbf{r},t) = \sum_i \frac{1}{2}\left[\psi_i^*(\mathbf{r},t)(-i\nabla + \mathbf{A}(t))\psi_i(\mathbf{r},t) + \text{c.c.}\right] \tag{2.14}$$

This is then averaged over the unit cell with volume Ω to calculate the macroscopic current density $J(t)$ along polarisation direction $\mathbf{E}_0$

$$J(t) = \frac{1}{\Omega}\int_\Omega d\mathbf{r}\mathbf{j}(\mathbf{r},t)\cdot\mathbf{E}_0/|E_0| \tag{2.15}$$

An interesting application of these methods is Ref. [107], where they studied the microscopic origins of HHG in bulk silicon using first-principles simulations. Most relevant to this thesis was the result that the emission spectrum is not affected by the full evolution of Hartree and exchange-correlation terms. This means that electron-electron interactions are insignificant in this system and justifies the use of the independent-particle approximation, used in the above methods and much of the literature on solid-state HHG. The same conclusion was arrived at in Ref. [122]. This underlies the distinction between the solids and models discussed so far and those that we want to investigate.

2.2.3 HHG in Strongly-Correlated Systems

These models often attempt to account for electron-electron interactions and other many-body effects by including a phenomenological dephasing term T_2, which determines the timescale over which electron-hole coherences are lost. A T_2 that is comparable or smaller than a single pulse cycle suppresses interband recollisions, increasing the contribution from the intraband current, whereas a large T_2 permits multiple recollisions to happen. Although there is debate about the choice of T_2, it is often the case that very small values are chosen. For example, Ref. [61] used $T_2 = 1.1$fs and Ref. [101] found that in order to get agreement with experiments it was necessary to use a value on the order of an optical half cycle, $T_2 \approx 5$fs. This suggests that many-body effects can be important even in weakly-correlated systems. However, we are interested in solids in which electron correlations are the dominant determiner of

the microscopic dynamics, requiring us to go beyond empirical dephasing terms.

2.2.3.1 Modelling HHG in Correlated Systems

We are approximating the interaction of electrons using the one-band Hubbard model, eq.(2.2), but to describe HHG it is also necessary to subject the system to a time-dependent laser field, $\mathbf{E}(t)$. This is introduced via a Peierls substitution of the hopping constant [18, 131]

$$t_0 \to t_0 \exp\left[-i\int_{\mathbf{r_i}}^{\mathbf{r_j}} d\mathbf{r}\cdot\mathbf{A}(\mathbf{r},t)\right] \tag{2.16}$$

where $\mathbf{A}(\mathbf{r},t)$ is the vector potential. Only spatially homogeneous fields will be considered, $\mathbf{A}(\mathbf{r},t) \to \mathbf{A}(t)$, and as a result the magnetic field can be neglected. The Peierls phase is defined as $\Phi(t) = \int_{\mathbf{r_i}}^{\mathbf{r_j}} d\mathbf{r}\cdot\mathbf{A}(\mathbf{r},t)$, but electrons in this model are restricted to discrete lattice sites that are separated by the lattice constant a, and can only hop between adjacent sites. All combined, this means that the Peierls phase simplifies to

$$\mathbf{\Phi}(t) = a\mathbf{A}(t) \tag{2.17}$$

The electric scalar potential can be conveniently removed by choosing the Landau gauge, $\phi(\mathbf{r},t) = 0$. As a result, the electric field, vector potential and Peierls phase are related to each other as follows[2]

$$\mathbf{E}(t) = -\frac{d\mathbf{A}(t)}{dt} \tag{2.18}$$

$$a\mathbf{E}(t) = -\frac{d\mathbf{\Phi}(t)}{dt} \tag{2.19}$$

The result is a modified Hubbard Hamiltonian given by

$$\hat{\mathcal{H}}(t) = \hat{\mathcal{K}}(t) + \hat{\mathcal{U}} \tag{2.20}$$

$$= -t_0 \sum_{\langle ij\rangle\sigma} \left\{ e^{-i\Phi(t)}\hat{c}^\dagger_{i\sigma}\hat{c}_{j\sigma} + e^{i\Phi(t)}\hat{c}^\dagger_{j\sigma}\hat{c}_{i\sigma} \right\} + U\sum_j \hat{n}_{j\uparrow}\hat{n}_{j\downarrow} \tag{2.21}$$

In this model, an electron can hop between nearest-neighbour lattice sites and pick up a complex hopping amplitude scaled by the field at that moment, as well as potentially

[2]Note, it follows directly from their relationship that zeroes in $E(t)$ occur at maxima in $A(t)$.

interact with another electron via the on-site repulsion U. The phase contribution for a hop between sites $i \to j$ along dimension k is the scaled component $\Phi = a\mathbf{A} \cdot \hat{\mathbf{e}}_k$.

Starting from a state $|\Psi(0)\rangle$, it is a far-from-trivial problem to actually use this Hamiltonian to generate the system's dynamics. This will be done using ED and tVMC, both of which will be discussed in detail in the next chapter.

The high harmonic emission originates from the current that is induced by the laser field. In many of the models discussed previously, it was common for the current to be explicitly separated into inter and intraband contributions, with the former expressing dipole polarisation and the latter the nonlinear velocity of electrons and holes; for example, eq.(2.10) and eq.(2.9) from the SBE. The excitation of an electron to the CB does not intrinsically involve motion in real space, and so it makes sense that the two mechanisms can often be written separately. However, in the correlated model eq.(2.21), excitations only form when electrons hop to adjacent sites and interact with other electrons, forming doublon-hole pairs (DHPs). It therefore seems reasonable that the inter and intraband contributions to the current in this model can be subsumed together. With that in mind, the paramagnetic current is given by

$$\hat{\mathcal{J}}(t) = -iat_0 \sum_{\langle ij \rangle \sigma} \left\{ e^{-i\Phi(t)} \hat{c}^\dagger_{i\sigma} \hat{c}_{j\sigma} - e^{i\Phi(t)} \hat{c}^\dagger_{j\sigma} \hat{c}_{i\sigma} \right\} \tag{2.22}$$

This does not explicitly depend on the interaction U but only on the kinetic energy $\hat{\mathcal{K}}(t)$, and can also be defined as $\hat{\mathcal{J}}(t) = -\partial \hat{\mathcal{K}}(t)/\partial A(t)$. A formal derivation starts by evolving the number density operator $\hat{n}_{j\sigma}$ using the Heisenberg equation

$$\frac{d\hat{n}_{j\sigma}(t)}{dt} = i \left[\hat{\mathcal{H}}(t), \hat{n}_{j\sigma}(t) \right] \tag{2.23}$$

The result can be written as a continuity equation, which in 1D takes the form [18]

$$\frac{d\hat{n}_{j\sigma}(t)}{dt} + \hat{J}_{j\sigma}(t) - \hat{J}_{j-1\sigma}(t) = 0 \tag{2.24}$$

where $\hat{J}_{j\sigma}$ is the current per site, given by

$$\hat{J}_{j\sigma} = -it_0 \left\{ e^{-i\Phi(t)} \hat{c}^\dagger_{j\sigma} \hat{c}_{j+1\sigma} - e^{i\Phi(t)} \hat{c}^\dagger_{j+1\sigma} \hat{c}_{j\sigma} \right\} \tag{2.25}$$

Eq.(2.22) is then the total current, $\hat{\mathcal{J}}(t) = -a \sum_{j\sigma} \hat{J}_{j\sigma}(t)$. The emission spectrum is

calculated as

$$\mathcal{S}(\omega) = \left| \mathcal{FT} \left\{ \frac{d\langle \hat{\mathcal{J}}(t) \rangle}{dt} \right\} \right|^2 \tag{2.26}$$

This HHG is averaged over the whole time domain, so information about the instantaneous emission is lost. However, it is still possible to resolve the spectrum in time, and this is discussed in the next chapter.

There is an alternative way of expressing eq.(2.22) that will be extremely useful. In 1D the current operator is

$$\hat{\mathcal{J}}(t) = -iat_0 \sum_{j\sigma} \left\{ e^{-i\Phi(t)} \hat{c}^\dagger_{j\sigma} \hat{c}_{j+1\sigma} - e^{i\Phi(t)} \hat{c}^\dagger_{j+1\sigma} \hat{c}_{j\sigma} \right\} \tag{2.27}$$

We can write the nearest-neighbour hopping expectation in polar form

$$\left\langle \Psi(t) \left| \sum_{j\sigma} \hat{c}^\dagger_{j\sigma} \hat{c}_{j+1\sigma} \right| \Psi(t) \right\rangle = R\left(\Psi\right) \mathrm{e}^{i\theta(\Psi)} \tag{2.28}$$

Substituting this into the current expectation gives

$$\mathcal{J}(t) = -iat_0 R(\Psi) \left(\mathrm{e}^{-i[\Phi(t) - \theta(\Psi)]} - \mathrm{e}^{i[\Phi(t) - \theta(\Psi)]} \right) \tag{2.29}$$

$$= -2at_0 R(\Psi) \sin\left[\Phi(t) - \theta(\Psi)\right] \tag{2.30}$$

This can be generalised to 2D, as will be discussed later. This is the form that was used for nearly all current calculations to come, partly because it has the advantage that it requires evaluating the correlation functions for one direction only, i.e. eq.(2.28) but not the forward hopping expectations. Similarly, the expectation value of the Hamiltonian in eq.(2.21) can be written in terms of eq.(2.28) and the double occupancy, $D = \frac{1}{L} \sum_j \langle \hat{n}_{j\uparrow} \hat{n}_{j\downarrow} \rangle$. In 1D this gives

$$\mathcal{H}(t) = -t_0 R(\Psi) \left(\mathrm{e}^{-i[\Phi(t) - \theta(\Psi)]} + \mathrm{e}^{i[\Phi(t) - \theta(\Psi)]} \right) + U \sum_j \langle \hat{n}_{j\uparrow} \hat{n}_{j\downarrow} \rangle \tag{2.31}$$

$$= -2t_0 R(\Psi) \cos\left[\Phi(t) - \theta(\Psi)\right] + ULD(t) \tag{2.32}$$

with an identical equivalent in 2D.

2.2.3.2 Previous Approaches to Correlated Electron HHG

HHG in strongly-correlated systems is an emerging and challenging field, with many unanswered questions. In this regime a single-particle picture is no longer applicable, and the notion of well-defined band energies becomes blurred because the correlations induce an exponential complexity of splittings in the bands, as well as changing intensities and band positions. The emission mechanisms change in fundamental ways, and the interplay of strong interactions with these intra and interband processes can lead to the emergence of photo-induced collective phenomena and HHG spectra that dramatically diverge from those in atomic and weakly-correlated systems. The total literature so far is fairly sparse compared to the large output of work on HHG in other solids. For numerical studies this is almost certainly due to the difficulty of the simulations, which quickly run up against exponentially-scaling Hilbert spaces. Most research has focused on either 1D systems [132–135], where the matrix product states (MPS) formalism is efficient, or effective infinite-D systems [136–138], where dynamical mean-field theory (DMFT) approaches can be applied [139].

An exception to this is Ref. [140], where they used the time-dependent density-functional theory + U method to investigate HHG in the charge-transfer insulator NiO. They found that the strong laser pulse caused a dramatic decrease in the Hubbard interaction U resulting from increased screening by excited electrons, and that this had a clear impact on the HHG spectrum. This suggests that electronic parameters of correlated materials can be modified by laser driving, which has potential technological applications.

In Ref. [132], ED was used to propagate the TDSE for 1D 12-site MIs, using the Hamiltonian eq.(2.21). They found that the laser field melts the Mott state and that HHG can be used to resolve the many-body dynamics in the frequency and time domains. A major aim of this thesis is to extend these results to 2D, and many of its findings will also be reproduced as part of that analysis. HHG in MIs was further investigated in several other papers. In Ref. [137], DMFT was used to evolve eq.(2.21) with $U = 8$ (mostly) and the addition of a thermal bath of non-interacting electrons. Under an AC field this system reaches a time-periodic non-equilibrium steady state, and several interesting features of the emission spectra emerged. They found that

interband recombination was the dominant process and caused a single plateau to form in the weak-field regime, followed by new plateaus as the field strength was increased, with the m'th plateau originating from the recombination of m'th nearest-neighbour DHPs. In both field regimes the cutoff scaled linearly, as in semiconductors, and there were clear similarities between their analysis and the 3SM. They then introduced a semiconductor model with the same dispersion as the MI, which was found to reproduce some of the MI's HHG characteristics but also persistently showed weaker emission intensity than it. These same methods and models were then used in Ref. [136] to do an in-depth analysis of the non-equilibrium steady states reached in MIs under these conditions. In Ref. [138], DMFT was applied to an electron-plasmon model and a multi-orbital Hubbard model, both of which have dynamics that are influenced by bosonic excitations.

In 1D, MPS-based approaches have been applied to go beyond small system sizes, either in the form of time-dependent density-matrix renormalization group algorithm (td-DMRG) [141] or the infinite time-evolving block decimation (iTEBD) method [142]. The latter was used in Ref. [135] to simulate eq.(2.21) with an extra term describing the effects of a staggered magnetic field, and with the system fixed in the strong correlation regime ($U = 10$). The interband current was again found to be the dominant contribution to the HHG spectra, and was responsible for the frequency range of the plateau, producing a cutoff that scaled linearly with field strength. They then performed a subcycle analysis and showed that important aspects of the DHP dynamics could be reproduced by a semiclassical analysis based on the 3SM. They concluded that the 3SM can be extended to MIs[3], and that there is a strong relationship between the HHG of MIs and the dispersion of DHPs with respect to their relative momentum. Furthermore, they found that the excitation dynamics are not necessarily fully captured by the single-particle spectrum due to the many-body nature of DHPs, and that the relationship between the HHG emission spectrum and the single-particle spectrum can be very different than in semiconductors. In Ref. [134], iTEBD was applied to an interacting spinless-fermion model and the transverse Ising model, both in a 1D dimer lattice. The HHG spectra exhibited threshold behaviour

[3]However, their analysis was limited to the strong-interaction regime, so these conclusions cannot be assumed to be true generally.

arising from the many-body dynamics, which was again explained in terms of a 3SM-like picture involving kink-antikink excitations.

Finally, HHG in Kondo lattice models was investigated in 1D [133] using td-DMRG, and in 2D [143] using tVMC. They simulated a Hamiltonian given by the tight-binding term of eq.(2.21) combined with a Kondo coupling term, and demonstrated that the charge-ordered GS underwent a dynamical phase transition, resulting in a metallic state. They found that the melting of the charge gap resulted in an enhancement of the HHG, and suggested that this could be used to experimentally identify the transition.

HHG in 2D systems is an active area of research with many interesting numerical [69, 144–146] and experimental [68, 77, 147] results. However, HHG in 2D correlated systems remains largely unexplored, especially numerically where there is an almost complete absence of appropriate methods. As far as I am aware, Ref. [143] is the only numerical study, and even in this case the system exhibited only very weak correlations, as evidenced by the tight-binding-esque HHG spectrum. The work in this thesis hopes to make a contribution to the field by extending our understanding of these models and methods to 2D.

2.3 Dielectric Breakdown in Mott Insulators

The quantum phase transition between a Mott insulating state and a conducting metallic state is one of the most widely studied phenomena related to strongly-correlated systems. One method of inducing these transitions is to introduce charge carriers through doping [5]. Another is to decrease the relative importance of Coulomb interactions compared to the electrons' kinetic energy, as described by the ratio U/t_0 in the Hubbard model. This can be achieved by the manipulation of external stimuli, for example temperature and pressure [148], or as will be the focus in this thesis, through photo-irradiation. The use of laser pulses and strong electric fields to melt Mott states is well established and has been demonstrated experimentally, including in Sr_2CuO_2 [149], cuprates [150], VO_2 [151], and ET-F_2TCNQ [152]. In the last section we saw how there is increasing interest in the idea of using HHG to resolve these phase transitions, which will be a recurring theme in this thesis. However, interpret-

ing this information requires an understanding of the physics taking place during the transition.

Dielectric breakdown in band insulators is understood in terms of Zener tunneling, where the electric field excites electrons across the band gap from the VB to the CB, triggering a breakdown [153, 154]. However, in MIs the gap is a many-body effect arising from electron interactions, so we would expect that this Zener breakdown description needs to be modified. The state of research into Mott breakdown is quite similar to that described in the literature review for correlated HHG, in that most studies have used the Hubbard or Hubbard-like models, and have often focused on 1D by using ED [155–157] and/or td-DMRG [158–162], or infinite-D using DMFT [136, 163, 164].

The following is a summary of important results derived in Refs. [161, 165] that will be used extensively in later chapters. These papers investigated dielectric breakdown in 1D MIs using the half-filled Hubbard Hamiltonian eq.(2.21), with analytical calculations performed by a combination of the Landau-Dykhne method and Bethe ansatz, and then compared against td-DMRG simulations. In 1D, the GS is Mott insulating for all $U > 0$ and has short-range antiferromagnetic (AFM) order that grows with increasing U, such that adjacent sites tend to have opposite spins. It is to this system that a subgap laser pulse of frequency ω_L is applied. The strong field excites electrons to overcome the Mott gap $\Delta(U)$ and form DHPs, i.e. doubly-occupied sites and corresponding empty sites, which replace the electron-hole excitations of semiconductors. If $\omega_L > \Delta$ then the system is in the linear response regime. However, we are interested in $\omega_L < \Delta$, where excitations require highly nonlinear processes. The mechanism responsible for these excitations depends on pulse and lattice parameters, as encoded in the Keldysh adiabaticity parameter

$$\gamma = \frac{\omega_L}{\xi E_0} \tag{2.33}$$

where E_0 is the peak field strength and ξ is the correlation length, given by

$$\frac{1}{\xi(U)} = \frac{4}{U}\int_1^\infty \frac{\ln(y+\sqrt{y^2-1})}{\cosh(2\pi y/U)}dy \tag{2.34}$$

in the thermodynamic limit. This describes the typical size of a DHP that has formed

in the GS through a virtual process.

The parameter eq.(2.33) delineates two clear regimes and a crossover region connecting them. Firstly, if $\gamma \ll 1$ then the system is in the tunneling regime, where $\omega_L \ll \Delta$ and the small photon energy means that the DC limit is approached. In this region the field distorts the Hubbard band energies, allowing electrons to tunnel over the gap and create charge carriers in the form of DHPs. The excitation density increases with the field amplitude $E(t)$ until a threshold field value E_{th} is reached, at which point there is a critical density of DHPs, resulting in the dielectric breakdown or 'melting' of the Mott state. This destroys the short-range AFM order and produces a conducting state. The threshold field (i.e. Schwinger limit) can be estimated by

$$E_{th} \approx \frac{\Delta}{2\xi} \tag{2.35}$$

where the Mott gap has the analytic form [166]

$$\Delta(U) = \frac{16}{U} \int_1^\infty \frac{\sqrt{y^2-1}}{\sinh[2\pi y/U]} dy \tag{2.36}$$

and $\Delta \propto U$ when correlations are large. This analysis builds on older work that attempted to tackle the problem by applying the Landau-Zener formalism to the many-body problem [155], despite it having been originally designed for one-body systems. This predicts a quadratic dependence $E_{th} \propto \Delta^2$, which is reproduced by eq.(2.35) in the small-U limit. The correlation length, Mott gap and threshold field are plotted in fig.2.2.

Secondly, when $\gamma \gg 1$ the system is in the multi-photon absorption regime, where the photon energy is large and ω_L is comparable to the gap (although still less than it). There is a Keldysh crossover between these regimes when $\omega_L = \xi E_0$.

Lastly, a particularly important characteristic is that the DHP distribution changes with ω_L. In the tunneling regime, the excitation probability can be approximated by

$$\mathcal{P} \approx \exp\left[-\frac{\pi}{2}\frac{\Delta}{\xi E_0}\right] = \exp\left[-\pi\frac{E_{th}}{E_0}\right] \tag{2.37}$$

This is momentum independent, which leads to uniform occupation of states throughout the 'upper Hubbard band' and has important consequences for high harmonic

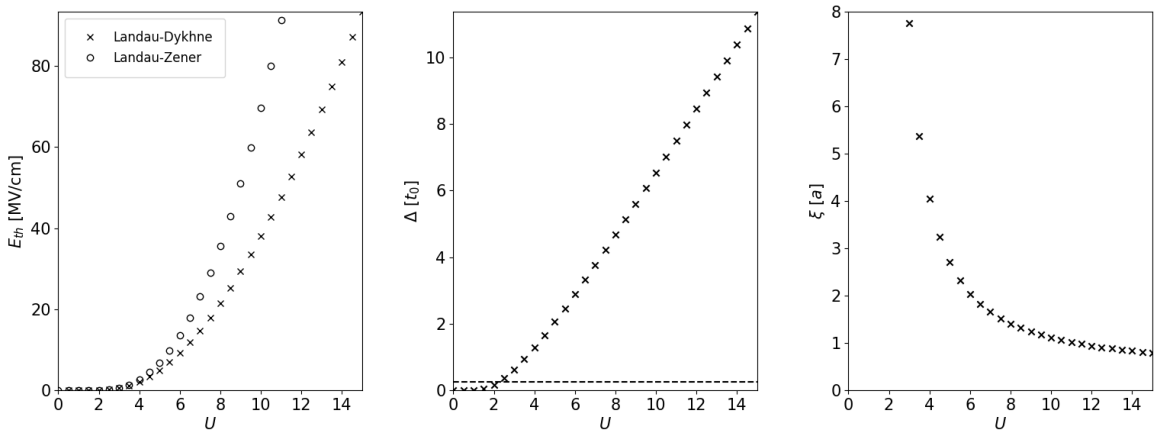

Figure 2.2: **Mott insulators in the 1D Hubbard model.** Threshold field strength (left) for the dielectric breakdown, as predicted by the Landau-Dykhne and Landau-Zener methods using analytical results for the Mott gap (middle) and correlation length (right). The dashed line in the $\Delta(U)$ plot shows $\omega_L = 32.9$THz, demonstrating how small it is compared to the gap (this frequency will be used extensively in Chapter 4).

emission in these systems, as will be discussed later. This is very different than the multi-photon regime, where DHPs are not evenly spread out in momentum space but are instead localised around the gap. We can see this in the tunneling probability, which at $k = 0$ is given by

$$\mathcal{P}_{k=0} \approx \left(\frac{E_0 \xi}{\omega_L} \right)^{2\frac{\Delta}{\omega_L}} \tag{2.38}$$

The exponent, $2\frac{\Delta}{\omega_L}$, is twice the number of absorbed photons, and has the consequence that excitations become clustered near the gap because that is the region that requires the fewest photons to be absorbed.

3

Numerical Methods

3.1 Correlated Wavefunctions

Despite being a simple model of correlation, the Hubbard Hamiltonian has exact solutions with an exponentially-scaling number of basis states, and it is therefore impractical or impossible in most cases of interest to calculate the full correlated wavefunction. Instead, it can be approximated with a parameterised trial wavefunction, $|\Psi\rangle = |\Psi(\alpha_1, ..., \alpha_P)\rangle$, which depends on P variational parameters, $\{\alpha_k\}$, that can be real or complex-valued.

The aim of the trial wavefunction is to capture as much of the system's physics as possible while using a polynomially-scaling number of parameters. The simplest choice would be a mean-field Slater determinant $|\Psi_{MF}\rangle$, with parameters that can be calculated for polynomial cost by the diagonalisation of a one-body Hamiltonian. This is the $U = 0$ solution, and of course contains no information about electron correlations, making it unsuitable for approximating all but the lowest U. We instead adopt a more sophisticated trial wavefunction of general form

$$|\Psi(t)\rangle = \hat{\mathcal{L}}\hat{\mathcal{P}}(t)\,|\phi(t)\rangle \tag{3.1}$$

where $\hat{\mathcal{L}}$ are quantum number projectors, $\hat{\mathcal{P}}(t)$ are correlation factors and $|\phi(t)\rangle$ is a Pfaffian wavefunction.

3.1.1 Pfaffian Wavefunctions

A Pfaffian wavefunction[1] (PWF) offers dramatic improvements over the Slater determinant (SD) description. For our case, where $S_z = 0$ is always true, the anti-parallel PWF is used [168]

$$|\phi(t)\rangle = \left(\sum_{i,j}^{L} f_{ij}(t) \hat{c}_{i\uparrow}^{\dagger} \hat{c}_{j\downarrow}^{\dagger} \right)^{N_e/2} |0\rangle \tag{3.2}$$

where L is the number of sites and N_e the number of electrons. No symmetry constraints are imposed on the variational parameters, $\{f_{ij}\}$, resulting in L^2 parameters that contribute a significant computational burden.

The SD can be expressed within this formulation. By definition it is given by

$$|\Psi_{MF}\rangle = \left(\prod_{n=1}^{N_e/2} \hat{\psi}_{n\uparrow}^{\dagger} \right) \left(\prod_{m=1}^{N_e/2} \hat{\psi}_{m\downarrow}^{\dagger} \right) |0\rangle \tag{3.3}$$

where

$$\hat{\psi}_{n\sigma}^{\dagger} = \sum_{i=1}^{L} \Phi_{in\sigma} \hat{c}_{i\sigma}^{\dagger} \tag{3.4}$$

and the orbital coefficients, $\{\Phi_{in\sigma}\}$, form an orthonormal basis: $\sum_{i=1}^{L} \Phi_{in\sigma} \Phi_{im\sigma} = \delta_{nm}$. It can then be shown that the SD is reproduced when [168]

$$f_{ij} = \sum_{n=1}^{N_e/2} \Phi_{in\uparrow} \Phi_{jn\downarrow} \tag{3.5}$$

The PWF is a generalisation of the SD and is capable of describing states that are inaccessible to the SD description, such as superconducting phases and quantum spin liquid states.

3.1.2 Correlation Factors

We would like to go beyond the SD or PWF and include explicit many-body correlation in the wavefunction. This can be done using correlation factors, which normally take the form of exponentiated two-body operators. The simplest extension is the

[1] In quantum chemistry this is often called the antisymmetrised geminal wavefunction [167].

Gutzwiller factor $\hat{\mathcal{P}}_G$ [169], with a single variational parameter g

$$\hat{\mathcal{P}}_G = \exp\left(-g\sum_{i=1}^{L}\hat{n}_{i\uparrow}\hat{n}_{i\downarrow}\right) \tag{3.6}$$

All correlation factors used in this thesis are diagonal in the basis of real-space configurations: $\hat{\mathcal{P}}\,|x\rangle = \mathcal{P}(x)\,|x\rangle$, for configuration $|x\rangle$. This is vital to ensuring that the overlap can be calculated for polynomial cost. For $\hat{\mathcal{P}}_G$ it follows that

$$\langle x|\hat{\mathcal{P}}_G|\phi\rangle = \exp\left(-gD\right)\langle x|\phi\rangle \tag{3.7}$$

where D is the number of doubly-occupied sites in $|x\rangle$. This shows that $\hat{\mathcal{P}}_G$ penalises double occupancy by assigning configurations with weights that decay exponentially with the value of D, with the intention of accounting for the effect of the Hubbard interaction term. However, this only includes on-site correlation and not correlation between doublons and holons. Once these charge fluctuations form they are free to move unimpeded, producing a conducting state. As a consequence, the Gutzwiller factor alone cannot describe the GS Mott transition in finite dimensions [170, 171], and an insulating state is only obtained in the limit $U \to \infty$, where g diverges and all doublons are excluded, freezing all charge fluctuations. In this limit it is known as the fully-projected Gutzwiller factor and takes the form [170]

$$\hat{\mathcal{P}}_\infty = \prod_i \left(\hat{n}_{i\uparrow} - \hat{n}_{i\downarrow}\right)^2 \tag{3.8}$$

To undergo a Mott transition at finite U the wavefunction must include long-range correlations [170, 172], which can be achieved using the Jastrow factor [173]

$$\hat{\mathcal{P}}_J = \exp\left(-\sum_{i\neq j}^{L} v_{ij}\hat{n}_i\hat{n}_j\right) \tag{3.9}$$

where $\hat{n}_i = \hat{n}_{i\uparrow} + \hat{n}_{i\downarrow}$. The total correlation factor is then

$$\hat{\mathcal{P}} = \hat{\mathcal{P}}_J\hat{\mathcal{P}}_G = \exp\left(-\sum_{i,j}^{L} v_{ij}\hat{n}_i\hat{n}_j\right) \tag{3.10}$$

where $v_{ii} = g$, or alternatively it could be chosen that the on-site parameters are allowed to vary by lattice site. In its most general form with no translational symmetry imposed, $\hat{\mathcal{P}}$ requires $(L^2 + L)/2$ parameters.

We can get a better understanding of how $\hat{\mathcal{P}}_J$ works by rewriting it in terms of doublon $\hat{D}_i = \hat{n}_{i\uparrow}\hat{n}_{i\downarrow}$ and holon $\hat{H}_i = (1 - \hat{n}_{i\uparrow})(1 - \hat{n}_{i\downarrow})$ number operators, such that $\hat{n}_i = 1 + \hat{D}_i - \hat{H}_i$ [174]

$$\hat{\mathcal{P}}_J \propto \exp\left(-\sum_{i\neq j}^{L} v_{ij}\left(\hat{D}_i\hat{D}_j + \hat{H}_i\hat{H}_j - \hat{D}_i\hat{H}_j - \hat{H}_i\hat{D}_j\right)\right) \tag{3.11}$$

The first two terms encode repulsive doublon-doublon and holon-holon correlations, and the latter two are attractive doublon-holon correlations. It is the attractive terms in particular that enable $\hat{\mathcal{P}}_J$ to successfully describe the GS Mott transition [172].

3.1.3 Quantum Number Projectors

For any symmetry of the Hamiltonian there is an associated conserved quantum number. Their conservation must be respected by any exact eigenstate, but this isn't guaranteed by the PWF. The idea behind quantum number projectors (QNPs), $\hat{\mathcal{L}}$, is to enforce conservation and thereby make the variational wavefunction closer to the exact state. As well as conserving known symmetries in the state, it affords the variational wavefunction more flexibility by allowing it to break symmetries in the knowledge that the overall state restores them before minimising the resulting energy. There are no parameters associated with QNPs because they are exact projectors into symmetry sectors of the space. Furthermore, it is important to note that $\hat{\mathcal{L}}$ and $\hat{\mathcal{P}}$ commute (i.e. $\hat{\mathcal{L}}\hat{\mathcal{P}} = \hat{\mathcal{P}}\hat{\mathcal{L}}$) so long as $\hat{\mathcal{P}}$ preserves the symmetries of $\hat{\mathcal{L}}\,|\phi\rangle$.

In this thesis, two QNPs will be used: the momentum projector $\hat{\mathcal{L}}_K$, and the point-group symmetry projector $\hat{\mathcal{L}}_P$. More details about their definition and function can be found in Refs. [168, 174]. $\hat{\mathcal{L}}_K$ projects the wavefunction onto a state with total momentum $\boldsymbol{K}$

$$\hat{\mathcal{L}}_K = \frac{1}{L}\sum_{\boldsymbol{R}} e^{i\boldsymbol{K}\cdot\boldsymbol{R}}\hat{\mathcal{T}}_{\boldsymbol{R}} \tag{3.12}$$

where $\hat{\mathcal{T}}_{\boldsymbol{R}}$ is the translational operator for vector $\boldsymbol{R}$. $\hat{\mathcal{L}}_P$ is given by

$$\hat{\mathcal{L}}_P = \frac{1}{N_g} \sum_{\boldsymbol{p}} g_\alpha(\boldsymbol{p})^{-1} \hat{\mathcal{T}}_{\boldsymbol{p}} \tag{3.13}$$

where $\hat{\mathcal{T}}_{\boldsymbol{R}}$ is the translational operator for vector $\boldsymbol{p}$, $g_\alpha(\boldsymbol{p})$ is the character for point-group operations and N_g is the number of elements in the point group.

$\hat{\mathcal{L}}_K$ requires that translational invariance be enforced in $\hat{\mathcal{P}}$ such that its parameters only depend on the distance between sites, i.e. $v_{ij} \to v_k$. The advantageous consequence of this is that the number of parameters to be optimised is significantly reduced, from $(L^2 + L)/2$ to $L/2 + 2$. Despite this, the application of the QNP is extremely costly and is one of the largest contributions to the overall calculation time. The total number of parameters in the trial wavefunction is then $L^2 + L/2 + 2$, compared with the dimension of the Hilbert space at half filling, $\binom{L}{L/2}^2$.

3.2 Variational Monte Carlo

VMC was first applied to fermionic systems in the 1970s [175] and has since become a widely used way of rapidly calculating expectation values using parameterised trial wavefunctions. VMC is unaffected by the notorious fermion sign problem that plagues other comparable methods such as diffusion Monte Carlo. Furthermore, that the method is based on variational wavefunctions confers both significant advantages and disadvantages. On the one hand, this makes it extremely flexible and widely applicable in ways that are not true with other methods, but it also makes the accuracy of results hostage to the quality of the chosen ansatz. In this thesis, VMC is indispensable as a way of calculating observables both for direct analysis and as important steps in other stochastic methods.

3.2.1 The Metropolis Algorithm

To calculate expectation values with Monte Carlo methods it is necessary to sample from probability distributions $P(x)$ that depend on lattice configurations $|x\rangle$. The Metropolis algorithm [176] is an efficient way of doing this.

In the context considered here, a Markov Chain is a sequence of configurations $\{|x_n\rangle\}$, for $n = 1, .., N_S$, in which each is related to the last by the stochastic hopping of one electron to another site. It is possible to construct a Markov chain whose elements are distributed according to $P(x)$, regardless of the choice of initial configuration $|x_0\rangle$. If the chain is in configuration $|x_{n-1}\rangle$ at step $n-1$, then a new configuration $|x'\rangle$ is proposed according to the transition probability $T(x'|x_{n-1})$, where we consider symmetric probabilities $T(x'|x_{n-1}) = T(x_{n-1}|x')$. The single hop that separates $|x_{n-1}\rangle$ and $|x'\rangle$ is then retained or rejected according to an acceptance condition that is chosen so as to ensure that the configurations are sampled with probability $P(x)$. More precisely, the algorithm works as follows:

Algorithm 1: Metropolis algorithm

Initialise $|x_0\rangle$;
for $(n = 1;\ n = N_s;\ n \mathrel{+}= 1)$**:**
    Propose new configuration $|x'\rangle$;
    $\eta \sim \mathcal{U}(0, 1)$;
    if $(\min\left\{1, \frac{P(x')}{P(x_{n-1})}\right\} > \eta)$**:**
        $|x_n\rangle = |x'\rangle$;
    else:
        $|x_n\rangle = |x_{n-1}\rangle$;

Some initial samples are discarded in order to equilibrate the chain. If the proposed configuration $|x'\rangle$ is more probable than the current one $|x_{n-1}\rangle$ then it is automatically accepted, otherwise it is accepted with probability $\frac{P(x')}{P(x_{n-1})}$. This means that the random walk will tend towards and linger in high-probability regions of the configuration space, while still allowing for the possibility of escape.

The detailed balance condition is given by $P(x \to x') = P(x' \to x)$, i.e. that transitions between $|x\rangle$ and $|x'\rangle$ happen with equal probability in both directions. In the Metropolis algorithm, the correct convergence to $P(x)$ is guaranteed if detailed balance is satisfied, and it can be shown that it is [170]. In fact, the acceptance condition in alg. (1) is designed specifically to enforce detailed balance.

3.2.2 Monte Carlo Calculation of Expectation Values

We can approximate the expectation value of an operator $\hat{\mathcal{O}}$ by sampling only a tiny subset of the exponentially large configuration space. In fact, in the results to come there are 14 orders of magnitude difference between the number of possible lattice configurations and the number of samples taken, and done using a trial wavefunction with only $\mathcal{O}(10^3)$ parameters. This is possible because the central limit theorem dictates the variance of the expected value, and does not explicitly depend on the dimensionality of the space being sampled.

This is achieved by rewriting the expectation as a sum of probabilities multiplied by matrix elements of $\hat{\mathcal{O}}$

$$\langle\hat{\mathcal{O}}\rangle = \frac{\langle\Psi|\,\hat{\mathcal{O}}\,|\Psi\rangle}{\langle\Psi|\Psi\rangle} = \frac{\sum_x \langle\Psi|x\rangle\,\langle x|\hat{\mathcal{O}}|\Psi\rangle}{\sum_x \langle\Psi|x\rangle\,\langle x|\Psi\rangle} \tag{3.14}$$

$$= \sum_x P(x)\mathcal{O}_L(x) \tag{3.15}$$

where the resolution of the identity, $\sum_x |x\rangle\,\langle x| = \mathbb{1}$, was used and

$$P(x) = \frac{|\Psi(x)|^2}{\sum_x |\Psi(x)|^2}, \quad \mathcal{O}_L(x) = \frac{\langle x|\hat{\mathcal{O}}|\Psi\rangle}{\langle x|\Psi\rangle} \tag{3.16}$$

$$= \sum_{x'} \langle x|\hat{\mathcal{O}}|x'\rangle\,\frac{\langle x'|\Psi\rangle}{\langle x|\Psi\rangle} \tag{3.17}$$

where $P(x)$ is a probability distribution as it has only positive values and is normalised, $\sum_x P(x) = 1$. $\mathcal{O}_L(x)$ is known as the local estimator of $\hat{\mathcal{O}}$, and in the case $\hat{\mathcal{O}} = \hat{\mathcal{H}}$ it is known as the local energy, $e_L(x)$. Finally, the expectation is approximated by the average of the local estimator over N_S configurations

$$\langle\hat{\mathcal{O}}\rangle \approx \frac{1}{N_S}\sum_{n=1}^{N_S} \mathcal{O}_L(x_n) \tag{3.18}$$

A path through the configuration space, $\{|x_n\rangle\}$, is taken by sampling $P(x)$ with the Metropolis algorithm, and for each configuration $\mathcal{O}_L(x_n)$ is calculated. The average is then taken over all $\{\mathcal{O}_L(x_n)\}$.

There are two components to the computation of eq.(3.15). The first is sampling

using the Metropolis algorithm, involving terms $\frac{P(x')}{P(x)}$, and the second is the calculation of the local operator, eq.(3.17). Both require finding ratios of the form

$$\frac{\langle x'|\Psi\rangle}{\langle x|\Psi\rangle} = \frac{\langle x'|\mathcal{P}|\phi\rangle}{\langle x|\mathcal{P}|\phi\rangle} = \frac{\mathcal{P}(x')\,\langle x'|\phi\rangle}{\mathcal{P}(x)\,\langle x|\phi\rangle} \tag{3.19}$$

where the PWF overlaps are expressed as Pfaffians: $\langle x|\phi\rangle = (N_e/2)!\mathrm{Pf}(X)$, where X is a $2N_e \times 2N_e$ skew-symmetric matrix. Calculating these ratios for each individual configuration would be extremely costly, but luckily this cost can be considerably reduced for both the Pfaffians and correlation factors by using fast-update schemes that use the fact that $|x\rangle$ and $|x'\rangle$ differ by only one electron hop. Furthermore, the sampling probabilities $\frac{P(x')}{P(x)}$ have the advantage that their potentially costly normalisation factors exactly cancel. And finally, the Hamiltonian and other operators of interest are highly local so that there are few non-zero matrix elements in eq.(3.17) and the sum need only extend over a small number of configurations instead of the whole Hilbert space.

The variance of eq.(3.18) is approximately

$$\sigma^2 \approx \frac{1}{N_S - 1} \sum_{n=1}^{N_S} \left(\mathcal{O}_L(x_n) - \langle\hat{\mathcal{O}}\rangle\right)^2 \tag{3.20}$$

and the error is estimated by $\tilde{\sigma} \approx \sigma/\sqrt{N_s}$. However, this is an underestimation of the true error because it does not account for the correlation that exists between configurations as a result of their origin in a Markov chain, where each sample is generated from the last and nearby samples are therefore not independent. The problem can be resolved using a technique called block analysis [170]. This divides the full set of local estimators $\{\mathcal{O}_L(x_n)\}$ into bins, each of which is averaged over. The resulting data set is approximately independent, and the variance can be calculated in the typical way. The squared error is then given by this variance divided by the number of bins.

3.3 Stochastic Reconfiguration

For a trial wavefunction $|\Psi\rangle = |\Psi(\boldsymbol{\alpha})\rangle$ and the parameters set at some specific values, the GS energy is approximated by

$$\varepsilon' = \frac{\langle\Psi|\,\hat{\mathcal{H}}\,|\Psi\rangle}{\langle\Psi|\Psi\rangle} \tag{3.21}$$

The Hamiltonian has eigenvalues and eigenvectors $\hat{\mathcal{H}}\,|\varepsilon_n\rangle = \varepsilon_n\,|\varepsilon_n\rangle$, with true GS ε_0. By subtracting this from the approximate value ε' it is possible to arrive at an extremely useful conclusion [170]

$$\epsilon = \varepsilon' - \varepsilon_0 \tag{3.22}$$

$$= \frac{\langle\Psi|\,\hat{\mathcal{H}}\,|\Psi\rangle}{\langle\Psi|\Psi\rangle} - \frac{\langle\varepsilon_0|\,\hat{\mathcal{H}}\,|\varepsilon_0\rangle}{\langle\varepsilon_0|\varepsilon_0\rangle} \tag{3.23}$$

$$= \sum_n |\omega_n|^2(\varepsilon_n - \varepsilon_0) \geqslant 0 \tag{3.24}$$

where the expansion $|\Psi\rangle = \sum_n \omega_n\,|\varepsilon_n\rangle$ has been used, with $\sum_n |\omega_n|^2 = 1$. This means that ε' is an upper bound of the exact energy, and therefore that the parameters can be optimised by minimising ε'. Of course, $\epsilon = 0$ only when the variational wavefunction is equal to the exact state.

Only a particular class of wavefunctions are accessible via a given parameterisation, which is a subset of the full class of valid wavefunctions accessible from the underlying Hilbert space. This subset is spanned by $|\Psi(\alpha_1, ..., \alpha_P)\rangle$, for all possible choices of the parameters $\boldsymbol{\alpha} = (\alpha_1, ..., \alpha_P)$. The variational principle dictates that the optimal parameter values for the GS are those that minimise the energy. Carrying out this minimisation is difficult for all but the simplest wavefunctions, e.g. $|\Psi\rangle = \mathcal{P}_G\,|\Psi_{MF}\rangle$, where there is only one parameter, g. In this case, it is just a matter of tracing through values of g, calculating the energy for each and taking whichever gives the smallest answer. However, the wavefunctions used in this thesis require thousands of parameters, making trial-and-error methods completely impossible. This problem was solved using the SR method [177, 178], which can simultaneously optimise tens or even hundreds of thousands of parameters. SR optimisations were carried out using the `mVMC` package [168, 179], which required extending it to

include complex-valued correlation factor parameters.

3.3.1 Derivation

The time-dependent variational principle (TDVP) [180, 181] can be applied in both real and imaginary time, which are related by $\tau = it$. SR requires working in the latter, where the Schrödinger equation is given by

$$\frac{d\,|\Psi(\boldsymbol{\alpha}(\tau))\rangle}{d\tau} = -\hat{\mathcal{H}}\,|\Psi(\boldsymbol{\alpha}(\tau))\rangle \tag{3.25}$$

The TDVP can then be used to derive the SR update equations [168, 182]. The aim is to calculate the parameters such that the difference between the two sides of eq.(3.25) is minimised

$$\min_{\boldsymbol{\alpha}} \left\| \frac{d\,|\Psi(\boldsymbol{\alpha}(\tau))\rangle}{d\tau} + \hat{\mathcal{H}}\,|\Psi(\boldsymbol{\alpha}(\tau))\rangle \right\| \geqslant 0 \tag{3.26}$$

where the equality holds only for the exact solution. The normalised wavefunction is

$$|\bar{\Psi}(\boldsymbol{\alpha}(\tau))\rangle = \frac{|\Psi(\boldsymbol{\alpha}(\tau))\rangle}{\sqrt{\langle\Psi(\boldsymbol{\alpha}(\tau))|\Psi(\boldsymbol{\alpha}(\tau))\rangle}} \tag{3.27}$$

and has imaginary-time evolution given by

$$\frac{d\,|\bar{\Psi}(\boldsymbol{\alpha}(\tau))\rangle}{d\tau} = \sum_k \dot{\alpha}_k\,|\partial_{\alpha_k}\bar{\Psi}(\boldsymbol{\alpha}(\tau))\rangle \tag{3.28}$$

$$= -\left(\hat{\mathcal{H}} - \langle\hat{\mathcal{H}}\rangle\right)|\bar{\Psi}(\boldsymbol{\alpha}(\tau))\rangle \tag{3.29}$$

The TDVP then becomes

$$\min_{\boldsymbol{\alpha}} \left\| \sum_k \dot{\alpha}_k\,|\partial_{\alpha_k}\bar{\Psi}(\boldsymbol{\alpha}(\tau))\rangle + (\hat{\mathcal{H}} - \langle\hat{\mathcal{H}}\rangle)\,|\bar{\Psi}(\boldsymbol{\alpha}(\tau))\rangle \right\| \geqslant 0 \tag{3.30}$$

Minimising this 'distance' gives

$$\sum_k \dot{\alpha}_k \mathrm{Re}\left\{\langle\partial_{\alpha_k}\bar{\Psi}|\partial_{\alpha_m}\bar{\Psi}\rangle\right\} = -\mathrm{Re}\left\{\langle\bar{\Psi}|(\hat{\mathcal{H}} - \langle\mathcal{H}\rangle)|\partial_{\alpha_m}\bar{\Psi}\rangle\right\} \tag{3.31}$$

The parameters are written as real because their real and imaginary parts are treated separately during calculations with no loss of generality. To write this in a useful

form it is necessary to define the derivative operators

$$\hat{\mathcal{O}}_k = \sum_x \left(\frac{1}{\langle x|\Psi\rangle} \frac{\partial \langle x|\Psi\rangle}{\partial \alpha_k} \right) |x\rangle \langle x| \tag{3.32}$$

$$= \sum_x \mathcal{O}_k(x) |x\rangle \langle x| \tag{3.33}$$

Finally, eq.(3.31) gives

$$\dot{\alpha}_k = -\sum_m S^{-1}_{km} g_m \tag{3.34}$$

and by discretising time we obtain a linear system of equations for the parameter updates

$$\Delta\alpha_k = -\Delta\tau \sum_m S^{-1}_{km} g_m \tag{3.35}$$

where

$$S_{km} = \mathrm{Re}\left\{ \langle \partial_{\alpha_k} \bar{\Psi} | \partial_{\alpha_m} \bar{\Psi} \rangle \right\} \tag{3.36}$$

$$= \mathrm{Re}\,\langle \hat{\mathcal{O}}^*_k \hat{\mathcal{O}}_m \rangle - \mathrm{Re}\,\langle \hat{\mathcal{O}}_k \rangle \,\mathrm{Re}\,\langle \hat{\mathcal{O}}_m \rangle \tag{3.37}$$

$$g_m = \mathrm{Re}\left\{ \langle \bar{\Psi} | (\hat{\mathcal{H}} - \langle \hat{\mathcal{H}} \rangle) | \partial_{\alpha_m} \bar{\Psi} \rangle \right\} \tag{3.38}$$

$$= \mathrm{Re}\,\langle \hat{\mathcal{H}} \hat{\mathcal{O}}_m \rangle - \langle \hat{\mathcal{H}} \rangle \,\mathrm{Re}\,\langle \hat{\mathcal{O}}_m \rangle \tag{3.39}$$

The elements of the matrix $\boldsymbol{S}$ and vector $\boldsymbol{g}$ are calculated using the Markov chain Monte Carlo method.

3.3.2 Implementation

Calculating the $\mathcal{O}_k(x)$ terms in eq.(3.33) requires taking the derivatives $\partial_{\alpha_k} \langle x|\Psi\rangle$ with respect to variational parameters α_k. If $\alpha_k \in f_{ij}$ from eq.(3.2) then derivatives of Pfaffians must be taken, which requires a fairly complicated calculation, the details of which can be found in Ref. [168]. However, terms involving the correlation factor are just derivatives of the expectation of the exponential eq.(3.10), and therefore only require evaluating simple correlation functions that are diagonal in the configuration basis.

The stochastic reconfiguration algorithm can be summarised as follows:

Algorithm 2: Stochastic reconfiguration

Initialise $\boldsymbol{\alpha}(0)$;

for $(\tau = 0;\ \tau = \Delta\tau * N_{\text{opt}};\ \tau \mathrel{+}= \Delta\tau)$**:**

Sample configurations: $\{|x_n\rangle\}$, $n = 1, ..., N_S$;

VMC: $\left\{\langle \hat{\mathcal{O}}_k^* \hat{\mathcal{O}}_m\rangle\,, \langle \hat{\mathcal{O}}_k\rangle\,, \langle \hat{\mathcal{H}}\hat{\mathcal{O}}_k\rangle\,, \langle \hat{\mathcal{H}}\rangle\right\}$;

Solve system: $\Delta\boldsymbol{\alpha} = -\Delta\tau \boldsymbol{S}^{-1}\boldsymbol{g}$;

Update parameters: $\boldsymbol{\alpha}(\tau + \Delta\tau) = \boldsymbol{\alpha}(\tau) + \Delta\boldsymbol{\alpha}$;

$N_{\text{opt}} \geqslant 2000$ optimisation steps were used, which is enough for the system to comfortably converge for the cases studied here. At each step, there is a warm-up period of 10 samples that are discarded in order to equilibrate the chain, and the number of samples (i.e. the chain length) was chosen depending upon the number of parameters in the trial wavefunction, which is determined by the size of the system. More details are discussed in Appendix A for the specific cases in this thesis. Finally, the parameter values for the last 10% of the optimisation steps were averaged over to give the optimised GS wavefunction.

3.4 Time-Dependent Variational Monte Carlo

In SR, the system is propagated in imaginary time and therefore approaches the GS, whereas evolution in tVMC allows us to calculate the full dynamics of systems whose size makes them inaccessible to exact diagonalisation methods. A major advantage of the method is that there is no inherent restriction on dimensionality, unlike other prominent methods such as td-DMRG (which is mostly limited to 1D) and DMFT approaches (which works in infinite dimensions). tVMC was originally applied to bosonic systems [183, 184], before being extended to interacting fermionic systems [185], and is now being combined with and improved upon using machine learning techniques [186–189].

When used with a sufficiently sophisticated parameterised wavefunction, tVMC is able to accurately describe a variety of time-dependent phenomena [143, 183–

191]. However, the ansatz is very much the limiting factor, and failure to include appropriate correlations or symmetries will restrict the accuracy of results and the applicability of the method. Of course, it is computationally costly to introduce more parameters or number projectors, as well as the fact that redundant parameters can deteriorate statistics, and so there is a balancing act which depends on the quantities and systems that are being studied. All calculations in this thesis involving SR and tVMC were performed using the following ansatz

$$|\Psi(t)\rangle = \hat{\mathcal{L}}_K \hat{\mathcal{L}}_P \hat{\mathcal{P}}(t) \, |\phi(t)\rangle \tag{3.40}$$

This was chosen because it combines high accuracy with computational cost which, while still significant, does not preclude simulating system sizes well beyond what is possible with exact methods.

tVMC was implemented by the author by extending the `mVMC` package [168, 179]. The ultimate goal of this was to calculate the real-time evolution of the expectation of the current operator, given by eq.(2.22), which was done using the VMC functionality of the `mVMC` package. More details of this process are described shortly.

3.4.1 Derivation

The dynamics of the system is contained within the trajectories of the parameters $\boldsymbol{\alpha}(t)$. To derive their equation of motion, we start from the Schrödinger equation with a time-dependent Hamiltonian and apply the TDVP

$$\min_{\boldsymbol{\alpha}} \left\| \frac{d \, |\Psi(\boldsymbol{\alpha}(t))\rangle}{dt} + i\hat{\mathcal{H}}(t) \, |\Psi(\boldsymbol{\alpha}(t))\rangle \right\| \geqslant 0 \tag{3.41}$$

We can then proceed as was done for SR by normalising the wavefunction. Equivalently, the norm-independent TDVP can be used [180, 185], which enforces the conservation of the norm

$$\min_{\boldsymbol{\alpha}} \left\| \left(1 - \frac{|\Psi(\boldsymbol{\alpha}(t))\rangle \langle \Psi(\boldsymbol{\alpha}(t))|}{\langle \Psi(\boldsymbol{\alpha}(t)) | \Psi(\boldsymbol{\alpha}(t)) \rangle} \right) \left[\frac{d \, |\Psi(\boldsymbol{\alpha}(t))\rangle}{dt} + i\hat{\mathcal{H}}(t) \, |\Psi(\boldsymbol{\alpha}(t))\rangle \right] \right\| \geqslant 0 \tag{3.42}$$

Carrying out this minimisation leads to

$$\dot{\alpha}_k = -i \sum_m S^{-1}_{km} g_m \tag{3.43}$$

This is very similar to eq.(3.34), with the crucial difference that the parameters are now necessarily complex, unlike in SR where it is optional (if the Hamiltonian is real). Deriving the update equations using the TDVP is the preferred method here because it underlines the connection between the tVMC and SR methods. A closely related, and more common, derivation is done by minimising the Euclidean distance in Hilbert space between the exact and variational wavefunctions [170, 183]. Alternatively, it can also be derived using the principle of stationary action [170].

3.4.2 Implementation

It would be preferable to implement tVMC in a similar way as alg. (2) on page 50, using the simple Euler method. This is an intuitive and easy-to-implement integration scheme, but suffers from aggressive error accumulation: the local truncation error, which is the error per timestep, is $\mathcal{O}(\Delta t^2)$, and the global truncation error is $\mathcal{O}(\Delta t)$. This is sufficiently accurate for GS optimisation in SR because the final state does not depend on the specific optimisation path in imaginary time. It can also provide sufficient accuracy for real-time evolution in tVMC for some cases, but not for the simulation of HHG in the required parameter regimes, where the Hamiltonian and wavefunction change exceptionally rapidly. Instead, eq.(3.43) was evolved using RK4, which requires four recursive integration steps instead of just one like in the Euler method, but has a local truncation error of $\mathcal{O}(\Delta t^5)$ and a global error of $\mathcal{O}(\Delta t^4)$. While the extra steps are obviously computationally expensive, its significant improvements in accuracy and stability mean that a larger timestep can be used. tVMC has other sources of error besides the choice of trial wavefunction and the integration method, most significant of which are stochastic errors from the Monte Carlo calculation of $\boldsymbol{S}$ and $\boldsymbol{g}$, and errors due to the discretisation of time into increments Δt. The required timestep and number of Monte Carlo samples depended on the system's correlation strength and size, and are discussed in Appendix A.

The combination of tVMC and RK4 was implemented as follows:

Algorithm 3: Time-dependent variational Monte Carlo

Definition: $\boldsymbol{f}(\boldsymbol{\alpha}, t) = -i\boldsymbol{S}^{-1}\boldsymbol{g}$;
Propagate in imaginary time to optimise GS, $\boldsymbol{\alpha}(0)$;
for $(t = 0;\ t = T;\ t \mathrel{+}= \Delta t)$**:**
Sample configurations: $\{|x_n\rangle\}$, $n = 1, ..., N_S$;
VMC: correlation functions, $\{\langle \hat{c}^\dagger_{i\sigma}\hat{c}_{j\sigma}\rangle\}$;
//First RK4 step;
VMC: $\left\{\langle \hat{\mathcal{O}}^*_k\hat{\mathcal{O}}_m\rangle, \langle\hat{\mathcal{O}}_k\rangle, \langle\hat{\mathcal{H}}(t)\hat{\mathcal{O}}_k\rangle, \langle\hat{\mathcal{H}}(t)\rangle\right\}$;
$\boldsymbol{\kappa_1} = \Delta t\boldsymbol{f}(\boldsymbol{\alpha}, t)$;
//Second RK4 step;
VMC: $\left\{\langle \hat{\mathcal{O}}^*_k\hat{\mathcal{O}}_m\rangle, \langle\hat{\mathcal{O}}_k\rangle, \langle\hat{\mathcal{H}}(t+\Delta t/2)\hat{\mathcal{O}}_k\rangle, \langle\hat{\mathcal{H}}(t+\Delta t/2)\rangle\right\}$;
$\boldsymbol{\kappa_2} = \Delta t\boldsymbol{f}(\boldsymbol{\alpha} + \boldsymbol{\kappa_1}/2, t + \Delta t/2)$;
//Third RK4 step;
VMC: $\left\{\langle \hat{\mathcal{O}}^*_k\hat{\mathcal{O}}_m\rangle, \langle\hat{\mathcal{O}}_k\rangle, \langle\hat{\mathcal{H}}(t+\Delta t/2)\hat{\mathcal{O}}_k\rangle, \langle\hat{\mathcal{H}}(t+\Delta t/2)\rangle\right\}$;
$\boldsymbol{\kappa_3} = \Delta t\boldsymbol{f}(\boldsymbol{\alpha} + \boldsymbol{\kappa_2}/2, t + \Delta t/2)$;
//Fourth RK4 step;
VMC: $\left\{\langle \hat{\mathcal{O}}^*_k\hat{\mathcal{O}}_m\rangle, \langle\hat{\mathcal{O}}_k\rangle, \langle\hat{\mathcal{H}}(t+\Delta t)\hat{\mathcal{O}}_k\rangle, \langle\hat{\mathcal{H}}(t+\Delta t)\rangle\right\}$;
$\boldsymbol{\kappa_4} = \Delta t\boldsymbol{f}(\boldsymbol{\alpha} + \boldsymbol{\kappa_3}, t + \Delta t)$;
Update parameters: $\boldsymbol{\alpha}(t+\Delta t) = \boldsymbol{\alpha}(t) + \frac{1}{6}\left(\boldsymbol{\kappa_1} + 2\boldsymbol{\kappa_2} + 2\boldsymbol{\kappa_3} + \boldsymbol{\kappa_4}\right)$;

The one-body correlation functions, $\{\langle \hat{c}^\dagger_{i\sigma}\hat{c}_{j\sigma}\rangle\}$, are required to calculate the current eq.(2.22), and are evaluated by taking $\hat{\mathcal{O}} = \hat{c}^\dagger_{i\sigma}\hat{c}_{j\sigma}$ in eq.(3.14). Furthermore, in order to speed up calculations, configurations are sampled once at the beginning of each timestep instead of at each individual RK4 step. However, this does not cause significant loss of accuracy, despite a small degree of statistical correlation between the evaluations of the functions required in the RK4 steps.

3.5 Exact Diagonalisation

It is a fundamental principle of quantum mechanics that quantum states evolve in time according to the Schrödinger equation, and so by integrating this forward we can calculate our model's dynamics in full. Of course, if this were achievable in general then entire branches of computational condensed matter physics would not need to exist. The reality is that classical computers struggle to simulate quantum systems, and ED is limited to a small number of sites. This is a consequence of the Hilbert space, whose dimension scales as $\dim(L) = \binom{L}{L/2}^2$. This is still exponential despite the symmetry imposed by the $S_z = 0$ requirement and the constraints of half filling and conserved electron number. For $L = 6$, dim $= 400$ and so the evaluation and propagation of the exact GS can be carried out very rapidly, but doubling the system to $L = 12$ requires handling complex-valued arrays with over 850,000 elements. This is made more challenging by the long timescales that are required, and this combined with rapidly-changing quantities of interest necessitates the use of small timesteps. It was found that $L = 14$ is the largest that is practically possible to simulate, which makes a 4×3 lattice the largest possible in 2D. As a result, all ED simulations in this thesis were with 12-site systems.

Despite these strict limitations on system size, ED is still an extremely useful method. Firstly, it provides a means of benchmarking tVMC to judge its accuracy before it is applied to larger systems. Secondly, ED can be used in situations where tVMC cannot, e.g. in regimes where stochastic noise limits its usefulness.

The aim is to 'exactly' solve the Schrödinger equation

$$\frac{d\,|\Psi(t)\rangle}{dt} = -i\hat{\mathcal{H}}(t)\,|\Psi(t)\rangle \tag{3.44}$$

for the Hamiltonian $\hat{\mathcal{H}}(t)$ with explicit time dependence. The initial state $|\Psi(0)\rangle$ is always taken as the GS, and is calculated using the full configuration interaction method [192].

One possible method would be to expand the general solution as follows:

$$|\Psi(t+\Delta t)\rangle = e^{-i\hat{\mathcal{H}}\Delta t}\,|\Psi(t)\rangle \tag{3.45}$$

$$= \sum_n \left(\frac{-i\hat{\mathcal{H}}\Delta t}{n!}\right)^n |\Psi(t)\rangle \tag{3.46}$$

and then select a cutoff order N beyond which the expansion is truncated. This does not require the full diagonalisation of the Hamiltonian, but instead only the repeated application of $\hat{\mathcal{H}}(t)$ to $|\Psi(t)\rangle$.

Instead of this, eq.(3.44) was solved by once again making use of RK4 integration, where each timestep requires four applications of $\hat{\mathcal{H}}(t)$ to $|\Psi(t)\rangle$, as follows:

Algorithm 4: Exact evolution

Calculate GS, $|\Psi(0)\rangle$;
for $(t=0;\ t=T;\ t \mathrel{+}= \Delta t)$**:**
  Expectation values: $\langle\hat{\mathcal{J}}\rangle$, $\langle\hat{\mathcal{H}}\rangle$, etc;
  $|\kappa_1\rangle = -i\Delta t\hat{\mathcal{H}}(t)\,|\Psi(t)\rangle$;
  $|\kappa_2\rangle = -i\Delta t\hat{\mathcal{H}}(t+\Delta t/2)\{|\Psi(t)\rangle + |\kappa_1\rangle/2\}$;
  $|\kappa_3\rangle = -i\Delta t\hat{\mathcal{H}}(t+\Delta t/2)\{|\Psi(t)\rangle + |\kappa_2\rangle/2\}$;
  $|\kappa_4\rangle = -i\Delta t\hat{\mathcal{H}}(t+\Delta t)\{|\Psi(t)\rangle + |\kappa_3\rangle\}$;
  $|\Psi(t+\Delta t)\rangle = |\Psi(t)\rangle + \frac{1}{6}(|\kappa_1\rangle + 2\,|\kappa_2\rangle + 2\,|\kappa_3\rangle + |\kappa_4\rangle)$;

No terms are truncated, but instead errors of order $\mathcal{O}(\Delta t^5)$ accumulate at each timestep due to the RK4 scheme. A timestep $\Delta t = 0.01$ was normally taken, as it was found that decreasing it further did not change the results. This step size is also sufficient to ensure that the norm is conserved, as the propagator is not strictly symplectic. Finally, expectation values are calculated by simply contracting the operator with the full wavefunction, e.g. $\langle\hat{\mathcal{H}}(t)\rangle = \langle\Psi(t)|\hat{\mathcal{H}}(t)|\Psi(t)\rangle$.

3.6 Correlated Bandstructure Model

The HHG produced by an irradiated correlated material originates ultimately from the interacting many-body dynamics of the system. However, the GS single-particle

bandstructure, and in particular the Mott gap, often plays a central role in investigations of the mechanisms responsible for emission. With that in mind, we introduce a novel effective single-particle model to explore the extent to which the opening of a gap changes the HHG beyond the simple tight-binding spectrum, and to what extent it can account for the observed features of the HHG as correlation and dimensionality are changed, but also the limitations of such a model and what that teaches us.

3.6.1 Bandstructure Engineering

The idea behind the CBM is to map the full driven Hubbard Hamiltonian onto a simple non-interacting model. Specifically, we aim to map features of the correlated GS bandstructure onto the spectrum of a non-interacting single-particle model, whose mean-field dynamics and HHG emission spectrum can then be calculated exactly.

This is done by starting with the tight-binding model and introducing fictitious auxiliary degrees of freedom. For an incident laser pulse with Peierls phase $\Phi(t)$, the Hamiltonian is given by

$$\begin{aligned}\hat{\mathcal{H}}(t) = &- t_0 \sum_{\langle ij\rangle\sigma} \left\{ e^{-i\Phi(t)} \hat{c}^\dagger_{i\sigma} \hat{c}_{j\sigma} + e^{i\Phi(t)} \hat{c}^\dagger_{j\sigma} \hat{c}_{i\sigma} \right\} \\ &+ V(U) \sum_{i\sigma} \left\{ \hat{c}^\dagger_{i\sigma} \hat{f}_{i\sigma} + \hat{f}^\dagger_{i\sigma} \hat{c}_{i\sigma} \right\} \\ &- \frac{U}{2} \sum_{i\sigma} \left\{ \hat{c}^\dagger_{i\sigma} \hat{c}_{i\sigma} + \hat{f}^\dagger_{i\sigma} \hat{f}_{i\sigma} \right\}\end{aligned} \tag{3.47}$$

where the fermionic operators $\hat{f}^{(\dagger)}$ couple each physical site to a corresponding auxiliary one with a strength determined by the parameter $V(U)$. The fictitious system hybridises with the physical lattice, mimicking the band splitting caused by true correlations. A second band is then formed by tracing out the auxiliary degrees of freedom, which opens an effective Mott gap, $\tilde{\Delta}(U)$.

We require a systematic way of uniquely mapping $U \to V(U)$, i.e. of fixing the non-interacting model for a given correlated system. This was done using the first spectral moment of the GS particle and hole density of states (DOS). This is the mean of the particle and hole distributions, and can be thought of as the centre of the Hubbard band. It is first calculated for the correlated system and then $V(U)$ is

optimised to reproduce it in the CBM.

We only need to consider the mean of the hole DOS, as symmetry then constrains the particle one. In the correlated system, the spectral moment can be written as an expectation of the GS wavefunction [193–195]

$$T = \frac{1}{L}\mathrm{Tr}\big[\langle\Psi_0|\hat{c}^\dagger_\beta[\hat{c}_\alpha,\hat{\mathcal{H}}]|\Psi_0\rangle\big] \tag{3.48}$$

$$= -\frac{t_0}{L}\sum_{\langle\alpha\beta\rangle}\rho_{\alpha\beta} + U\left(2D - \frac{1}{2}\right) \tag{3.49}$$

where $\rho_{\alpha\beta}$ is the one-body density matrix (DM), with $\{\alpha,\beta\}$ labelling spin orbitals, and D is the GS double occupancy. This is calculated by VMC using the GS wavefunction, itself optimised with SR. For small systems it can also be calculated exactly by diagonalising the full Hamiltonian, and it was found that doing this for 12 and 16-site systems gives moments that closely match those from VMC for much larger systems, with the exception of the 4×3 lattice which had some (fairly minor) differences.

The mean-field moment in the CBM is given by

$$\mathcal{T}_{MF} = \frac{2}{L}\sum_{\alpha}\sum_{\varepsilon_j<\mu} C_{\alpha j}C_{\alpha j}(\varepsilon_j - \mu) \tag{3.50}$$

where μ is the chemical potential and $(\boldsymbol{C};\varepsilon)$ are the eigenvectors and eigenvalues of eq.(3.47), i.e. the Hamiltonian of the combined physical $\oplus$ auxiliary system. The scalar-valued parameter $V(U)$ is optimised by simply tracing through possible values, calculating $\mathcal{T}_{MF}$ for each and matching it to the moment of the correlated system. At $U=0$, the Hubbard Hamiltonian reduces to the tight-binding model, so it must be that $V(0)=0$ and eq.(3.47) is exact. $V(U)$ then steadily increases with increasing U, as larger correlations cause the Mott gap to grow and the Hubbard bands to move further apart, increasing $\mathcal{T}$.

It is possible to write the dispersion in a compact form by Fourier transforming eq.(3.47) at $t=0$

$$\hat{\mathcal{H}}(\boldsymbol{k}) = \sum_{\boldsymbol{k}\sigma}\begin{pmatrix}\hat{c}^\dagger_{\boldsymbol{k}\sigma} & \hat{f}^\dagger_{\boldsymbol{k}\sigma}\end{pmatrix}\begin{pmatrix}e(\boldsymbol{k})-\frac{U}{2} & V(U)\\ V(U) & -\frac{U}{2}\end{pmatrix}\begin{pmatrix}\hat{c}_{\boldsymbol{k}\sigma}\\ \hat{f}_{\boldsymbol{k}\sigma}\end{pmatrix} \tag{3.51}$$

where $e(\boldsymbol{k})$ is the dispersion of the tight-binding model for dimension d

$$e(\boldsymbol{k}) = -2t_0 \sum_{n=1}^{d} \cos[\boldsymbol{k}_n a] \tag{3.52}$$

The dispersion $\varepsilon(\boldsymbol{k})$ satisfies $\det(\boldsymbol{H} - \varepsilon\mathbb{1}) = 0$, where

$$\boldsymbol{H} = \begin{pmatrix} e(\boldsymbol{k}) - \frac{U}{2} & V(U) \\ V(U) & -\frac{U}{2} \end{pmatrix} \tag{3.53}$$

Solving this leads to

$$\varepsilon(\boldsymbol{k}) = \frac{1}{2}\left(\alpha(\boldsymbol{k}) \pm \sqrt{\alpha^2(\boldsymbol{k}) + 4\beta(\boldsymbol{k})}\right) \tag{3.54}$$

where

$$\alpha(\boldsymbol{k}) = e(\boldsymbol{k}) - U \tag{3.55}$$

$$\beta(\boldsymbol{k}) = V^2(U) + \left(e(\boldsymbol{k}) - \frac{U}{2}\right)\frac{U}{2} \tag{3.56}$$

The plus and minus terms of eq.(3.54) are the CB and VB, respectively. The dispersion is shown in fig.3.1 for 1D and 2D at $U = 0$, 3, 7, corresponding in 1D to $V \approx 0$, 1.3, 3.3 and in 2D to $V \approx 0$, 1.1, 3.1.

Furthermore, the spectral function can be used to estimate the GS bandstructure

$$A(\omega) = -\frac{1}{\pi L}\mathrm{Tr}\left[\mathrm{Im}\left\{G(\omega + i\lambda)\right\}\right] \tag{3.57}$$

where λ is the broadening parameter and $G(\omega) = \hat{P}(\omega\mathbb{1} - \hat{\mathcal{H}})^{-1}\hat{P}$ is the one-body Green's function, with $\hat{P}$ a projection operator into the physical lattice. Examples of the resulting DOS are plotted in fig.3.2, again for effective $U = 0$, 3, 7 in both 1D and 2D.

Fig.3.1 and fig.3.2 mimic features of the correlated GS spectrum. They show that the introduction of the parameter $V(U)$ causes the formation of an effective Mott gap, $\tilde{\Delta}(U)$, separating the occupied ($\omega < \mu$) and unoccupied ($\omega > \mu$) states. In 1D, the Hubbard GS is described by the Bethe ansatz, resulting in Mott gaps given by eq.(2.36) and a dispersion that can also be written in closed form [18, 165]. In 2D, the Hubbard GS cannot be described analytically, but there have been numerous

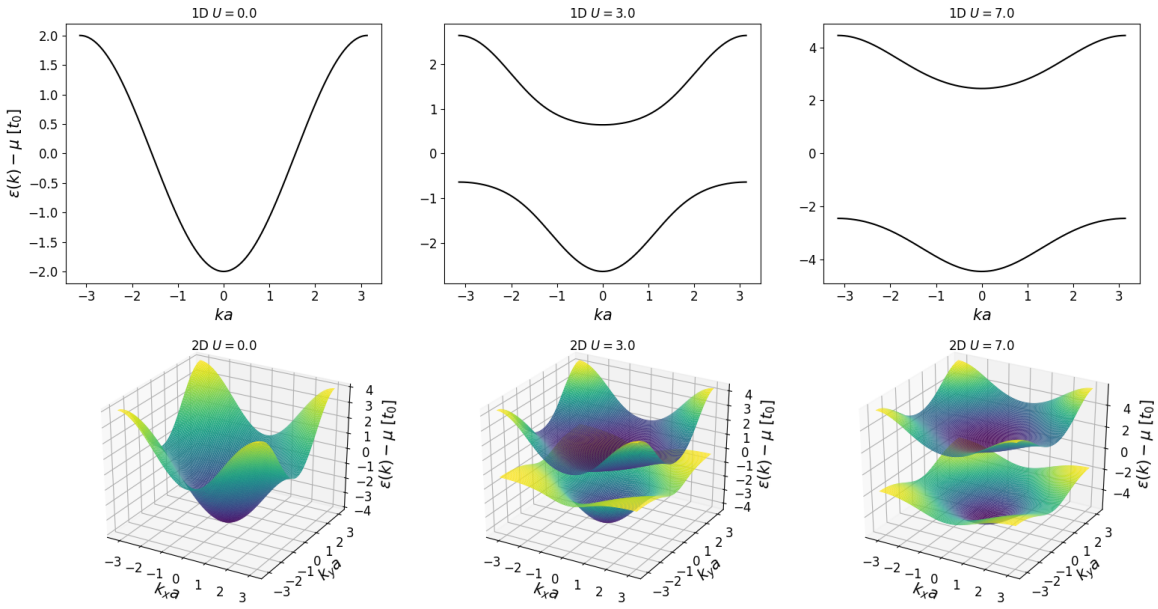

Figure 3.1: **Effects of correlation and dimensionality on the dispersion in the CBM.** Energy as a function of quasi-momentum in 1D (top) and 2D (bottom) estimated using eq.(3.54) for $U = 0$, 3, 7, corresponding in 1D to $V \approx 0$, 1.3, 3.3 and in 2D to $V \approx 0$, 1.1, 3.1.

investigations into its proprieties, including for small systems using ED [196, 197] and in the thermodynamic limit using cluster perturbation theory [198, 199].

Despite the CBM's many approximations, fig.3.1 and fig.3.2 reproduce important qualitative features of the correlated bandstructure. In particular, they predict that the gap is larger in 1D for all U, which agrees with results from cluster perturbation theory and the Bethe ansatz [198, 199], and that the bandwidth is twice as large in 2D. Furthermore, the 2D DOS in fig.3.2 correctly replicate the distinctive Van Hove singularities near the gap, which are far more pronounced than in 1D [196, 197]. These GS characteristics have key implications for any subsequent HHG, and will appear frequently in the coming analysis. However, the CBM's 1D gap predictions were compared against the equivalent analytical values from eq.(2.36) and were found to be overestimates for all correlation strengths, i.e. $\tilde{\Delta}(U) > \Delta(U)$, which implies that the 2D predictions are also overestimates. The CBM is therefore not suitable for making precise predictions at a given U, but is instead useful for analysing broad qualitative trends and the relationships between GS properties and the HHG.

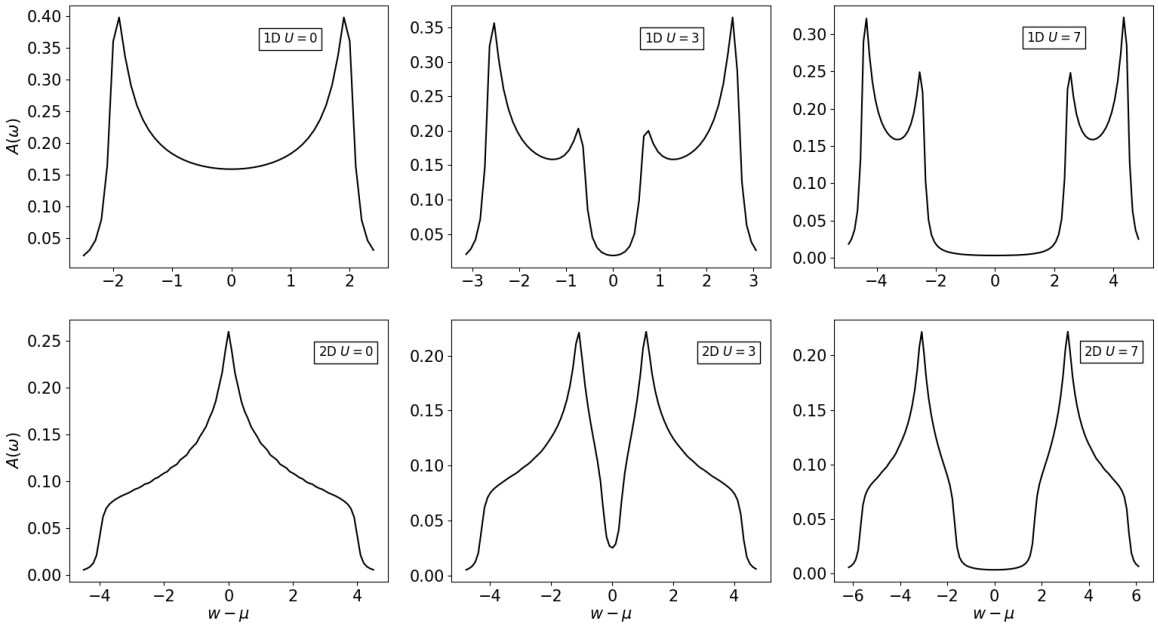

Figure 3.2: **Effects of correlation and dimensionality on the bandstructure in the CBM.** The DOS in 1D (top) and 2D (bottom) estimated using eq.(3.57) with $\lambda = 0.1t_0$ for $U = 0$, 3, 7, corresponding in 1D to $V \approx 0$, 1.3, 3.3 and in 2D to $V \approx 0$, 1.1, 3.1.

3.6.2 Time Evolution

Once $V(U)$ has been optimised for a given U, Hartree-Fock methods from the `PySCF` package [192] are used to calculate the GS one-body DM of the physical $\oplus$ auxiliary system, $\hat{\rho}_{P+A}$. The dynamics of the GS are then given by the Von Neumann equation

$$\frac{\partial \hat{\rho}_{P+A}(t)}{\partial t} = -i\left[\hat{\mathcal{H}}_{P+A}(t), \hat{\rho}_{P+A}(t)\right] \tag{3.58}$$

where $\hat{\mathcal{H}}_{P+A}(t)$ is eq.(3.47). The propagation was carried out using RK4, where at each timestep the reduced DM of the physical system, $\hat{\rho}_P(t)$, is calculated by tracing out the auxiliary degrees of freedom, which is then used to calculate the current and any other observables of interest. This can be summarised as follows:

Algorithm 5: Evolution in the correlated bandstructure model

Mean-field DM, $\hat{\rho}_{P+A}(0)$;
for $(t = 0;\ t = T;\ t \mathrel{+}= \Delta t)$**:**
$\hat{\rho}_P(t) = \mathrm{Tr}_A\left[\hat{\rho}_{P+A}(t)\right]$;
Expectation values: $\langle\hat{\mathcal{J}}\rangle$, $\langle\hat{\mathcal{H}}_P\rangle$, etc;
$\kappa_1 = -i\left[\hat{\mathcal{H}}_{P+A}(t), \hat{\rho}_{P+A}(t)\right]$;
$\kappa_2 = -i\left[\hat{\mathcal{H}}_{P+A}(t + \Delta t/2), \hat{\rho}_{P+A}(t) + \kappa_1/2\right]$;
$\kappa_3 = -i\left[\hat{\mathcal{H}}_{P+A}(t + \Delta t/2), \hat{\rho}_{P+A}(t) + \kappa_2/2\right]$;
$\kappa_4 = -i\left[\hat{\mathcal{H}}_{P+A}(t + \Delta t), \hat{\rho}_{P+A}(t) + \kappa_3\right]$;
$\hat{\rho}_{P+A}(t + \Delta t) = \hat{\rho}_{P+A}(t) + \frac{1}{6}\left(\kappa_1 + 2\kappa_2 + 2\kappa_3 + \kappa_4\right)$

It is instructive to decompose eq.(3.47) into four distinct quadrants, representing the connections between the physical and auxiliary degrees of freedom

$$\hat{\mathcal{H}}_{P+A}(t) = \begin{pmatrix} \hat{\mathcal{H}}_P(t) & V(U)\mathbb{1} \\ V(U)\mathbb{1} & -\frac{U}{2}\mathbb{1} \end{pmatrix} \tag{3.59}$$

$\hat{\mathcal{H}}_P(t)$ is the Hamiltonian of the physical lattice, and is given by the tight-binding term of eq.(3.47) shifted down the diagonal by the single particle chemical potential, $-\frac{U}{2}\sum_{i\sigma}\hat{c}^\dagger_{i\sigma}\hat{c}_{i\sigma}$. Furthermore, the chemical potential term for the auxiliary degrees of freedom ensure the conservation of particle number, but also have the consequence that the number of electrons in the auxiliary space equals that of the physical space, which therefore requires doubling the total number of electrons to be propagated. However, the computational cost of evolution is still small, and the main limiting factor is the memory involved in the mean-field calculation of the GS.

Many of the required expectation values can be calculated by taking the trace, e.g. $\langle\hat{\mathcal{J}}\rangle = \mathrm{Tr}[\hat{\rho}_P\hat{\mathcal{J}}]$. For other observables, we can make use of the mean-field nature of the method to write two-body expectation values in terms of the elements of the one-body reduced DM. Doing this for the double occupancy gives $D = \frac{1}{L}\sum_j\langle\hat{n}_{j\uparrow}\hat{n}_{j\downarrow}\rangle = \frac{1}{L}\sum_i\langle\hat{n}_{i\uparrow}\rangle\langle\hat{n}_{i\downarrow}\rangle$. These number operators are the diagonal elements of $\hat{\rho}_P$ and are constant, giving $D = \frac{1}{L}\sum_i(\frac{1}{2})^2 = 0.25$ and ensuring that D is constant for all $V(U)$,

and therefore also in the Hubbard model at $U = 0$. This shows that while the CBM can attempt to mimic the one-body properties of the system (e.g. the Mott gap), it is not designed to correctly describe two-particle properties such as $D(t)$. Furthermore, the nearest-neighbour spin-spin correlation is defined as

$$\eta = \frac{1}{dL} \sum_{\langle ij \rangle} \langle \hat{\boldsymbol{S}}_i \cdot \hat{\boldsymbol{S}}_j \rangle \tag{3.60}$$

for dimension d. This can be simplified to the form

$$\eta = \frac{3}{2dL} \sum_{\langle ij \rangle} \left(\langle \hat{n}_{i\uparrow} \hat{n}_{j\uparrow} \rangle - \langle \hat{n}_{i\uparrow} \hat{n}_{j\downarrow} \rangle \right) \tag{3.61}$$

which can then be decomposed as follows

$$\eta = \frac{3}{2dL} \sum_{\langle ij \rangle} \Big(\langle \hat{n}_{i\uparrow} \rangle \langle \hat{n}_{j\uparrow} \rangle - \langle \hat{c}^\dagger_{i\uparrow} \hat{c}_{j\uparrow} \rangle \langle \hat{c}^\dagger_{j\uparrow} \hat{c}_{i\uparrow} \rangle - \langle \hat{n}_{i\uparrow} \rangle \langle \hat{n}_{j\downarrow} \rangle \Big) \tag{3.62}$$

3.7 Emission Resolution

Irradiation causes the creation and acceleration of charge excitations, which subsequently emit light. In both of our models, eq.(2.21) and eq.(3.47), information about this HHG is encoded in the current, eq.(2.22). The dipole acceleration is given by

$$a(t) = \frac{d \langle \hat{\mathcal{J}}(t) \rangle}{dt} \tag{3.63}$$

The Fourier transform is then used to extract the frequency content of the signal, from which the HHG spectrum is calculated as follows

$$\mathcal{S}(\omega) = |\mathcal{FT}\{a(t)\}|^2 \tag{3.64}$$

These spectra can suffer from spectral leakage, which is a numerical artifact of the discrete Fourier transform and has the effect of introducing spurious frequency components that obscure structure, particularly at low intensities. Welch's method can be used to deal with this problem by dividing the time series into blocks, calculating the spectrum of each block and then averaging. In general this method was not used, but will be explicitly stated in cases where it is.

Spectra of this type tell us no information about how the emission changes in time. This is particularly important for photo-induced Mott transitions, as eq.(3.64) is completely blind to them but they could be directly observed with an appropriate time resolution. The Gabor transform [200] is the most commonly used method of time-dependent analysis for HHG, e.g. in Refs. [132, 201]. It is a Fourier transform but on a signal that has been acted upon by a Gaussian window $g(t-\tau)$, thereby introducing a dependence on not just frequency but also time. It takes the form

$$a(\omega, \tau_n) = \mathcal{FT}\left\{a(t)g(t-\tau_n)\right\} \tag{3.65}$$

$$g(t-\tau_n) = \exp\left(-\frac{(t-\tau_n)^2}{\sigma^2}\right) \tag{3.66}$$

where time and therefore frequency have been discretised, and $\mathcal{FT}\{...\}$ represents the discrete Fourier transform. The window function at a given τ_n localises the signal in time around that point, with the variance σ^2 determining the degree of localisation. Decreasing σ^2 narrows the window and improves time resolution, but at the expense of frequency resolution. This trade-off is dictated by the generalised uncertainty principle, which puts a limit on how much information can be simultaneously extracted in the frequency and time domains. Conversely, increasing the variance widens $g(t-\tau)$ and therefore improves the frequency resolution while also leaking temporal information, such that in the limit $\sigma^2 \to \infty$ the window widens to encompass the entire signal and the Fourier transform is recovered. By tracing through τ_n the window slides over the signal, localising it at each point and then transforming it to extract frequency information.

A significant improvement on this can be achieved with the discrete wavelet transform, which takes the convolution of a wavelet $\psi(\eta)$ with the acceleration [202]

$$a(s_k, t_n) = \sum_{t_{n'}=0}^{N-1} a(t_{n'})\psi^*\left[\frac{(t_{n'}-t_n)\Delta t}{s_k}\right] \tag{3.67}$$

where $s_k = \omega_0/\omega_k$ are the wavelet scales, with non-dimensional constant ω_0 that is used to control the relative time-frequency resolution. These scales are a generalisation of the width σ^2 in the Gabor transform. Their important feature is that they are not constant but instead vary depending on the frequency, such that the width is

wide for low ω_k, where the time resolution does not need to be high, and is conversely narrow for high ω_k, where time resolution does need to be good. This allows it to capture information for frequencies that might have fallen out of the range of the Gabor transform.

The Gabor and wavelet transforms were implemented[2] and compared. The latter was found to give superior time and frequency resolution, and captured features of the HHG that were lost or obscured by the Gabor transform, e.g. peaks that are narrow in the frequency domain and emission at very low harmonics. These are structures that will play an important part of the coming discussion, and so wavelet analysis was chosen to generate all spectrograms in this thesis. Throughout, the wavelet $\psi(\eta)$ was taken as a Morlet wavelet, which is a plane wave modulated by a Gaussian. A common alternative is the Ricker wavelet, which was also tried but was found to be less effective for the required cases. Regardless of the method used, once the acceleration has been time-resolved the spectrum is calculated as follows

$$\mathcal{S}(\omega, t) = |a(w, t)|^2 \tag{3.68}$$

This allows us to build a heatmap of the emission, at each timestep providing the generated harmonics and their intensity of emission.

[2]Wavelet analysis was done by adapting and extending [203].

4

High Harmonic Generation in Correlated Systems

In this chapter, HHG in correlated 1D and 2D systems is investigated using the Fermi-Hubbard model, given by eq.(2.21), combined with the effective single-particle model in eq.(3.47), with the aim of understanding in detail how correlation and dimensionality impact the high harmonic emission. The backbone of the analysis is based on the results in Ref. [1]. The effects of varying pulse and lattice parameters are also explored, and the chapter is concluded by a discussion of potential directions for future research.

We consider a monochromatic driving pulse of frequency ω_L and peak field strength E_0, acting on a system with lattice constant a. The vector potential has peak value $A_0 = E_0/\omega_L$, and is composed of a sinusoidal carrier wave and sin-squared envelope function $f(t)$, together giving a pulse of the form

$$A(t) = A_0 f(t) \sin[\omega_L t] \tag{4.1}$$

$$= \frac{E_0}{\omega_L} \sin^2\left[\frac{\omega_L t}{2N_c}\right] \sin[\omega_L t] \tag{4.2}$$

where $N_c = 10$ is the number of cycles. The Peierls phase is $\mathbf{\Phi}(t) = \Phi(t)\hat{\boldsymbol{e}} = aA(t)\hat{\boldsymbol{e}}$, where $\hat{\boldsymbol{e}}$ controls the polarisation. In 2D, we take the pulse to be applied along the diagonal, $\hat{\boldsymbol{e}} = (1, 1)$, such that both directions are subject to the same field at all times. Unless otherwise stated, the following system and pulse setup is used. The lattice parameters are chosen as $a = 4$Å and hopping constant $t_0 = 0.52$eV, which means that the non-interacting single-particle bandwidth of the material in 1D and 2D is ~ 2eV and ~ 4eV respectively, where the bandwidth is $W = 4dt_0$ for dimension d. Atomic units are used ($e = \hbar = 1$), and the energy unit is set as the hopping constant,

such that $t_0 = 1$. The mid-IR frequency and peak field strength are $\omega_L = 32.9$THz and $E_0 = 10\text{MVcm}^{-1}$, which in our t_0-normalised atomic units are $\omega_L = 0.262$ and $E_0 = 5.325$, along with lattice constant $a = 1.444$. This corresponds to a total pulse duration of $T = \frac{2\pi N_c}{\omega_L} \approx 300$fs. These are all experimentally realistic values that have been used in past studies [61, 204]. Finally, periodic boundary conditions are maintained throughout for 1D chain and 2D square lattice systems.

Simulations were carried out using tVMC with 36-site lattices, which is comparable to or larger than was used in the related literature that was discussed in Sec. 2.2.3.2. Appendix A gives more details about the simulation setup, as well as benchmarking results and demonstrations of the convergence of the HHG with system size. However, throughout this chapter the tVMC simulations are supplemented by ED calculations performed on 12-site systems. This was done in regimes where tVMC is not accurate, or on occasions where a very large data set was required that made using tVMC impractical. These limitations and regimes of applicability are discussed further in Appendix A. Despite their small size, the 12-site systems used in ED have emission spectra that reproduce the important qualitative and quantitative features observed in the larger systems, and so are considered a useful and valid part of the analysis. In the one case where the small system size does cause an issue, it will be accounted for and does not change the conclusions of the analysis.

4.1 Photo-Induced Mott Transitions

As discussed in Sec. 2.3, quantum tunneling is the dominant excitation process when $\gamma \ll 1$, where γ is the Keldysh adiabaticity parameter, defined by eq.(2.33). In 1D, our choice of parameters puts the system deep in the tunneling regime. For example, at $U = 5$ and 7 the Keldysh parameter is $\gamma \approx 0.125$ and 0.2 respectively, and the crossover point at $\gamma = 1$ isn't reached until $U \approx 85$! As would be expected in this regime, the frequency is small compared to the Mott gap[1], with $\omega_L > \Delta(U)$ only for weak correlation strengths, when approximately $U < 2$. It is reasonable to suspect that 2D systems are also in the tunneling regime, although this cannot be confirmed

[1]This is shown in fig.2.2.

analytically as there are no equivalent expressions for the gap and correlation length. As long as the 2D gaps are not radically different than 1D's then we would expect it to remain in the same regime, because the probability of excitation by multi-photon absorption decreases exponentially with the number of absorbed photons, $N_\gamma \sim \Delta/\omega_L$, and this number must be large if $\omega_L \ll \Delta$. However, we can check that it is true in 2D by observing dielectric breakdowns with threshold behaviour, which are present in the tunneling regime and have been observed in numerical studies in not only 1D [165] but also infinite-D systems [136, 137, 163].

The THz pulse is in the DC limit and can be considered quasi-static because the timescale of electron hoppings is small compared to a laser cycle. Recall that the correlation length ξ describes the approximate effective separation of a virtual DHP in the GS such that it becomes on-shell. We can think of E_{th} as the minimum field strength that separates the charge carriers by the distance $\xi \sim \Delta/E_{th}$ required to distinguish them. Another way of understanding it is that the static component of the field distorts the Hubbard bands and E_{th} can then induce tunneling by providing an energy $\xi E_{th} \sim \Delta$ that is comparable to the gap. In 1D this threshold field can be estimated by eq.(2.35) and occurs at a time t_c, which is related to the vector potential by $E_{th}(t_c) = -dA(t_c)/dt$. This leads to

$$\frac{\Delta}{2\xi} = -E_0 \left[\sin^2\left(\frac{\omega_L t_c}{2N_c}\right) \cos(\omega_L t_c) + \frac{1}{2N_c} \sin\left(\frac{\omega_L t_c}{N_c}\right) \sin(\omega_L t_c) \right] \tag{4.3}$$

which can be solved for t_c numerically. For the stated parameters, eq.(4.3) predicts that transitions can happen up to $U \approx 6$, beyond which the correlations are too strong for the breakdown to occur.

As will be discussed later, it is possible to clearly observe these transitions in the frequency-time domain. However, insight can also be gained by propagating observables that are not experimentally accessible. Firstly, the double occupancy calculates the average number of DHPs per site

$$D(t) = \frac{1}{L} \sum_{j=1}^{L} \left\langle \hat{c}^\dagger_{j\uparrow} \hat{c}_{j\uparrow} \hat{c}^\dagger_{j\downarrow} \hat{c}_{j\downarrow} \right\rangle = \frac{1}{L} \sum_{j=1}^{L} n_{j\uparrow} n_{j\downarrow} \tag{4.4}$$

And the energy is simply

$$\varepsilon(t) = \langle \Psi(t) | \hat{\mathcal{H}}(t) | \Psi(t) \rangle \tag{4.5}$$

Changes in the magnetic order can be observed using the nearest-neighbour spin-spin correlation per bond

$$\eta(t) = \frac{1}{dL} \sum_{\langle ij \rangle} \left\langle \hat{\boldsymbol{S}}_i \cdot \hat{\boldsymbol{S}}_j \right\rangle \tag{4.6}$$

for dimension d. In 1D this is

$$\eta(t) = \frac{1}{L} \sum_{j} \left\langle \hat{\boldsymbol{S}}_j \cdot \hat{\boldsymbol{S}}_{j+1} \right\rangle \tag{4.7}$$

Finally, the overlap probability allows us to track the persistence of the GS

$$W(t) = | \langle \Psi(0) | \Psi(t) \rangle |^2 \tag{4.8}$$

These observables are plotted in fig.4.1 and fig.4.2 for 1D and 2D. In the 4×3 square lattice there is an artificial phase transition in the GS at $U \approx 6$. This arises from frustration in the y-direction that prohibits the formation of AFM order. It can be seen most clearly in the spin correlation in fig.4.2, where there is a sharp decrease in the GS value for $U > 6$, followed by evolution that in some cases is quite erratic. This transition is due to the small system size in the y-direction, which is confirmed by GS ED calculations with the 4×4 lattice and VMC calculations with various larger lattices, which all show that the transition is not present in the thermodynamic limit. To compensate for this, the equivalent tilted lattice system with unit cell (4,0) (3,3) is also included. Frustration does not develop in this system and it can therefore support perfect antiferromagnetism, resulting in no artificial GS phase transition. This means that for some of these observables the tilted lattice is potentially a better representation of the square system in the thermodynamic limit. However, it is important to note that even with the GS transition the conclusions of the analysis are not fundamentally changed.

Fig.4.1 shows the time-dependence of $D(t)$ and $\varepsilon(t)$ and their variation with correlation and dimensionality, and fig.4.2 similarly shows $\eta(t)$ and $W(t)$. The system begins in its GS, which at $U > 0$ is a MI with AFM order that increases with U, corresponding to decreasing double occupancy. This means that interactions force the

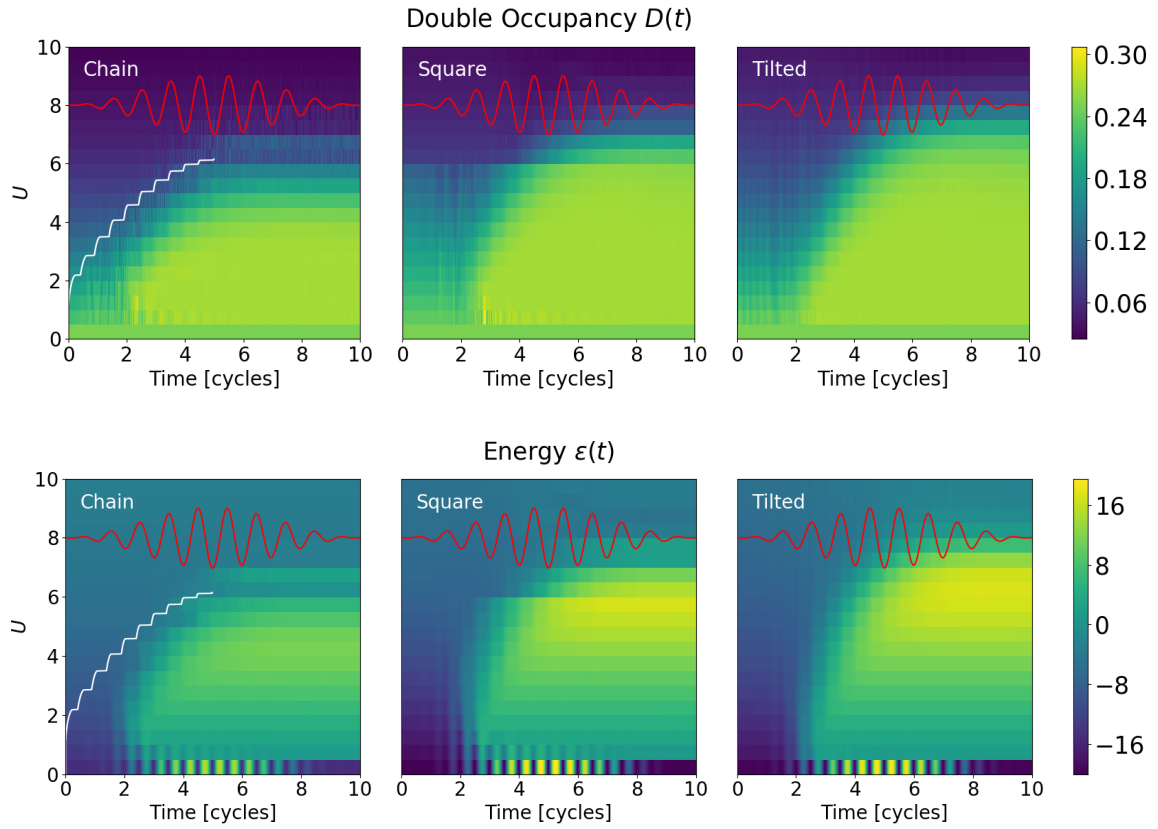

Figure 4.1: **Time-resolved photo-induced Mott transitions, demonstrated using $D(t)$ and $\varepsilon(t)$.** Time evolution, under the driving field shown in red, of the doublon density and energy, for varying correlation strength. Shown for 1D chain (left), 2D square (middle) and 2D tilted (right) geometries, all calculated using ED on 12-site lattices. The white lines in 1D show the time that E_{th} is reached, calculated using eq.(2.35).

electrons away from each other and onto different sites, with neighbouring sites tending to have opposite spins. A pulse is then applied, destroying the Mott insulating state and inducing an insulator-to-metal transition.

When $U = 0$ the system is already metallic, so no transition occurs and in both dimensions the double occupancy simply remains constant at $D = 0.25$, because there is equal probability of a site being in any one of its four possible states. But with non-zero interactions $D(t)$ starts to depend on the field strength. In 1D, the doublon density does not change greatly until the threshold field is reached, after

which it increases rapidly and ultimately converges to a metallic state with large and constant carrier density, at a value that is often larger than the $D = 0.25$ of the $U = 0$ system. Eq.(2.35) predicts that $E_{th} > E_0$ when approximately $U > 6$, and this is clearly reflected in a sharp decline in DHP production beyond this point, until at very large U the repulsion becomes too strong for any noticeable increase in double occupancy. In this limit, the tunneling probability remains small, so the excitation density is insufficient to cause melting and the system retains its insulating nature. The 2D heatmap shares many of the same qualitative features and it is clear that Mott breakdowns also occur and do so with threshold behaviour, but with the important difference that the phase transitions continue to happen up to higher correlation strengths than in 1D.

The system's energy $\varepsilon(t)$ reflects the underlying competition between kinetic and Coulombic processes. At $U = 0$ it is entirely kinetic in origin, as without interactions it is simply due to independent electrons being accelerated by the field, resulting in large oscillations that return to the GS energy every half cycle. When $U > 0$ the repulsive interactions block electron motion, and instead energy is added to the system when DHPs are formed, which can subsequently be accelerated and contribute kinetic energy. The final energy that the system converges to depends on the competition between these contributions, with kinetic energy dominating at low U such that the energy remains negative, and Coulomb interactions dominating as U increases, resulting in positive energies with behaviour that mirrors $D(t)$. In 2D these converged energies are much larger than 1D for strong to intermediate U, reflecting larger doublon densities in this region. Finally, in 1D when $E_{th} > E_0$ the energy does not deviate much from its GS value because insulating states inhibit DHP formation. This signature of insulating behaviour does not happen in 2D until much larger correlation strengths, again implying that Mott transitions can occur beyond the point where they are possible in 1D.

The spin correlation $\eta(t)$ allows us to directly observe the destruction of magnetic order. In 1D, the MI melts into a paramagnetic state within approximately 2 cycles of the threshold field being reached, and converges to a value that is close to zero (and would be zero in the thermodynamic limit). There are a number of interesting differences in 2D. Firstly, the transitions appear to begin sooner such that the saturated

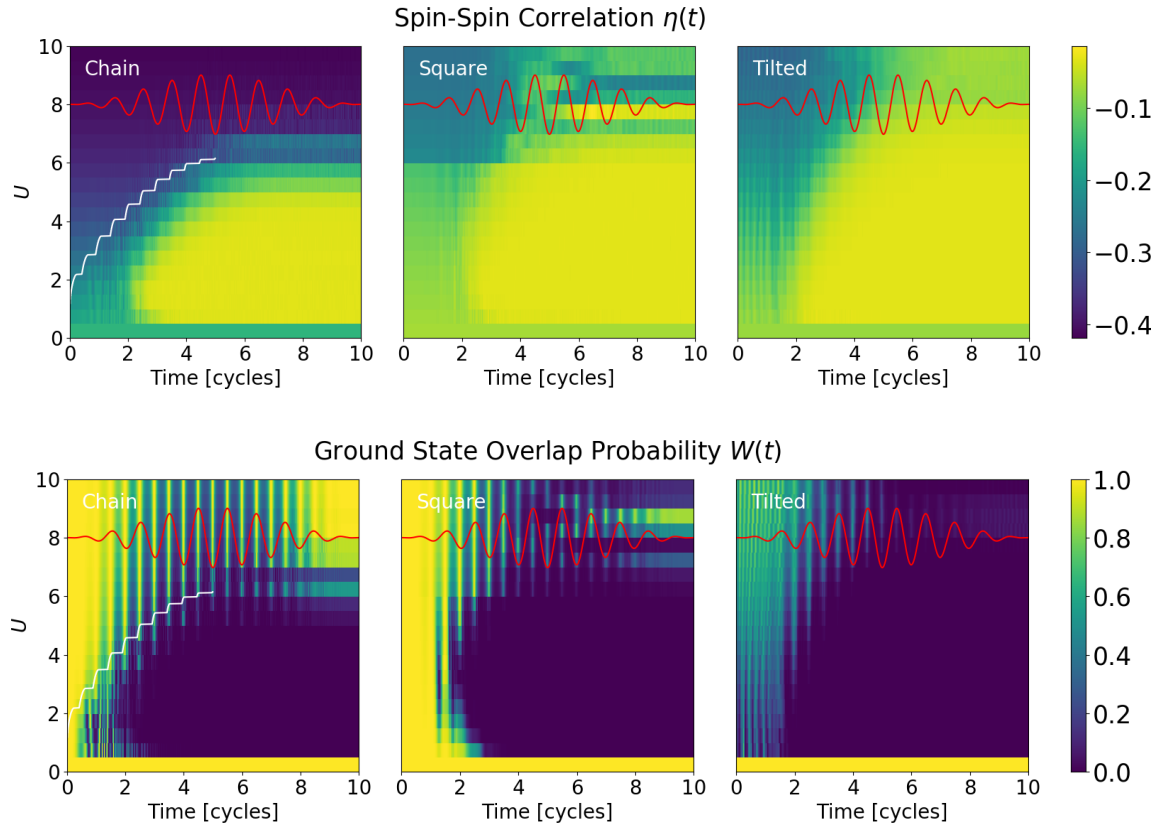

Figure 4.2: **Time-resolved photo-induced Mott transitions, demonstrated using $\eta(t)$ and $W(t)$.** Time evolution, under the driving field shown in red, of the spin-spin correlation function and overlap probability, for varying correlation strength. Shown for 1D chain (left), 2D square (middle) and 2D tilted (right) geometries, all calculated using ED on 12-site lattices. The white lines in 1D show the time that E_{th} is reached.

state is arrived at more quickly, particularly in the region below $U = 6$. Furthermore, Mott breakdown occurs up to larger interaction strengths, as is the case with all the observables in fig.4.1 and fig.4.2. These two things together suggest that the threshold field for a given U is smaller in 2D, which could arise from differences in bandstructure (i.e. Mott gap) and/or correlation length. This will be returned to later as it has important consequences. Lastly, there is interesting behaviour in the region $U > 7$. The double occupancy and energy suggest that this is the insulating limit where Mott transitions cannot occur, and in 1D this regime is also clearly insulating as large AFM

order is maintained throughout. However, in 2D there is a persistently high density of charge carriers, and the magnetic order appears to partially melt at all correlation strengths.

Finally, the overlap probability is sensitive to small changes in electronic configuration and therefore allows us to precisely track the depletion and eventual destruction of the GS. In 1D, as the threshold field is approached the wavefunction oscillates between the GS and a heavily-depleted state, with the GS returned to at peaks in $E(t)$. These oscillations correspond to fluctuations in the double occupancy which are too small to clearly see in the heatmap but still cause large changes in $W(t)$. Once the threshold field is reached, $W(t)$ shows that the rapid rise in $D(t)$ leads to the destruction of the Mott state in less than a single cycle, often before $D(t)$ and $\eta(t)$ have even converged. When $E_{th} > E_0$ no transition can occur, so the overlap continues to oscillate with the field and ultimately returns to $W(t) = 1$, which shows that the GS survives. This is qualitatively similar to the 2D square lattice results, because $W(t)$ is not greatly affected by the artificial GS frustration and so the square lattice is the more reliable of the two in this case when estimating the thermodynamic limit. As with the other observables, the 2D overlap supports the observations that transitions occur sooner and up to larger interaction strengths.

4.2 Emission Mechanisms

The laser pulse induces a highly complex optical response that can act as a window into the underlying physics. This response originates in the dynamics of the many-body charge excitations, i.e. the photo-induced DHPs. Electron correlations fundamentally alter the single-particle bandstructure picture used to model the HHG in semiconductors that results from excited electrons and holes. However, important lessons can be learnt from this description, and the single-particle language of renormalised excitations remains vital to the analysis of MIs. Excitations are now considered, especially at large U, to occur between the 'lower Hubbard band' (LHB) and the 'upper Hubbard band' (UHB), instead of between the VB and CB as in semiconductors. The analytical description available in 1D, and discussed in Sec. 2.3, offers important insights into the origins of the system's HHG. In particular, it is im-

portant to consider the GS dispersion relating the energy of DHPs to their momenta, which predicts that the available energies of a single excitation are between Δ and $\Delta + 8t_0$ [132, 165].

To analyse the emission we must build some understanding of the mechanisms that cause the charge carriers to generate high harmonics. As was discussed in Sec. 2.2.1 and Sec. 2.2.2, in atomic systems HHG has long been analysed using the 3SM, which was then extended to solid state systems. The natural question is to what extent a similar picture can be developed for MIs, given that their properties differ in important ways. In semiconductors, an electron promoted to the CB is delocalised and free to undergo acceleration, whereas in MIs this is not true because the excitations are restrained by Pauli blocking (due to the exclusion principle) and the localising effects of Coulomb interactions. The consensus of the literature, as discussed in Sec. 2.2.3.2, is that HHG in the (single-band) Hubbard model originates from two main mechanisms that are both directly analogous to those in semiconductors. Firstly, there is an intraband current arising from the hopping of doublons and holes in the upper and lower Hubbard bands, respectively. The emission is due to their acceleration either through momentum space or around it via BOs, in which the field drives the quasiparticles to the edge of the Brillouin zone, causing them to rapidly change their momenta and emerge from the other side, accompanied by oscillations in real space. Secondly, interband polarisation builds up between doublons and holes, followed by their recombination and the emission of light. This leads to a phenomenological 3SM similar to those discussed previously: the field induces the tunneling of an electron over the Mott gap to form a DHP, which is then accelerated by the laser, until the doublon and hole oscillate back towards each other and recombine. Clearly these processes are heavily influenced by the correlated bandstructure, whose properties are mimicked in fig.3.1 and fig.3.2. These figures will be useful for gaining an intuition into the mechanisms at work and the differences between them in 1D and 2D.

It is not a priori clear which of the inter and intraband processes will contribute more to the emission. Interband was found to be dominant for MIs in 1D [135] and infinite-D [137] when U is large, and the HHG from semiconductors under mid-IR pulses has also been found to be dominated by interband processes [118]. This will be an important property to look at for general U, and especially in 2D.

4.3 HHG Spectra

The charge dynamics produce a current, given by eq.(2.22), and therefore a dipole acceleration, which gives rise to high harmonic emission. We will use HHG to resolve the many-body dynamics in the frequency and time domains, allowing us to directly observe metallic and insulating behaviour, as well as transitions between them. The HHG will first be analysed using eq.(3.64), in which the emission during the whole pulse is summed over. The variation of this emission with correlation and dimensionality is shown from fig.4.3 to fig.4.6, which were calculated using a combination of mean-field methods, tVMC and ED. They plot the log of the HHG spectrum against the emitted harmonics, where the harmonics are multiples of the input frequency, ω_L. All 1D spectra are shown in the left-hand columns, and 2D in the right-hand ones, with rows given in order of increasing correlation (when applicable).

4.3.1 Metallic Regime

When $U = 0$ the system is in the Fermi liquid regime and the Hamiltonian eq.(2.21) becomes the tight-binding model

$$\hat{\mathcal{H}}(t) = -t_0 \sum_{\langle ij\rangle\sigma} \left\{ e^{-i\Phi(t)} \hat{c}^\dagger_{i\sigma} \hat{c}_{j\sigma} + e^{i\Phi(t)} \hat{c}^\dagger_{j\sigma} \hat{c}_{i\sigma} \right\} \tag{4.9}$$

In the conducting limit there are no interactions and therefore no Mott gaps, so HHG arises entirely from the intraband current. We can therefore revert to a one-electron description and consider individual independent electrons and holes that are accelerated beyond the Fermi energy by the laser field. This produces the spectrum shown in fig.4.3. It is composed of narrow and distinct peaks at the odd harmonics[2] $\omega = 1, 3, 5...$, with the first two at intensities that are at least an order of magnitude larger than the peaks in any $U > 0$ spectrum. These properties are typical of tight-binding spectra [58], as well as of experimentally-observed HHG that is thought to originate from intraband acceleration, such as in Dirac semimetals [205, 206]. Fig.4.3

[2]This spectrum extends up to $\omega = 11$ at $S(11) \approx -10$, but at intensities below this the spectrum is obscured by spectral leakage. The Welch method can be applied, and doing so extends the spectrum up the 17th harmonic where $S(17) \approx -22$.

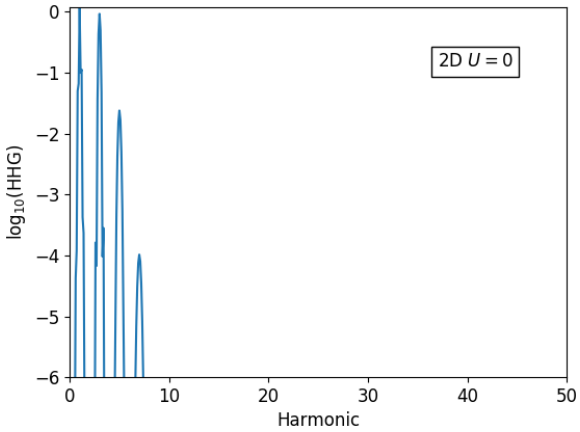

Figure 4.3: **HHG spectrum in the absence of correlation.** Harmonic emission at $U = 0$ in 2D, and the spectrum is the same in 1D up to a constant factor. Calculated on a 6×6 lattice using eq.(4.10) and mean-field methods. The simulations were repeated using tVMC and the CBM, and both reproduced the same result.

only shows the 2D case, but the spectrum is the same in 1D up to a constant factor, which can be understood using the 1D current expectation in the form eq.(2.30). When $U = 0$ it is true throughout the pulse duration that $\theta = 0$ and $R(\Psi) = R(\Psi_{MF})$ is constant. This results in a current with time dependence that only enters through the Peierls phase

$$\mathcal{J}(t) = -2at_0 R(\Psi_{MF}) \sin\left[\Phi(t)\right] \tag{4.10}$$

In 2D, the current can be resolved into its x and y components

$$\begin{aligned} \mathcal{J}(t) &= \mathcal{J}_x(t) + \mathcal{J}_y(t) && (4.11)\\ &= -2at_0 \left\{R_x(\Psi_{MF}) \sin\left[\Phi(t)\right] + R_y(\Psi_{MF}) \sin\left[\Phi(t)\right]\right\} && (4.12)\\ &= -2at_0 R(\Psi_{MF}) \sin\left[\Phi(t)\right] && (4.13) \end{aligned}$$

where $R(\Psi_{MF}) = R_x(\Psi_{MF}) + R_y(\Psi_{MF})$. The ratio of emission in both dimensions at any frequency is constant in time and given by

$$\frac{\mathcal{S}_{2D}(\omega)}{\mathcal{S}_{1D}(\omega)} = \frac{|R_{2D}(\Psi_{MF})|^2}{|R_{1D}(\Psi_{MF})|^2} \approx 1.5 \tag{4.14}$$

because all other terms cancel, resulting in spectra that are proportional to each other and with 2D having a larger intensity.

The same mean-field methods that were applied to the CBM can also be used to calculate the current of the $U = 0$ system, as this is just the $V(0) = 0$ case. However, it is not necessary to do a full evolution of eq.(3.58), and instead once the

GS one-body DM has been found it can be used to calculate $R(\Psi_{MF})$, at which point eq.(4.10) gives the current. This means that the non-interacting system only requires knowledge of the GS and the pulse in order to calculate the full time-evolution of the HHG.

4.3.2 Interacting Regime

When $U > 0$ a Mott gap $\Delta(U)$ is opened, leading to dramatically different HHG spectra. The intraband current typically causes the emission of low harmonics with regular structure, but an UHB introduces much larger excitation energies, which can broaden the emission to include high harmonics with highly irregular structure. Furthermore, intra and interband processes become coupled in interesting ways that depend on the correlation strength, further adding to the complexity of the HHG.

4.3.2.1 1D Systems

We first analyse the 1D spectra, shown in fig.4.4 for $U = 1$ and fig.4.5 for $U = 3$, 5, 7 (in the left-hand column). At $U = 1$ the gap is very small, $\Delta(1) \approx 0.005$, but it is enough to cause significant changes to the HHG as compared to the tight-binding case. The emission intensity is comparatively suppressed, but the spectrum extends beyond the 30th harmonic, far higher than is possible with only an intraband current (at this field strength). Because $\Delta(U)$ is so small it is not possible to separate the spectrum into discrete sections above and below the gap, which makes it difficult to match emission mechanisms with spectral features. The HHG peak is near the 1st harmonic and retains a narrow and regular structure, implying that it originates mostly from the intraband current. However, at larger harmonics the structure becomes increasingly irregular and originates from the interband current. This is clear from the fact that the emitted harmonics sit neatly within the available excitation energies Δ to $\Delta + 8t_0$, which are the set of single charge-conserving optical excitations from the correlated GS, and can be calculated using eq.(2.36) from the Bethe ansatz [18, 165, 166]. The peak excitation, $\Delta + 8t_0$, is the Mott gap plus twice the 1D single-particle bandwidth, $W_{1D} = 4t_0$, and therefore represents the interaction energy plus the maximum kinetic energy of the DHP. This is similar to the atomic cutoff energy that was discussed

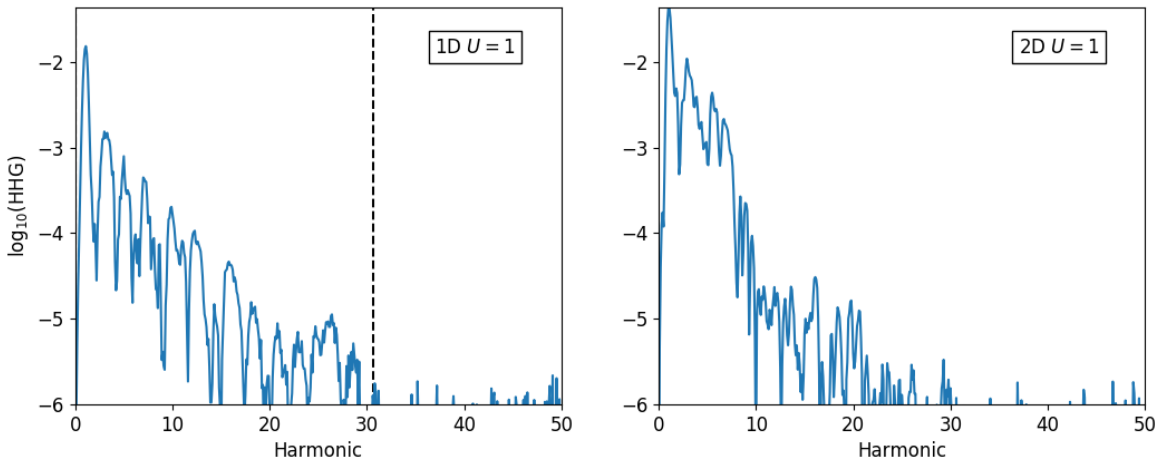

Figure 4.4: **HHG spectra in weakly-correlated systems.** Harmonic emission at $U = 1$ in 1D and 2D. The dashed line in the 1D plot shows the excitation energies Δ to $\Delta + 8t_0$, although the former is so small that it is obscured by the y-axis. Calculated using tVMC on 36-site lattices.

earlier, $I_p + 3.17U_P$, where I_p is the ionisation potential and $3.17U_P$ the maximum possible kinetic energy.

When $U > 1$ a substantial Mott gap forms, and fig.4.5 shows that this results in a shifting of the spectra to larger harmonics. Interband recombination is unambiguously the dominant process as the majority of emission falls within the DHP excitation energies, which form a moving interval of just over 30 harmonics that peak over a region centered around $N \sim U/\omega_L$. This agrees with previous research that also found the interband current to dominate in 1D far from the metallic limit [132, 135].

The relative contribution of intra and interband processes changes greatly as electron correlation increases. At $U = 3$ the intraband current is still a significant contribution, as there is a large peak below the gap. However, even this peak is an order of magnitude less than its $U = 1$ equivalent, and at larger U the low harmonics are increasingly suppressed. This occurs due to the intricate coupling that exists between the emission mechanisms. DHPs are the charge carriers, which means that the intraband current is inherently tied to the existence of interband polarisation, and in fact the intraband current's emission intensity is heavily dependent upon the occupation of the UHB. This is because in the tunneling regime, when $\gamma \ll 1$, the tunneling probability is nearly momentum-independent, which can cause the UHB to become

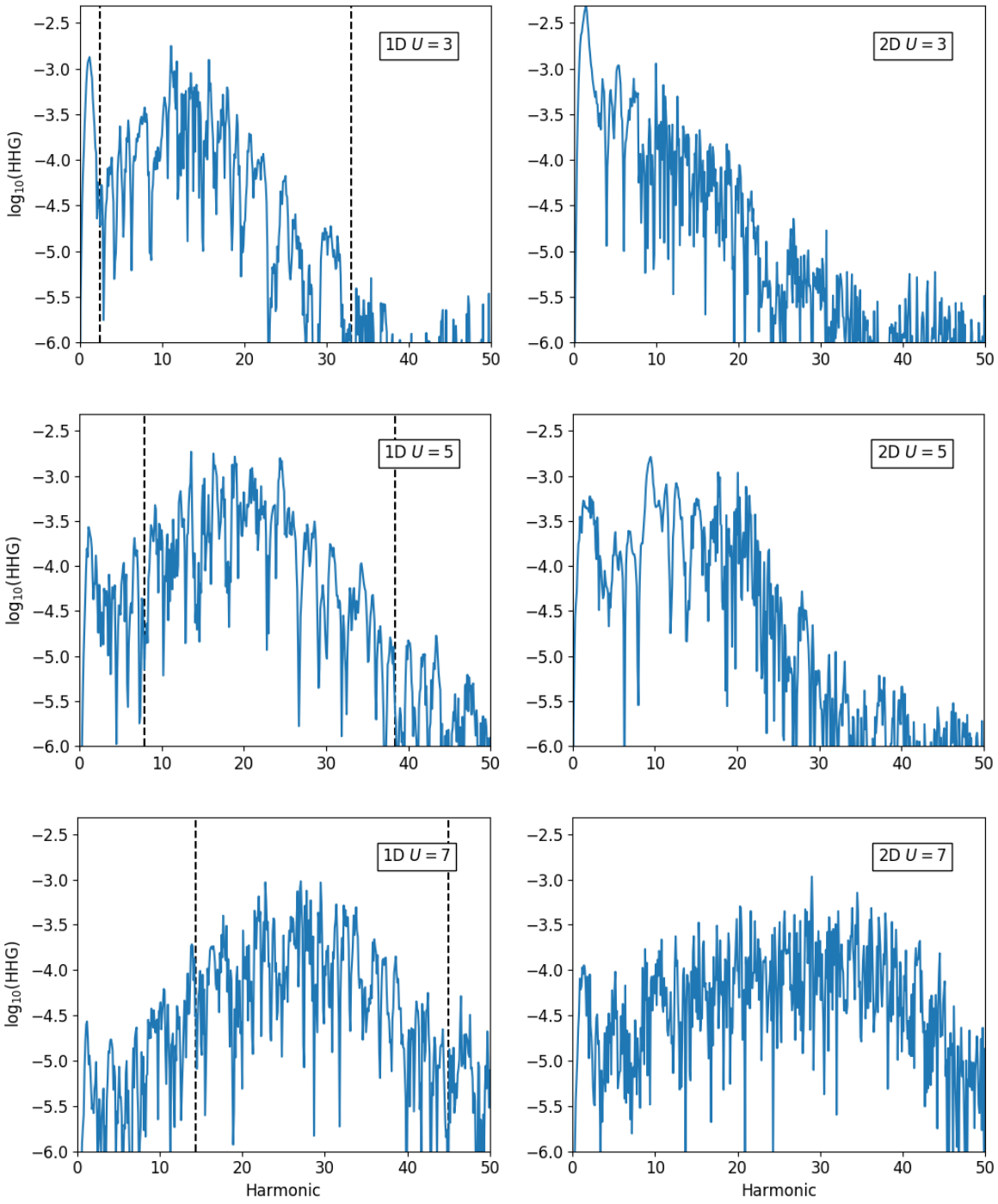

Figure 4.5: **HHG spectra in the interacting regime.** Harmonic emission at $U = 3$, 5, 7 in 1D and 2D. The dashed lines in 1D show the excitation energies Δ to $\Delta + 8t_0$. Calculated using tVMC on 36-site lattices.

saturated by photocarriers [165]. As a result, quasi-momenta states become unavailable for charge oscillations and so low harmonics are suppressed [132]. This effect is most pronounced in the Mott breakdown regime, where $E_{th} < E_0$ and there is a high rate of carrier creation. However, it can also occur in cases where the correlation is too strong to permit Mott transitions, e.g. $U = 7$ in fig.4.5 shows suppression of low harmonics despite the fact that we know a transition cannot occur because $E_0 = 10\text{MVcm}^{-1}$, but $E_{th}(7) \approx 14.8\text{MVcm}^{-1}$. It must be that the small fluctuations in double occupancy that can be observed in fig.4.1 can populate the UHB enough to block the intraband current, even if it is not enough to initiate breakdown. Another factor reducing the emission of low harmonics is the physical lattice itself, as in 1D a DHP only has two adjacent sites to hop to, which could be blocked by other electrons, particularly at large U where the interactions have a strong localising effect.

4.3.2.2 2D Systems

The 1D and 2D spectra start the same (up to a constant factor) in the conducting $U = 0$ limit, but fig.4.5 shows that they rapidly diverge as correlation is increased. Many of the characteristic features of the 1D HHG stop being true in 2D, and so dimensionality appears to have an important impact on the emission of these MIs.

In 2D, an interesting feature is the persistent presence of low harmonics, as opposed to the suppression of them observed in 1D for all but small interaction strengths. There is no analytic expression available for $\Delta_{2\text{D}}(U)$, nor is there a simple way to calculate them numerically, so it is sometimes not possible to definitively assign responsibility to either intra or interband processes for the continued low harmonic emission. In the $U = 3$ case, there is not significant broadening of the HHG compared to the $U = 1$ spectrum, implying that its Mott gap remains small. This again makes the origin of its low-harmonic peak somewhat ambiguous, and it is probably composed of contributions from both emission mechanisms. However, low harmonics persist at all correlation strengths shown in fig.4.5, beyond the point where a considerable gap has certainly formed and at intensities approximately an order of magnitude larger than their 1D equivalents. This leads to a clear separation between the initial peaks around the 1st harmonic, whose origin is in intraband processes, and

the broad spectrum of emission extending up to tens of harmonics, which is due to recombination.

These low harmonics are necessarily driven by a retention of significant levels of intraband current, indicating a persistence of mobile collective charge carriers that avoid recombination over substantial timescales. This is supported by fig.4.2, which shows the melting or partial melting of AFM order at all U, including values where in fig.4.1 $D(t)$ indicates that Mott breakdowns are not occurring, and where in 1D there is an absence of charge-carrying quasiparticles because $E_{th} < E_0$. This might be a direct result of the higher dimensionality in 2D, as the excitations are better able to avoid each other and to continue undergoing driven dynamical oscillations without recombination. Furthermore, the 2D single-particle bandwidth is $W_{2D} = 8t_0 = 2W_{1D}$, as shown in fig.3.2. This increased bandwidth is an important contributing factor as it means there are more quasi-momenta states available, ensuring that the UHB does not become as saturated as in 1D systems and can continue to support intraband currents in the presence of strong electron interactions.

An interesting question is whether the longer excitation lifetimes of DHPs in 2D reduce the intensity of the HHG at larger harmonics, as it might decrease the total number of recombination events compared to 1D, where the lattice and bandstructure inhibit extended oscillations. This could perhaps have a noticeable effect on the $U = 3$ spectrum, where the intraband current is the most important emission mechanism and the intensity of higher harmonics, whose origin is in recombination, is considerably lower than its 1D equivalent. In three-dimensional (3D) systems, the additional dimension would be expected to even more effectively support intraband currents, and therefore to further enhance low harmonics, as well as to potentially cause a larger reduction in the intensity of higher harmonics. Together this means that in 3D MIs it is expected that low harmonics dominate the spectrum for low-to-medium interaction strengths.

Another noteworthy feature of the 2D spectra is the nature of the peak HHG. At $U = 5$, where correlation is moderately strong, there is a single well-defined peak at $\omega_{max} \approx 9.5$, which is large enough that it must originate from recombination. This can be said with confidence because it is above the 1D gap, $\Delta_{1\mathrm{D}}(5) \approx 8\omega_L$, and we know that $\Delta_{1\mathrm{D}}(U) > \Delta_{2\mathrm{D}}(U)$, as was discussed in Sec. 3.6.1 and is visible in fig.3.2.

These characteristics are distinct from 1D, where the maximal emission occurs over an extended region instead of a single narrow peak. They also occur at much larger harmonics in 1D, in this case centered around $N \sim 5/\omega_L \approx 19$, which is approximately double the 2D peak's location, $\omega_{max} \approx 9.5$.

Some of these differences in the $U = 5$ emission can be explained by the DOS, because in 2D there are strong quasiparticle peaks (Van Hove singularities) either side of the gap, which are far more pronounced than in 1D [196, 197]. These can be seen clearly in fig.3.2. In 2D, we would therefore expect a high density of excitations to occur near $\Delta(U)$, which could explain the location of the peak at comparatively small harmonics, given that $\Delta_{2D}(5) < 8\omega_L$. Furthermore, the peak's narrow shape directly follows from the structure of the DOS, which is concentrated in these quasiparticle peaks and then tapers off. Conversely, in 1D the DOS is more uniformly distributed across the available excitation energies, resulting in the broader spread of peak HHG in fig.4.5.

In the strongly-correlated regime, shown here at $U = 7$, a high density of localised magnetic moments begin to form and we see dramatic changes in the structure of the spectrum. The bulk of emission is not linearly dependent on U as in 1D, but instead the spectrum broadens over more than 40 harmonics. This is caused by a combination of large gap; the increased bandwidth compared to 1D, which makes more high-energy excitations available; and the retention of the intraband current, which extends the spectrum to also include lower harmonics.

4.3.3 Large-U Regime

Here we consider the region given by approximately $U \geq 8$, where the correlation is extremely strong (the gap is similar to or larger than the non-interacting bandwidth) but the system is still in the tunneling regime. In 1D, the boundary of this regime can be estimated using eq.(2.33), which states that quantum tunneling remains the primary excitation process up until the Keldysh crossover at $U \approx 85$. As we will see, HHG in this large-U limit has interesting and unusual properties. As U grows, the field strength increasingly struggles to overcome $\Delta(U)$, such that $E_{th} \gg E_0$ and the system remains firmly in the insulating regime. We will look at the specific case of

$U = 10$, where in 1D the threshold field is $E_{th}(10) \approx 38$ MVcm^{-1}, nearly four times larger than E_0.

Because $\Delta(U)$ becomes so large, it might be expected that DHP recombination is the dominant emission mechanism, as it is in fig.4.5 for all but weak correlations. However, this is actually not the case, and as U increases there is an inversion of the relative contributions of the intra and interband currents that also depends heavily on dimensionality. This is demonstrated in fig.4.6 for $U = 10$. In 1D, when the field is at its peak strength $E(t) = E_0$, the probability for an electron in the GS to tunnel over the gap and form a DHP can be approximated by eq.(2.37), which gives $\mathcal{P} \approx 0.21$, 9.7×10^{-3}, 6.3×10^{-6} for $U = 5$, 7 and 10, respectively. This exponential decay of the tunneling probability when $E_{th} > E_0$ helps to explain the threshold behaviour observed in the Schwinger limit, defined by eq.(2.35). This has the effect of severely reducing the occupation of the UHB as $U \to \infty$, making many quasi-momenta states available for intraband oscillations and thereby causing the emergence of low harmonics. This diminished doublon density also leads to an accompanying reduction in the intensity of higher harmonics that originate from recombination, such that they become orders of magnitude less than their equivalents in fig.4.5.

An enhancement of the intraband current can in fact be predicted from the dispersion, because as $U \to \infty$ we would expect the bands to become flatter, i.e. less dispersive. This increases mobility in k-space because the energy change between states becomes smaller, which promotes intraband motion. The flattening of the bands can be observed in the CBM's dispersions, fig.3.1, and this tendency continues as effective U is increased further until the bands are almost parallel.

Fig.4.6 shows that in 1D the main consequence of this is a peak at the 1st harmonic, along with lower-intensity emission below the gap. In 2D, the lobe-like structure below the 20th harmonic is approximately two orders of magnitude more intense than the rest of the spectrum, and will later be shown by a time-dependent analysis to be intraband in origin. We can see therefore that charge oscillations become by far the largest source of HHG when correlations are extremely large, despite the presence of a substantial gap.

The relative effects of this intraband enhancement in 1D and 2D can again be understood in terms of differences in the bandstructure and lattice. In 1D, with the

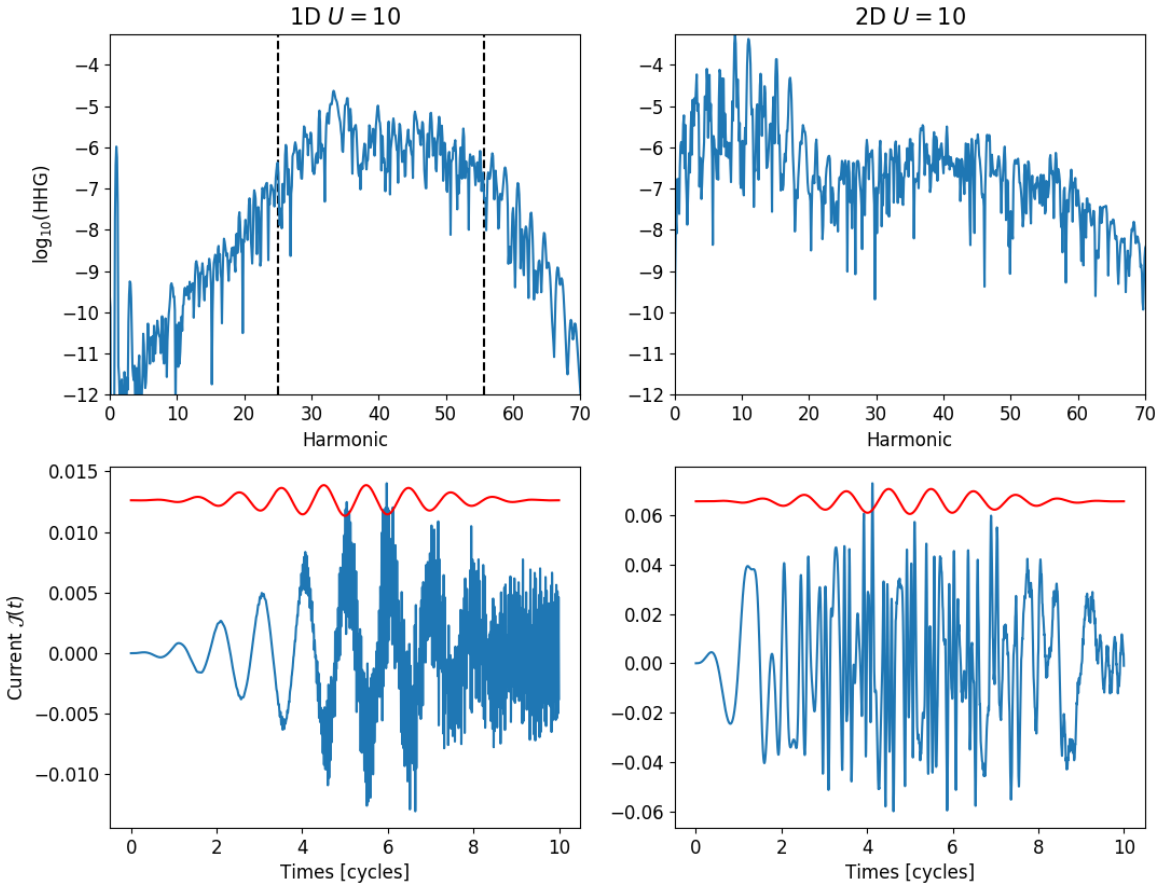

Figure 4.6: **HHG spectra in the large-U limit.** Harmonic emission and corresponding currents at $U = 10$ in 1D (left) and 2D (right). The dashed lines in 1D are the excitations Δ to $\Delta + 8t_0$, and the red lines are the electric field $E(t)$. Welch's method was applied to access the low-intensity emission. Calculated using ED on 12-site lattices.

exception of the 1st harmonic, frequencies below the gap are in fact even more aggressively suppressed than in fig.4.5. This is likely caused by the competing effects of lower UHB occupation, which encourages DHPs to delocalise, versus the localisation caused by very strong Coulomb repulsion combined with Pauli blocking due to the 1D lattice's low coordination number, which together inhibit the mobility of charge carriers. Conversely, in 2D the existing effects of a larger bandwidth and coordination number are reinforced by the desaturation of the UHB, resulting in mobile DHPs and therefore intense low harmonics.

The currents in fig.4.6 give a window into the differences in both system's intra-

band currents. The 2D current indicates extremely strong BOs, particularly near the centre of the pulse where the field strength is strongest. The relationship between BOs and the current will be discussed more in later sections, but it suffices here to say that they are very strong in this case. This is not true in 1D, where the BOs are less clear and instead the current is simply aligned with the electric field (hence the 1st harmonic peak in the spectrum), with later fluctuations due to recombination. This indicates that BOs are weak, and instead the 1D intraband current is mostly caused by anharmonic oscillations within the UHB, instead of around it in BOs. This would limit the intensity of the resulting harmonics, and so would explain the spectrum.

4.4 Time-Resolved Emission

Valuable information is destroyed when the dipole acceleration is Fourier transformed and its magnitude is taken. As a result, the wavelet analysis of eq.(3.67) was used to capture the time-dependence of the charge dynamics, with the HHG then calculated using eq.(3.68). This allows us to directly observe insulator-to-metal transitions in real time and to learn more about the underlying emission mechanisms.

4.4.1 Metallic Regime

Fig.4.7 shows spectrograms of the 2D $U = 0$ system, along with its current and dipole acceleration. The HHG is displayed for two different intensity ranges, one with only large intensity emission and another where much weaker intensities are also included. The 1D equivalent has the exact same structure but shifted to smaller intensities. This HHG is caused by purely intraband processes as there is only a single band, and is therefore very useful as it shows the characteristic features of intraband emission, which can then be looked for in $U > 0$ systems.

The two spectrograms reveal different structures. The first, with only the strongest emission included, shows distinct bands around the 1st, 3rd and 5th harmonics, with intensities that depend on the field strength and therefore peak at the pulse centre, where $E(t) = E_0$. Emission at the 1st harmonic starts at $t = 0$ and occurs continuously thereafter, whereas the other bands begin later in the pulse once the laser

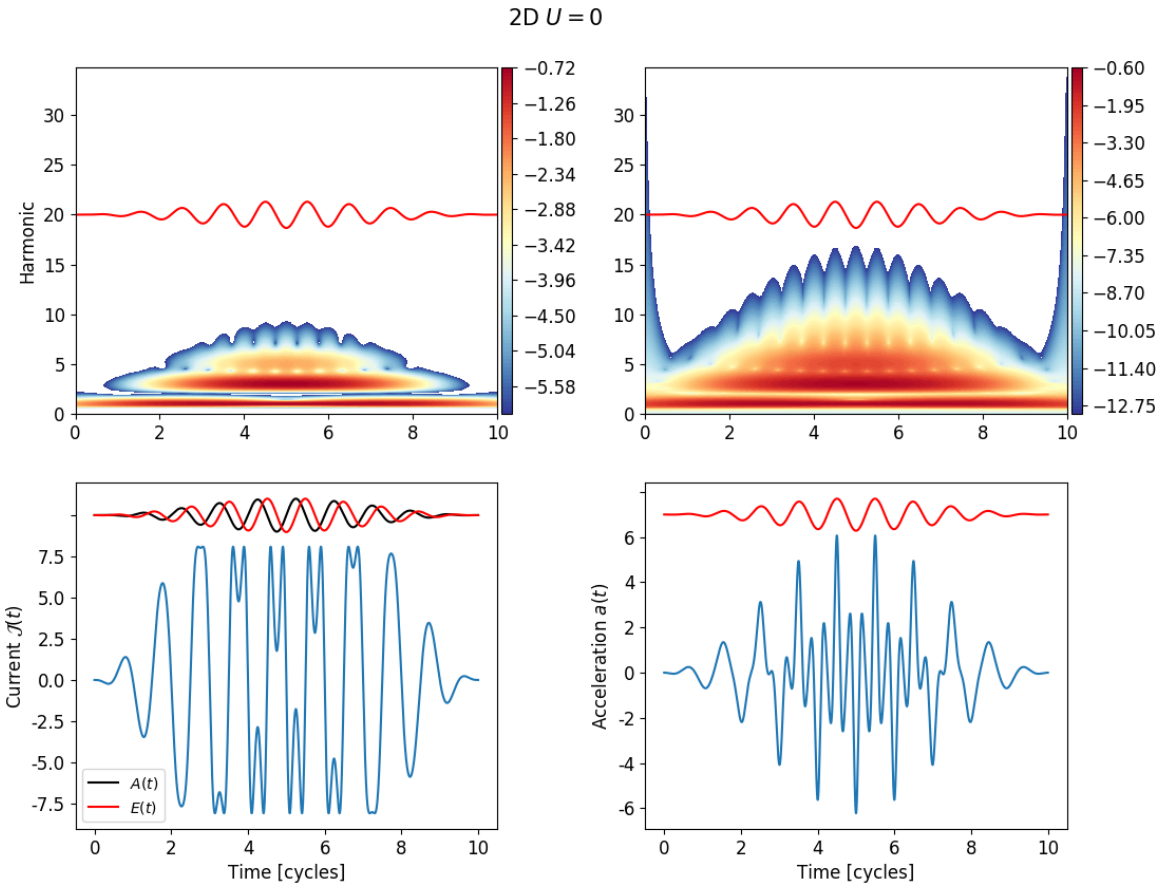

Figure 4.7: **Time-resolved HHG in the absence of correlation.** Spectrograms with the corresponding current and acceleration at $U = 0$. The spectrograms are for the same system but with different intensity ranges: the left one includes only the largest few orders of magnitude, whereas the right image has a much wider range that includes weak HHG. The spectrum is the same in 1D up to a constant factor. Colourscale denotes the log of the spectral emission intensity. Red lines show the incident electric field $E(t)$, and the black line in the current is the corresponding vector potential $A(t)$, where they are related to each other by $E(t) = -dA(t)/dt$. Calculated using eq.(4.10) on a 6×6 lattice, and the same results were also found using tVMC and the CBM.

amplitude has increased sufficiently. Just below the 10th harmonic there is a hint of field alignment, but it is not very distinct. However, including weaker intensities reveals that the HHG has a rich sub-cycle structure. Larger harmonics are generated and show clear alignment with the electric field, producing two emission peaks per cycle that are maximal at the pulse centre.

The current can help us understand the origin of this emergent structure. Initially there is a linear response, but as the field strength increases the current develops kinks that align with peaks in the vector potential $A(t)$ and therefore also with the phase, $\Phi(t)$. This system has no electron correlation so we can use an independent-electron description and consider the dynamics of individual electrons and holes. With this in mind, the kinks can be identified as BOs in which electrons are accelerated beyond the maximum quasi-momentum at the Brillouin zone boundary, $|k| = \frac{\pi}{a}$, causing them to Bragg scatter and reemerge at the other side of the Brillouin zone. In this case, $E(t)$ is only strong enough to cause a maximum of one Bloch cycle per half-cycle of the pulse, which is still enough to generate rapid oscillations in real space and the emission of high frequencies. The development of these kinks near the 3rd pulse cycle coincides with the onset of the larger field-aligned harmonic peaks in the spectrogram, with the highest harmonics produced around the pulse centre where the field strength and therefore BOs are strongest, as indicated by the depth of the kinks.

An intuitive semi-classical description of the electron dynamics is given by the Bloch acceleration theorem, which relates the quasi-momentum $\mathbf{k}(t)$ with the electric field as follows [65, 100, 125]

$$\frac{d\mathbf{k}(t)}{dt} = -\mathbf{E}(t) \implies \mathbf{k}(t) = -\int_{-\infty}^{t} d\tau \mathbf{E}(\tau) \tag{4.15}$$

$$= \mathbf{k}(0) + \mathbf{A}(t) \tag{4.16}$$

This shows that the k-space dynamics are directly dictated by the vector potential. For a given $\mathbf{k}(0)$, the trajectory in k-space can be easily calculated and folded into the Brillouin zone so as to enforce $|k| \leq \frac{\pi}{a}$.

We can also express the dipole acceleration, eq.(3.63), in an interesting form that explicitly depends on the field. The tight-binding Hamiltonian in eq.(4.9) can be written in an alternative form using eq.(2.32) with $U = 0$, and recalling that in the

non-interacting system $\theta = 0$ and $R(\Psi) = R(\Psi_{MF})$ is constant

$$\mathcal{H}(t) = -2t_0 R(\Psi_{MF})\cos[\Phi(t)] \tag{4.17}$$

This is the $U = 0$ energy in fig.4.1. Combining it with the electric field, $aE(t) = -\frac{d\Phi(t)}{dt}$, gives

$$a(t) = \frac{d\mathcal{J}(t)}{dt} = 2a^2 t_0 R(\Psi_{MF})E(t)\cos[\Phi(t)] \tag{4.18}$$

$$= -a^2 E(t)\mathcal{H}(t) \tag{4.19}$$

We get a hint of this in fig.4.7, as the acceleration's peaks align with those of $E(t)$.

4.4.2 Transition Regime

The HHG spectra of Sec. 4.3 are largely blind to Mott transitions and give little indication of whether breakdown has occurred and when it happened, or if the system is in the regime $E_{th} > E_0$ where they are not possible. In the $U = 0$ case there is no insulating state to undergo melting, but when $U > 0$ the spectra often do not provide enough information to confidently determine if the system's AFM order has survived irradiation or has been destroyed. The observables in fig.4.1 and fig.4.2 do provide a way of analysing transitions, but they are not experimentally obtainable. This all makes the time resolution of the emission particularly interesting and important, as it provides a window into the transition dynamics on electronic timescales in a way that is potentially experimentally achievable, e.g. in Ref. [61] where the pulse parameters were very similar to those used here.

For both 1D and 2D, fig.4.8 shows the spectrograms of the $U = 1$ systems, and fig.4.9 of the $U = 3, 5$ systems. They demonstrate that in the above-threshold regime, where $E_{th} \leq E_0$, the optical signature of Mott transitions is a brief period of intense HHG, which is closely synchronised with the sudden rise of DHPs and destruction of spin magnetic order that is observed in fig.4.1 and fig.4.2. The emission then exponentially decays and is followed by weak flaring at intensities 2 or 3 orders of magnitude lower than the peak, and that continues fairly uniformly for the rest of the pulse. In 2D, breakdown is initiated roughly 1 cycle sooner after irradiation and also

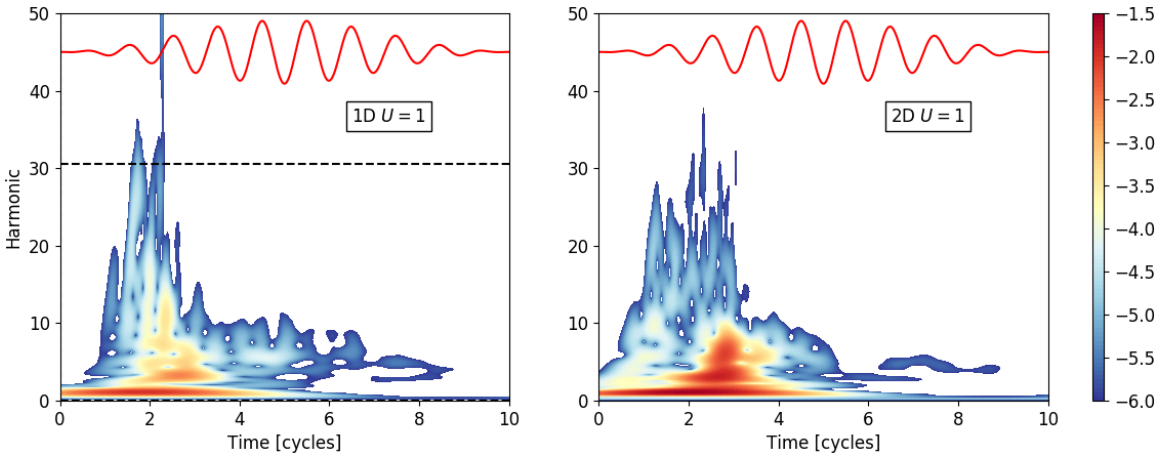

Figure 4.8: **Time-resolved HHG in weakly-correlated systems.** Spectrograms at $U = 0$ in 1D and 2D. Colourscale denotes the log of the spectral emission intensity. Red lines show the incident electric field, $E(t)$. In 1D, the horizontal dashed lines show the excitation energies Δ to $\Delta + 8t_0$, and there is a vertical dashed line showing the time when $E(t) = E_{th}$, but it is obscured by the y-axis. Calculated using tVMC on 36-site lattices.

finishes more quickly once it has started, within approximately just 1 cycle compared to about 2 cycles in 1D. The first of these observations agrees with the spin-spin correlation function and GS overlap in fig.4.2, which both show a more rapid onset of breakdown in 2D when $U \gg 1$.

For any pulse setup, it is the gap $\Delta(U)$ that determines if and when a transition will occur. This is clear from the 1D spectrograms, where the emission is controlled by $E_{th} = \Delta/2\xi$ and peaks soon after $E(t_c) = E_{th}$. Recall that the Mott gap for a given U is smaller in 2D according to cluster perturbation theory [198, 199] and the CBM, as shown in fig.3.2. This can explain many of the observed differences between dimensionalities, as it means that the threshold field is lowered in 2D and so the breakdowns occur sooner. It also accounts for why fig.4.1 and fig.4.2 found transitions to continue happening beyond the correlation strengths that are possible in 1D, as smaller $\Delta(U)$ means that a given E_0 will cause melting to persist up to larger U. Finally, it could contribute to why at low-to-intermediate interaction strengths in fig.4.5 the peak emission is shifted to lower harmonics compared to 1D. This all points to the importance of the GS bandstructure in determining the properties of these insulator-to-metal transitions and their resulting HHG, as well as on the effects

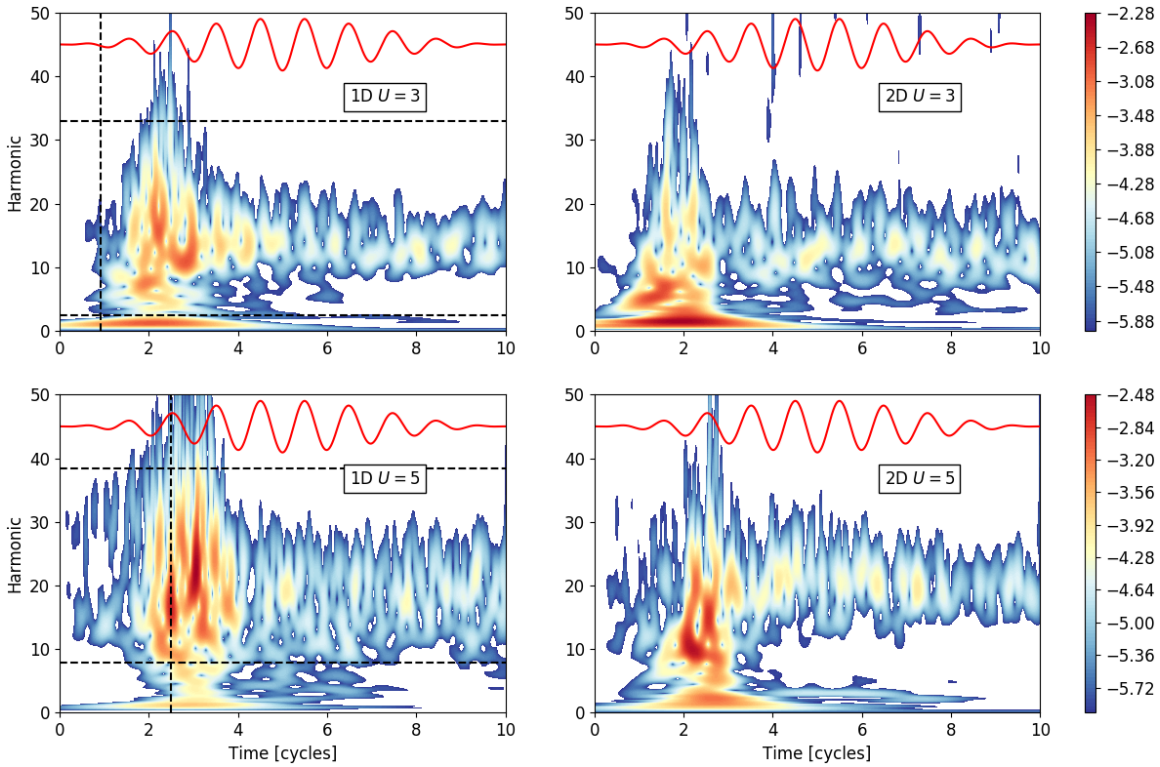

Figure 4.9: **Time-resolved HHG demonstrating the photo-induced breakdown of Mott insulators.** Spectrograms at $U = 3, 5$ in 1D and 2D. Colourscale denotes the log of the spectral emission intensity, and a separate scale is used for each U. Red lines show the incident electric field, $E(t)$. In 1D, the horizontal dashed lines show the excitation energies Δ to $\Delta + 8t_0$, and the vertical dashed lines show the times when $E(t) = E_{th}$. Calculated using tVMC on 36-site lattices.

of dimensionality and correlation. The CBM is therefore very useful, despite its many approximations, because it helps us to understand the general properties of the systems' bandstructures, which we can then use to identify the origin of specific spectral features.

In Sec. 4.3, it was sometimes not possible to determine the primary mechanisms responsible for different sections of the spectra. This is mostly a problem in 2D because no analytical gaps are available, so it is not possible to clearly define the boundary between intra and interband-induced emission. This was an issue for 2D $U = 1$ in fig.4.4 and 2D $U = 3$ in fig.4.5, where the origins of their low-harmonic peaks were uncertain. However, time-frequency profiles can help to clear up this ambiguity,

as we can compare the uncertain cases with ones that we know for certain come from intraband processes. Specifically, we can use the $U = 0$ spectrogram in fig.4.7, but also the 1D $U = 3$ spectrogram in fig.4.9 because its gap is available. In both these cases, their low harmonics start immediately upon irradiation at high intensity, and have a distinctive narrow band-like structure. These properties clearly resemble the 2D $U = 1, 3$ cases, and show that their low harmonics originate in intraband motion. This same reasoning also applies to the ambiguous 1D $U = 1$ case, where a gap is available but is too small to define separate regions.

Fig.4.9 shows that in the $U \gg 1$ regime there is a visible separation between the low harmonics originating from intraband oscillations, and the recombination-induced bulk of emission that constitutes the Mott transition. In 1D this can be seen explicitly because of the plotted excitation energies, but in 2D the distinction is even clearer and suggests that the $U = 5$ gap is near the 4th or 5th harmonic, as that separates the two regions of HHG and can also be seen in fig.4.5. The interband emission is only triggered near $E(t) \approx E_{th}$, where the tunneling probability increases greatly. This is in contrast to the intraband emission, which starts immediately or soon after the initial irradiation. It then peaks during the transition, where there are a high density of itinerant excitations available for acceleration, before dying off within 2 cycles of its completion, matching the convergence of the observables in fig.4.1 and fig.4.2. At all U, this band of low-harmonic HHG is far stronger in 2D, because the charge carriers are better able to undergo dynamical oscillations due to the lattice and bandstructure, as previously discussed.

The $U = 1$ spectrograms in fig.4.8 show significant differences due to their tiny gaps. Eq.(2.36) predicts that $\Delta_{1D}(1) \approx 0.005$, which means that the threshold field is reached almost instantly. Given this, it initially seems strange that higher frequencies are emitted comparatively late, after approximately the 2nd cycle. But this can be understood by looking at the HHG as $\Delta(U) \to 0$, which shows that these features are actually intraband in origin and not part of the Mott breakdown. By comparing them with the profiles of the $U = 0$ and $U = 0.5$ systems, in fig.4.7 and fig.4.10 respectively, we can see that the 'late' $U = 1$ high harmonics continuously morph into the bands of the $U = 0$ system. They are therefore intraband emission that persists due to the small gap, whereas the HHG associated with the phase transitions occurs earlier and

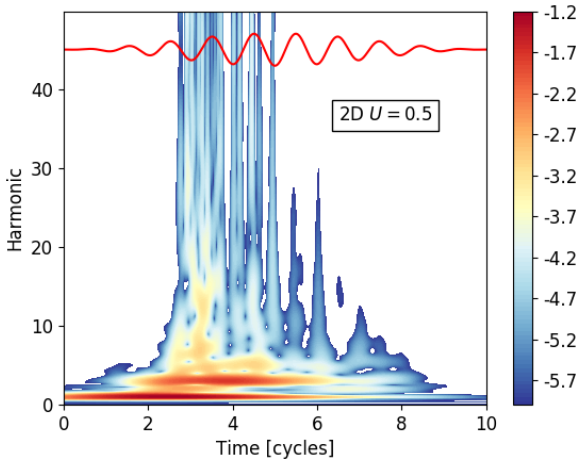

Figure 4.10: **Convergence of the emission in the $U \to 0$ limit.** Time-resolved emission in the $U = 0.5$ system, showing how the HHG continuously morphs from fig.4.8 into the non-interacting limit, fig.4.7. The red lines show the incident electric field, $E(t)$. Calculated using tVMC on a 6×6 lattice.

is mostly at lower intensities than shown here, which is hinted at by the curved shape of the spectra.

The emission in fig.4.9 is highly irregular and there is no obvious alignment with the pulse, other than through E_{th}. However, these spectrograms were presented in a way that maximises the clarity of the Mott transitions, and other substructures within the HHG can be resolved by looking at different frequency and intensity scales. This is done in fig.4.11 at $U = 5$, which includes emission intensities up to 10 orders of magnitude smaller than in fig.4.9 and frequencies up to the 100th harmonic. The Mott transitions become mostly obscured, but new weak-intensity shadow-structures start to emerge that show interesting variation with dimensionality. Its analysis is facilitated by comparison with the GS overlap probability $W(t)$, given by eq.(4.8), which is also plotted.

In 1D, there is a period of highly regular HHG in which field and emission peaks align closely. This starts during the phase transition and peaks soon after it, with emission reaching up to approximately the 80th harmonic, several times larger than $\sim U/\omega_L$ where the lower harmonics are maximal. The emission ultimately loses its structure as the field strength reduces towards the end of the pulse. This is mirrored by the overlap, which crests (troughs) at electric field peaks (zeroes), and converges to nearly zero in-sync with the destruction of the emission form.

This behaviour in 1D can be understood in terms of an extended 3SM. If we start at a $E(t)$ trough (say, at the 2nd cycle), where the system has a large overlap

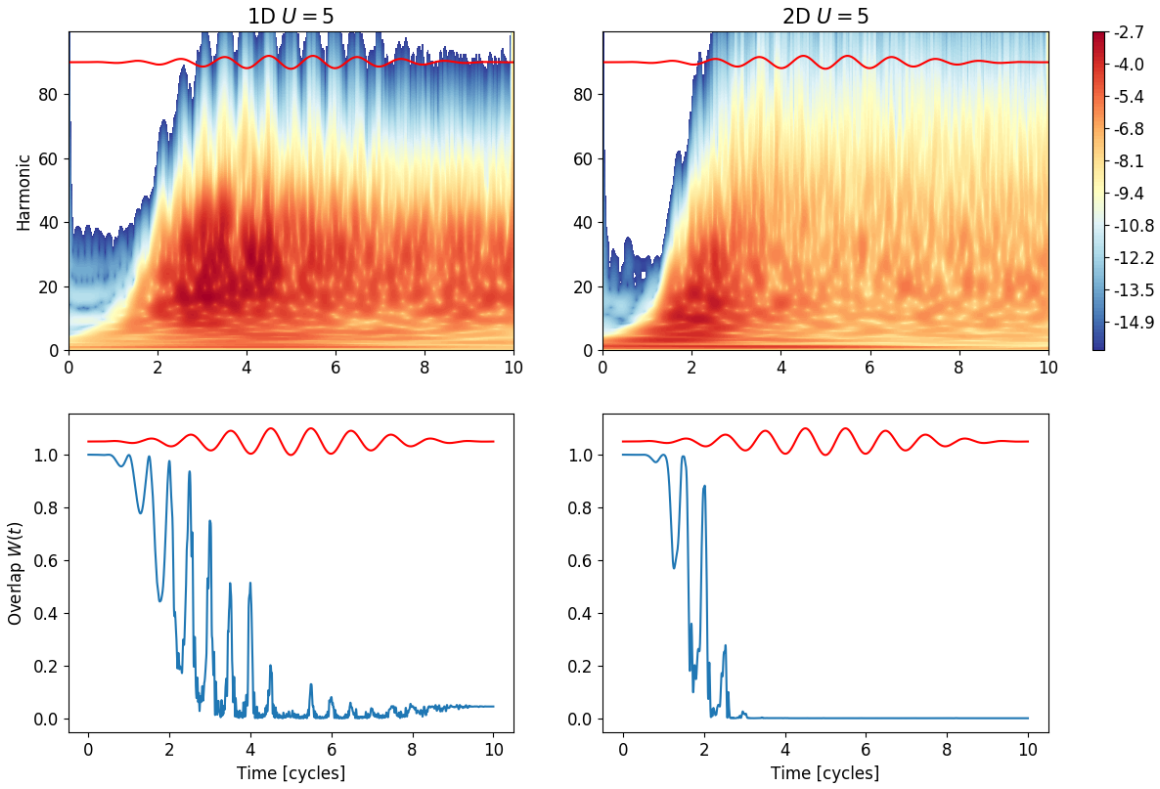

Figure 4.11: **Time-resolution of the low-intensity structure of the HHG.** Spectrograms at $U = 5$ in 1D (left column) and 2D (right column). Below each is plotted the overlap probability with the GS, eq.(4.8). Colourscale denotes the log of the spectral emission intensity. The scale is chosen to highlight the high-frequency, low-intensity emission required to observe sub-cycle structure that cannot be seen in fig.4.9. Red lines show the incident electric field, $E(t)$. Calculated using ED on 12-site lattices.

with the GS, then as the field increases there is continuous generation of double-hole excitations, causing $W(t)$ to plummet. These DHPs are subsequently accelerated and undergo intraband oscillations. They start to recombine once the field has changed direction, with recombination peaking as the field approaches its next minimum at the 3rd cycle, causing a peak in the emission spectrum and a corresponding one in $W(t)$ as excitations return to the GS. In 1D, the above-gap HHG in fig.4.11 during a given half-cycle is caused by the recombination of excitations that were created in the previous half-cycle, with the sum effect that there are 2 emission peaks per cycle.

In 2D there is a more complicated and irregular sub-cycle structure to the HHG,

composed of flaring that often occurs multiple times per half-cycle and not exclusively at the field peaks. This persists fairly uniformly near the 80th harmonic from its onset until the end of the pulse. The overlap shows that the insulating state is destroyed before low-intensity features have fully developed, and instead the emergence of visible structure coincides with the completion of the breakdown and onset of weak flaring observed in fig.4.9. These features are therefore not directly related to the melting of Mott order, and in fact they will be shown to emerge generally once the field strength is sufficiently strong. Its irregular form is likely caused by the larger number of trajectories that DHPs can take in 2D, which results in complicated combinations of constructive and destructive interference patterns. A promising area of future research would involve calculating the complex phase of the dipole acceleration and using it to resolve the dynamical trajectories of the excitations.

Fig.4.11 was calculated using ED because the stochastic noise inherent to tVMC obscures emission at low intensities, and the method is instead better suited to studying only the largest few orders of magnitude of the HHG spectrum. This means that we have to consider the impact of finite-size effects on the low-intensity features of the 2D spectrogram, as there might be contributions from long-time charge dynamics whose subsequent HHG is affected by the small lattice size. The potential influence of these effects is a limitation of the results, however, the emission features are predominantly caused by sub-cycle dynamics that occur on very short timescales and therefore will not in general be able to travel large enough distances for it to become a major problem. The convergence of the HHG with respect to lattice size was tested insofar as is possible, and is discussed in Appendix A.

4.4.3 Below Threshold Regime

Finally, we turn to the case where the peak field strength is below the threshold for DC breakdown of the Mott gap. In the absence of an analytical expression for $\Delta(U)$, calculating the time-dependence of the HHG provides a direct method of qualitatively determining if an insulator-to-metal transition has occurred. In addition to this, spectrograms in the $U \to \infty$ limit allow us to understand the origins of the unusual spectral properties discussed in Sec. 4.3.3 and shown in fig.4.6.

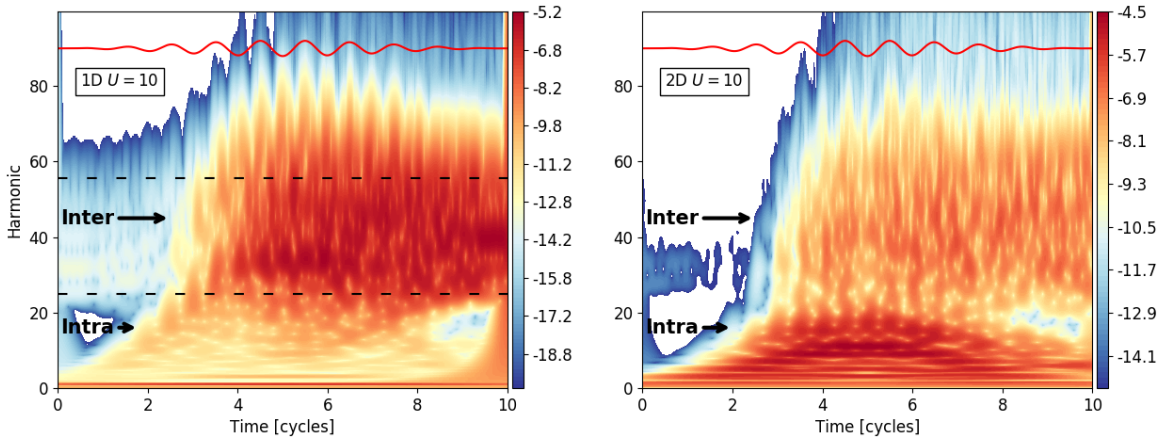

Figure 4.12: **Time-resolved HHG in the $E_{th} \gg E_0$ regime.** Spectrograms at $U = 10$ in 1D and 2D. As $U \to \infty$, the HHG splits into two sectors with different origins, which are indicated here with labels. Red lines show the incident electric field, $E(t)$. In 1D, the horizontal dashed lines show the excitation energies Δ to $\Delta + 8t_0$. Calculated using ED on 12-site lattices.

Given that in the $U \to 0$ limit the system becomes conducting and has HHG entirely from charge oscillations, we might expect that in the opposite regime the emission is caused entirely by recombination. However, fig.4.12 demonstrates that this is not the case, again using the example of $U = 10$. In both dimensionalities there is a partitioning of the spectrum into overlapping regions of intra and interband-induced emission. The former dominates below approximately the 30th harmonic, where the HHG resembles the metallic system in fig.4.7, with the characteristic field-aligned structure caused by BOs combined with intense low harmonics (especially the 1st harmonic) that start immediately at $t = 0$. This confirms the intraband origin of the various low-frequency features observed in fig.4.6, in particular the prominent lobe-like structure in 2D below the 30th harmonic.

At larger harmonics, the considerable Mott gaps leads to field-synchronised HHG that begins when $E(t)$ is sufficient to cause excitations and then simply continues for the rest of the pulse, peaking near the pulse centre where the field is strongest but always maintaining high intensity. This field dependence is the characteristic feature of spectrograms in the $E_{th} > E_0$ regime, because there is an absence of the threshold behaviour observed in fig.4.9, where there is a sudden onset of intense

emission that peaks soon after E_{th} and then rapidly decays, signifying a transition to a metallic-like state with high charge mobility. Instead, in fig.4.12 the insulating GS survives irradiation and there is continuous emission at fairly uniform intensities. This is also true of the intraband low harmonics, which in fig.4.9 rapidly decay once the breakdown has converged and are limited to very small harmonics only, but in fig.4.12 occur throughout and have a wide range of emitted harmonics that depends on field strength only; all properties shared by the $U = 0$ system.

In 1D, the HHG caused by BOs actually extends beyond the gap and blends with interband harmonics, which might be responsible for the bump in fig.4.6 at approximately the 33rd harmonic. However, their intensity is comparatively weak and is many orders of magnitude lower than in 2D, where BOs are the main source of HHG. Given the strong electron interactions in the 2D system and the fact it is in a heavily-insulating state, it initially seems surprising that charge oscillations are so prominent. However, this can be explained by the formation of localised magnetic moments as U increases, resulting in intraband currents that do not form from the oscillation of itinerant doublons and holes, but instead develop during the recombination of localised excitations in a background of local moments.

Some of the properties of the highest harmonics' low-intensity structure mirror those of the $U = 5$ case in fig.4.11. In particular, in 1D the 3SM again leaves its fingerprints through highly-ordered field-aligned HHG near the 80th harmonic that is most pronounced when the emission intensity is maximal, i.e. around the pulse centre at $U = 10$ and during the transition at $U = 5$. Furthermore, the 2D HHG again has a more irregular and featured sub-cycle structure, reflecting the larger dimensionality. The finite-size effects at such a large correlation strength are likely small because of the localising effects of the interactions. Therefore, the persistence of the HHG's irregularity is evidence that these are also genuine structures in fig.4.11 and not numerical figments.

4.5 The Correlated Bandstructure Model

The HHG of MIs emerges from the full correlated dynamics of the many-body system. However, the past sections have made frequent use of one-body language and

have made the GS bandstructure a vital part of the analysis. Using an effective single-particle model - the correlated bandstructure model (CBM) of Sec. 3.6 - we will investigate the extent to which a simple single-electron characterisation of the bandstructure can reproduce the qualitative features of the HHG in the Hubbard model. We will look at the regimes in which the model succeeds or fails and what that can teach us, and will use it as a way of substantiating past suggestions about the origins of features in the interacting systems' emission.

4.5.1 Summary and Limitations of the CBM

In the CBM for a given U, the non-interacting (tight-binding) bandstructure is modified by the introduction of a parameter $V(U)$, which couples each 'physical' site to a fictitious one, as described by the Hamiltonian eq.(3.47). Once these auxiliary degrees of freedom are traced out the resulting GS bandstructure resembles the correlated one, with a second band and an effective Mott gap $\tilde{\Delta}(U)$. The GS one-body DM, $\rho(0)$, is then calculated and propagated using RK4 to simulate pulse irradiation. This is a non-interacting dynamical mean-field theory, which means it can be simulated rapidly in the true bulk limit [3]. It only requires the optimisation of a single parameter, which aids in interpretability and enables us to consider the gap-driven emission in isolation.

However, the model has some significant limitations that are worth considering before it is used for analysis. Firstly, the effective minimal self-energy does not change with time, unlike non-equilibrium DMFT for example, but instead is fixed by the GS correlations. Secondly, the fictitious sites are only coupled locally, so there can be no long-range, momentum-dependent modifications to the effective interactions. Lastly, no spin-dependent parameters are optimised, precluding the formation of GS AFM order, and therefore of Mott melting.

[3] All CBM calculations were done for 36-site systems in order to make them directly comparable to the tVMC results. This does not affect the analysis because the HHG has converged by this size, and increasing it does not change the qualitative features of the results.

4.5.2 HHG in the CBM

An understanding of the CBM's GS bandstructure is required to analyse its HHG, and so it is worth briefly recapitulating its most important properties. The dispersion and DOS were discussed in Sec. 3.6.1, and are shown in fig.3.1 and fig.3.2, respectively, for effective $U = 0$, 3, 7 in 1D and 2D. It was found that for a given U the Mott gap in 1D is always larger than 2D, but also that both are overestimates of the true correlated gaps, $\tilde{\Delta}(U) > \Delta(U)$. Furthermore, there are distinctive differences between the DOS in 1D and 2D, with the latter showing strong quasiparticle peaks near the gap. The available one-body excitations lie between $\tilde{\Delta}(U)$ and $\tilde{\Delta}(U) + W = \tilde{\Delta}(U) + 4dt_0$, resulting in a bandwidth that is twice as large in 2D. In 1D, this restricts most higher harmonic emission to a narrow corridor of $4t_0 \approx 15$ harmonics, and means that the 2D spectra will always be considerably wider for any U.

The model is exact in the uncorrelated limit, where $U = V(0) = 0$ and eq.(3.47) reduces to the tight-binding model. When $V > 0$, interband recombination begins and leads to the emission of a broad spectrum of high harmonics. This is shown in fig.4.13 for 2D $U = 5$ (left) and $U = 7$ (right), corresponding to $V \approx 2.1$ and 3.1, respectively. The HHG has many familiar properties, especially compared to those observed in 1D. In particular, most emission falls between the available excitation energies, and the peak emission goes as $\sim U/\omega_L$. Furthermore, at $U = 7$ we see the broadening of the spectrum due to the addition of intraband-induced sub-gap harmonics, as was observed in fig.4.5 in 2D.

However, the effective gaps $\tilde{\Delta}(U)$ are a primary source of error due to their overestimated sizes. They cause the HHG at a given U to be shifted to higher harmonics than they should be, and also cause the premature exponential decay of emission intensity as correlation increases. Finally, the distinctive Van Hove singularities in the 2D DOS in fig.3.2 have visible consequences for the spectra. These structures were suggested to be the origin of the sharp peak in fig.4.5 in the 2D $U = 5$ system, and this is supported by the appearance of a similar peak in fig.4.13, although it is at approximately $U/\omega_L \approx 19$ instead of ≈ 10 due to its overestimated Mott gap.

The effectiveness of the CBM is divided by correlation strength between those U for which a Mott transition occurs in the Hubbard model, and those in which

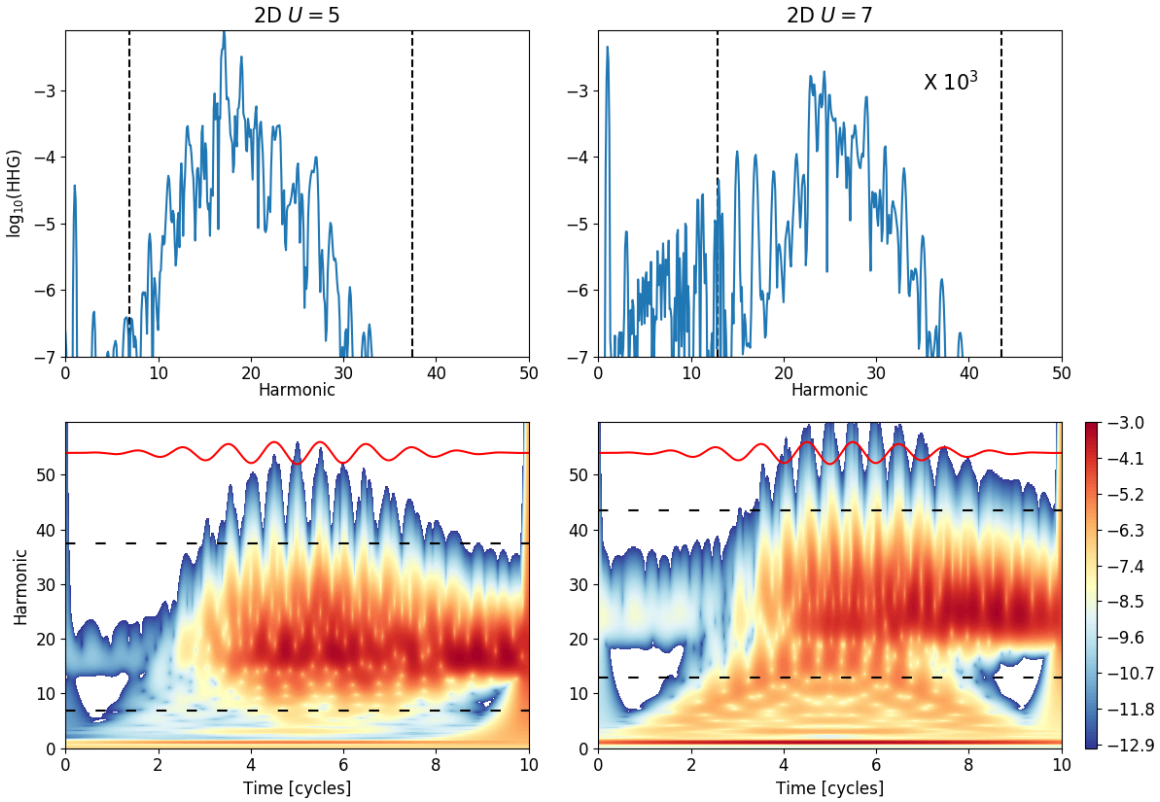

Figure 4.13: **HHG in the effective single-particle model.** Emission spectra and spectrograms in 2D for effective correlation strengths $U = 5$ (left) and $U = 7$ (right, multiplied by 10^3), corresponding to optimised parameters $V \approx 2.1$ and $V \approx 3.1$, respectively. The dashed lines show the single-particle excitations $\tilde{\Delta}(U)$ and $\tilde{\Delta}(U) + 8t_0$. Welch's method was applied to the HHG spectra to remove spectral leakage. Red lines show the incident electric field, $E(t)$. Calculated using mean-field methods on a 6×6 lattice.

$E_{th} > E_0$. This is caused by the absence of AFM order in the GS, as can be confirmed by calculating the spin-spin correlation $\eta(t)$ using eq.(3.62). Doing this shows that the system maintains a paramagnetic phase throughout, with a rapidly oscillating $\eta(t)$ that always remains near to zero. This is interesting because it allows us to directly observe the effects on the HHG of removing GS spin order in a system that otherwise has a similar bandstructure.

The consequences of this can be seen in fig.4.13 at $U = 5$, where the spectrogram does not exhibit threshold behaviour like in fig.4.9, but instead recombination is triggered once the field strength is sufficiently strong and then simply continues

thereafter; i.e. the characteristic behaviour of below-threshold spectrograms.

Related to this is the low-harmonic emission, which at $U = 5$ is mostly limited to the 1st harmonic and is emitted continuously at fairly uniform intensity that is roughly two orders of magnitude smaller than the recombination peak. In fact, the strong low harmonics observed in fig.4.5 are mostly absent and harmonics below the gap are suppressed, with most emission instead falling between the excitations. This indicates, as previously suggested, that in the transition regime of the 2D Hubbard model there is a strong relationship between the formation of intraband currents and the Mott melting process itself, as during this time there is an extremely high density of DHP excitations being created and made available for oscillation. This coupling can be seen in fig.4.9, where the intraband-induced low-harmonic emission strongly peaks during the Mott transition and then rapidly decays after it. The lack of a breakdown means that the CBM cannot capture this, and instead has intraband emission that simply varies directly with the strength of $E(t)$ and therefore peaks at the pulse centre, where $E(t) = E_0$.

Finally, we once again see the emergence of highly pulse-synchronised emission at large harmonics, however, compared to fig.4.11 and fig.4.12 it more closely resembles the structure found in 1D, and does not reproduce the complexity caused by interfering trajectories in 2D. This interesting difference shows the impact of an absence of explicitly correlated many-body dynamics in 2D lattices.

We have seen the limitations of a semiconductor-like model of MIs for describing transition-regime interaction strengths, and it showed clearly that correlated systems are fundamentally different and require a many-body description. However, their defining distinction is the photo-induced Mott transition, and we can in fact use our simple mean-field model to recover the qualitative features of the dynamics and HHG of systems in the limit $U \to \infty$, where dielectric breakdown is not possible because $E_{th} \gg E_0$. An example is fig.4.14, which shows the HHG produced in the Hubbard model by the 1D $U = 12$ system, and demonstrates properties that clearly match those of effective $U = 7$ in fig.4.13.

This regime was discussed in Sec. 4.3.3 and Sec. 4.4.3, and has very distinctive characteristics. The extremely strong Coulomb repulsion reduces the probability of DHP formation, leading to a sparsely populated UHB that can readily support in-

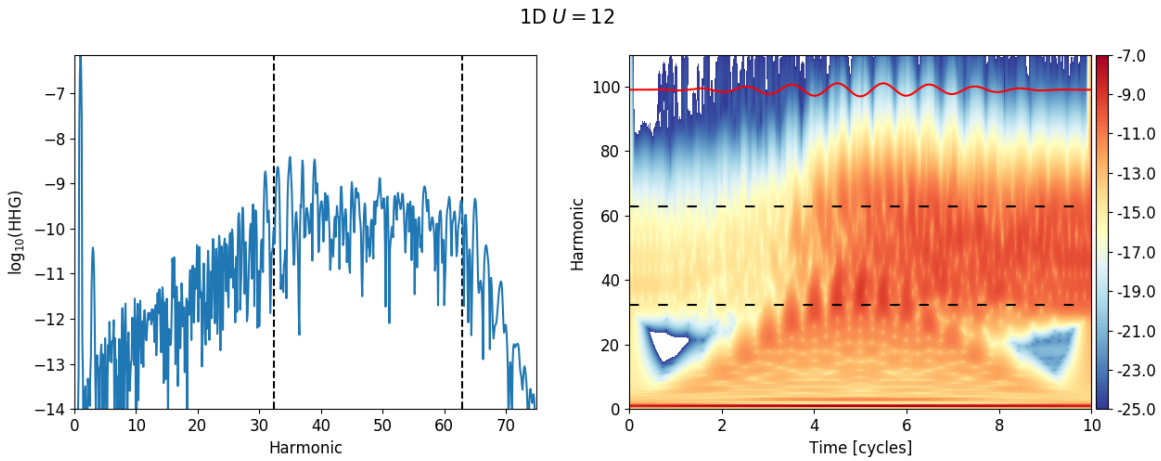

Figure 4.14: **Convergence of the Hubbard model and CBM as correlation strength increases.** Emission spectrum and spectrogram at $U = 12$ in the 1D Hubbard model. Compared to effective $U = 7$ in fig.4.13, this shows the convergence of the qualitative properties of the HHG in the Hubbard model and the CBM in the limit $U \to \infty$. Red line shows the incident electric field $E(t)$, and the dashed lines show the excitation energies Δ to $\Delta + 8t_0$. Calculated using ED on 12-site lattices.

traband currents. As a result, emission due to BOs becomes significant and extends beyond the low harmonics seen in e.g. fig.4.9, instead going into the tens of harmonics and leading to a visible division between these and even larger recombination-induced harmonics. This was seen in both dimensionalities at $U = 10$ in fig.4.6 and fig.4.12, but is clearer still in fig.4.14 at $U = 12$, where the massive gap has pushed up the above-gap harmonics and reduced overlap between the regions. These properties are perfectly reproduced by the CBM, as shown in fig.4.13 for the example of effective $U = 7$. This demonstrates that the static properties of the GS bandstructure become the dominant determiner of HHG as correlation increases in the Hubbard model, and that the sub-cycle dynamics can be well-approximated by considering single-particle excitations within this bandstructure. This is a somewhat ironic convergence, as it is the most strongly-correlated systems that start to resemble uncorrelated semiconductor systems, whereas even e.g. $U = 1$ in fig.4.8 has radically different properties due to its GS spin order and subsequent breakdown.

Finally, while the maximum emission intensities are converging to very similar orders in both models, the actual harmonics emitted remain different, with the CBM

mostly limited to below the 50th harmonic, whereas the Hubbard model at large U causes significant emission up to approximately the 100th harmonic. This is due to the available energies of the CBM's single-particle electron-hole excitations compared to the many-body DHP excitations of the Hubbard model. The differences between these two cases are a demonstration of the general possibility that the many-body interactions of strongly-correlated materials can cause HHG at much higher harmonics than is possible in semiconductors.

4.6 Varying the Simulation Setup

The following sections show the effects of varying individual simulation parameters while keeping all others constant at the same values used previously. The aim is to compare the HHG between different examples to understand the physics behind the observed changes, and to learn more about how each parameter impacts the Mott breakdown process.

4.6.1 Pulse Parameters

So far the pulse setup has been kept constant so that the effects of correlation and dimensionality could be identified and analysed. The peak field strength has been fixed at $E_0 = 10\text{MVcm}^{-1}$ and the frequency at $\omega_L = 32.9\text{THz}$, but in this section these two parameters will be varied and the HHG compared, using the 2D $U = 5$ system as a representative case. In particular, we are interested in the impact that E_0 and ω_L have on the Mott transition, and how the breakdown can be controlled by changing them. Eq.(4.2) will still be used as the pulse, with its sin-squared envelope and sinusoidal carrier wave.

4.6.1.1 Peak Field Strength, E_0

Before investigating the correlated case it is informative to first look at the non-interacting $U = 0$ system, as this allows us to observe the effects of E_0 on BOs unimpeded by the complications that interactions introduce. Fig.4.15 plots the currents and resulting HHG spectra for $E_0 = 5\text{MVcm}^{-1}$ (left) and 20MVcm^{-1} (right)

in the 2D $U = 0$ system, to be compared to $E_0 = 10\text{MVcm}^{-1}$ in fig.4.3 and fig.4.7. When $U > 0$, the current becomes so complicated that it is often difficult to learn much from, but these tight-binding systems provide a useful window into the electron dynamics.

At $E_0 = 5\text{MVcm}^{-1}$, the current has no visible signs of BOs (i.e. no kinks), and is simply synchronised with $A(t)$ without any further structure. This means that the field strength is not enough to drive electrons up to the Brillouin zone boundary, and instead they oscillate with the field and produce a mostly linear response. As a result, the emission spectrum shows few high harmonics and is dominated by the 1st harmonic, which is unsurprising because the current's main frequency component is visibly the same as the pulse's. Doubling the peak strength to $E_0 = 10\text{MVcm}^{-1}$ causes kinks to emerge in fig.4.7, representing 1 Bloch cycle per pulse half-cycle, with a corresponding production of high harmonics in the spectrum of fig.4.3, although the 1st harmonic is still the largest contribution. Doubling again to $E_0 = 20\text{MVcm}^{-1}$ causes more dramatic effects as it permits multiple Bragg scatterings to occur per half cycle, as can be seen in the current, resulting in a shift in the spectrum to higher harmonics beyond the 1st.

We can get a better understanding of what is happening using the solution to Bloch's acceleration theorem, eq.(4.16). The quasi-momentum in either direction is $k(t) = k(0) + A(t)$, which means for BOs to occur it is a minimum requirement that

$$|k(0) + \max\{A(t)\}| > \frac{\pi}{a} \tag{4.20}$$

This can be approximated by $k(0) + A_0 = k(0) + \frac{E_0}{\omega_L} > \frac{\pi}{a}$, which corresponds to the quasi-momentum of an electron at the pulse centre where the field is strongest. In units of $\frac{\pi}{a}$, we have $\frac{E_0}{\omega_L} \approx 1.9$ at $E_0 = 20\text{MVcm}^{-1}$, meaning that during the central part of the pulse all electrons will undergo BOs, regardless of their initial momenta. Conversely, $\frac{E_0}{\omega_L} \approx 0.47$ at $E_0 = 5\text{MVcm}^{-1}$, so for a system starting in the GS with electrons stacked up to the Fermi level, there will be no $k(0)$ large enough to permit BOs, and the intraband current is composed only of oscillations within the conduction band that are never able to reach its edge. The effects of changing frequency at $U = 0$ can be analysed in the same way, and doing this shows that decreasing ω_L encourages BOs and therefore shifts the spectrum to higher frequencies, and conversely increasing

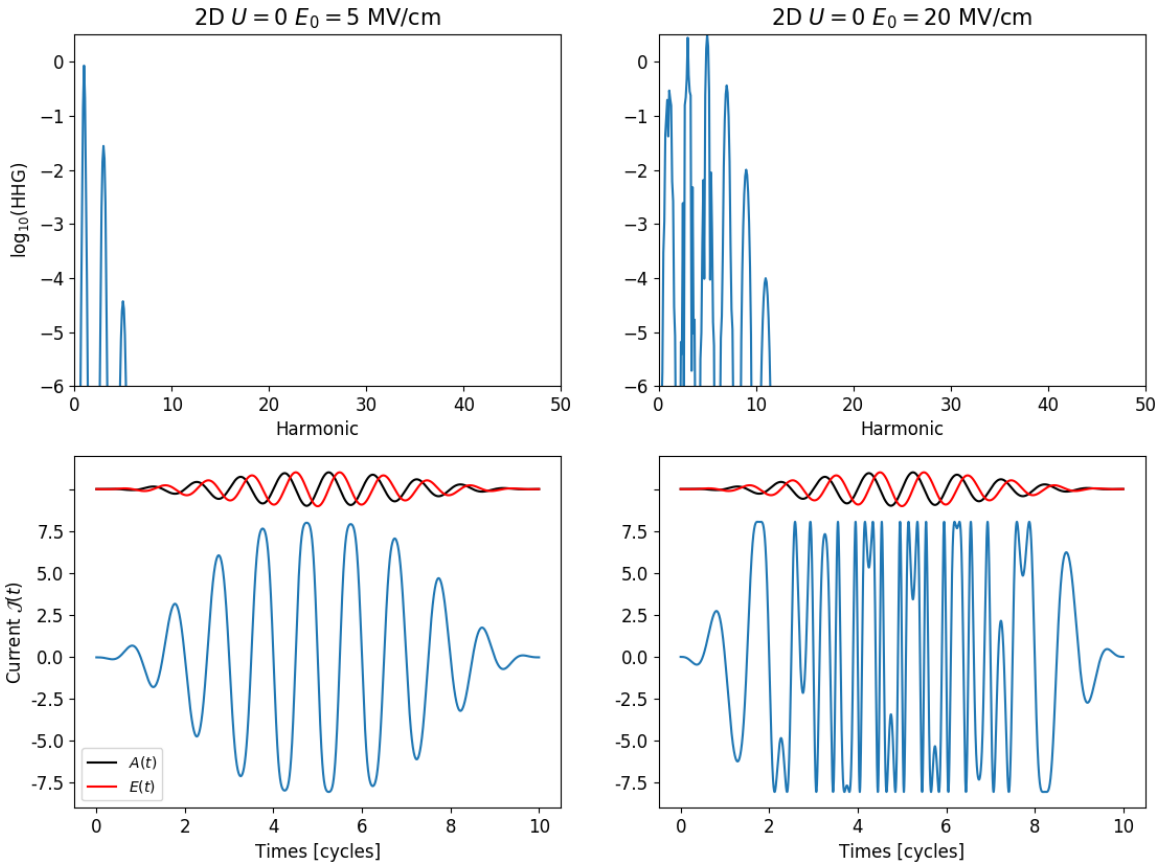

Figure 4.15: **The effects of varying peak field strength in the uncorrelated system.** HHG spectra with the corresponding currents in 2D at $U = 0$ and $E_0 = 5$, 20MVcm^{-1}, compared to $E_0 = 10$MVcm^{-1} in fig.4.3 and fig.4.7. Red lines show the incident electric field $E(t)$, and the black lines are the corresponding vector potential $A(t)$. Calculated using eq.(4.10) and mean-field methods on a 6×6 lattice.

it causes BOs to recede and ultimately stop.

Fig.4.16 shows the equivalent plots in the 2D transition regime at $U = 5$, again for $E_0 = 5$, 20MVcm^{-1}, compared to $E_0 = 10$MVcm^{-1} in fig.4.5 and fig.4.9. Unlike the non-interacting regime, varying the peak field strength does not cause dramatic changes in the HHG. This includes the cutoff frequency, which is unaffected. The same was found in small 1D systems in Ref. [132], and is in contrast to the linear E_0-dependence observed in semiconductor systems. This interesting difference arises because of the GS bandstructure of these correlated systems, as the cutoff is confined

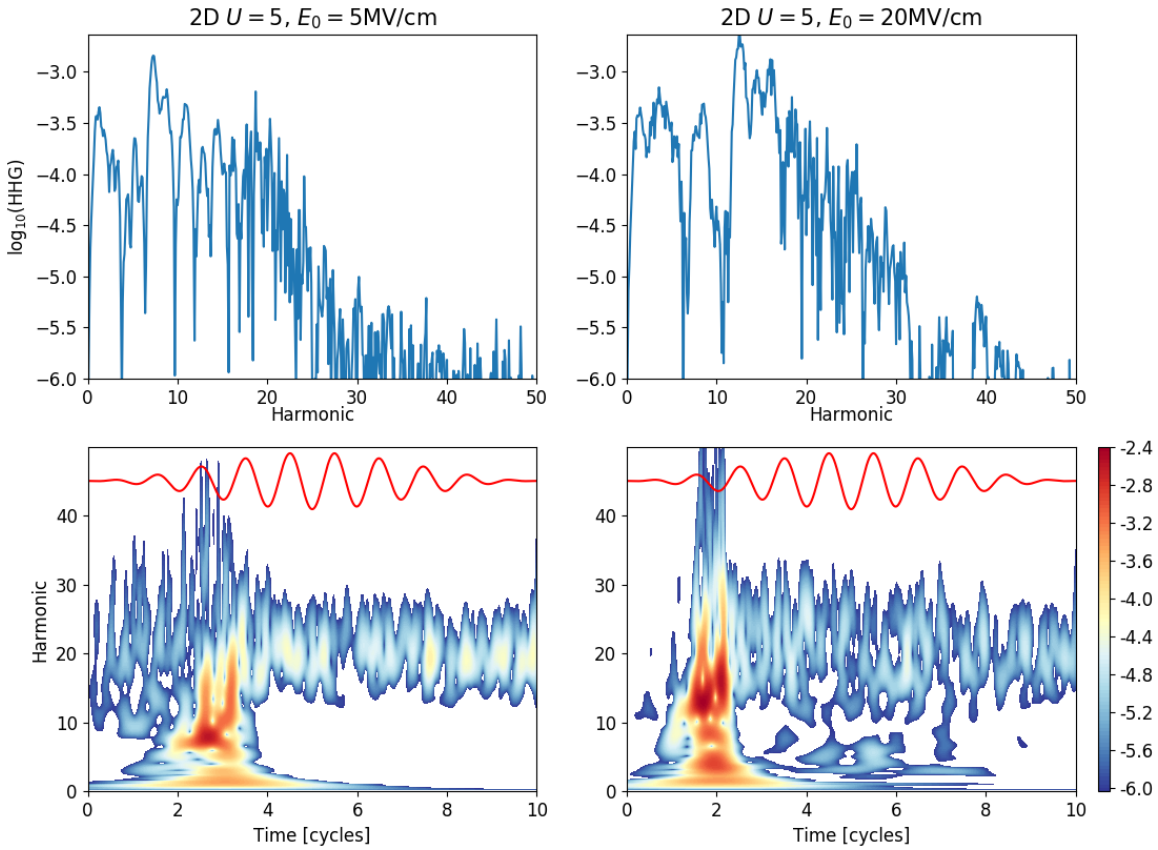

Figure 4.16: **The effects of varying peak field strength in the transition regime.** Emission spectra and spectrograms in 2D at $U = 5$ and $E_0 = 5$, 20MVcm^{-1}, compared to $E_0 = 10$MVcm^{-1} in fig.4.5 and fig.4.9. Red lines show the incident electric field $E(t)$. Calculated using tVMC on a 6×6 lattice.

to be within the available energies of the UHB[4], and in the transition regime all of these energies are readily accessible, which leads to a saturated UHB and therefore no change in the maximum possible excitation energy as E_0 is increased. This is distinct from single-particle bandstructure systems, where the maximum kinetic energy can be increased by raising the field strength, thereby increasing the cutoff. A multi-band Hubbard model would have a more complicated E_0-dependence in the transition regime, and so could be a potential avenue for future research. However, even within our single-band model there are significant changes to the cutoff as $U \to \infty$, where

[4]I.e. in 1D, the energies Δ to $\Delta + 8t_0$.

$E_{th} \gg E_0$ and the UHB is no longer saturated. This regime was found to have a linear dependence on E_0 in 1D [135] and infinite-D [137], and confirming this in 2D is a natural next step, although it is complicated by the fact that, as seen in fig.4.6 and fig.4.12, the highest-intensity structure in 2D becomes intraband in origin due to the depopulation of the UHB. Furthermore, Ref. [137] found distinct cutoff relationships to arise in the strong and weak-field regimes, with the former developing multiple plateaus at increasing harmonics that also have a linear field dependence. An initial analysis using ED found that these plateaus also form in 2D (and in the CBM), and a more in-depth study would be very interesting.

One significant property that does change in fig.4.16 is the maximum-intensity harmonic, which appears to migrate to slightly higher frequencies with increasing field strength, with small accompanying rises in the emission intensity. Fig.4.5 showed that at $E_0 = 10\text{MVcm}^{-1}$ the peak is highly localised at $\omega_{max} \approx 9.5$, whereas at $E_0 = 5$ and 20MVcm^{-1} it is $\omega_{max} \approx 7.5$ and 12.5, respectively. Its structure is similar in each case, with a distinctive shape that is likely a consequence of the Van Hove singularities in the DOS. The smallest harmonics at which this structure can form are due to DHPs being excited from one Van Hove singularity to the other, which upon recombination produces emission peaks very near to the gap. However, increasing E_0 might cause a higher density of excitations to (from) energies beyond (below) the Van Hove singularity, resulting in peaks forming at larger harmonics. This could also explain the peaks' thickening as E_0 grows, because a broader range of energies become significant contributors. This is likely aided by the large bandwidths in 2D, which increase the availability of states and therefore the number of potential excitation pathways.

Its spectrogram shows that decreasing the field strength to $E_0 = 5\text{MVcm}^{-1}$ is clearly not enough to remove the system from the tunneling regime, and in fact it remains sufficient to pass the threshold field required to initiate melting. The overall time-frequency characteristics of the Mott transition are largely unaffected by varying E_0 within the range of values such that $E_0 \geq E_{th}$. One exception is the transition duration, which reduces as E_0 is ramped up, as suggested by the $E_0 = 20\text{MVcm}^{-1}$ spectrogram where the entire breakdown appears to finish in less than a single cycle after its onset. However, the main consequence of the field strength is to

determine how rapidly the threshold is achieved, thereby changing the onset of the dynamical phase transition. In 2D, where no analytical description is available, the time of maximum intensity emission can be used to estimate when the breakdown is occurring because it closely follows E_{th} being reached[5]. This predicts that the transitions in our three cases are separated by half a cycle, with peak intensities occurring at approximately 1.5, 2 and 2.5 cycles, at $E_0 = 20$, 10 and 5MVcm^{-1}, respectively. In other words, by increasing E_0 the onset of the transition is brought forward, and vice versa[6]. This also agrees with a simple qualitative comparison of the spectrograms, because $E_0 = 20$MVcm^{-1} is visibly shifted towards the beginning of the pulse compared to $E_0 = 5$MVcm^{-1}.

4.6.1.2 Frequency, ω_L

Fig.4.17 shows the effects of varying the pulse frequency in the 2D $U = 5$ system, with representative examples $\omega_L = 50$THz (left) and 25THz (right), compared to $\omega_L = 32.9$THz in fig.4.5 and fig.4.9. The number of cycles is maintained at $N_c = 10$, resulting in a fairly large variation in total pulse duration between the three cases: $T \approx 200$, 300, 400fs, in order of decreasing frequency, where $T = \frac{N_c}{f_L} = \frac{2\pi N_c}{\omega_L}$.

Decreasing (increasing) ω_L produces a generalised shifting of the spectrum to larger (smaller) harmonics, causing the cutoff to develop a strong frequency dependence. This includes corresponding changes to the peak harmonics[7], which have migrated approximately 1-2 harmonics in either direction compared to $\omega_L = 32.9$THz. The effects are particularly noticeable in the $\omega_L = 25$THz case where there is a broad region of peak emission, somewhat similar to its 1D equivalent in fig.4.5 and unlike the localised peaks at higher frequencies. This means that ω_L controls the relative contribution of the intra and interband currents, with the latter becoming more dominant as the frequency decreases. These properties can be explained by the GS bandstruc-

[5]In 1D this was confirmed by comparing ED and tVMC peak intensity times against the threshold time t_c, calculated using eq.(4.3), and it was found that the maximum emission occurs roughly a half cycle after t_c (although this varies with U). The transitions occur more rapidly in 2D so we would expect it to be even less than a half cycle.

[6]The latest a transition can be triggered is if $E(t) = E_{th} = E_0$ at the pulse's centre.

[7]In 1D it is immediately clear that the same pattern will be observed because the region of peak HHG is centered at $\sim U/\omega_L$.

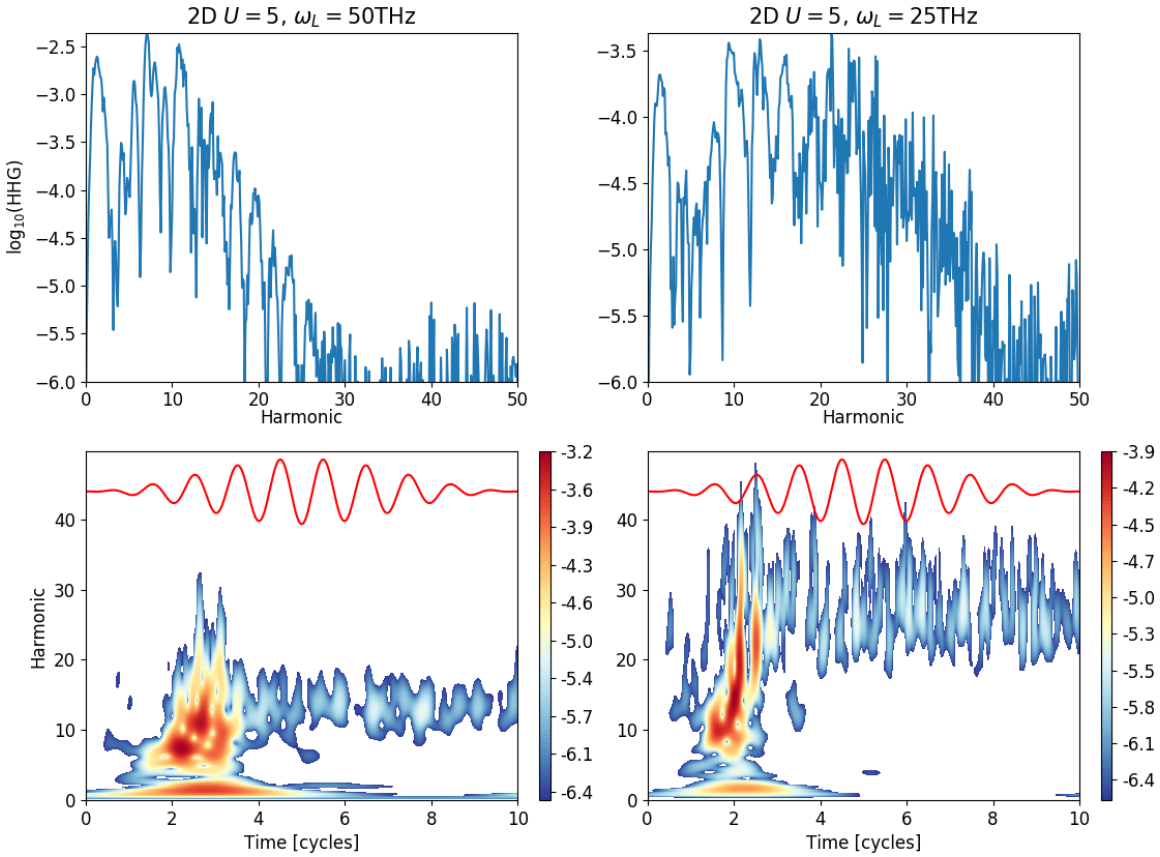

Figure 4.17: **The effects of varying pulse frequency in the transition regime.** Emission spectra and spectrograms in 2D at $U = 5$ and $\omega_L = 25$, 50THz, compared to $\omega_L = 32.9$THz in fig.4.5 and fig.4.9. In order to fully bring out the structure, separate colorscales are used for each case and with a slightly larger intensity range than in fig.4.9. Red lines show the incident electric field $E(t)$. Calculated using tVMC on a 6×6 lattice.

ture because the harmonics due to a single DHP recombination range from $\Delta(U)/\omega_L$ to the maximum excitation $\varepsilon_{max}(U, t_0)/\omega_L$, and therefore have an inverse dependence that will cause the emitted frequencies to increase (decrease) as ω_L is made smaller (larger). This will therefore shift the cutoff and all above-gap HHG to higher harmonics. It also suggests an explanation for why the overall emission intensity rises with the frequency (in fig.4.17, by an order of magnitude when ω_L is doubled), because the possible DHP energies are made more tightly packed in frequency space, so we might expect emission over that smaller range of harmonics to increase in intensity.

The Schwinger limit, given by eq.(2.35), depends on the static field strength and

not on ω_L. As a result, the onset of the Mott transition is independent of frequency[8], provided it is not increased so much as to approach the Keldysh crossover, at which point the excitation mechanism tends towards multi-photon absorption and so threshold behaviour is lost. One deceiving difference between the spectrograms in fig.4.17 is the duration of the breakdowns, which appears to occur more rapidly at $\omega_L = 25$THz. This is true relative to the pulse cycles in each case, but not when measured in femtoseconds because the total pulse length is half as long at $\omega_L = 50$THz [9].

The conclusions reached here, concerning both E_0 and ω_L, appear to be broadly true in 1D as well. So far this analysis has only been done for small systems using ED, but it showed very similar patterns of change. However, a noticeable difference was found in the peak emission as E_0 is varied, because in 1D it is not strongly affected like in fig.4.16 - although this seems to break down somewhat at $E_0 > 30\text{MVcm}^{-1}$, and is definitely worth investigating further.

4.6.2 Lattice Parameters

So far the lattice parameters have been kept constant so that the effects of varying correlation and dimensionality could be identified and analysed. They have been fixed at the hopping constant $t_0 = 0.52$eV and lattice constant $a = 4$Å, values that were originally designed to mimic the material Sr_2CuO_3 [165, 207]. Fig.4.18 gives examples of the impact of changing these parameters in 2D systems. In each case, t_0 is again used as the energy unit (within a system of atomic units), resulting in adjusted values of the other parameters. Firstly, the top row shows $U = 5$, 7 for $a = 5$Å and $t_0 = 0.22$eV, which in the model's units are $a = 0.0764$, $\omega_L = 0.618$, $E_0 = 29.751$. Secondly, the bottom row plots $U = 5$, 12 for $a = 10$Å and $t_0 = 0.1$eV, resulting in $a = 0.0694$, $\omega_L = 1.361$, $E_0 = 143.996$. These two lattice parameter sets mimic the materials $[Ni(cnxn)_2Br]Br_2$ [165, 207] and ET-F_2TCNQ [152, 165], respectively.

The effects of the lattice constant are predicable from the vector potential eq.(4.2), because it appears at the same location as E_0. Its only other contribution to the

[8] At each of the 3 frequencies discussed here, the peak emission (used to approximate when the transition is happening) occurred at the same time, just after the 2nd pulse cycle.

[9] As previously stated, $T \approx 200$fs compared to 400fs at $\omega_L = 25$THz.

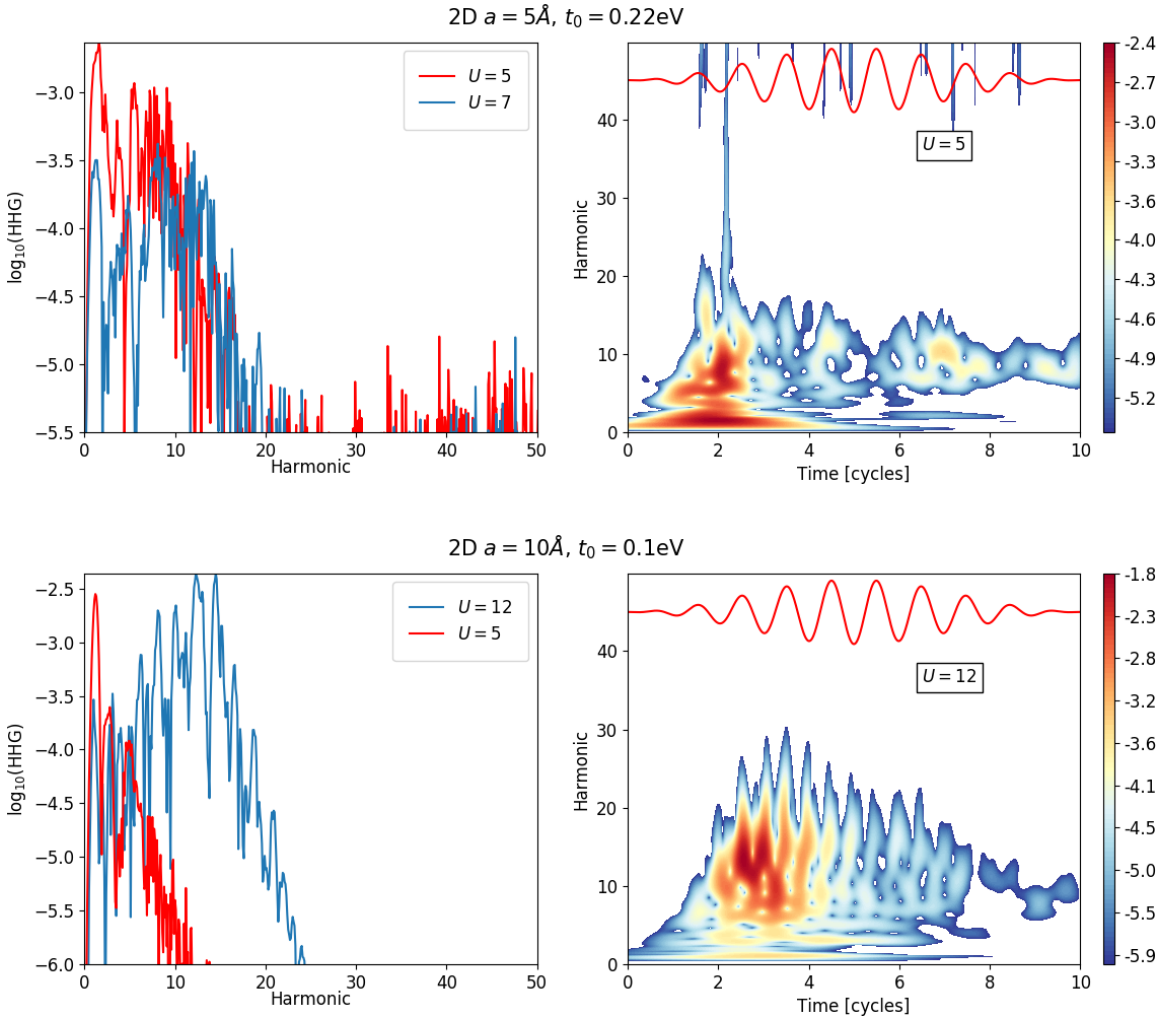

Figure 4.18: **The effects of varying lattice parameters.** Emission spectra and spectrograms for two examples of systems with different lattice and hopping constants, both in 2D. The top row shows $U = 5$, 7 with $a = 5$Å and $t_0 = 0.22$eV; and the bottom row shows $U = 5$, 12 with $a = 10$Å and $t_0 = 0.1$eV. Colourscale denotes the log of the spectral emission intensity, and in the top row plot a slightly smaller intensity range is used in order to improve clarity. The red lines in the spectrograms show the electric field, $E(t)$. The top plots were calculated using tVMC on a 6×6 lattice, and the bottom using ED on a 4×3 lattice.

emission spectrum is via the current eq.(2.30), where it is a multiplicative constant, resulting in an a^2 scaling of the spectrum. The overall effect of the lattice constant is therefore the same as discussed in Sec. 4.6.1.1, but with an additional upward spectral shift.

The gap is a function of U/t_0, and recall that the single-particle bandwidth is $W = 4dt_0$ and that the 1D maximum excitation energy is $\Delta + 8t_0$, with some t_0-dependent equivalent in 2D. As a result, t_0 strongly influences the range of emitted harmonics resulting from recombination, and therefore also the cutoff frequency. Fig.4.18 demonstrates the effects of these parameters for two cases where a is increased and t_0 decreased. They show that a smaller hopping constant means both $\Delta(U)/\omega_L$ and $\varepsilon_{max}(U, t_0)/\omega_L$ are reduced, and causes aggressive narrowing of the spectra. At $U = 5$, the intraband current is retained and becomes the dominant contribution, whereas above-gap emission is suppressed, resulting in spectra that resemble previous low-U systems (e.g. fig.4.4 or $U = 3$ in fig.4.5). These parameters also have significant influence over the Mott transition. From eq.(2.35) we see that E_{th} is inversely proportional to a, and t_0 impacts E_{th} via the gap. In fig.4.18, both the large lattice constants and small hoppings cause E_{th} to be small compared to E_0, causing rapid breakdowns and the ability to reach the threshold field at extremely large correlation strengths. For example, in the $t_0 = 0.1$eV case breakdowns can continue in 1D up to approximately $U = 18$, according to the analytical expressions. Fig.4.18 shows one at $U = 12$, demonstrating radically different behaviour than the highly insulating state in fig.4.14.

4.7 Summary and Outlook

In this chapter, a combination of ED, tVMC and mean-field methods were used to investigate the ultrafast high harmonic spectroscopy of correlated lattice systems. Mott insulating materials were modelled using the Fermi-Hubbard Hamiltonian and an effective single-particle model, and were propagated in real time to simulate their irradiation by a strong-field laser pulse. The resulting HHG was analysed in detail across dimensionality and correlation regimes and under varying simulation parameters, enabling the resolution of the attosecond charge dynamics in both the frequency

and time domains.

The logical next step in this research would be to make closer connections with real materials. This would likely require exploring more general doping, and going beyond chain and square lattice systems. This could be approached using the Fermi-Hubbard model, either by retaining it in the form that was used here, or by extending it to include some combination of beyond-nearest-neighbour hopping, off-site interactions and multiple bands. This could then be used to simulate HHG in specific materials, for example in graphene with a honeycomb lattice and $U \approx 1.6$ [29]. Alternatively, we could go beyond the Hubbard model entirely and use more realistic models, as the flexibility of ED and tVMC would enable new models to be implemented relatively easily. However, any extensions of course come with the caveat that computational cost will increase, which risks limiting the investigation to small system sizes.

Computational cost was a severe limiting factor with both ED and tVMC. In particular, it restricted the former to 12-site systems, which in 2D led to the problem of artificial frustration in the GS. It might be possible to carry out at least some 4×4 simulations using a faster and highly-parallelised implementation of an exact propagation method. For example, the HΦ package [208] includes limited functionality for real-time evolution using eq.(3.45), and could be extended and applied to any desired case.

The results in this chapter highlight the advantages and disadvantages of using tVMC. A significant advantage is that it is not limited by dimensionality in the same way that DMRG is to 1D, and DMFT to infinite-D. However, stochastic noise imposes strict limitations and essentially restricts accurate calculations of HHG to approximately the largest four orders of magnitude of the spectral intensity, and to within the first 50 or so harmonics. For the systems that were studied here, these limitations are sufficiently broad to capture the most important regions of the spectra, and to do so precisely enough that the emission can be time-resolved with great clarity. However, as we have seen, this becomes a problem in cases where we would like to study the low-intensity and/or very high harmonic structure of the HHG, which requires reverting to ED. Unsurprisingly, tVMC also becomes less accurate as U increases, and it was found to be most effective for $U \leq 6$. For the pulse and lattice parameters chosen in this thesis, these correlation strengths constitute most or all of

the transition regime, which includes the physics that we are most interested in. As a result, despite its limitations tVMC can still be an extremely effective method that can probe regimes and dimensionalities that are completely inaccessible to most other comparable numerical methods.

Improving the trial wavefunction would reduce stochastic noise and increase accuracy over a wide range of correlation strengths, harmonics and intensities. This could be done by adding an additional QNP to the current combination of momentum and point-group symmetry projectors, eq.(3.12) and eq.(3.13). For example, a total-spin projector, $\hat{\mathcal{L}}_S$ [168, 174], could be used. Alternatively, a doublon-holon correlation factor, $\hat{\mathcal{P}}_{dh}$ [168, 174], could be introduced in order to account for more many-body effects. Lastly, the PWF could be improved by introducing backflow correlations or by using the power-Lanczos method. However, in each of these cases the increased accuracy causes significant additional computational costs that are potentially prohibitive. To get around this it might be necessary to use different numerical methods, such as one of the neural networks approaches to quantum dynamics that are currently being developed [186, 188]. Another possibility is the Feynman's clock method [209], where quantum many-body dynamics is mapped to a GS eigenvalue problem, and so could be implemented using SR and VMC. It should be a less costly method, and so could potentially allow a more accurate wavefunction to be chosen. Another option is to keep the current trial wavefunction but use it to probe systems larger than the 36 sites that we have been limited to, such as the 8×8 lattice or perhaps even 3D systems, although this would likely be limited to the $4 \times 4 \times 4$ lattice.

There are many ways of extending the CBM in order to address or alleviate the limitations that were discussed in Sec. 4.5.1. For example, the model could be improved by introducing time dependence, $V(U) \rightarrow V(U,t)$, and/or by optimising parameters to match both charge and spin gaps. The latter would help the model mimic GS AFM order, which would enable it to simulate Mott melting. Of course, any of these additions would increase the computational cost of the model and complicate the interpretability of the results. On the other hand, it would allow us to hone in on the origin of the HHG's features by varying the inclusion of time-dependence and charge/spin-matching, and observing the resulting changes. A major source of inaccuracy in its HHG spectra originates in the model's overestimation of Mott

gaps, $\tilde{\Delta}(U) > \Delta(U)$. This could be addressed in future work by e.g. imposing an additional constraint during the optimisation of $V(U)$ to boost the accuracy of the gap estimation.

The pulse was kept fixed to eq.(4.2) throughout, but an interesting area for future research would be to study the effects of varying either or both of the envelope and carrier wave, with e.g. Gaussian or cosine choices, possibly including a carrier-envelope phase of the form $\sin[\omega_L t + \varphi]$. We could go further still by allowing the pulse to vary in each direction, for example by introducing an ellipticity parameter[10], $\epsilon \in [-1, 1]$. The vector potential then has the general form

$$\boldsymbol{A}(t) = A_0 f(t) \left(\frac{1}{\sqrt{1+\epsilon^2}} \cos[\omega_L t] \hat{\boldsymbol{e}}_x + \frac{\epsilon}{\sqrt{1+\epsilon^2}} \sin[\omega_L t] \hat{\boldsymbol{e}}_y \right) \tag{4.21}$$

where $f(t)$ is the envelope function. The ellipticity-dependence of HHG in solids has been studied in e.g. [129], but no work has yet been done investigating this in MIs.

The results in fig.4.16 and fig.4.17 hint at what is possible by varying the pulse parameters at a given U. Going further, this could enable us to manipulate many aspects of the Mott melting process and essentially 'design' a transition with the desired properties. Firstly, E_0 can be used to modulate both the breakdown's onset time and duration. The former can be controlled precisely and made to start as quickly as required by increasing E_0, or turned off entirely by reducing it below the threshold field[11]. The frequency then offers a further control knob, allowing us to adjust both the intensity and spread of the emission. For example, by ramping up ω_L it is possible to generate HHG that is highly concentrated into a narrow band of high-intensity harmonics, whose position can then be shifted in the time and frequency domains by altering E_0. It could be possible to achieve even more control by changing some combination of the envelope function, carrier wave and other pulse properties; for example, by designing the pulse shape to reach E_{th} at a particular time. Once again, the flexibility of tVMC means that these avenues could be investigated with minimal additional alterations to the existing implementation.

[10] $\epsilon = -1$ generates left-handed circular polarisation, $\epsilon = 1$ is right-handed circular polarisation and $\epsilon = 0$ is linear polarisation.

[11] This is of course more true in 1D because the Bethe ansatz results permit the necessary pulse parameters to be explicitly calculated.

5

Current Tracking

In this chapter, a protocol for current tracking is derived and demonstrated, with the aim of controlling and manipulating the optical response of many-body strongly-correlated materials. Starting in a given system, the approach takes as its input a predetermined current and then dynamically calculates the driving or 'control' field required to induce this current within our system, with it then described as having been 'tracked'. This enables the optical properties of one system to be imitated by another, regardless of how different they may be. The method is completely general in the sense that it can be applied to generate the desired evolution for an expectation value of any observable, and without being constrained to a specific Hamiltonian. However, in this thesis only the electric current will be considered and calculations will be limited to the 2D Fermi-Hubbard Hamiltonian. Arbitrary polarisations will be introduced in order to maximise flexibility and enable direction-dependent tracking over the full range of correlation strengths between the non-interacting and heavily Mott-insulating limits, but always with a focus on the transition regime and on obtaining experimental viability. This extends the work of the previous chapter, and explores the limits to which we can control and design the desired response of an interacting system, and the ways in which these control fields can be constructed.

5.1 Tracking Protocol

The current has a highly nonlinear dependence on the incident laser field, making its control a challenging and interesting problem. Various techniques have been developed to try and tackle the general question of quantum control [210, 211], including so-called optimal [212–214] and local [215] control methods. The strategy used here

falls under a third class called tracking control [216, 217], in which the system is evolved such that its expectation value for a chosen observable matches a predefined trajectory. The model discussed in this section was first derived in Refs. [2, 3], and was done in collaboration with Gerard McCaul and others at Tulane university, with my contribution being to the development of the code. Those papers used ED to analyse small 1D systems, and here this will be further extended to 2D, along with new results and analysis that go beyond the published data and combine tVMC in the construction of the tracking protocol.

5.1.1 Tracking in 1D

Our system is propagated under the 1D Fermi-Hubbard model

$$\hat{\mathcal{H}}(t) = -t_0 \sum_{j\sigma} \left\{ e^{-i\Phi(t)} \hat{c}^\dagger_{j\sigma} \hat{c}_{j+1\sigma} + e^{i\Phi(t)} \hat{c}^\dagger_{j+1\sigma} \hat{c}_{j\sigma} \right\} + U \sum_i \hat{n}_{i\uparrow} \hat{n}_{i\downarrow} \tag{5.1}$$

The current operator in 1D is given by eq.(2.27). As previously discussed, by using the nearest-neighbour hopping expectation in polar form

$$\left\langle \Psi \left| \sum_{j\sigma} \hat{c}^\dagger_{j\sigma} \hat{c}_{j+1\sigma} \right| \Psi \right\rangle = R\left(\Psi\right) \mathrm{e}^{i\theta(\Psi)} \tag{5.2}$$

it is possible to write the current expectation as

$$\mathcal{J}^{(1\mathrm{D})}(t) = -2at_0 R(\Psi) \sin\left[\Phi(t) - \theta(\Psi)\right] \tag{5.3}$$

We consider a system with correlation strength U_I, whose irradiation by the pulse $\Phi(t)$ induces a current[1], $\mathcal{J}^{(U_I)}(t)$. The aim is to reproduce this current in a second system that has a different correlation strength, U_T, and that produces the current $\mathcal{J}_T^{(U_T)}(t)$ when under a control field $\Phi_T^{(1\mathrm{D})}(t)$. In other words, we want the $\Phi_T^{(1\mathrm{D})}(t)$ required to propagate the U_T system such that $\mathcal{J}_T^{(U_T)}(t) = \mathcal{J}^{(U_I)}(t)$. This control field

[1] We are not limited to currents of this nature, and we could choose an arbitrary function instead of the expectation of the current operator under some laser field.

can be calculated by inverting eq.(5.3)

$$\Phi_T^{(1\mathrm{D})}(t) = \arcsin\left(\frac{-\mathcal{J}_T^{(U_T)}(t)}{2at_0R(\Psi)}\right) + \theta(\Psi) \tag{5.4}$$

This field is evaluated dynamically by calculating the correlation functions in eq.(5.2) at each timestep, and then using eq.(5.4) to find $\Phi_T^{(1\mathrm{D})}(t)$. This field then evolves the system forward by one step, with RK4 again used to carry out the propagation in all cases.

5.1.2 Tracking in 2D

There are (at least) two ways of implementing the tracking scheme in 2D, with equivalent derivations in higher dimensions as well. The first is a straightforward generalisation of the 1D case, using the hopping expectation

$$\left\langle \Psi \left| \sum_{\langle ij\rangle\sigma} \hat{c}_{j\sigma}^\dagger \hat{c}_{i\sigma} \right| \Psi \right\rangle = R\left(\Psi\right) \mathrm{e}^{i\theta(\Psi)} \tag{5.5}$$

Just as in 1D, the current is then given by

$$\mathcal{J}^{(2\mathrm{D})}(t) = -2at_0R(\Psi)\sin\left[\Phi(t) - \theta(\Psi)\right] \tag{5.6}$$

which leads to a control field of the form

$$\Phi_T^{(2\mathrm{D})}(t) = \arcsin\left(\frac{-\mathcal{J}_T^{(U_T)}(t)}{2at_0R(\Psi)}\right) + \theta(\Psi) \tag{5.7}$$

It is applied along the diagonal of the square lattice in order to track the system's total current and without any consideration of its spatial variation, thereby enforcing that the laser field is identical in each direction, $\Phi_x(t) = \Phi_y(t)$.

However, the second tracking scheme considers the general case of arbitrary polarisation, $\Phi_x(t) \neq \Phi_y(t)$, which opens up the possibility of directional tracking. To do this, the total current operator is written in terms of its contributions in both

directions

$$\hat{\mathcal{J}}(t) = -iat_0 \sum_{\langle ij\rangle\sigma} \left\{ e^{-i\Phi_{ij}(t)} \hat{c}^\dagger_{i\sigma} \hat{c}_{j\sigma} - e^{i\Phi_{ji}(t)} \hat{c}^\dagger_{j\sigma} \hat{c}_{i\sigma} \right\} \tag{5.8}$$

$$= -iat_0 \left[\sum_{\langle ij\rangle_x\sigma} \left\{ e^{-i\Phi_x(t)} \hat{c}^\dagger_{i\sigma} \hat{c}_{j\sigma} - h.c. \right\} + \sum_{\langle ij\rangle_y\sigma} \left\{ e^{-i\Phi_y(t)} \hat{c}^\dagger_{i\sigma} \hat{c}_{j\sigma} - h.c. \right\} \right] \tag{5.9}$$

$$= \hat{\mathcal{J}}_x(t) + \hat{\mathcal{J}}_y(t) \tag{5.10}$$

where $\sum_{\langle ij\rangle_k\sigma}$ refers to hops from site i to an adjacent site j in the k direction. By defining hopping expectations in each direction the current can be partitioned as follows

$$\left\langle \Psi \left| \sum_{\langle ij\rangle_x\sigma} \hat{c}^\dagger_{i\sigma} \hat{c}_{j\sigma} \right| \Psi \right\rangle = R_x(\Psi) e^{i\theta_x(\Psi)} \implies \mathcal{J}_x(t) = -2at_0 R_x(\Psi) \sin\left[\Phi_x(t) - \theta_x(\Psi)\right]$$

$$\left\langle \Psi \left| \sum_{\langle ij\rangle_y\sigma} \hat{c}^\dagger_{i\sigma} \hat{c}_{j\sigma} \right| \Psi \right\rangle = R_y(\Psi) e^{i\theta_y(\Psi)} \implies \mathcal{J}_y(t) = -2at_0 R_y(\Psi) \sin\left[\Phi_y(t) - \theta_y(\Psi)\right] \tag{5.11}$$

This produces two separate control fields, in principle allowing the simultaneous tracking of two entirely distinct currents, $\mathcal{J}^{(x)}_T(t)$ and $\mathcal{J}^{(y)}_T(t)$

$$\Phi^{(x)}_T(t) = \arcsin\left(\frac{-\mathcal{J}^{(x)}_T(t)}{2at_0 R_x(\Psi)} \right) + \theta_x(\Psi) \tag{5.12}$$

$$\Phi^{(y)}_T(t) = \arcsin\left(\frac{-\mathcal{J}^{(y)}_T(t)}{2at_0 R_y(\Psi)} \right) + \theta_y(\Psi) \tag{5.13}$$

It is important to note that a system's total current, $\hat{\mathcal{J}}(t) = \hat{\mathcal{J}}_x(t) + \hat{\mathcal{J}}_y(t)$, produces a harmonic spectrum that is not the simple sum of the spectra of its x and y directions, because

$$\mathcal{S}(\omega) = \left| \mathcal{FT}\left\{ \frac{d\mathcal{J}(t)}{dt} \right\} \right|^2 = \left| \mathcal{FT}\left\{ \frac{d}{dt}\Big(\mathcal{J}_x(t) + \mathcal{J}_y(t) \Big) \right\} \right|^2 \tag{5.14}$$

$$= |a_x(\omega)|^2 + |a_y(\omega)|^2 + 2a_x(\omega)a_y(\omega) \tag{5.15}$$

In the future discussion, the spectrum due to the current in the x (y) direction refers to the first (second) of these terms, whereas the total current's spectrum has the additional cross-term. The nonlinear dependence between the terms is induced by the correlated dynamics and so cannot be solved for independently, even though $\mathcal{S}_y(\omega)$ only depends on $\mathcal{J}_y(t)$ instantaneously.

Finally, it is worth reiterating that this general tracking protocol can be applied to an extremely broad range of models for irradiated N-electron systems, including continuous systems, and can do so for any finite dimension. Furthermore, its application is not limited to the electric current, but can be used to track an arbitrary function of any observable. A detailed discussion of these points can be found in Ref. [3]. While this thesis is interested specifically in HHG in correlated lattice models, these other avenues offer rich possibilities for future research.

5.1.3 Tracking in the Metallic Limit

Introducing correlation into our tracking systems enormously increases the computational cost and complexity of the calculations, but in the $U_T \to 0$ limit the evolution equations simplify and become very rapid to evaluate.

As previously discussed, when $U = 0$ it is always true that $\theta(\Psi) = 0$ and $R(\Psi) = R(\Psi_{MF})$ is constant. The 1D current becomes

$$\mathcal{J}^{(1\mathrm{D})}(t) = -2at_0 R(\Psi_{MF})\sin\left[\Phi(t)\right] \tag{5.16}$$

The control field is therefore

$$\Phi_T^{(1\mathrm{D})}(t) = \arcsin\left(\frac{-\mathcal{J}_T^{(0)}(t)}{2at_0 R(\Psi_{MF})}\right) \tag{5.17}$$

In 2D, the general form of the total current is

$$\mathcal{J}^{(2\mathrm{D})}(t) = -2at_0\Big(R_x(\Psi_{MF})\sin\left[\Phi_x(t)\right] + R_y(\Psi_{MF})\sin\left[\Phi_y(t)\right]\Big) \tag{5.18}$$

which if split by direction leads to the driving pulses

$$\Phi_T^{(x)}(t) = \arcsin\left(\frac{-\mathcal{J}_T^{(x,0)}(t)}{2at_0 R_x(\Psi_{MF})}\right) \tag{5.19}$$

$$\Phi_T^{(y)}(t) = \arcsin\left(\frac{-\mathcal{J}_T^{(y,0)}(t)}{2at_0 R_y(\Psi_{MF})}\right) \tag{5.20}$$

If $\Phi_x(t) = \Phi_y(t) = \Phi(t)$, then eq.(5.18) becomes

$$\mathcal{J}^{(2\mathrm{D})}(t) = -2at_0\big(R_x(\Psi_{MF}) + R_y(\Psi_{MF})\big)\sin\left[\Phi(t)\right] \tag{5.21}$$

$$= -2at_0 R(\Psi_{MF})\sin\left[\Phi(t)\right] \tag{5.22}$$

where $R(\Psi_{MF}) = R_x(\Psi_{MF}) + R_y(\Psi_{MF})$. This leads to a control field that resembles eq.(5.17).

These control fields derive their time dependence solely from the currents they are tracking, and can be evaluated entirely from the initial state without the need to use RK4. This underlines that it is the interactions that couple these currents together and in general lead to intractable problems. The fields are calculated by finding the non-interacting GS using the Hartree-Fock method, which is then used to find $R(\Psi_{MF})$, from which the phases can be generated in full. To test this mean-field formulation, $U_T = 0$ tracking simulations were repeated with ED and tVMC and were found to give identical results.

5.1.4 Tracking Constraints

Using functional analysis, it can be shown that a solution $|\Psi(t)\rangle$ needs to satisfy two simple constraints in order to guarantee that it is unique and solves the tracking problem via unitary evolution. If we define

$$X(\Psi, t) = \frac{\mathcal{J}_T(t)}{2at_0 R(\Psi)} \tag{5.23}$$

then the two constraints are [3]

$$|X(\Psi, t)| < 1 - \epsilon_1 \tag{5.24}$$

$$R(\Psi) > \epsilon_2 \tag{5.25}$$

where $\epsilon_{1/2}$ are small positive constants. These ensure that the control field $\Phi_T(t)$ uniquely tracks the inputted current. Violations in eq.(5.24) cause a loss of Her-

miticity in the Hamiltonian, and so this constraint is required to maintain unitary evolution. The physical meaning of eq.(5.25) is not immediately clear, but can be shown to correspond to the condition that the electrons are not frozen and have non-zero kinetic energy [3], which of course has to be true for a current to form.

Together, these constraints impose limits on the currents that can be tracked by a system with some U_T while also maintaining a physically meaningful and singularity-free control field. Simulations show that eq.(5.25) tends to be satisfied without issue, and instead it is eq.(5.24) that needs to be carefully monitored. Regardless of the size of $\max\{\mathcal{J}_T\}$, it is always possible to satisfy eq.(5.24) using a heuristic scaling of the control field's argument. This could be done by considering the lattice constant to be a tunable parameter and then scaling by some factor c_S, such that $a_T^{(U_T)} = c_S a^{(U_I)}$. This was the chosen method in Refs. [2, 3], where $c_S = 60$ was required for the case $U_I = 0$ and $U_T = 7$. However, in this thesis only current scale factors α_S will be used, such that the target current $\mathcal{J}_T \to \alpha_S \mathcal{J}_T$. The shape and spectral properties are all unchanged, and the resulting tracked current can be easily unscaled once the simulation is complete. In general, these scalings become increasingly necessary when $U_T > U_I$, which can be understood by comparing the spectra peaks of small and large-correlation systems, which makes it clear that the maximum current amplitude increases as $U \to 0$. An appropriate choice of c_S or α_S guarantees that the control field does not have singularities, and is a major advantage of the method compared to other quantum control schemes.

Because this algorithm enforces the tracking by construction, we would like a way of checking if a solution represents a physical evolution free of any numerical irregularities. We can do this by writing the tracked current in terms of independent expectations, and then checking that both sides identically match over the course of the tracking evolution. One possibility is to take the derivative of the current as defined in eq.(5.6) (or eq.(5.3) in 1D)

$$\begin{aligned}\frac{d\mathcal{J}(t)}{dt} = -2at_0\Big(&\dot{\Phi}_T(t)R(\Psi)\cos\left[\Phi_T(t) - \theta(\Psi)\right] - \\ &\dot{\theta}(\Psi)R(\Psi)\cos\left[\Phi_T(t) - \theta(\Psi)\right] + \\ &\dot{R}(t)\sin\left[\Phi_T(t) - \theta(\Psi)\right]\Big)\end{aligned} \tag{5.26}$$

This is an analytic expression for the acceleration in terms of the expectations in eq.(5.5) (or eq.(5.2)), however, it is not clear if these expectations are truly independent of the tracked current. A better check can be found by starting with the original definition of the current, and then taking the derivative and expectation of its split form in eq.(5.9)

$$\frac{d\mathcal{J}(t)}{dt} = -iat_0\Bigg[\sum_{\langle ij\rangle_x\sigma}\Big\{-i\dot{\Phi}_T^{(x)}(t)e^{-i\Phi_T^{(x)}(t)}\left\langle\hat{c}_{i\sigma}^\dagger\hat{c}_{j\sigma}\right\rangle - ie^{-i\Phi_T^{(x)}(t)}\Big\langle\left[\hat{\mathcal{H}}_x(t),\hat{c}_{i\sigma}^\dagger\hat{c}_{j\sigma}\right]\Big\rangle - \text{h.c.}\Big\}+ \sum_{\langle ij\rangle_y\sigma}\Big\{-i\dot{\Phi}_T^{(y)}(t)e^{-i\Phi_T^{(y)}(t)}\left\langle\hat{c}_{i\sigma}^\dagger\hat{c}_{j\sigma}\right\rangle - ie^{-i\Phi_T^{(y)}(t)}\Big\langle\left[\hat{\mathcal{H}}_y(t),\hat{c}_{i\sigma}^\dagger\hat{c}_{j\sigma}\right]\Big\rangle - \text{h.c.}\Big\}\Bigg] \tag{5.27}$$

This is an example of an Ehrenfest theorem, and must be respected for the evolution to be physical. Its commutator terms come from the derivatives of the hopping operators

$$\frac{d\left\langle\hat{c}_{i\sigma}^\dagger\hat{c}_{j\sigma}\right\rangle}{dt} = i\Big\langle\left[\hat{\mathcal{H}}(t),\hat{c}_{i\sigma}^\dagger\hat{c}_{j\sigma}\right]\Big\rangle \tag{5.28}$$

and it is these expectations that are unambiguously independent of the tracked current. We can write eq.(5.27) in a form more amenable to numerical evaluation by defining the expectations $C_k(\Psi)$ and $\kappa_k(\Psi)$ as follows

$$\frac{1}{U}\sum_{\langle ij\rangle_k\sigma}\Big\langle\left[\hat{\mathcal{H}}_k(t),\hat{c}_{i\sigma}^\dagger\hat{c}_{j\sigma}\right]\Big\rangle = C_k(\Psi)e^{i\kappa_k(\Psi)} \tag{5.29}$$

for dimension k. Eventually this leads to eq.(5.6)

$$\frac{d\mathcal{J}(t)}{dt} = -2at_0\Big(\dot{\Phi}_T^{(x)}(t)R_x(\Psi)\cos\left[\Phi_T^{(x)}(t)-\theta_x(\Psi)\right] + UC_x(\Psi)\cos\left[\Phi_T^{(x)}(t)-\kappa_x(\Psi)\right]+ \dot{\Phi}_T^{(y)}(t)R_y(\Psi)\cos\left[\Phi_T^{(y)}(t)-\theta_y(\Psi)\right] + UC_y(\Psi)\cos\left[\Phi_T^{(y)}(t)-\kappa_y(\Psi)\right]\Big) \tag{5.30}$$

Doing the equivalent in 1D gives

$$\frac{d\mathcal{J}(t)}{dt} = -2at_0\Big(\dot{\Phi}_T(t)R(\Psi)\cos\left[\Phi_T(t)-\theta(\Psi)\right] + UC(\Psi)\cos\left[\Phi_T(t)-\kappa(\Psi)\right]\Big) \tag{5.31}$$

By checking for violations of the Ehrenfest theorem we can ensure that there are no

unphysical numerical aberrations in the tracking trajectory. This is done by calculating the right-hand side of eq.(5.30) during the tracking evolution and comparing it against the tracked dipole acceleration.

When calculated numerically, the complex phase $\theta(\Psi)$ is automatically restricted or 'wrapped' to within $[-\pi, \pi]$. As a consequence, if $\theta(\Psi)$ evolves over this threshold during a timestep update by an amount δ, then a numerical discontinuity is introduced, $\theta(\Psi) = \pm\pi \pm \delta \rightarrow \mp\pi \pm \delta$. In some cases, $\theta(\Psi)$ undergoes large oscillations that result in $|\theta(\Psi)| > \pi$ and therefore in wrapping, which then cause these artificial discontinuities to emerge in the control fields. One possibility is to choose a smaller α_S, as this stops the discontinuities forming in the first place by reducing the size of $\theta(\Psi)$ oscillations. However, the preference is always to keep α_S as close to 1 as possible. Instead, the problem can be resolved by appeal to the Ehrenfest theorem, as it is sensitive to the discontinuities and eq.(5.30) is not obeyed if $\Phi_T^{(k)}(t)$ and $\theta_k(\Psi)$ include any. We must therefore remove them by 'unwrapping' $\Phi_T^{(k)}(t)$ (or $\theta_k(\Psi)$), which can be done straightforwardly by searching for sudden jumps and undoing them by adding or subtracting factors of 2π as appropriate.

5.2 Spectral Mimicry

This method allows the reproduction of one system's optical properties by an entirely different system. There are various potential technological applications of this, for example, in materials science and chemistry it could be used to mimic the properties of an expensive and hard-to-produce material in a cheaper and readily-available alternative. In principle, we can make any system generate any optical spectrum at all, including flipping dimensionality by making something look like a lower or higher dimensional equivalent, or not looking at physical currents at all and instead tracking an arbitrary function.

Throughout this chapter, all tracked currents originate from simulations of an 8-cycle pulse with $\omega_L = 50$ THz, such that the total pulse duration is approximately 160fs. Unless otherwise stated, the setup of these tracked systems is identical to the default used in the last chapter, with $a = 4$Å, $E_0 = 10\text{MVcm}^{-1}$, etc. We will concentrate entirely on 2D systems because they introduce new and interesting possibilities

that are not available in 1D and enable us to go beyond the results in Refs. [2, 3]. This first section exclusively uses linearly polarised control fields, and all simulations were done using ED on the 4×3 lattice in order to generate a large data set and allow analysis of the results in a general way without having to consider the effects of stochastic noise. Building on that, the section after will then use tVMC to look at arbitrarily-polarised pulses in extended systems.

5.2.1 Proof of Concept

To demonstrate the capabilities of this technique we consider the metallic $U_I = 0$ and strongly correlated $U_I = 8$ systems. The driving pulse eq.(4.2) is applied along the diagonal at these two interaction strengths, producing currents $\mathcal{J}^{(0)}(t)$ and $\mathcal{J}^{(8)}(t)$ with radically different properties. The first is a conducting system with a simple spectrum originating entirely from intraband oscillations and composed of distinct sharp peaks, whereas the latter is deep in the insulating regime and has a broad spectrum that emerges from the complex dynamics of its many-body charge excitations, both within and between its bands. The aim is then to swap their spectral characteristics, causing the $U_T = 0$ ($U_T = 8$) system to generate $\mathcal{J}^{(8)}(t)$ ($\mathcal{J}^{(0)}(t)$) via a control field $\Phi_T^{(0)}(t)$ ($\Phi_T^{(8)}(t)$). This laser pulse is also applied along the lattice diagonal, such that $\Phi_T^{(x)}(t) = \Phi_T^{(y)}(t)$ at all times. The plotted control fields refer to the pulse in one direction, instead of being shown as 3D plots.

This photo-mimicry is demonstrated in fig.5.1, which shows the HHG spectrum of each system being perfectly reproduced by the other. Further details of these simulations are given in fig.5.2, showing that the control fields required in each case differ greatly. For $\mathcal{J}_T^{(8)}(t) = \mathcal{J}^{(0)}(t)$, the pulse $\Phi_T^{(8)}(t)$ needs to have considerable strength because it is trying to induce a large current in a heavily-insulating system, and conversely to generate $\mathcal{J}_T^{(0)}(t) = \mathcal{J}^{(8)}(t)$ requires only a very weak laser field. How large the pulse amplitude needs to be relative to the original driving pulse, $\Phi(t)$, can be roughly gauged by the ratio $\max\{\mathcal{J}^{(0)}(t)\}/\max\{\mathcal{J}^{(8)}(t)\} \approx 28$, which indicates that to reproduce $\mathcal{J}^{(8)}(t)$ requires a pulse much weaker than $\Phi(t)$ and vice versa. However, this is complicated by the constraint eq.(5.24) and the subsequent choice of α_S, as will be discussed shortly.

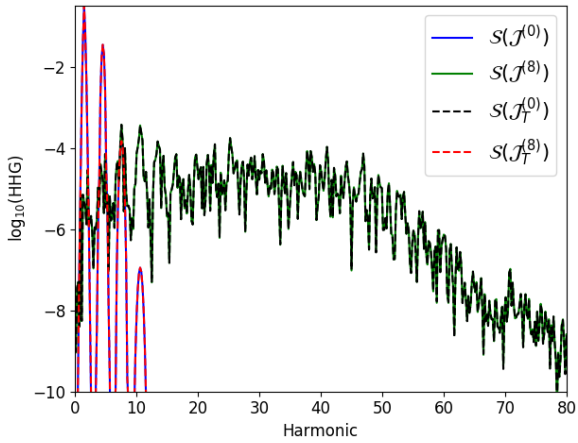

Figure 5.1: **Spectral mimicry of a conductor by an insulator and vice versa.** The emission spectrum at $U_I = 0$ ($U_I = 8$) reproduced perfectly by the $U_T = 8$ ($U_T = 0$) system. The control fields required to do this are shown in fig.5.2. In the legend, e.g. $\mathcal{S}(\mathcal{J}_T^{(0)})$ refers to the spectrum generated by the current $\mathcal{J}_T^{(0)}$. Calculated using ED on a 4×3 lattice.

For both simulations, fig.5.2 also compares the dipole accelerations calculated numerically (i.e. by taking the numerical derivative of the tracked current) with those found from the two physicality tests: the analytic check given by eq.(5.26), and the Ehrenfest theorem in eq.(5.30). These three values of $a(t)$ align exactly[2] in both simulations and at all times. The results show that the control fields are valid and the product of physical evolutions.

In fig.5.2, the $\mathcal{J}_T^{(8)}(t)$ simulation used a scale factor $\alpha_S = 0.01$ on the target current, such that $\mathcal{J}_T^{(8)}(t) = 0.01\mathcal{J}^{(0)}(t)$. This was required to ensure that the constraint eq.(5.24) was abided by at all times. Weakly correlated systems typically have large currents and nearest-neighbour magnitudes, $R(\Psi)$, and vice versa for strongly correlated systems. As a result, in general the constraint is automatically obeyed when tracking in conductors, but becomes a critical issue when doing it in insulators. In the latter case, the choice of α_S strongly impacts the internal state of the tracking system, although the resulting current is the same (up to its overall scaling). Fig.5.3 shows the effects of increasing α_S on the doublon density and required control field for $\mathcal{J}_T^{(8)}(t) = \mathcal{J}^{(0)}(t)$, and demonstrates that tracking not only controls the optical response of the material but can also change its electronic properties.

The driving field $\Phi(t)$ is unable to cause a Mott transition at $U = 8$, i.e. $E_{th} > E_0$[3]. The same must also be true for tracking when $U_T = 8$ and $\alpha_S = 0.01$, as fig.5.3 shows

[2]This is also true of all other ED simulations in this section.

[3]We cannot analytically determine this as we can in 1D, but it is clearly indicated by its spectrogram and the observables in fig.4.1 and fig.4.2.

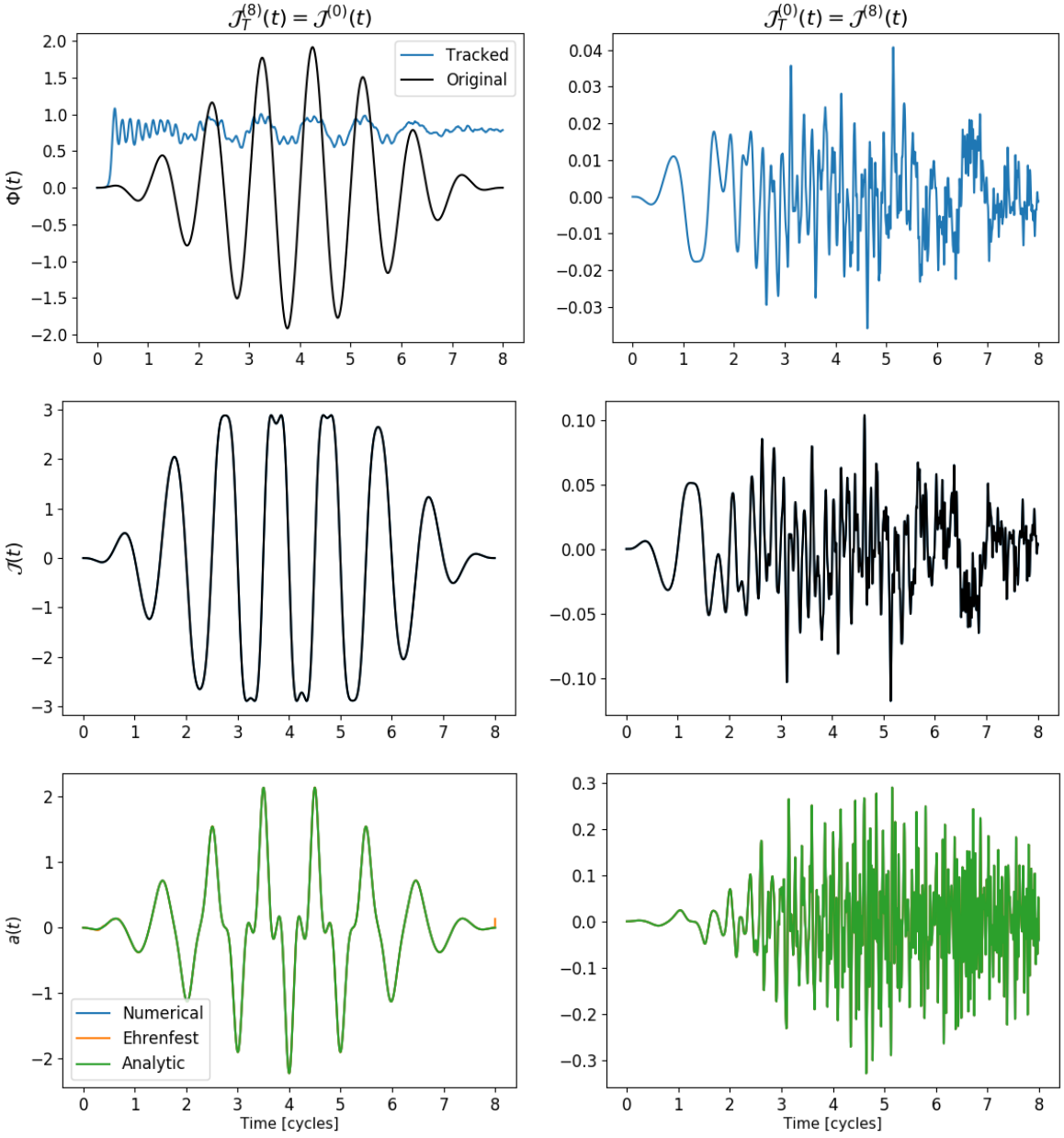

Figure 5.2: **Mimicry of a conductor by an insulator and vice versa.** Left (right) column shows the $U_T = 8$ ($U_T = 0$) system tracking the current (and therefore spectrum) of the $U_I = 0$ ($U_I = 8$) system. The rows from top to bottom show: the required control fields and original $\Phi(t)$; the original and tracked currents; the acceleration compared against the physicality checks, eq.(5.30) and eq.(5.26). A scale factor $\alpha_S = 0.01$ was used for $\mathcal{J}_T^{(8)}(t)$, whereas $\mathcal{J}_T^{(0)}(t)$ did not require scaling, i.e. $\alpha_S = 1$. Calculated using ED on a 4×3 lattice.

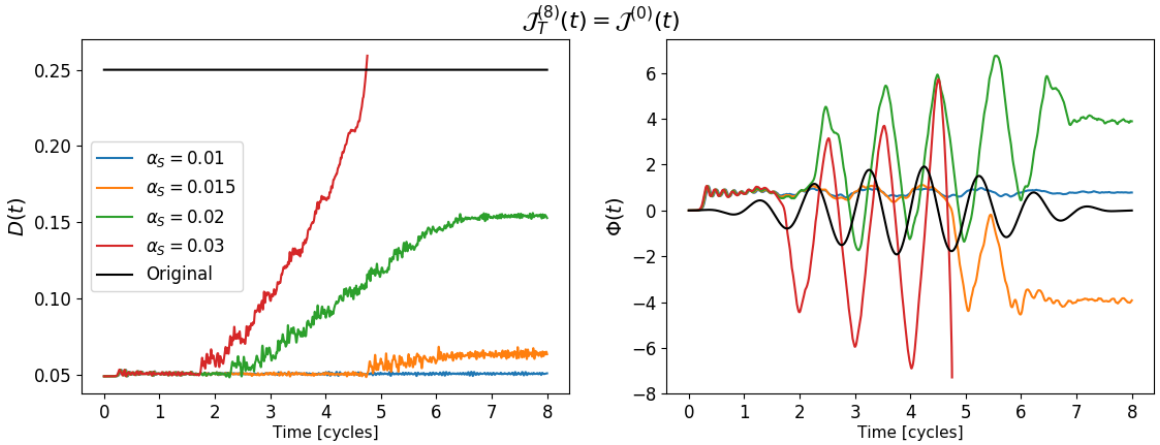

Figure 5.3: **Photo-induced transition of the insulating tracking system.** For the $\mathcal{J}_T^{(8)}(t) = \mathcal{J}^{(0)}(t)$ case, this shows the control fields and resulting doublon densities when the tracked current is scaled by $\alpha_S = 0.01, 0.015, 0.02, 0.03$. $D(t)$ in the $U = 0$ system under the original driving field is also shown. Calculated using ED on a 4×3 lattice.

that the resulting control field has a weaker peak amplitude than $\Phi(t)$, which is given by $\Phi_0 = aA_0 = aE_0/\omega_L \approx 1.9$. This is confirmed by its doublon density, which remains largely unchanged throughout the pulse. If we gauge the degree of conductivity by the double occupancy, then this shows that an insulating tracking system does not have to become a conductor in order to mimic the spectrum of one. However, as α_S rises there is an accompanying increase in the number of DHPs. The control field has to grow in strength in order to ensure there are enough charge carriers to generate the required current, until eventually $E_0 > E_{th}$ and a dielectric breakdown occurs. This can be seen in fig.5.3, where the peaks of the control fields become larger than Φ_0, and in fact oscillations in $\theta(\Psi)$ are so aggressive that $\Phi_T^{(8)}(t)$ required unwrapping. However, if the scaling is increased too much then the tracking constraint is violated and the simulation becomes unphysical. This is shown in fig.5.3 by the example $\alpha_S = 0.03$.

In the reverse situation, $\mathcal{J}_T^{(0)}(t) = \mathcal{J}^{(8)}(t)$, no scaling is needed (i.e. $\alpha_S = 1$) as the mimicry only requires inducing a small current in an already-conducting system. This has no effect on its conductive properties, and the doublon density simply remains the same at $D(t) = 0.25$ throughout the pulse.

5.2.2 Control Fields

Using this protocol it is possible to induce an arbitrary optical response in any chosen system. However, it is not at all obvious what the general properties of the required control fields are, and how they change with dimensionality or the correlation strength of the tracked and tracking systems, i.e. U_I and U_T, respectively.

Tracking in the $U_T \to 0$ limit was discussed in Sec. 5.1.3. The necessary control field is given by

$$\Phi_T(t) = \arcsin\left(\frac{-\mathcal{J}_T^{(0)}(t)}{2at_0R(\Psi_{MF})}\right) \tag{5.32}$$

where $R(\Psi_{MF})$ is constant. When $\Phi_T(t)$ is small it is possible to simplify further

$$\sin\left[\Phi_T(t)\right] \approx \Phi_T(t) = -\gamma\mathcal{J}_T^{(0)}(t) \tag{5.33}$$

where $\gamma = 1/(2at_0R(\Psi_{MF}))$ is a small constant. In other words, the control field is simply the scaled inverse of the current being tracked, as is visible in fig.5.2 for $\mathcal{J}_T^{(0)}(t) = \mathcal{J}^{(8)}(t)$, where $\Phi_T(t)$ is clearly just the current flipped and multiplied by a small number. This simple relationship tends to be especially true when U_I is large, as in this limit the current is often weak and so $\Phi_T(t)$ is too, ensuring that the small-angle approximation in eq.(5.32) holds. This is essentially a linear-response regime, however, when $U_T > 0$ the phase instead evolves according to eq.(5.7), resulting in a highly nonlinear evolution of the wavefunction and compensatory oscillations in $\Phi_T(t)$. An example is shown in fig.5.4 for $\mathcal{J}_T^{(4)}(t) = \mathcal{J}^{(8)}(t)$, which is more oscillatory than the $U_T = 0$ equivalent in fig.5.2[4]

As well as its time dependence, we are also interested in the harmonic content of $\Phi_T(t)$ and how a given frequency component relates to the tracked current and spectrum. When $U_T = 0$, eq.(5.33) shows that there is an entirely linear relationship between the two, whereas the opposite is true when on-site repulsion is large. This can be demonstrated by imposing a low-pass filter on $\Phi_T(t)$, such that harmonics above a cutoff ω_c are removed: $\mathcal{FT}\left\{\Phi_T(t)\right\}(\omega > \omega_c) = 0$. When this is done and the resulting driving field is reapplied to the U_T GS, the spectrum becomes exponentially

[4]Although this example still benefits from the small magnitude of the $U_I = 8$ current, which greatly simplifies the required driving field.

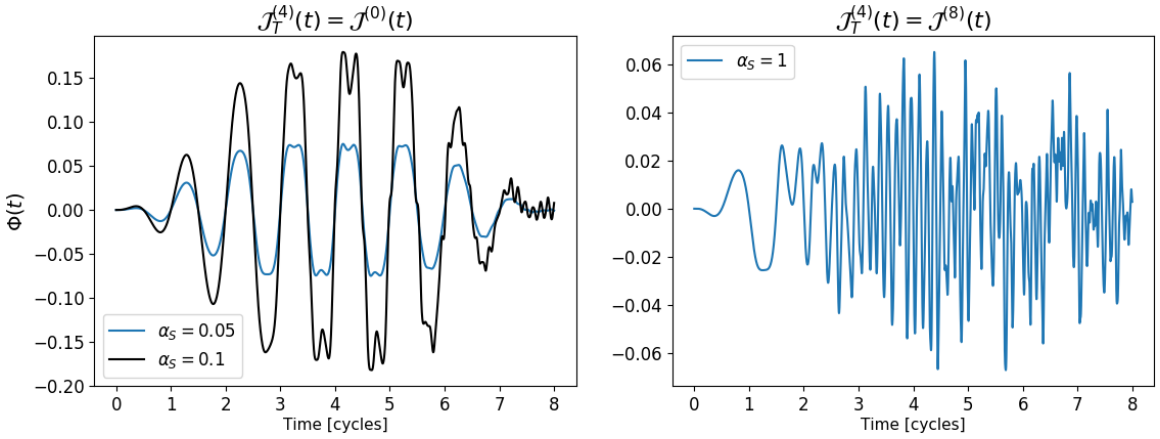

Figure 5.4: **Mimicry of a conductor and insulator by an intermediate-strength system.** The control fields required to track $U_I = 0$, 8 in the $U_T = 4$ system, where the former has $\alpha_S = 0.05$, 0.1, and the latter $\alpha_S = 1$. Calculated using ED on a 4×3 lattice.

suppressed for $\omega > \omega_c$ if $U_T = 0$, whereas when $U_T \gg 0$ a highly nonlinear relationship exists between ω_c and the frequency at which the spectrum is suppressed. Cutoffs will be implemented and discussed more in later sections, and will be found to be useful tools to simplify tracking simulations.

The $\Phi_T(t)$ necessary to track a given current is of course dependent upon the properties of that current, and therefore varies considerably with U_I. For the specified pulse parameters and some fixed U_T, as U_I increases the control field requires a smaller maximum amplitude but a wider bandwidth, and conversely, as U_I decreases $\Phi_T(t)$ needs a narrower frequency range but a larger maximum strength, potentially much larger than Φ_0. This distinction is clear in fig.5.2 when comparing $U_I = 0$ and $U_I = 8$, as the latter has a weak amplitude but broad frequency content and vice versa. More specifically, if $U_I > U_T$ then no scaling is required and the simulation can be done without issue. Eq.(5.33) is the limiting case, but if $U_T > 0$ is weak then it will tend to be true that $\theta(\Psi)$ is small and $R(\Psi)$ large, with the consequence that

$$\Phi_T(t) \approx -\gamma(t)\mathcal{J}^{(U_I)}(t) \tag{5.34}$$

such that the control field is simply the inverse target current modulated by an oscillatory and small $\gamma(t)$, resulting in a low-amplitude driving field. An example is the tracking of $\mathcal{J}^{(8)}(t)$ in fig.5.4. On the other hand, the reverse case where $U_I < U_T$

normally requires $\alpha_S < 1$ and is far more challenging to track because the ratio $\mathcal{J}_T^{(U_T)}/R(\Psi)$ tends to hover near one. These trends are amplified by the distance in the phase diagram, $|U_I - U_T|$, as can be seen in the difference between the fields required to track $\mathcal{J}^{(0)}(t)$ with $U_T = 4$ compared to $U_T = 8$, plotted in fig.5.4 and fig.5.3, respectively. The latter example is attempting to generate a significant current in a heavily-insulating system, and so requires considerable field strength that results in the transformation of the system's conductive properties, often inducing Mott breakdown. This is not true in the $U_T = 4$ case, where only a weak driving pulse is sufficient with peak amplitude far below E_{th}.

We can then apply this knowledge and ask about the general properties of control fields needed to track the currents of conductors, insulators and systems undergoing phase transitions. Of course, this also depends on U_T, but in broad terms it is true that mimicking a conductor's optical response can be achieved with narrow-band and high-amplitude driving pulses, whereas those of insulators require a much broader range of input frequencies but with amplitudes often far below E_0. However, to reproduce transition-regime currents requires driving lasers intermediate in bandwidth and strength, but with more complex time-variation that reflects the existence of the transition in the original system[5]. These have not been discussed so far, but will be at length in later sections.

This analysis has assumed fixed pulse parameters, but of course changing the ω_L and/or E_0 of the original pulse $\Phi(t)$ produces currents with a wide variety of properties that then require very different control fields to track. For example, decreasing ω_L will simultaneously broaden the spectrum and increase its intensity, e.g. fig.4.17, with corresponding changes to the necessary control field. Similarly, the dimensionality of the tracked system is important because 2D spectra are often shifted to lower harmonics compared to 1D, which makes them reproducible with a narrower range of frequencies than their 1D equivalents. Lastly, the dimensionality of the tracking system itself also has to be considered. In 2D, an electron at a given site has twice the number of possibilities for hopping than it does in 1D, and as a result $R(\Psi)$ at some U_T will be larger, making it easier to conform to the constraint eq.(5.24), and

[5]Unlike tracking conductors, where the control fields can sometimes have a semi-periodic structure originating from the original current, such as the $\mathcal{J}^{(0)}(t)$ case in fig.5.4.

in general reducing the field strength required and increasing the maximum α_S that can be used[6]. This hints at added possibilities in 3D, although simulating this in the short term would be very difficult for all but the smallest systems.

5.2.3 Experimental Feasibility

The tracking simulations carried out so far have produced control fields that exactly reproduce their target currents. However, in all or most of these cases the driving pulses are experimentally unrealistic because no constraints were imposed on their bandwidth or amplitude. Recent experiments have demonstrated seven-colour laser sources [218, 219], which although impressive is insufficient to reproduce tracking fields, some of which have more than a hundred significant frequency contributions spanning tens of harmonics. On the other hand, field amplitude is not an issue because the maximum required in fig.5.2 is approximately 30MVcm^{-1}, but experiments have achieved beyond 100MVcm^{-1} [220]. It is therefore the bandwidth and frequency requirements of the tracking pulses that pose a problem and need to be addressed.

In order to make the tracking scheme experimentally feasible it is necessary to find a way of approximating the control fields with a small number of frequencies and more limited range. The simplest method would be to impose a cutoff of the type previously discussed, where all frequencies above some ω_c are suppressed. However, this still requires an impractically large number of frequencies, and independent control over each one. Instead, the exact control fields, $\Phi_T(t)$, were fitted to models with D distinct frequencies to produce approximations, $\bar{\Phi}_T(t)$, that are experimentally viable while potentially still able to reproduce the most important spectral features. The following fitting model was used

$$\bar{\Phi}_T(t) = \mathcal{E}(t) \sum_{j=1}^{D} \left(\frac{a_T E_j}{\omega_j} + \Delta_j t \right) \sin\left[\omega_j t - \phi_j\right] \tag{5.35}$$

where ω_j are the frequency components, E_j are field amplitudes, ϕ_j are phases, Δ_j are chirps[7] and $\mathcal{E}(t)$ is the envelope function. The latter was calculated using the Hilbert

[6]Although these systems still only have 12 sites, meaning $R(\Psi)$ tends to be quite small and so $\alpha_S \ll 1$ is often required.

[7]In general, a chirped laser pulse is one that has a time-dependent instantaneous frequency.

transform $\mathrm{H}\left[\Phi_T(t)\right]$, whose magnitude provides a parameterless means of estimating the envelope

$$\mathcal{E}(t) = \left|\mathrm{H}\left[\Phi_T(t)\right]\right| \tag{5.36}$$

Depending on the pulse's precise form, the following two-parameter Gaussian model can also be effective

$$\mathcal{E}(t) = \mathrm{e}^{-\alpha(t-\mu)^2} \sin^2\left[\frac{\pi t}{T}\right] \tag{5.37}$$

and both sin-squared and Gaussian envelopes are commonly used experimentally. Furthermore, when $U_I < 0.5$ it was often found that including the original driving pulse helps to capture the tracking field's shape

$$\bar{\Phi}_T(t) = \Phi(t) + \mathcal{E}(t) \sum_{j=1}^{D} \left(\frac{a_T E_j}{\omega_j} + \Delta_j t\right) \sin\left[\omega_j t - \phi_j\right] \tag{5.38}$$

The chirp parameters are included because doing so was found to provide the best fit, but in general both models can be simplified by setting $\Delta_j = 0$ without a significant impact on the results. Finally, in this section $D = 3$ was always chosen as there was found to be little or no benefit to increasing it. Overall then, this form is experimentally achievable with current technology and is composed of a shaped chirped pulse of three frequencies ω_j, with amplitudes E_j and phases ϕ_j.

Fig.5.5 demonstrates this method with the examples $U_I = 5,\ U_T = 1$ (left-hand column) and $U_I = 1,\ U_T = 4$ (right-hand column), which are compared against the exact tracking simulations. To generate these results, the following steps were performed:

1. The driving pulse $\Phi(t)$ was applied to the 2D $U_I = 5$ and $U_I = 1$ systems, producing currents $\mathcal{J}^{(5)}(t)$ and $\mathcal{J}^{(1)}(t)$ via ED propagation.

2. These currents were tracked by the 2D $U_T = 1$ and $U_T = 4$ systems, respectively, producing currents $\mathcal{J}_T^{(1)}(t)$ and $\mathcal{J}_T^{(4)}(t)$ via the control fields $\Phi_T^{(1)}(t)$ and $\Phi_T^{(4)}(t)$.

3. These driving pulses were fitted to the model eq.(5.35) with envelope eq.(5.36), producing control fields $\bar{\Phi}_T^{(1)}(t)$ and $\bar{\Phi}_T^{(4)}(t)$ that are shown in the top row of fig.5.5.

4. The new driving pulses were reapplied to the $U_T = 1$ and $U_T = 4$ systems, generating new currents $\bar{\mathcal{J}}_T^{(1)}(t)$ and $\bar{\mathcal{J}}_T^{(4)}(t)$, again via ED. These are plotted in the middle row of fig.5.5, with corresponding spectra shown in the bottom row.

The fitting model's optimised parameters are in tab.5.1 and tab.5.2, and both cases require specifications that are experimentally achievable.

	1	**2**	**3**
$\frac{E_j}{E_0}$	0.13	0.28	0.24
$\frac{\omega_j}{\omega_L}$	1.07	3.10	5.85
$\frac{\Delta_j}{\omega_L}$	0.01	-0.019	5.8×10^{-3}
ϕ_j	0.02π	0.4π	3.52π

Table 5.1: Fit parameters for $\bar{\Phi}_T^{(1)}(t)$, optimised for the model eq.(5.35) and envelope eq.(5.36), for $U_I = 5$ and $U_T = 1$.

	1	**2**	**3**
$\frac{E_j}{E_0}$	0.19	0.017	8.5×10^{-3}
$\frac{\omega_j}{\omega_L}$	1.00	2.95	5.02
$\frac{\Delta_j}{\omega_L}$	2.08×10^{-3}	5.35×10^{-3}	-3.41×10^{-4}
ϕ_j	-0.06π	-0.26π	0.44π

Table 5.2: Fit parameters for $\bar{\Phi}_T^{(4)}(t)$, optimised for the model eq.(5.35) and envelope eq.(5.36), for $U_I = 1$ and $U_T = 4$.

These two examples are reverses of each other in the sense that one tracks a (fairly) large correlation strength in a weakly-correlated system, and the other does the opposite. In both cases, somewhat surprisingly our simple fitted model with only three frequencies is sufficient to reproduce the most important spectral characteristics, and to maintain a good match down to small emission intensities and over a wide range of harmonics. It does particularly well at low harmonics where it successfully tracks the peaks, including the two prominent ones that dominate the $U_I = 1$ spectrum.

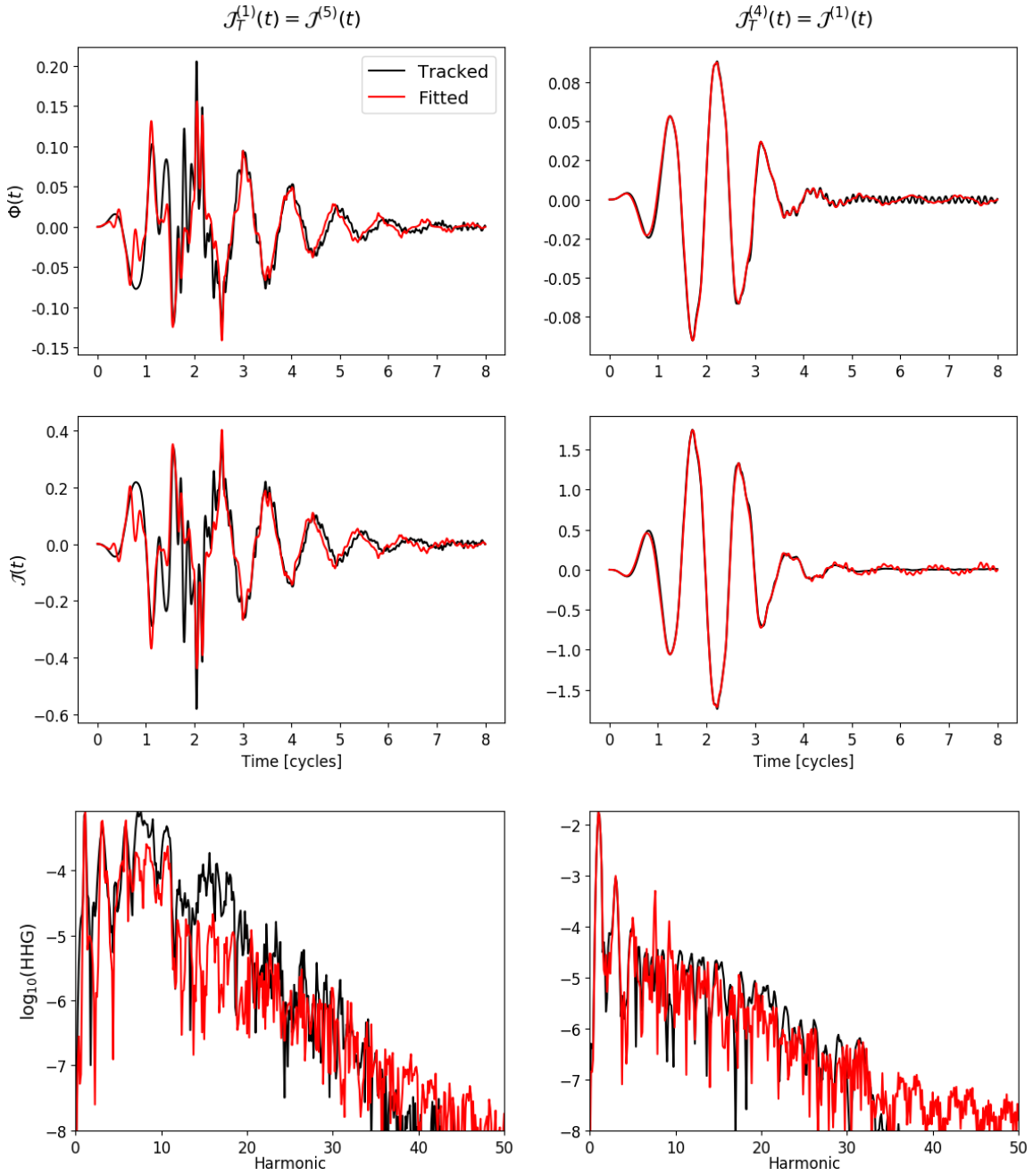

Figure 5.5: **Reproduction of spectra using fitted control fields.** For tracking simulations $U_I = 5$ $U_T = 1$ ($\alpha_S = 1$) and $U_I = 1$ $U_T = 4$ ($\alpha_S = 0.1$), the tracking control fields (top row) were fitted and then reapplied to the respective U_T GSs, generating currents and spectra that are plotted in the middle and bottom rows, respectively. Calculated using ED on a 4×3 lattice.

Unsurprisingly, the match is less precise at larger harmonics, and in the $U_I = 5$ case it does not exactly reproduce the main peaks. Fig.5.5 shows that the control fields do not need to be a perfect fit in order to produce good results, as both cases have significant deviations from their tracking fields, particularly $\bar{\Phi}_T^{(1)}(t)$.

Although these examples were successful, in general the method has many limitations and is often inapplicable. U_I is the main determiner because, as previously discussed, the control fields inherit properties from the currents they are tracking. Broadband target currents necessitate broadband driving fields and are therefore difficult to fit with so few frequencies, with the result that $U_I \geq 6$ is essentially impossible for all $U_T > 0$. Conversely, weakly-correlated systems have spectra dominated by low harmonics, which lead to control fields that are more amenable to fitting. However, as we have seen these fields can vary hugely in complexity depending on U_T, e.g. fig.5.4 compared to fig.5.3, both of which track $U_I = 0$. The latter cannot be fitted for any of the plotted α_S, and in particular it is their behaviour early in the pulse that causes issues. This is clearer in fig.5.2, where $\Phi_T^{(8)}(t)$ rapidly ascends during the first half a cycle, forming a 'stem' that the fitting models cannot capture. It is always possible to reduce α_S further until the stem is removed from the control field, but this is not preferable as we would like to keep α_S as close to one as possible.

Finally, 1D spectra peak in the region U/ω_L, which limits fitting to approximately $U_I \leq 2$ and means that 2D spectra can generally be fitted up to much larger interaction strengths than 1D. For example, compare $U = 3$ in fig.4.5 between 1D and 2D; the former cannot be fitted, whereas the latter can because it is dominated by its first harmonic.

5.3 Tracking Control Using Arbitrary Polarisation

So far only linearly polarised control fields have been used, in which $\Phi_T^{(x)} = \Phi_T^{(y)}$ is imposed at all times. This limits the information that can be tracked, and as a result only the total current has been targeted, with no consideration of its spatial variation. By allowing $\Phi_T^{(x)} \neq \Phi_T^{(y)}$ it is possible to acquire much finer control over the system's optical properties, including tracking the current in each direction as explained in Sec. 5.1.2 and Sec. 5.1.3.

There are still limitations to what can be achieved with this because we are using homogeneous fields, so there is no control of how the current varies over each individual row and column of the lattice, only over the total current in each direction. However, this still offers many interesting possibilities that are not achievable in 1D.

The total current is $\mathcal{J}_T(t) = \mathcal{J}_T^{(x)}(t) + \mathcal{J}_T^{(y)}(t)$. If the aim is to track $\mathcal{J}_T(t)$, then there are now infinite possible ways of doing this because we can choose to track any combination of $\mathcal{J}_T^{(x)}(t)$ and $\mathcal{J}_T^{(y)}(t)$ so long as they sum to $\mathcal{J}_T(t)$. This means that with arbitrary polarisation, there is an infinite degeneracy of control fields that will generate a given current over the whole system. However, from this point the total will not be tracked, and instead each direction's current will be controlled independently without consideration of their sum. Of course, the control fields that track these separate currents are not independent because they are calculated using expectations over the system's total state $|\Psi(t)\rangle$, and so are coupled through the nonlinear evolution of the electronic structure to an extent that increases with U_T. In the limit $U_T = 0$, the system's state does not deviate from its single Slater determinant GS, $|\Psi_{MF}\rangle$, resulting in control fields given by eq.(5.19) and eq.(5.20), which are truly independent.

Using ED to separately track $\mathcal{J}_T^{(x)}(t)$ and $\mathcal{J}_T^{(y)}(t)$ is far from optimal because it is limited to the 4×3 lattice, meaning that $\Phi_T^{(y)}(t)$ will be applied over fewer sites than $\Phi_T^{(x)}(t)$, which will affect its magnitude and ability to satisfy eq.(5.24). Instead, to do tracking simulations with a larger lattice in which $L_x = L_y$ required using a modified version of tVMC. It was found that tVMC is a stable and reliable method of doing tracking control[8], and allows us to go beyond the limitations of ED. As a result, all simulations in the remainder of this chapter were calculated using tVMC with a 6×6 lattice, and the currents being tracked again originated from 8-cycle pulses with $\omega_L = 50$THz and all other pulse and lattice parameters the same as used previously, unless otherwise stated. These results are currently unpublished but are in the process of being written into a paper.

[8]This is discussed more later.

5.3.1 Direction-Dependent Mott Transitions

Directional control of the current introduces many interesting possibilities. A natural extension of the last section would be to start with a strongly-correlated system and then 'turn off' the insulating behaviour in one direction and replace it with that of a conductor, while retaining its normal behaviour in the other direction, and vice versa if $U_T = 0$. Using the example from Sec. 5.2.1, this could be achieved by mimicking e.g. $U_I = 0$ in the x-direction and $U_I = 8$ in the y-direction, while starting in either GS. Instead, the spectral characteristics of a system will be manipulated to generate directional Mott transitions, which will be demonstrated by time-resolving the HHG. Following on from this, the aim will be to reproduce the behaviour in ways that are potentially experimentally feasible using either current or future technology.

5.3.1.1 Directional Tracking

Fig.5.6 demonstrates this capability for the example $\mathcal{J}_T^{(x,3)}(t) = \mathcal{J}^{(x,0)}(t)$ along with $\mathcal{J}_T^{(y,3)}(t) = \mathcal{J}^{(y,3)}(t)$. In other words, the $U_T = 3$ system is subjected to the control fields necessary to mimic the x-component of the $U = 0$ current in the x-direction, while in the y-direction it is made to retain the same optical response it would have under the original pulse $\Phi(t)$. The following steps were taken:

1. The pulse eq.(4.2) was applied to the $U_I = 0$ system using the default pulse parameters, with the exception that $E_0 = 25\text{MVcm}^{-1}$. This generated a current $\mathcal{J}^{(0)}(t)$, from which the x-component $\mathcal{J}^{(x,0)}(t)$ was taken.

2. The pulse eq.(4.2) was applied to the $U_I = 3$ system using the default pulse parameters. This generated a current $\mathcal{J}^{(3)}(t)$, from which the y-component $\mathcal{J}^{(y,3)}(t)$ was taken.

3. These two currents, $\mathcal{J}^{(x,0)}(t)$ and $\mathcal{J}^{(y,3)}(t)$, were simultaneously tracked in the $U_T = 3$ system along its x and y directions, respectively, with scale factors $\alpha_S^{(x)} = 0.4$ and $\alpha_S^{(y)} = 1$.

The peak amplitudes used for the initial irradiations are labelled $E_0^{(x)} = 25\text{MVcm}^{-1}$ and $E_0^{(y)} = 10\text{MVcm}^{-1}$ in order to clearly distinguish between them.

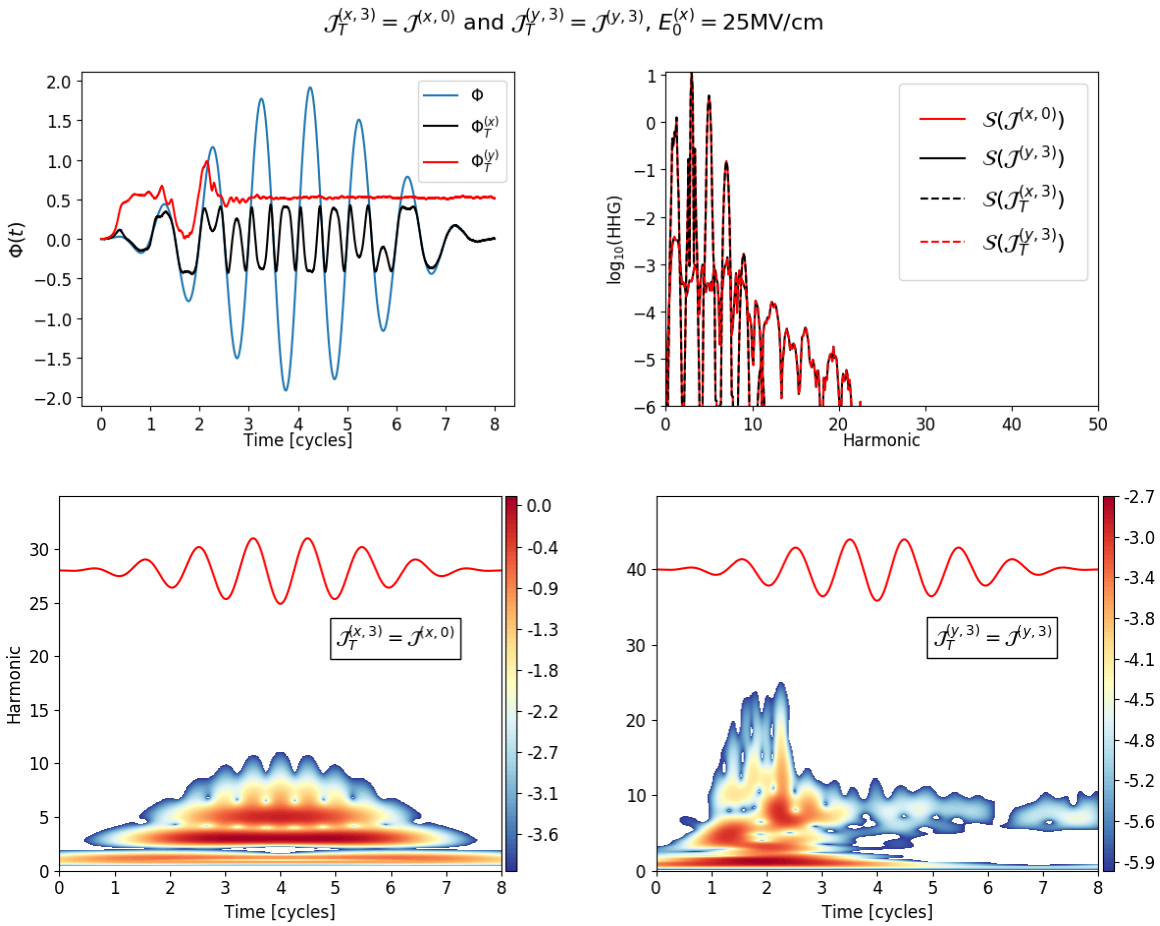

Figure 5.6: **Tracking control used to simultaneously resolve a Mott transition and Bloch oscillations in perpendicular directions.** The $U_I^{(x)} = 0$ and $U_I^{(y)} = 3$ currents tracked in the x and y directions, respectively, of the $U_T = 3$ system. Image shows the resulting control fields (top left), for comparison plotted with the pulse $\Phi(t)$, $E_0^{(y)} = 10\text{MVcm}^{-1}$. The HHG spectra (top right) and spectrograms (bottom) are shown for each direction. In the former's legend, e.g. $\mathcal{S}(\mathcal{J}^{(x,0)})$ refers to the spectrum generated by the current $\mathcal{J}^{(x,0)}$, and the red lines in the latter show the form of the electric field, $aE(t) = -d\Phi(t)/dt$, of the original pulse. The scale factors $\alpha_S^{(x)} = 0.4$ and $\alpha_S^{(y)} = 1$ were applied, as well as the cutoff frequencies $\omega_c^{(x)} = 13$ and $\omega_c^{(y)} = 24$. Calculated using tVMC on a 6×6 lattice.

Fig.5.6 shows the resulting directionally-resolved control fields (top left) and emission spectra (top right), and we can see that the y-spectrum has the expected properties of an intermediate-strength system - similar to e.g. fig.4.5 - while in the x-direction these have been replaced with a tight-binding spectrum. In general, HHG spectra are not a definitive indicator of dielectric breakdown, as it is a process more clearly understood and defined by the system's behaviour over time. As a result, fig.5.6 also includes spectrograms, but resolved separately for each direction instead of for the overall current. This demonstrates simultaneous tracking in both the time and frequency domains, as well as a degree of spatial tracking. Optically, this is a directional Mott transition, where the y-direction generates the signature emission of a rapid breakdown, while in the x-direction the Mott insulating nature of the GS has been transformed into that of a conductor, with its distinctive BOs and bands of continuous emission. $E_0^{(x)} = 25\text{MVcm}^{-1}$ was chosen specifically to enhance the clarity of the BOs, as the default combination of E_0 and ω_L produce weak ones that are hard to discern.

Both control fields reflect the properties of their parent systems via the tracked currents. Firstly, $\Phi_T^{(x)}(t)$ has a complex structure that is aligned with $\Phi(t)$ and directly encodes the BOs of the $U = 0$ system. This can be seen in its kinks that coincide with peaks in $\Phi(t)$ and become more aggressive near the pulse centre, corresponding to the increasing strength of the BOs that are being tracked. Secondly, $\Phi_T^{(y)}(t)$ is dominated by the structure between the 1st and 3rd cycles that coincides with and reproduces the Mott transition. Specifically, the pulse's two rapid oscillations either side of the 2nd cycle correspond to concurrent emission bursts in the spectrogram.

One might expect that $\Phi_T^{(y)}(t)$ would look similar to $\Phi(t)$ given that it is the response to $\Phi(t)$ that is being tracked, but that is not how the tracking scheme works when $U_T > 0$. First we consider the field needed for $\mathcal{J}_T^{(k,0)}(t) = \mathcal{J}^{(k,0)}(t)$, i.e. tracking the k'th component of the $U = 0$ current in the k-direction of the $U_T = 0$ system.

This requires the control field

$$\Phi_T^{(k)}(t) = \arcsin\left(\frac{-\mathcal{J}^{(k,0)}(t)}{2at_0R_k(\Psi_{MF})}\right) \tag{5.39}$$

$$= \arcsin\left(\sin\left[\Phi_k(t)\right]\right) \tag{5.40}$$

$$= \Phi(t) \tag{5.41}$$

because

$$\mathcal{J}^{(k,0)}(t) = -2at_0R_k(\Psi_{MF})\sin\left[\Phi_k(t)\right] \tag{5.42}$$

and $\Phi_k(t) = \Phi(t)$. In other words, when $U_I^{(k)} = U_T = 0$ the control field simply reduces to the original pulse that induced the response we're tracking. It is worth noting that this solution only remains unique if $|\Phi(t)| < \pi/2$, which is not always true in this case; in fact, in the $U_I = 0$ system it is the times when $|\Phi(t)| > \pi/2$ that electrons are driven over the Brillouin zone edge and undergo BOs, which ultimately manifests in $\Phi_T^{(x)}(t)$ as kinks and oscillations.

However, this simplification of the control field does not hold if $U_I^{(k)} = U_T > 0$, where the field is given by

$$\Phi_T^{(k)}(t) = \arcsin\left(\frac{-\mathcal{J}^{(k,U_T)}(t)}{2at_0R_k(\Psi)}\right) + \theta_k(\Psi) \tag{5.43}$$

$R_k(\Psi)$ and $\theta_k(\Psi)$ are now time dependent and immediately begin to deviate from the values they have under $\Phi(t)$ due to coupling between the $k = x, y$ directions. This has the consequence that $\Phi_T^{(k)}(t) \neq \Phi(t)$ for all $t > 0$. The opposite happens in the directionally-uncoupled $U_T = 0$ case, where $k = x, y$ are independent of each other because the total state $|\Psi(t)\rangle = |\Psi_{MF}\rangle$ remains constant and does not change in response to the control fields.

Fig.5.6 shows that tVMC is able to perfectly track currents with no visible stochastic fluctuations[9]. An important part of this is the imposition of cutoff frequencies ω_c, where if $\tilde{\mathcal{J}}(\omega) = \mathcal{FT}\left\{\mathcal{J}(t)\right\}$, then

$$\tilde{\mathcal{J}}(\omega > \omega_c) = 0 \tag{5.44}$$

This removes the contributions of all harmonics above the cutoff, and in doing so

[9]Fluctuations become visible under sufficient zooming, but are not visible in these images.

removes the noise present at larger harmonics[10] that would otherwise cause aggressive stochastic oscillations in the control fields. In fig.5.6, $\omega_c^{(x)} = 13$ and $\omega_c^{(y)} = 24$ were chosen because harmonics above these values do not significantly contribute to the spectra in the intensity ranges shown in these images. An approximately linear relationship can be assumed between ω_c and its cutoff effect on the spectra because $U_T = 3$ is still quite weakly correlated.

5.3.1.2 Double-Pulse Fitting

This removal of stochastic noise from the control fields is important if they are to be used as the basis of real-world experiments. Unfortunately, they are still not experimentally accessible with existing technology, particularly $\Phi_T^{(y)}(t)$. We can see in fig.5.6 that its field strength is not an issue, as $\max\left\{\left|\Phi_T^{(y)}(t)\right|\right\}$ is approximately half of $\max\{|\Phi(t)|\}$. The difficulty instead comes from its main structure following the 1st cycle, which is complex and clearly composed of many frequency components, and therefore needs to be fitted to a simpler approximate form. During the 1st cycle it forms a 'stem' shape whose height is equal to the zeroth Fourier coefficient, also known as the signal's DC component, which is given by the average magnitude of the signal. However, this stem cannot be fitted using the methods discussed so far, and so it is necessary to extend them slightly.

This was achieved using 'double-pulse' fitting, where the control field is split into two sections that are then fit separately, with the intention being that experimentally the field could be generated using two successive pulses. The first section is used to fit the stem, and is roughly given by the pulse's opening half-cycle. It is essentially just an exponential ramping up of the field in order to reach the required amplitude, and so a simple two-parameter exponential model was chosen

$$\bar{\Phi}_T^{(y,\mathrm{stem})}(t) = \alpha e^{\beta t} \tag{5.45}$$

The rest of the control field was then fitted to eq.(5.35) with $D = 5$ frequencies and the DC component added as well, which simply amounts to a constant phase term. This was used with the envelope function eq.(5.36), which was found to produce more

[10] At approximately $\omega > 50$.

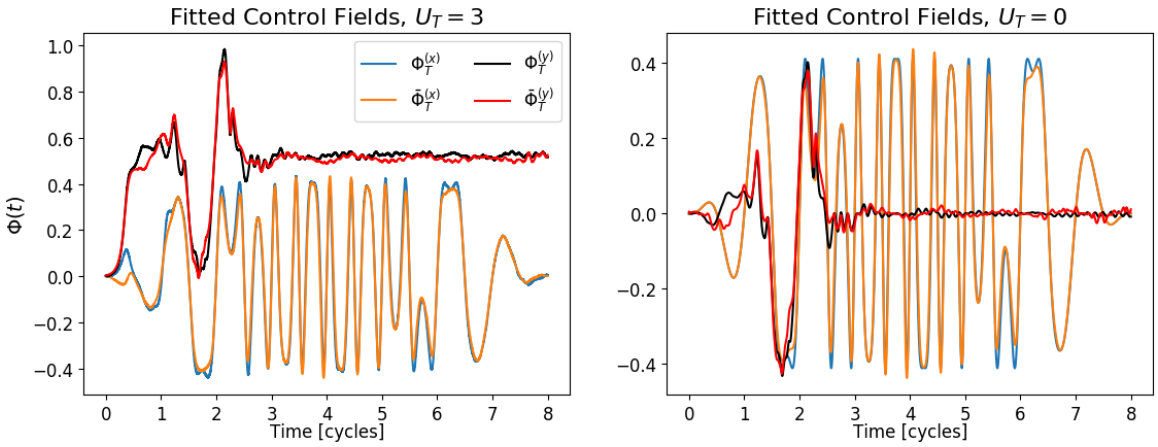

Figure 5.7: **The fitting of directionally-resolved control fields.** The tracking pulses in both directions and attempts at fitting them, for simulations with $U_T = 0$ and 3. For both U_T, $\bar{\Phi}_T^{(x)}(t)$ was constructed using eq.(5.38) with envelope eq.(5.36). At $U_T = 0$, $\bar{\Phi}_T^{(y)}(t)$ used eq.(5.35) with eq.(5.36), whereas $U_T = 3$ required an additional initial stem fit, eq.(5.45). All fitted control fields are formed from $D = 5$ distinct frequencies.

accurate HHG than the Gaussian envelope, eq.(5.37).

When both fits are combined, the opening exponential section followed by the remaining bulk of the pulse together form an approximation to the entire control field. This is shown in fig.5.7 (left-hand plot), with parameters in tab.5.4. It was necessary to also apply a Savitzky–Golay filter to the stem and its connection point with the rest of the pulse in order to smooth over the join section and avoid a discontinuity. Although precise details are not reproduced, overall the fit does a reasonably good job of capturing the pulse's shape, especially during the vital opening 3 cycles, where most of the interesting physics is generated.

The double-pulse method is not required for $\Phi_T^{(x)}(t)$ because it has no stem, and so eq.(5.38) with eq.(5.36) were sufficient to fit the whole pulse. The parameters are given in tab.5.3. If U_T were increased then a greater amplitude field would be required and would likely lead to a stem forming.

The same simulation was repeated but with $U_T = 0$, and both the tracked[11] and fitted control fields are shown in fig.5.7 (right-hand plot). Rather than mimicking a

[11]The same scale factors were used in the tracking simulation in order to make the results directly comparable with $U_T = 3$.

conductor while retaining a correlated response, this instead generates the optical response of a Mott breakdown along one dimension despite the system being completely uncorrelated, while simultaneously preserving its native tight-binding emission along the other. In terms of real-world applications, this type of tracking is potentially more useful than $U_T = 3$ because it allows a mundane conductor to generate the complex properties of an interacting system. These tracking simulations are very rapid to do because tVMC is not necessary, and fitting also becomes much easier because no stems form, in this case allowing $\Phi_T^{(y)}(t)$ to be fitted using a single pulse and the combination of eq.(5.35) with envelope eq.(5.36), while $\Phi_T^{(x)}(t)$ again required eq.(5.38) and eq.(5.36). The control fields' parameters are in tab.5.5 and tab.5.6.

	1	**2**	**3**	**4**	**5**
$\frac{E_j}{E_0}$	0.17	0.08	0.05	0.02	7.2×10^{-3}
$\frac{\omega_j}{\omega_L}$	1.00	3.00	5.01	7.00	9.00
$\frac{\Delta_j}{\omega_L}$	2.17×10^{-4}	-3.63×10^{-5}	-1.68×10^{-4}	-1.47×10^{-5}	-2.26×10^{-7}
ϕ_j	-0.01π	0.02π	0.05π	0.01π	-0.02π

Table 5.3: Fit parameters for $\bar{\Phi}_T^{(x)}(t)$, optimised for the model eq.(5.38) and envelope eq.(5.36), for $U_I^{(x)} = 0$ and $U_T = 3$.

	Stem	**1**	**2**	**3**	**4**	**5**
α	3.4×10^{-3}					
β	0.80					
$\frac{E_j}{E_0}$		0.20	0.098	0.096	0.11	0.05
$\frac{\omega_j}{\omega_L}$		0.87	3.34	5.05	6.92	8.91
$\frac{\Delta_j}{\omega_L}$		-0.019	-6.1×10^{-3}	-8.9×10^{-3}	-8.1×10^{-3}	3.4×10^{-3}
ϕ_j		-0.58π	1.28π	-0.21π	-1.61π	0.14π

Table 5.4: Fit parameters for $\bar{\Phi}_T^{(y)}(t)$, optimised for the stem model eq.(5.45) combined with eq.(5.35) and envelope eq.(5.36), for $U_I^{(y)} = 3$ and $U_T = 3$.

	1	**2**	**3**	**4**	**5**
$\frac{E_j}{E_0}$	0.17	0.082	0.056	0.022	7.5×10^{-3}
$\frac{\omega_j}{\omega_L}$	1.0	3.0	5.0	7.0	9.0
$\frac{\Delta_j}{\omega_L}$	-1.82×10^{-12}	-1.04×10^{-12}	4.66×10^{-12}	1.66×10^{-11}	3.53×10^{-11}
ϕ_j	0.0	0.0	0.0	0.0	0.0

Table 5.5: Fit parameters for $\bar{\Phi}_T^{(x)}(t)$, optimised for the model eq.(5.38) and envelope eq.(5.36), for $U_I^{(x)} = 0$ and $U_T = 0$.

	1	**2**	**3**	**4**	**5**
$\frac{E_j}{E_0}$	0.13	0.13	0.26	0.21	0.20
$\frac{\omega_j}{\omega_L}$	0.87	3.41	4.57	6.58	9.06
$\frac{\Delta_j}{\omega_L}$	0.019	-8.37×10^{-3}	-0.024	0.016	-0.011
ϕ_j	-0.61π	1.55π	-1.47π	-2.59π	1.71π

Table 5.6: Fit parameters for $\bar{\Phi}_T^{(y)}(t)$, optimised for the model eq.(5.35) and envelope eq.(5.36), for $U_I^{(y)} = 3$ and $U_T = 0$.

These approximated control fields were then reapplied to the GS at their respective U_T, with the aim of reproducing the same general properties observed in fig.5.6. The resulting spectrograms are shown in fig.5.8 for $U_T = 3$ (top row) and $U_T = 0$ (bottom row), and in both cases the desired behaviour is unambiguously reproduced, creating a clear directional split in the emission.

At $U_T = 3$, the stochastic nature of the method and the tracking system's correlation combine to make the simulation quite challenging. However, in the x-direction both the BOs and the bands of continuous emission are clearly visible, and so the two most prominent characteristics of a conducting system's HHG have been successfully recreated, despite noise obscuring the BOs at lower intensities and causing emission above the cutoff frequency used in the original tracking simulation. In the y-direction, the double-pulse fitting accurately reproduces the breakdown with little additional noise above or below the cutoff.

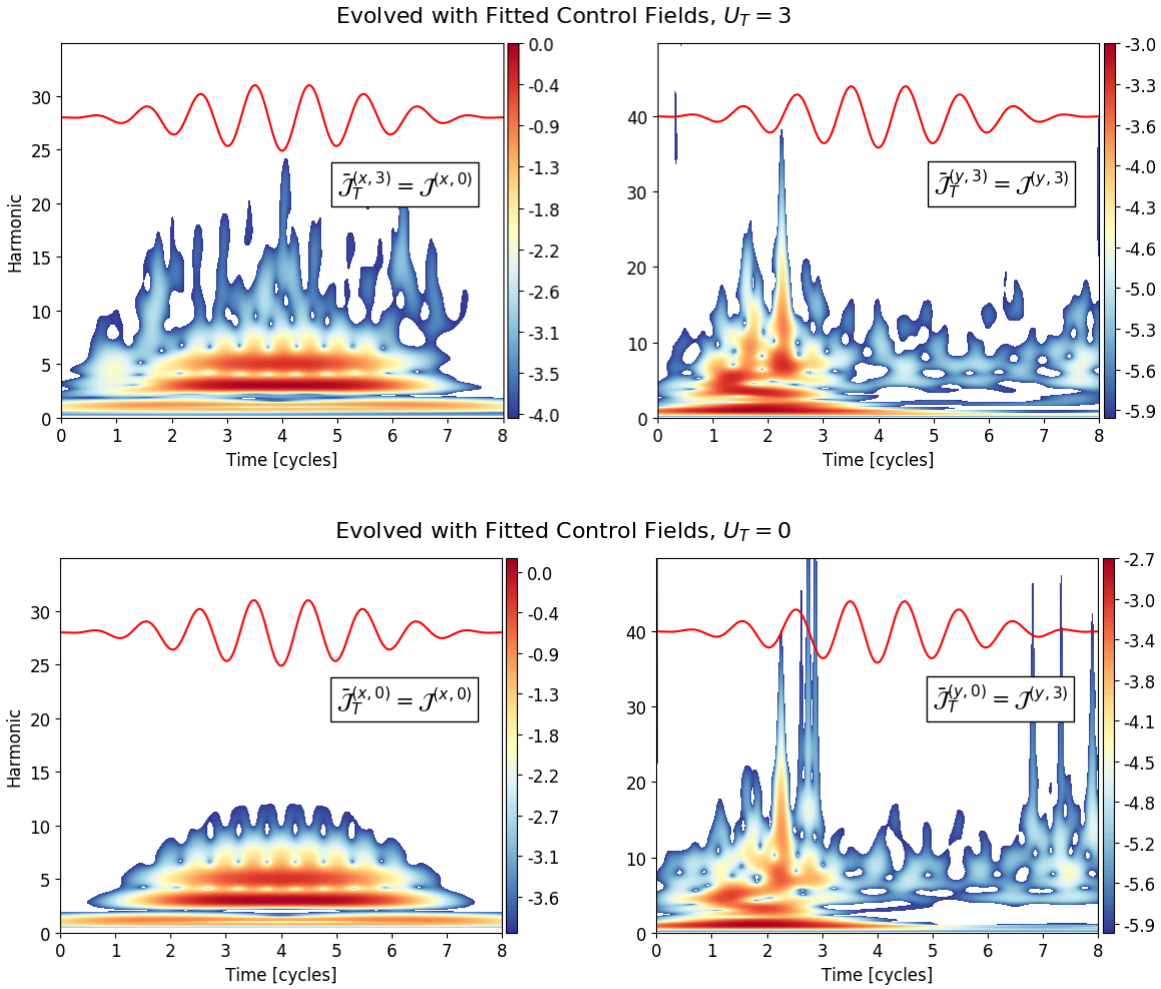

Figure 5.8: **Spectrograms resulting from evolution under fitted control fields.** The $U_T = 3$ (top row) and $U_T = 0$ (bottom row) systems were propagated using the pulses in fig.5.7. These spectrograms show the resulting time-resolved emission that is attempting to reproduce the characteristics in fig.5.6. The red lines show the form of the electric field, $aE(t) = -d\Phi(t)/dt$, of the original pulse. Calculated using tVMC on a 6×6 lattice.

Similarly, the $U_T = 0$ spectrograms duplicate the tracked HHG in both directions. We would expect them to be far superior than any $U_T > 0$ equivalent because the simulation is done using an exact mean-field method, and therefore does not suffer from stochastic noise or errors due to an approximate trial wavefunction, but instead has a non-interacting wavefunction $|\Psi_{MF}\rangle$ that remains exactly correct throughout. Furthermore, when $U_T > 0$ any errors are likely to compound and combine across the dimensions because of the coupling that exists between them. Lastly, the absence of correlation has significant effects on the required control fields, especially on $\Phi_T^{(y)}(t)$ which does not develop a stem and can therefore be fitted to greater precision. In fact, inaccuracies in the fitted versions of the control fields are the only source of error when $U_T = 0$.

Fig.5.8 shows that these factors combine to produce a close match in the x-direction, without any noise and with the lower-intensity BOs also included. However, in the y-direction there is actually more noise than at $U_T = 3$, which originates entirely from fitting errors and shows that the absence of a stem does not necessarily lead to improvements. Both simulations in fig.5.8 show that, perhaps unsurprisingly, the best reproduction happens in the direction where $U_I^{(k)} = U_T$, i.e. where the system is regenerating its native spectrum.

Finally, these results demonstrate that with only a small number of frequencies it is possible to transform the emission of a system in both the frequency and time domains by inducing directional transition/conduction behaviour. This perhaps suggests that the complexity of the control fields does not necessarily preclude an experimental demonstration of the technique, especially given that the specifics of the tracking fields do not seem to be vitally important, as both cases in fig.5.7 have visible errors and yet still faithfully mimic the emission. Furthermore, for both $U_T = 0$ and 3, fitting with $D = 5$ distinct frequencies was chosen because it led to the best results, but the calculations were repeated with $D = 3$ and were found to produce similar spectrograms. In fact, even $D = 2$ gives reasonably good fits[12], which shows that the first frequency component is the dominant contribution, and demonstrates the importance of the envelope function. Several other fitting models were also tried

[12]Although the fitted evolution under $D = 2$ has not been done yet, so it could be that the decent fits do not translate into close spectral reproduction.

and were again found to produce similar spectrograms. This means that if it were experimentally necessary, then $D = 3$ or fewer frequencies could be used, and perhaps with different fitting models, depending on which is easiest to construct experimentally. In terms of its actual implementation, these experiments might be approached using two entirely separate pulses that are arranged at right-angles to each other, one facing each axis. This is of course speculative, but is an interesting possibility.

5.3.1.3 Stability Check

Evolution under these tracking control fields introduces an additional layer of stochastic error compared to the results in Chapter 4, because not only is the evolution stochastic, but the field itself is stochastically-derived. It is therefore important to check for reliability and stability by taking the pulses calculated by the tracking protocol and shown in fig.5.6, and reapplying them to the $U_T = 3$ GS. For us to have confidence in the control fields, this propagation should produce spectrograms that look similar to fig.5.6, i.e. to those that the fields were calculated to track! The results of this check are plotted in fig.5.9, which shows that the spectrograms are accurately reproduced, with the addition of some stochastic noise at larger harmonics. They are similar to those generated under fitted fields in fig.5.8, but the fine-structure of the emission is more closely recreated in fig.5.9, for example, in the x-direction's BOs.

It is not obvious how the stability of the implementation's results would be affected by the complexity of the tracked currents or subsequent control fields. This was investigated by carrying out the same simulation as fig.5.6 but with $E_0^{(x)} = 50\text{MVcm}^{-1}$, as the strong pulse amplitude produces a current with intense BOs, which in turn leads to a complex tracking field. The results are plotted in fig.5.10, and shows the tracking control fields (left) and x-direction spectrogram (right), while the y-direction emission is identical to fig.5.6 and so is not shown. The stability check was then done for this case, and is plotted in fig.5.11. Once again, the spectrograms look very similar to the originals, with the only significant aberration being some stochastic noise that is mostly confined to higher harmonics, particularly ones $\omega > \omega_c$. In fact, the check was repeated for several different tracking simulations, and in each case the correct HHG was reproduced with similar precision. This suggests that the method remains

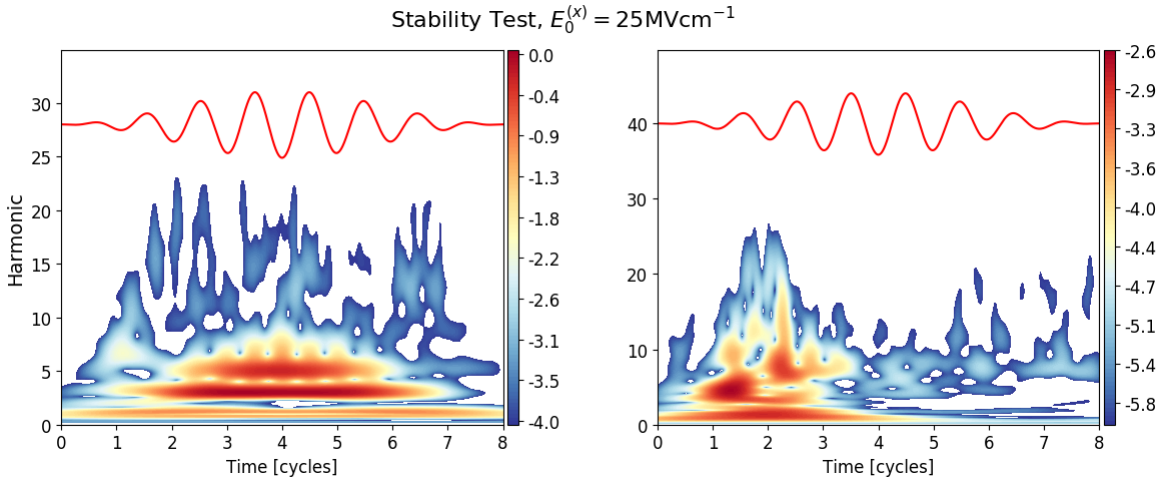

Figure 5.9: **Stability test for $E_0^{(x)} = 25\mathbf{MVcm}^{-1}$.** Spectrograms calculated by propagating under the tracking control pulses in fig.5.6, in order to check that similar HHG is produced. Calculated using tVMC on a 6×6 lattice.

stable and accurate for all $\mathcal{J}_T^{(k)}(t)$, without much variation due to its specific form.

It is not possible to fit the fields in fig.5.10 with existing methods, and so approximating them with fewer frequencies requires specifications that go beyond current experimental capabilities. This is investigated in Appendix B using a harmonic selection method, where the most significant contributing frequencies are identified and combined to produce simplified versions of the fields.

Fig.5.9 and fig.5.11 also demonstrate the maximum possible accuracy that fitted fields could give for these cases, i.e. any approximate form of the control fields could never produce more accurate spectrograms than these results. They show that the approximate nature of tVMC is not a fundamental barrier to generating the original spectral features to very high precision, and that a sufficiently well-fitted pulse could reproduce them to better accuracy than fig.5.8. However, they also show that stochastic noise limits how well the low-intensity structure can be recreated, which mirrors the limitations found in Chapter 4. Developing strategies to mitigate this noise is therefore an important way that the accuracy of results could be improved.

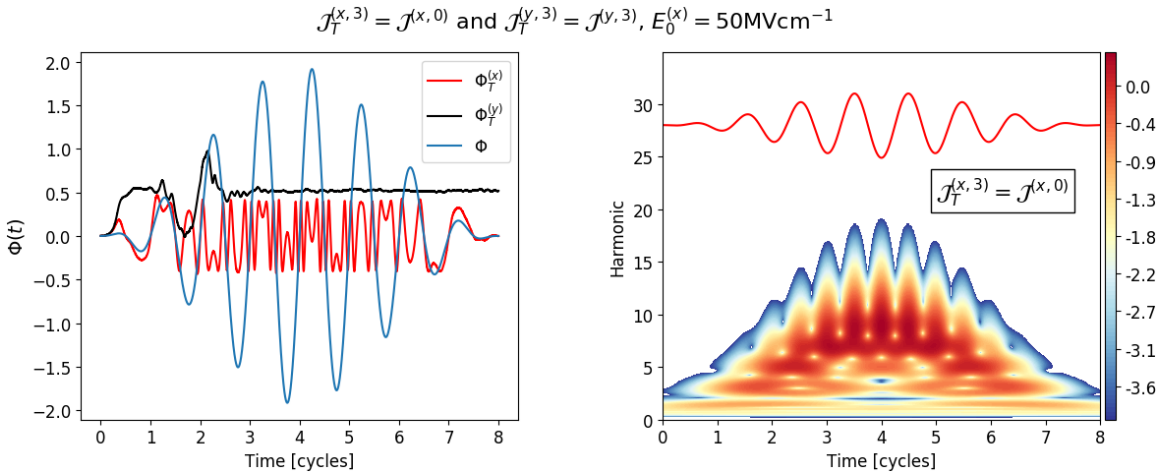

Figure 5.10: **Tracking control used to simultaneously resolve a Mott transition and aggressive Bloch oscillations in perpendicular directions.** The same simulation as fig.5.6 but with $E_0^{(x)} = 50\text{MVcm}^{-1}$. Image shows the resulting control fields, for comparison plotted with the default pulse $\Phi(t)$, $E_0^{(y)} = 10\text{MVcm}^{-1}$. The time-resolved emission is shown for the x-direction, along with the electric field, $aE(t) = -d\Phi(t)/dt$. The y-direction spectrogram is the same as fig.5.6. The scale factors $\alpha_S^{(x)} = 0.4$ and $\alpha_S^{(y)} = 1$ were applied, as well as the cutoff frequencies $\omega_c^{(x)} = 16$ and $\omega_c^{(y)} = 24$. Calculated using tVMC on a 6×6 lattice.

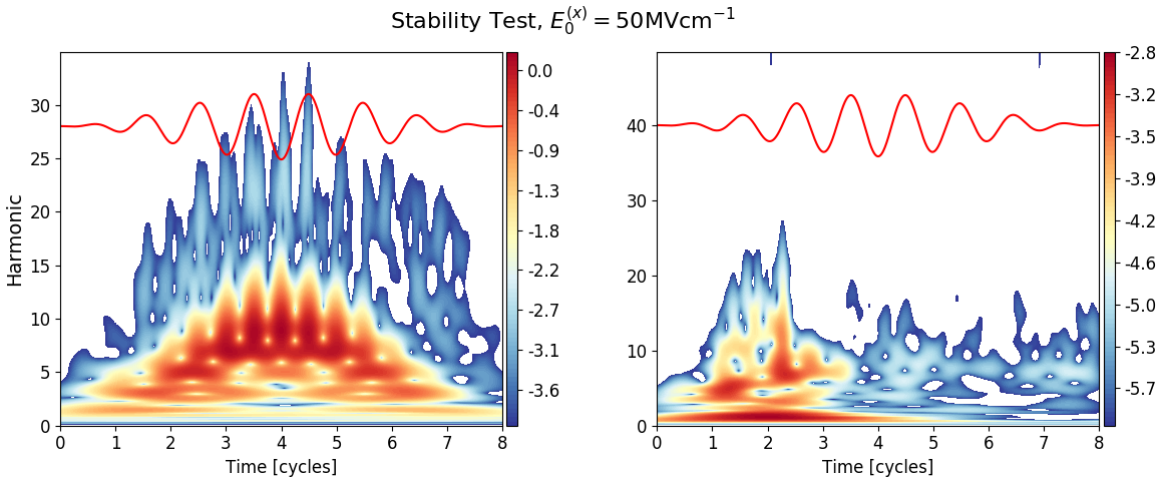

Figure 5.11: **Stability test for $E_0^{(x)} = 50\mathbf{MVcm}^{-1}$.** Spectrograms calculated by propagating under the tracking control pulses in fig.5.10, in order to check that similar HHG is produced. Calculated using tVMC on a 6×6 lattice.

5.3.2 Harmonic Enhancement

A major advantage of the presented tracking control protocol is its adaptability and wide applicability. An interesting example is to the longstanding question of how to enhance the yield of selected harmonics [221–225]. This is important, as HHG is increasingly used as a way to generate ultra-intense, ultra-short high frequency light pulses, so having a way to tailor them to specific needs would be advantageous. Current tracking can be applied to this problem, and is able to calculate the control fields necessary to boost any harmonic, potentially to any desired intensity.

This is achieved by creating a new artificial current, which is then tracked to give the requisite driving field. Starting in a system with interaction strength U_I that generates a current $\mathcal{J}(t)$ under some pulse $\Phi(t)$, if we would like to boost the HHG spectrum at the harmonic ω_E then we can simply add that component to its current

$$\mathcal{J}(t) \to \mathcal{J}(t) + \beta \sin\left[\omega'_E t\right] \tag{5.46}$$

where $\omega'_E = \omega_E \omega_L$ and β is a boost factor that determines the degree of enhancement. This is then tracked in a system with U_T, producing the control field $\Phi_T(t)$ required to reproduce the enhanced spectrum. It was found that this process sometimes produces yield boosts that are too narrow in the frequency domain, so in order to widen them W additional adjacent harmonic terms were introduced

$$\mathcal{J}(t) \to \mathcal{J}(t) + \sum_{n=0}^{W} \beta_n \sin\left[\left(\omega'_E + n\Delta\omega\right) t\right] = \mathcal{J}'(t) \tag{5.47}$$

$$\mathcal{J}'(t) \to \mathcal{J}'(t) + \sum_{n=0}^{W} \beta_n \sin\left[\left(\omega'_E - n\Delta\omega\right) t\right] \tag{5.48}$$

where $\Delta\omega = \frac{2\pi}{N\Delta t}$. This was chosen because $\frac{1}{N\Delta t}$ is the interval between adjacent frequency components of a discrete Fourier transform for some timestep Δt and total number of steps N, which means that $\frac{2\pi}{\omega_L}\frac{1}{N\Delta t}$ is the harmonic interval. If $W = 0$ then only eq.(5.47) is kept and eq.(5.46) is recovered, but if $W > 0$ then terms are both added and subtracted in order to symmetrise the boost. Lastly, $\beta_n = \beta$ was always selected, although $\{\beta_n\}$ could potentially be specified more precisely in order to control the shape of the boost, perhaps in combination with narrower and more

numerous choices of $\Delta\omega$.

There is no restriction on U_T or the choice of $\mathcal{J}(t)$, so we can of course choose $U_I \neq U_T$ and boost the spectrum of any system in any other system. Additionally, in 2D the polarisation of the pulse can be used to induce directional enhancements, such that different harmonics are amplified in each dimension. An example of this is fig.5.12, which shows the enhancement of the y-component of the $U_I = 1 = U_T$ current[13], $\mathcal{J}^{(y,1)}(t)$, with simultaneous boosting of the harmonics $\omega_E^{(x)} = 4.5$ and $\omega_E^{(y)} = 10.5$, both with width $W = 1$. The enhancement factors were

$$\beta^{(x)} = \frac{1}{20}\max\left\{\mathcal{J}^{(y,1)}(t)\right\} \text{ and } \beta^{(y)} = \frac{1}{50}\max\left\{\mathcal{J}^{(y,1)}(t)\right\} \tag{5.49}$$

These were chosen in a somewhat ad hoc way to amplify the harmonics above the peak of the $U = 1$ spectrum.

Fig.5.12 shows how these enhancements introduce additional oscillations into the currents which then manifest in the spectra as new peaks. $\Phi_T(t)$ also picks up compensatory oscillations, in this case at approximately the same frequencies as the boosts. This simple relationship between $\omega_E^{(k)}$ and the tracking fields is due to the system's weak correlation, but as U_T is increased there is an increasingly nonlinear relationship between them. Finally, the spectrogram shows that the boosts are continuous and time-independent[14], and that they bleed into adjacent harmonics[15]. Note, these extra oscillations in the control fields do not greatly affect their ability to be fitted, and tests have demonstrated that it is often possible to accurately reproduce the new peaks, although this is a topic that needs further work.

The boosts in eq.(5.49) were picked by a degree of trial and error, but in some cases it should be possible to determine in advance the required values for a given spectrum intensity. We want to find the factor β_E needed to boost the harmonic ω_E to the spectrum intensity $\mathcal{S}_E(\omega)$. The relationship between these quantities is

$$\mathcal{S}_E(\omega'_E) = \left|\mathcal{FT}\left\{a(t) + \beta_E \frac{d}{dt}\sin[\omega'_E t]\right\}\right|^2 \tag{5.50}$$

[13]The y-component was tracked in both directions because it improves the clarity of the results and makes analysis easier.

[14]Oddly, the intensity of the boost appears to reduce slightly towards the end of the pulse, but this is likely just a numerical artifact.

[15]This can also be seen in the HHG spectra by the boosts' thick bases.

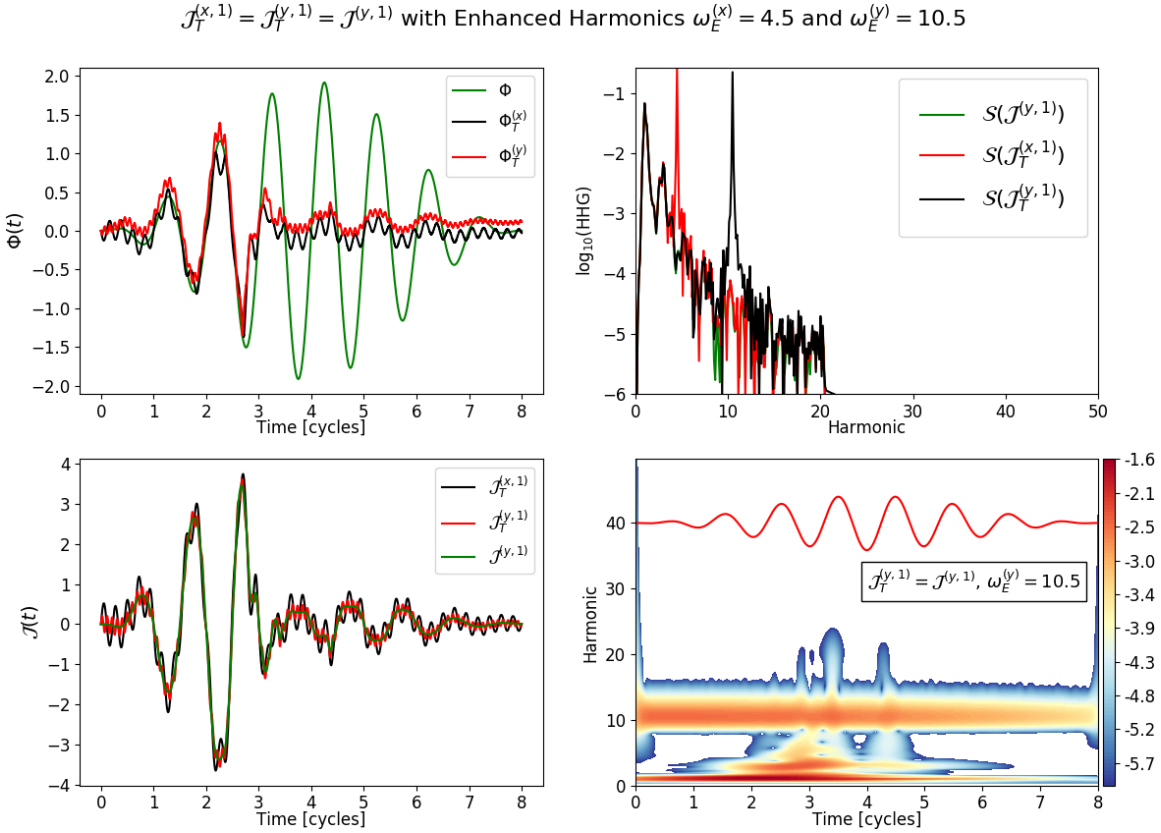

Figure 5.12: **Tracking currents with enhanced harmonics.** $U_I^{(y)} = 1$ current simultaneously tracked along both components of the $U_T = 1$ system, with harmonics $\omega_E^{(x)} = 4.5$ and $\omega_E^{(y)} = 10.5$ boosted to produce emission above the normal peak. Image shows the necessary control fields (top left) plotted with the pulse $\Phi(t)$, $E_0^{(y)} = 10\text{MVcm}^{-1}$, that induced the original current. Also shown are the pre- and post-enhanced currents (bottom left), and their HHG spectra (top right). In the latter's legend, e.g. $\mathcal{S}(\mathcal{J}^{(y,1)})$ refers to the spectrum generated by the current $\mathcal{J}^{(y,1)}$. The time-evolution of this enhanced emission is shown for the component $\mathcal{J}_T^{(y,1)}(t)$ (bottom right), with the electric field, $aE(t) = -d\Phi(t)/dt$, in red. Scale factors were not used, $\alpha_S^{(x)} = \alpha_S^{(y)} = 1$, and the cutoff $\omega_c^{(y)} = 20.5$ was applied before tracking. Calculated using tVMC on a 6×6 lattice.

and it can be inverted to find β_E. However, the problem becomes more complicated for any $W > 0$, and is probably inapplicable if the Welch method is used. This topic needs to be researched further, but it is likely within the capabilities of the method to specify the enhancement of both the harmonic and its intensity.

5.4 Summary and Outlook

In this chapter, a technique for tracking control was derived and subsequently demonstrated using a combination of ED, tVMC and mean-field methods. The protocol was implemented using the Fermi-Hubbard Hamiltonian as an example, and enabled the arbitrary manipulation of the optical response of interacting systems across regimes, from conductors to insulators. This included the resolution of 'directional Mott transitions' and the enhancement of specific harmonics. Significantly, it was shown that these capabilities can be well-approximated by comparatively simple laser fields that are potentially within existing experimental limitations.

This tracking protocol is extremely flexible and has a broad potential for interesting applications and future research, although it also has limitations imposed on it by tVMC and the available fitting methods. Given the success of the directional transition simulations in fig.5.8, it might be possible to go further and apply the protocol to more challenging cases. That could mean changing either U_I, U_T or both, for example by trying to mimic the HHG of more strongly-correlated systems. A tempting alternative simulation would be to again retain the y-direction but now change the x to be a high-U system, which would produce a directional transition by replacing the emission signature of a conductor with that of a typical insulator. This would have the advantage that $\Phi_T^{(x)}(t)$ would only require a weak amplitude, owing to the comparatively small currents at large U. However, it would probably not be possible due to the extremely broadband nature of the currents, and $U_I < 6$ is the realistic range using the available fitting methods, as to go beyond this would likely require more accurate techniques. In the short term, a simpler and potentially viable alternative would be to repeat fig.5.8 but with e.g. $U_I^{(y)} = U_T = 5$, as this would create a more distinctive Mott transition in the spectrogram, along with a more interesting $\Phi_T^{(y)}(t)$ that has a highly nonlinear relationship between its frequency components and

those in the resulting spectrum. In the long term, moving beyond the single-band Hubbard model is an important next step because this would enable real materials to be simulated, with the aim ultimately to collaborate with experimentalists in order to demonstrate some aspect of tracking control in the lab.

The harmonic enhancement discussed in Sec. 5.3.2 was a simple example of a concept that has many possible extensions. This capability could be expanded upon by introducing a chirped enhancement instead of a single constant frequency, and the boost factor could be made arbitrarily complicated, $\beta_n \to \beta_n(t)$. These extensions combined with different choices of eq.(5.47) and eq.(5.48) might allow for a great deal of control over the nature of the spectral enhancements, potentially enabling the construction of 'designer spectra'. This leads naturally to the idea of spectrum tracking, where we start from the spectrum that we would like to track instead of the current. However, it is a difficult problem ripe for future research because the derivation used for currents cannot be straightforwardly extrapolated to HHG spectra. This is because of the absolute square in the spectrum's definition, eq.(3.64), which destroys phase information and thereby creates a redundancy whose resolution is not at all obvious.

6

Conclusions

In this thesis, a range of numerical methods were applied to the ultrafast high harmonic spectroscopy of correlated lattice systems subject to strong-field laser pulses. This provided an attosecond-scale window into the many-body charge dynamics of Mott insulating systems across dimensions and correlation regimes, as well as enabling the near-arbitrary control and manipulation of the optical response in the time, frequency and even spatial domains via tracking control. The focus throughout was on 2D lattices, which have previously been almost completely absent in the literature and exist at the frontier of the non-equilibrium physics of correlated materials. To pursue these challenging problems, a fusion of exact, mean-field and stochastic approaches were implemented, with the Fermi-Hubbard model providing the foundation, and supplemented by a novel effective single-particle model. These were combined with the ubiquitous use of wavelet analysis in order to time-resolve the emission and provide a highly accurate means of characterising and comparing the sub-cycle dynamics.

The aim of Chapter 4 was to describe, explain and compare the frequency and time-resolved emission in these correlated models in both 1D and 2D, and to repeat this across all interaction regimes. This was primarily done using tVMC in order to access extended system sizes, but was replaced with ED in cases where its use was impractical or impossible. This was accompanied by the frequent use of mean-field methods for the $U = 0$ limit, but also as part of the CBM. The analysis began by using ED to calculate the evolution of several system observables across a wide range of U values. The results demonstrated that in both dimensionalities there are three clear regimes: a non-interacting limit where the system begins and remains conducting; a transition regime in which the photo-induced breakdown of the Mott insulating state and magnetic order can be seen to occur with threshold behaviour; an insulating

regime where the field strength is not strong enough to induce breakdown. While this is true in both 1D and 2D, there were also important distinctions between them that reappeared frequently in later sections, including that in 2D the transitions were initiated earlier and finished more quickly, but also persisted up to larger correlation strengths. These results were repeated for tilted lattice systems in order to account for the effects of artificial frustration in the y-direction of the 4×3 square lattice, which illustrates the limitations of using ED for 2D systems.

This was followed by an investigation into the optical response associated with these complex charge dynamics, starting with the HHG spectra across the three regimes. In the $U = 0$ limit, the spectra exhibited typical properties of tight-binding systems, including distinct narrow peaks at odd harmonics. In this metallic regime, it was found that up to a constant factor the emission does not vary between dimensions. However, when interactions are introduced Mott gaps develop and transform the spectra, creating clear distinctions between 1D and 2D. In 1D, increasing correlation is accompanied by a transfer from spectra that are dominated by intraband-induced low harmonics, to broader and more irregular spectra composed mostly of high harmonics that originate from DHP recombination, and that have regions of peak emission proportional to U. In 2D however, low harmonics exist at all interaction strengths, signalling the persistent presence of intraband currents, including regimes in which they are suppressed in 1D. These and other properties and differences were explained by considering the lattice, bandwidth, gap size and DOS, among other things, and together showed that dimensionality has a clear impact on the HHG. Finally, the large-U regime was considered, and it was shown that the UHB becomes depopulated as the Mott gap widens, which in turn causes the emergence of strong intraband currents and therefore intense low-harmonic emission.

Having analysed the HHG purely in the frequency domain, its time dependence was then resolved and investigated using wavelet analysis, enabling direct observation of the charge dynamics and Mott transitions. In the metallic regime, field-aligned BOs are clearly identifiable, allowing us to characterise the appearance of intraband currents, which is useful when analysing interacting systems as it helps to identify the origin of different parts of the emission. In the transition regime, the signature of the photo-induced breakdown was determined to be a brief period of intense HHG that

subsides within one or two laser cycles. Differences found in the double occupancy and other observables were also found to arise in the spectrograms; for example, that the transitions begin earlier in 2D and occur more rapidly. Many of these properties were explained by the Mott gaps, which are smaller in 2D for a given U. This was followed by the resolution of the low-intensity structure of the HHG, which found that regular field-aligned emission emerges in 1D, whereas in 2D the increased dimensionality leads to interference between trajectories that causes the emission to develop a more irregular form. Finally, in the heavily-insulating regime in which no breakdowns can occur, the spectrograms showed two overlapping but distinct sectors at low and high harmonics, corresponding to intraband and interband-induced emission, respectively. This was followed by an analysis of the CBM's HHG, where it was shown that this simple mean-field model converges with the Hubbard model as $U \to \infty$, thereby demonstrating that in this limit the sub-cycle dynamics can be well-described by a single-particle picture.

The final section of Chapter 4 investigated how the 2D transition-regime emission changes with varying simulation parameters. Raising the maximum laser amplitude E_0 was found to slightly shift the peak HHG to higher harmonics, but did not affect the cutoff or overall structure of the spectrum because a saturated UHB limits the set of excitation energies that can be accessed. On the other hand, the frequency ω_L had dramatic effects on the spectrum peak and cutoff, increasing (decreasing) them as ω_L is decreased (increased). These two parameters also had significantly different effects on the Mott breakdown process, which was shown to be largely independent of the frequency, whereas E_0 controls its onset time by determining when the threshold field E_{th} is reached. Finally, the hopping constant t_0 was found to have powerful effects on a system's emission by controlling the width of possible excitation energies, and on the Mott transition via its influence on the gap.

Chapter 5 moved away from analysing the electronic and optical responses of a system subject to a given driving field, and instead investigated how the laser pulse can be designed to manipulate the response to produce any predetermined outcome. The protocol required to do this was demonstrated using ED examples of spectral mimicry, in which the HHG of an insulator was generated by a conductor and vice versa. The doublon density was used to show that the electronic response depends on

the choice of scale factor α_S. This has the consequence that a given HHG spectrum, up to a constant factor, can be generated by both an insulating system and a system undergoing Mott breakdown. The general properties of the control fields that are needed in different cases were then discussed, and it was found that they often require unrealistically large bandwidths that cannot be reproduced experimentally. To tackle this problem, fitting models were introduced that enable extremely complex control fields to be approximated using only a small number of frequencies, making them potentially viable.

The tVMC method was reintroduced, and was found to be a stable and accurate way of carrying out tracking control simulations. By easing restrictions on the polarisation of the tracking pulse, it was possible to simultaneously track entirely separate currents along each direction. The main result was the demonstration of a directional phase transition, where a Mott breakdown's HHG was generated in one direction and characteristically-conducting emission along the other. The control fields were then approximated in an experimentally-achievable form and were shown to correctly reproduce the same behaviour. This was followed by benchmarking of the accuracy of tVMC for tracking to show that it was an appropriate method to use. The chapter finished with an example of the application of tracking to the problem of harmonic enhancement, where selected frequencies are boosted.

The research in this thesis only scratches the surface of an extremely broad and complex topic. There are many directions that future work could take simply using the methods and models discussed here, let alone the enormous variety of more realistic models that could be investigated. Ultimately, future progress in simulating these realistic models in 2D and 3D depends on the availability of appropriate numerical methods, and it is this that is currently the main limiting factor.

A

Benchmarking

In this appendix, the suitability of tVMC and the chosen ansatz are justified and discussed. Firstly, more details are given into the simulation setup that was used throughout, such as the choice of timestep and number of Monte Carlo samples. Then the accuracy of tVMC is checked by comparing 12-site simulations against their ED equivalents. Finally, the convergence of the results with respect to lattice size is confirmed insofar as is possible given the limitations imposed by the method's heavy computational costs.

A.1 Simulation Setup

The same general simulation setup was used for all results in this thesis. The minimum required timestep Δt was found to depend upon the correlation strength of the system: for all $U \leq 3$, $\Delta t = 10^{-2}$ was chosen, whereas $\Delta t = 5 \times 10^{-3}$ was selected for $U > 3$. A similar dependence on U was also found to be necessary in Ref. [185], where they used $\Delta t = 10^{-2}/U$ for $U > 1$, which often leads to smaller timesteps than were used here.

The number of Monte Carlo samples S was chosen depending upon the number of parameters P in the ansatz, which depends upon the system size. The general rule was that the minimum number of required samples is $S \geq 10P$ [170]. The ansatz for 12-site systems has $P \approx 150$, and for 36 sites has $P \approx 1500$. As a result, the former used $S \geq 2500$ for optimising the GS and $S \geq 5000$ for the real-time evolution; whereas the latter always used $S = 15000$ and $S = 25000$ for the imaginary and real-time evolutions, respectively.

Finally, it was typically found that the best results were produced by averaging

over two or occasionally three simulation runs. Each run produces similar results that have the same qualitative features, but by averaging it is possible to reduce stochastic noise, especially at larger harmonics, and to sharpen and reinforce spectral features.

A.2 Comparison with Small Systems

Following the example of Ref. [185], linear ramp quenches were initially used to test the tVMC implementation and to analyse the main error sources: stochastic errors from the Monte Carlo sampling; the discretisation of time into steps of size Δt; the integration method[1]; and the form of the trial wavefunction. It was also used to provisionally choose an ansatz that balances accuracy with costliness, which led to eq.(3.40) being selected.

Following on from this, to check the suitability and accuracy of tVMC and the trial wavefunction, ED and tVMC results were compared against each other for 12-site systems, examples of which are given in fig.A.1 and fig.A.2 for 2D $U = 3$ and $U = 5$, respectively. These show that the important qualitative features of the frequency and time-resolved emission are reproduced, demonstrating the suitability of the ansatz for the qualitative physics of HHG in MIs. Furthermore, this was done for both 1D and 2D at all U values that were calculated for 36-site systems in Chapter 4, and in each case the most important qualitative features were duplicated in the time and frequency domains. The only exceptions to this were the spectrograms at $U = 7$ in both dimensionalities, because the large correlation strength causes the development of noise early in the pulse, which somewhat obscures the boundary between the noise and the genuine onset of emission. As a result, the equivalent spectrograms were not used for 36-site systems, and instead ED was used for all cases where the time-domain HHG of large-U systems was required. However, other than this noise, the $U = 7$ spectrograms still reproduced the most important features, namely that the Mott transitions are replaced by continuous emission at roughly uniform intensities. It is likely that by decreasing the timestep this noise could be reduced, however, this is not realistic due to the increased computational cost.

[1]The Euler method was compared against RK4.

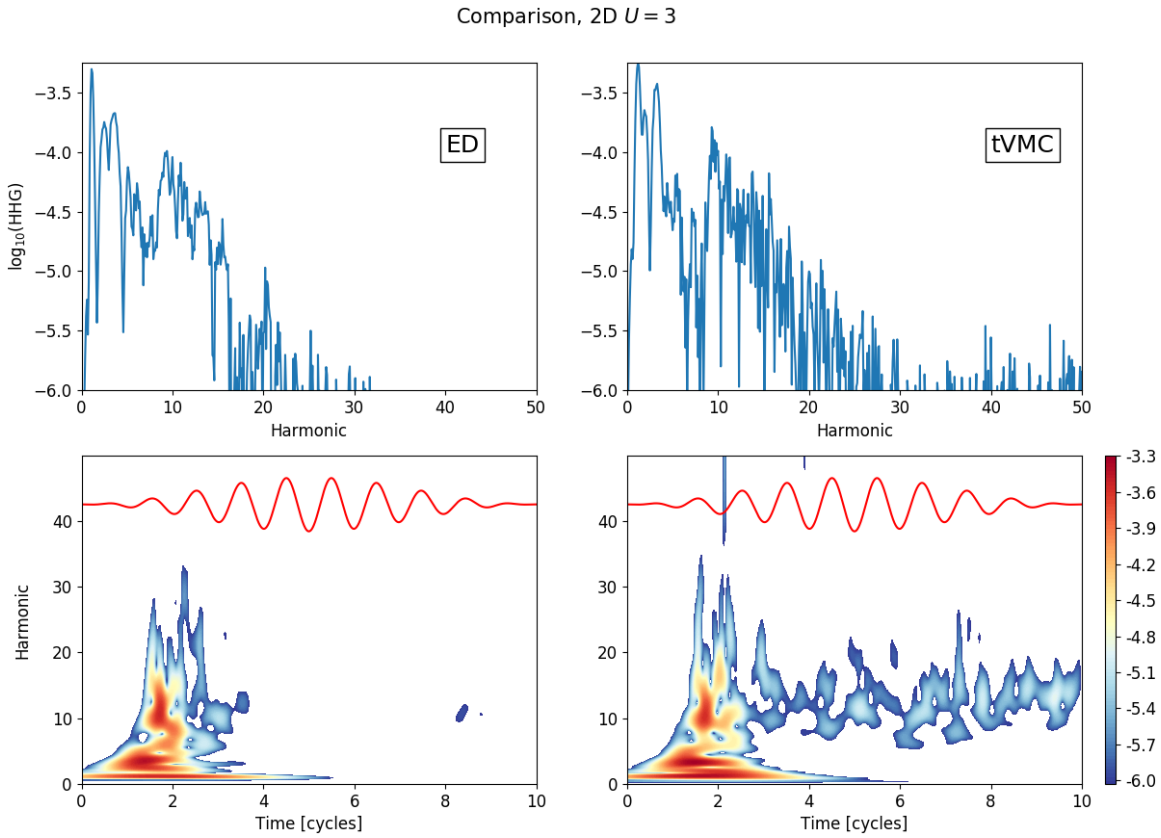

Figure A.1: **Comparison between tVMC and ED for 2D $U = 3$.** Emission spectra and spectrograms in the 4×3 system at $U = 3$ for ED (left column) and tVMC (right column). The red lines in the spectrograms show the incident electric field, $E(t)$.

In general, across both dimensionalities and at all U, it was found that tVMC can be used to accurately calculate the emission within the spectra's first 50 or so harmonics, corresponding to the largest 3 to 5 orders of magnitude of the emission intensity, depending on U. Beyond this region, stochastic noises renders tVMC ineffective and inapplicable. As a consequence of this, the results in Chapter 4 were calculated with ED in cases where the low-intensity structure and ultra-high frequency domains were required. This then leads to the question of convergence of the HHG with system size, which must be true (or at least true to a good approximation) for the results to be useful.

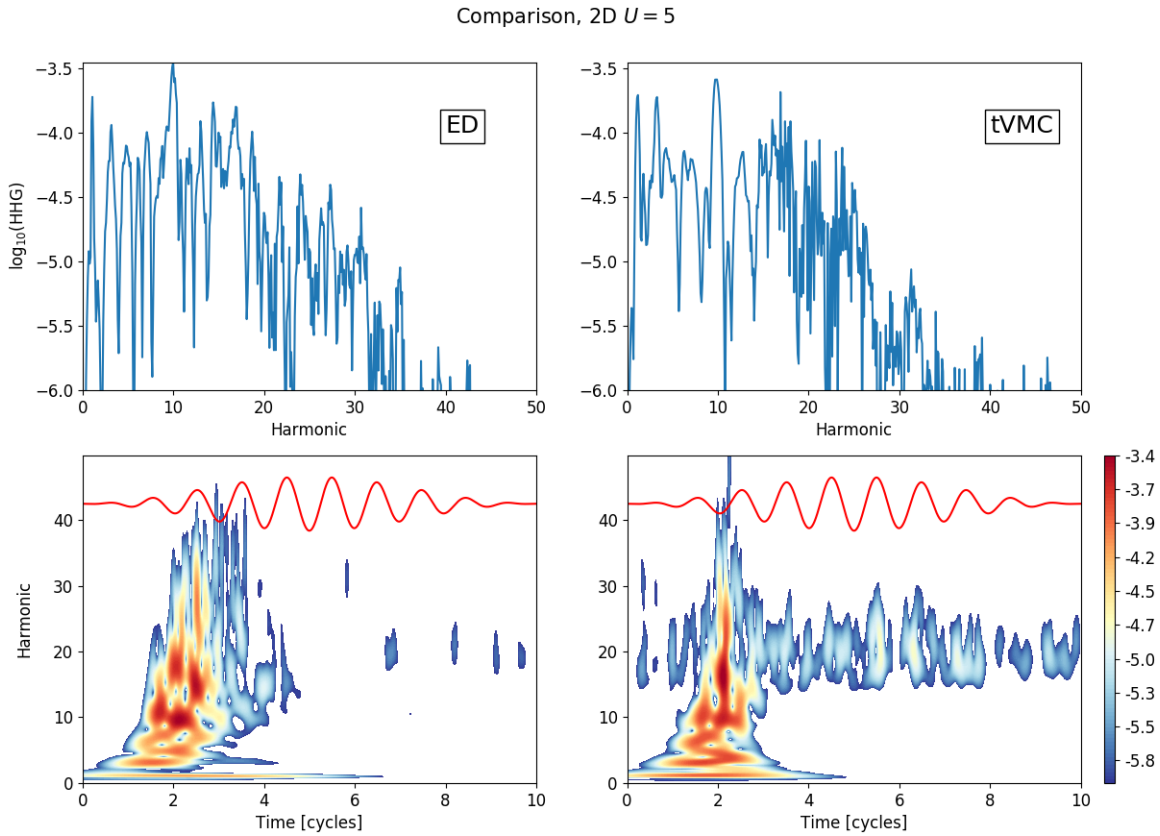

Figure A.2: **Comparison between tVMC and ED for 2D $U = 5$.** Emission spectra and spectrograms in the 4×3 system at $U = 5$ for ED (left column) and tVMC (right column). The red lines in the spectrograms show the incident electric field, $E(t)$.

A.3 Convergence of the HHG

We would like to check that the results include minimal or no contributions from finite-size effects. In 2D we are restricted to lattices that have relatively few sites in each direction, and the concern is that the charge carriers might traverse a very large number of sites before recombination occurs, such that the limited lattice dimensions start to influence the HHG in ways that are not present in the thermodynamic limit. In particular, this is a concern for ED calculations due to the small 4×3 lattice. We would expect that these effects are more pronounced when the correlation U is low because interactions have a localising effect that reduces charge mobility, so that weak correlation results in carriers that can travel over larger distances and are therefore

more susceptible to finite-size effects. Having said that, in the $U = 0$ limiting case, the correlation length becomes infinite and the electrons can roam unimpeded, and yet the emission is not affected by system size at all[2]. This means that the concern lies with the full coupled correlated dynamics and not purely with intraband oscillations, despite these being responsible for the motion of the charge carriers.

We can test that the HHG results have converged by repeating calculations for bigger lattice sizes and confirming that the results are qualitatively the same. However, the number of variational parameters in the trial wavefunction increases as $\mathcal{O}(L^2)$, which results in a rapid escalation of the computational costs as the number of sites increases. As a result, the 8×6 lattice was found to be the largest 2D system that can realistically be simulated with the available resources. Fig.A.3 shows comparisons between simulations using 6×6 and 8×6 lattices for $U = 1$ and $U = 3$, and in both cases the qualitative features of the HHG remain unchanged. These are both weakly-correlated systems, and so a lack of finite-size effects is encouraging, and also means we can expect that systems with $U > 3$ have similarly converged. Note, the number of samples was not increased for the 8×6 simulations in order to limit cost, and this results in a somewhat block-like appearance that would likely disappear with larger S, as this effect has been observed in other simulations where too few samples were used.

Fig.A.3 plots the high-intensity region of the HHG, but this does not necessarily mean that the low-intensity structure shown in fig.4.11 and fig.4.12 has also converged. Stochastic noise makes this inaccessible to tVMC, so it is not possible to do convergence tests with the 8×6 lattice. However, the low-intensity analysis using ED was repeated for various $U \geq 1$, and they were all found to reproduce the same basic properties discussed in Sec. 4.4.2 and Sec. 4.4.3: 1D has ordered field-aligned emission and 2D has more complex sub-cycle structure. This also continues to persist at $U > 10$, where the correlations are so strong that multi-site charge dynamics are severely restricted, and so finite-size effects are likely insignificant. The fact that these features exist over all U, including those that we are confident have converged due to their strong interactions, suggests that these are genuine properties and not

[2]Increasing L has the effect of shifting the emission upwards by a constant factor, but the structure of the emission does not change in the frequency or time domains.

numerical figments. This is likely because the carrier dynamics occur on sub-cycle timescales during which multiple sites cannot be easily traversed, thereby limiting finite-size effects.

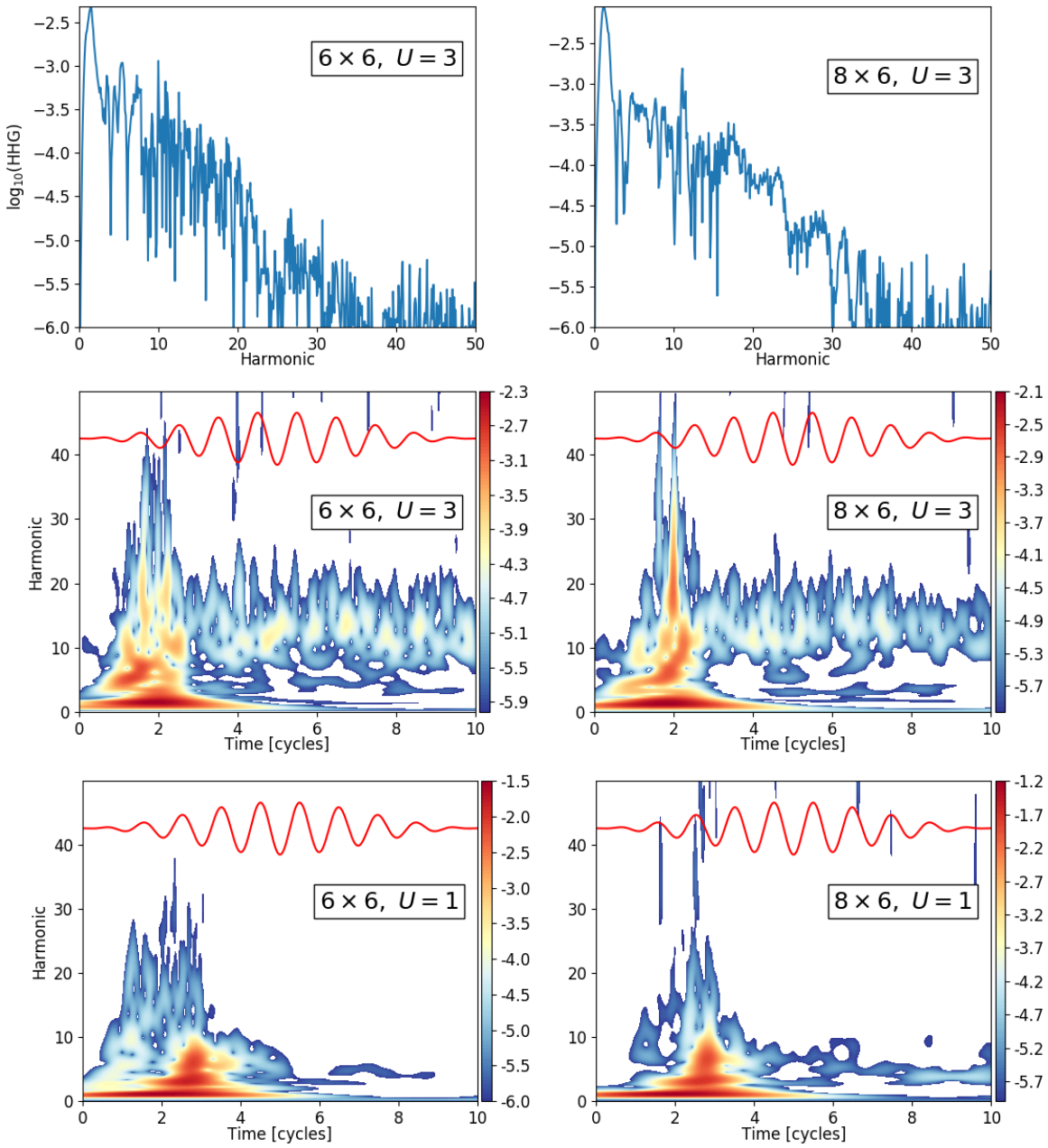

Figure A.3: **Convergence of the HHG profile with system size.** Comparisons between the emission for simulations using 6×6 and 8×6 lattices. The top two rows show the spectra and spectrograms of the 2D $U = 3$ system, and the bottom row shows the spectrograms for 2D $U = 1$. The 6×6 cases are those previously plotted in Sec. 4.3.2 and Sec. 4.4.2. Calculated using tVMC.

B

Harmonic Selection

This appendix introduces a simple method for constructing approximate control fields. The tracking pulses in fig.5.6 are at the limit of what can be fit with the available methods. However, noise somewhat obscures the BOs at lower intensities in fig.5.8 at $U_T = 3$, and we would like the BOs to be as distinct as possible to aid identification in any potential experiments and enable unambiguous demonstrations of directional phase transitions. They could be made more resilient to noise by amplifying the conducting behaviour, and this can be achieved by raising the field strength, $E_0^{(x)}$, that is applied to the $U_I = 0$ system before tracking. An example of this was shown in fig.5.10, which plots the control fields required to track the same situation as fig.5.6 but with $E_0^{(x)} = 50\text{MVcm}^{-1}$. This produces identical emission in the y-direction but considerably stronger BOs in the x, as was discussed in Sec. 5.3.1.3.

This additional structure comes at the cost of a significantly more complex and broadband control field that cannot be fitted using the methods discussed so far - even when $U_T = 0$. Instead, alternative methods must be developed that require a much larger number of frequencies than is currently experimentally obtainable. As a first attempt at this, harmonic selection was used, where each control field is resolved into its component frequencies via a Fourier transform, and then the N_ω maximum-contributing frequencies are chosen and combined into a new approximate pulse. More precisely, a control field $\Phi_T(t)$ is first Fourier transformed and then has a cutoff frequency ω_c imposed in order to remove noise and any harmonics that are larger than required for our analysis

$$\mathcal{FT}\left\{\Phi_T(t)\right\} = \tilde{\Phi}_T(\omega) \rightarrow \tilde{\Phi}_T(\omega \leq \omega_c) \tag{B.1}$$

The magnitude of the resulting field is then calculated, $\left|\tilde{\Phi}_T(\omega)\right|$, and the N_ω maximally-

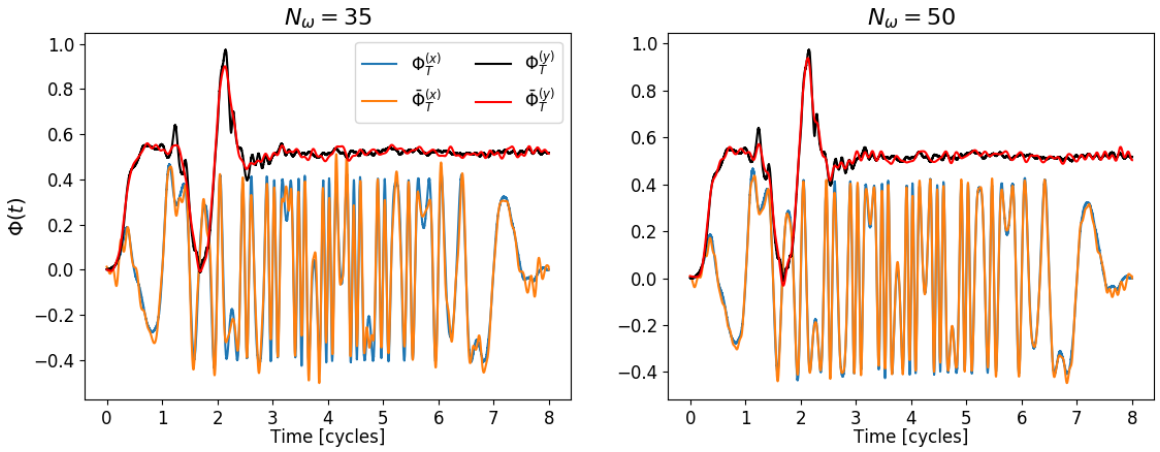

Figure B.1: **Control fields reconstructed using harmonic selection.** The images show the $U_T = 3$ pulses being approximated by $N_\omega = 35$ and 50 frequencies. The harmonics were selected based on the magnitudes of their Fourier components, and under the constraints that a fraction $f_\omega = 0.1$ and 0.2 of them, respectively, must be $\omega > 5$.

contributing frequencies are selected to form $\bar{\tilde{\Phi}}_T(\omega)$. This is then inverse transformed to give a new approximation of $\Phi_T(t)$

$$\bar{\Phi}_T(t) = \mathcal{FT}^{-1}\left\{\bar{\tilde{\Phi}}_T(\omega)\right\} \tag{B.2}$$

The exact tracking field is recovered as N_ω increases, $\bar{\Phi}_T(t) \to \Phi_T(t)$. However, when calculating $\bar{\Phi}_T^{(y)}(t)$ it was found that the selected harmonics had a tendency to cluster below approximately $\omega < 5$, unless N_ω is taken to be very large. This is a problem because it means that the spectrogram's structure at $\omega > 5$ is poorly reconstructed. In an attempt to account for this, the condition was enforced that a minimum fraction f_ω of the selected harmonics must be $\omega > 5$.

Fig.B.1 shows the pulses that result from this process for the two examples $N_\omega = 35$ with $f_\omega = 0.1$, and $N_\omega = 50$ with $f_\omega = 0.2$. Both of these appear to reproduce the pulses' qualitative features, and $\Phi_T^{(y)}$ look to be closer approximations than their fitted equivalents in fig.5.7. Increasing from $N_\omega = 0$ (and without using f_ω, i.e. $f_\omega = 0$), the fields' basic shapes are crudely recovered by $N_\omega \approx 20$, but $\Phi_T^{(x)}(t)$ and $\bar{\Phi}_T^{(x)}(t)$ do not become (approximately) visually indistinguishable until at least $N_\omega > 80$, so there are clearly a significant number of contributing frequencies, which makes it clear why fitting was difficult. $\Phi_T^{(y)}(t)$ is actually even more difficult to perfectly match because

of the transition-encoding structure between the 1st and 3rd cycles, which requires an extremely large number of harmonics to be completely reproduced.

Several examples of these composite control fields were then applied to the GS of $U_T = 3$ in order to see how features of the emission emerge with increasing N_ω. Fig.B.2 shows the resulting spectrograms for both fields in fig.B.1 as well as $N_\omega = 110$, with the intention of the latter being to show a near 'exact' case where the control fields appear very closely matched.

In most of these cases, the approximate fields struggle to accurately reproduce the conducting and transition features of the spectrograms. This is surprisingly considering that $\bar{\Phi}_T^{(k)}(t)$ appear qualitatively close to $\Phi_T^{(k)}(t)$ in fig.B.1, and underscores the complexity involved in producing good approximations of these control fields. These spectrograms are significantly less accurate than those produced using fitted fields and shown in fig.5.8. This discrepancy might partially originate in the different currents being tracked in the x-direction of each case, which also affects the y-direction via coupling. This could be tested by reproducing fig.5.6 for various N_ω and comparing them to the results under fitted evolution, and to fig.B.2. This might lead to improved fitting methods by helping to identify which specific features of the control fields are required to successfully mimic the HHG, which can then be selected for in new fitting models or by explicitly introducing those frequencies.

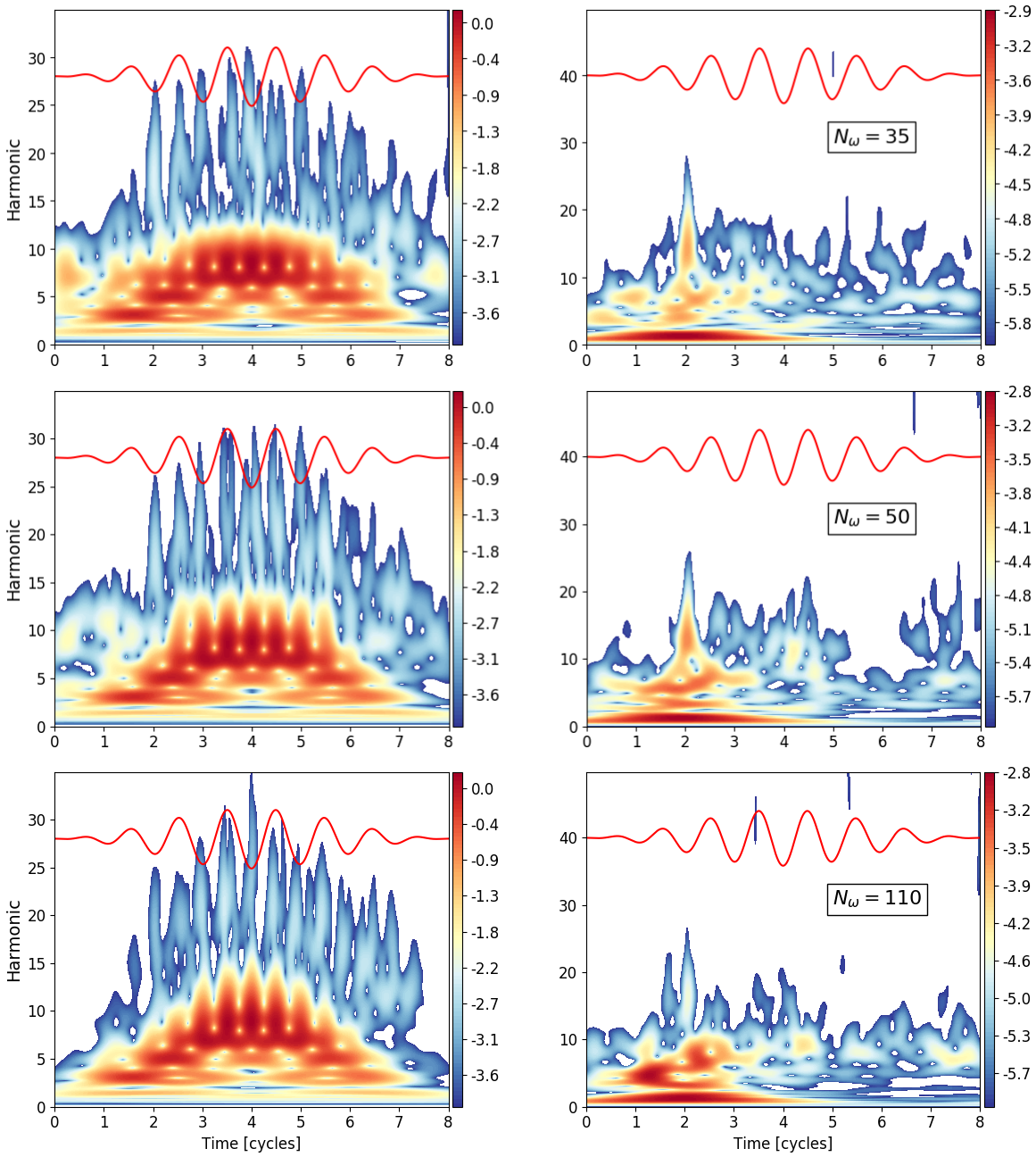

Figure B.2: **Spectrograms resulting from harmonic selection.** Time-resolved emission for the $U_T = 3$ system propagated under control fields composed of $N_\omega = 35$, 50 and 110 frequencies, with imposed fractions $f_\omega = 0.1$, 0.2, 0, respectively. These are attempting to reproduce the characteristics of fig.5.10 and the y-direction of fig.5.6. The red lines show the form of the original electric field. Calculated using tVMC on a 6×6 lattice.

References

1. Orthodoxou, C., Zaïr, A. & Booth, G. H. "High harmonic generation in two-dimensional Mott insulators". *npj Quantum Materials* **6,** 76 (2021).
2. McCaul, G., Orthodoxou, C., Jacobs, K., Booth, G. H. & Bondar, D. I. "Driven Imposters: Controlling Expectations in Many-Body Systems". *Physical Review Letters* **124,** 183201 (18 2020).
3. McCaul, G., Orthodoxou, C., Jacobs, K., Booth, G. H. & Bondar, D. I. "Controlling arbitrary observables in correlated many-body systems". *Physical Review A* **101,** 053408 (5 2020).
4. Martin, R. M., Reining, L. & Ceperley, D. M. "Interacting Electrons: Theory and Computational Approaches" (Cambridge University Press, 2016).
5. Imada, M., Fujimori, A. & Tokura, Y. "Metal-insulator transitions". *Review of Modern Physics* **70,** 1039–1263 (4 1998).
6. Bednorz, J. G. & Muller, K. A. "Possible high Tc superconductivity in the Ba-La-Cu-O system". *Zeitschrift für Physik* **64,** 189–193 (1986).
7. Dagotto, E. "Correlated electrons in high-temperature superconductors". *Review of Modern Physics* **66,** 763–840 (3 1994).
8. Lee, P. A., Nagaosa, N. & Wen, X. G. "Doping a Mott insulator: Physics of high-temperature superconductivity". *Review of Modern Physics* **78,** 17–85 (1 2006).
9. Kamihara, Y. *et al.* "Iron-Based Layered Superconductor: LaOFeP". *Journal of the American Chemical Society* **128,** 10012–10013 (2006).

10. Mott, N. F. "The Basis of the Electron Theory of Metals, with Special Reference to the Transition Metals". *Proceedings of the Physical Society. Section A* **62,** 416–422 (1949).

11. Hubbard, J. & Flowers, B. H. "Electron correlations in narrow energy bands". *Proceedings of the Royal Society of London. Series A. Mathematical and Physical Sciences* **276,** 238–257 (1963).

12. Hubbard, J. & Flowers, B. H. "Electron correlations in narrow energy bands. II. The degenerate band case". *Proceedings of the Royal Society of London. Series A. Mathematical and Physical Sciences* **277,** 237–259 (1964).

13. Hubbard, J. & Flowers, B. H. "Electron correlations in narrow energy bands III. An improved solution". *Proceedings of the Royal Society of London. Series A. Mathematical and Physical Sciences* **281,** 401–419 (1964).

14. Hubbard, J. & Flowers, B. H. "Electron correlations in narrow energy bands - IV. The atomic representation". *Proceedings of the Royal Society of London. Series A. Mathematical and Physical Sciences* **285,** 542–560 (1965).

15. Hubbard, J. & Flowers, B. H. "Electron correlations in narrow energy bands V. A perturbation expansion about the atomic limit". *Proceedings of the Royal Society of London. Series A. Mathematical and Physical Sciences* **296,** 82–99 (1967).

16. Hubbard, J. & Flowers, B. H. "Electron correlations in narrow energy bands VI. The connexion with many-body perturbation theory". *Proceedings of the Royal Society of London. Series A. Mathematical and Physical Sciences* **296,** 100–112 (1967).

17. Gutzwiller, M. C. "Effect of Correlation on the Ferromagnetism of Transition Metals". *Physical Review Letters* **10,** 159–162 (5 1963).

18. Essler, F. H. L., Frahm, H., Goehmann, F., Kluemper, A. & Korepin, V. E. "The One-Dimensional Hubbard Model" (Cambridge University Press, 2005).

19. Bulla, R. "Zero Temperature Metal-Insulator Transition in the Infinite Dimensional Hubbard Model". *Physical Review Letters* **83,** 136–139 (1 1999).

20. Macridin, A., Jarrell, M., Maier, T. & Sawatzky, G. A. "Physics of cuprates with the two-band Hubbard model: The validity of the one-band Hubbard model". *Physical Review B* **71,** 134527 (13 2005).

21. Lieb, E. H. & Wu, F. Y. "Absence of Mott Transition in an Exact Solution of the Short-Range, One-Band Model in One Dimension". *Physical Review Letters* **20,** 1445–1448 (25 1968).

22. Karabach, M., Müller, G., Gould, H. & Tobochnik, J. "Introduction to the Bethe Ansatz I". *Computers in Physics* **11,** 36–43 (1997).

23. Karbach, M., Hu, K. & Müller, G. "Introduction to the Bethe Ansatz II". *Computers in Physics* **12,** 565–573 (1998).

24. Karbach, M. & Muller, G. "Introduction to the Bethe Ansatz III". 2000. arXiv: `arXiv:cond-mat/0008018v1 [cond-mat.stat-mech]`.

25. Metzner, W. & Vollhardt, D. "Correlated Lattice Fermions in $d = \infty$ Dimensions". *Physical Review Letters* **62,** 324–327 (3 1989).

26. Gebhard, F. "The Mott Metal-Insulator Transition" (Springer, 1997).

27. Arovas, D. P., Berg, E., Kivelson, S. & Raghu, S. "The Hubbard Model". 2021. arXiv: `2103.12097 [cond-mat.str-el]`.

28. Changlani, H. J., Zheng, H. & Wagner, L. K. "Density-matrix based determination of low-energy model Hamiltonians from ab initio wavefunctions". *The Journal of Chemical Physics* **143,** 102814 (2015).

29. Schüler, M., Rösner, M., Wehling, T. O., Lichtenstein, A. I. & Katsnelson, M. I. "Optimal Hubbard Models for Materials with Nonlocal Coulomb Interactions: Graphene, Silicene, and Benzene". *Physical Review Letters* **111,** 036601 (3 2013).

30. Foley, A., Verret, S., Tremblay, A.-M. S. & Sénéchal, D. "Coexistence of superconductivity and antiferromagnetism in the Hubbard model for cuprates". *Physical Review B* **99,** 184510 (18 2019).

31. Wosnitza, J. "Superconductivity of Organic Charge-Transfer Salts". *Journal of Low Temperature Physics* **197,** 250–271 (2019).

32. Delannoy, J.-Y. P., Gingras, M. J. P., Holdsworth, P. C. W. & Tremblay, A.-M. S. "Low-energy theory of the $t-t'-t''-U$ Hubbard model at half-filling: Interaction strengths in cuprate superconductors and an effective spin-only description of La_2CuO_4". *Physical Review B* **79,** 235130 (23 2009).

33. Wang, Y. *et al.* "Emergence of quasiparticles in a doped Mott insulator". *Communications Physics* **3,** 210 (2020).

34. Franken, P. A., Hill, A. E., Peters, C. W. & Weinreich, G. "Generation of Optical Harmonics". *Physical Review Letters* **7,** 118–119 (4 1961).

35. Hawkins, P. G. "High Harmonic Generation in Periodic Systems". PhD thesis (Imperial College London, 2016).

36. Lompre, L. A., Mainfray, G., Manus, C. & Thebault, J. "Multiphoton ionization of rare gases by a tunable-wavelength 30-psec laser pulse at 1.06 μm". *Physical Review A* **15,** 1604–1612 (4 1977).

37. Ferray, M. *et al.* "Multiple-harmonic conversion of 1064 nm radiation in rare gases". *Journal of Physics B: Atomic, Molecular and Optical Physics* **21,** L31–L35 (1988).

38. Corkum, P. B. "Plasma perspective on strong field multiphoton ionization". *Physical Review Letters* **71,** 1994–1997 (13 1993).

39. Krause, J. L., Schafer, K. J. & Kulander, K. C. "High-order harmonic generation from atoms and ions in the high intensity regime". *Physical Review Letters* **68,** 3535–3538 (24 1992).

40. Krause, J. L., Schafer, K. J. & Kulander, K. C. "High-order harmonic generation from atoms and ions in the high intensity regime". *Physical Review Letters* **68,** 3535–3538 (24 1992).

41. Schafer, K. J., Yang, B., DiMauro, L. F. & Kulander, K. C. "Above threshold ionization beyond the high harmonic cutoff". *Physical Review Letters* **70,** 1599–1602 (11 1993).

42. Lewenstein, M., Balcou, P., Ivanov, M. Y., L'Huillier, A. & Corkum, P. B. "Theory of high-harmonic generation by low-frequency laser fields". *Physical Review A* **49,** 2117–2132 (3 1994).

43. Keldysh, L. V. "Ionization in the Field of a Strong Electromagnetic Wave". *Journal of Experimental and Theoretical Physics* **20,** 1307–1314 (1965).

44. Corkum, P. B. & Krausz, F. "Attosecond science". *Nature Physics* **3,** 381–387 (2007).

45. Krausz, F. & Ivanov, M. "Attosecond physics". *Review of Modern Physics* **81,** 163–234 (1 2009).

46. Li, J. *et al.* "Attosecond science based on high harmonic generation from gases and solids". *Nature Communications* **11,** 2748 (2020).

47. Itatani, J. *et al.* "Tomographic imaging of molecular orbitals". *Nature* **432,** 867–871 (2004).

48. McFarland, B. K., Farrell, J. P., Bucksbaum, P. H. & Gühr, M. "High Harmonic Generation from Multiple Orbitals in N_2". *Science* **322,** 1232 (2008).

49. Smirnova, O. *et al.* "High harmonic interferometry of multi-electron dynamics in molecules". *Nature* **460,** 972–977 (2009).

50. Salières, P., Maquet, A., Haessler, S., Caillat, J. & Taïeb, R. "Imaging orbitals with attosecond and Ångström resolutions: toward attochemistry?" *Reports on Progress in Physics* **75,** 062401 (2012).

51. Pullen, M. G. *et al.* "Imaging an aligned polyatomic molecule with laser-induced electron diffraction". *Nature Communications* **6,** 7262 (2015).

52. Haertelt, M., Bian, X.-B., Spanner, M., Staudte, A. & Corkum, P. B. "Probing Molecular Dynamics by Laser-Induced Backscattering Holography". *Physical Review Letters* **116,** 133001 (13 2016).

53. Baltuška, A. *et al.* "Attosecond control of electronic processes by intense light fields". *Nature* **421,** 611–615 (2003).

54. Chini, M., Zhao, K. & Chang, Z. "The generation, characterization and applications of broadband isolated attosecond pulses". *Nature Photonics* **8,** 178–186 (2014).

55. Ramasesha, K., Leone, S. R. & Neumark, D. M. "Real-Time Probing of Electron Dynamics Using Attosecond Time-Resolved Spectroscopy". *Annual Review of Physical Chemistry* **67,** 41–63 (2016).

56. Calegari, F., Sansone, G., Stagira1, S., Vozzi, C. & Nisoli, M. "Advances in attosecond science". *Journal of Physics B: Atomic, Molecular and Optical Physics* **49,** 062001 (2016).

57. Sabbar, M. *et al.* "State-resolved attosecond reversible and irreversible dynamics in strong optical fields". *Nature Physics* **13,** 472–478 (2017).

58. Ghimire, S. *et al.* "Observation of high-order harmonic generation in a bulk crystal". *Nature Physics* **7,** 138–141 (2011).

59. Zaks, B., Liu, R. B. & Sherwin, M. S. "Experimental observation of electron–hole recollisions". *Nature* **483,** 580–583 (2012).

60. Schultze, M. *et al.* "Controlling dielectrics with the electric field of light". *Nature* **493,** 75–78 (2013).

61. Hohenleutner, M. *et al.* "Real-time observation of interfering crystal electrons in high-harmonic generation". *Nature* **523,** 572–575 (2015).

62. McDonald, C. R., Amin, K. S., Aalmalki, S. & Brabec, T. "Enhancing High Harmonic Output in Solids through Quantum Confinement". *Physical Review Letters* **119,** 183902 (18 2017).

63. You, Y. S. *et al.* "Laser waveform control of extreme ultraviolet high harmonics from solids". *Optics Letters* **42,** 1816–1819 (2017).

64. Kaneshima, K. *et al.* "Polarization-Resolved Study of High Harmonics from Bulk Semiconductors". *Physical Review Letters* **120,** 243903 (24 2018).

65. Schubert, O. *et al.* "Sub-cycle control of terahertz high-harmonic generation by dynamical Bloch oscillations". *Nature Photonics* **8,** 119–123 (2014).

66. You, Y. S., Reis, D. A. & Ghimire, S. "Anisotropic high-harmonic generation in bulk crystals". *Nature Physics* **13,** 345–349 (2017).

67. Sørngård, S. A., Simonsen, S. I. & Hansen, J. P. "High-order harmonic generation from graphene: Strong attosecond pulses with arbitrary polarization". *Physical Review A* **87,** 053803 (5 2013).

68. Yoshikawa, N., Tamaya, T. & Tanaka, K. "High-harmonic generation in graphene enhanced by elliptically polarized light excitation". *Science* **356,** 736–738 (2017).

69. Chizhova, L. A., Libisch, F. & Burgdörfer, J. "High-harmonic generation in graphene: Interband response and the harmonic cutoff". *Physical Review B* **95,** 085436 (8 2017).

70. Cox, J. D., Marini, A. & de Abajo, F. J. G. "Plasmon-assisted high-harmonic generation in graphene". *Nature Communications* **8,** 14380 (2017).

71. Mrudul, M. S. & Dixit, G. "High-harmonic generation from monolayer and bilayer graphene". *Physical Review B* **103,** 094308 (9 2021).

72. Yang, Y. *et al.* "High-harmonic generation from an epsilon-near-zero material". *Nature Physics* **15,** 1022–1026 (2019).

73. Silva, R. E. F., Jiménez-Galán, Á., Amorim, B. & Ivanov, M. "Topological strong-field physics on sub-laser-cycle timescale". *Nature Photonics* **13,** 849–854 (2019).

74. Bai, Y. *et al.* "High-harmonic generation from topological surface states". *Nature Physics* **17,** 311–315 (2021).

75. Takayoshi, S., Murakami, Y. & Werner, P. "High-harmonic generation in quantum spin systems". *Physical Review B* **99,** 184303 (18 2019).

76. Luu, T. T. *et al.* "Extreme ultraviolet high-harmonic spectroscopy of solids". *Nature* **521** (2015).

77. Liu, H. *et al.* "High-harmonic generation from an atomically thin semiconductor". *Nature Physics* **13,** 262–265 (2017).

78. Säynätjoki, A. *et al.* "Ultra-strong nonlinear optical processes and trigonal warping in MoS2 layers". *Nature Communications* **8,** 893 (2017).

79. You, Y. S. *et al.* "High-harmonic generation in amorphous solids". *Nature Communications* **8,** 724 (2017).

80. Ndabashimiye, G. *et al.* "Solid-state harmonics beyond the atomic limit". *Nature* **534,** 520–523 (2016).

81. Ghimire, S. *et al.* "Strong-field and attosecond physics in solids". *Journal of Physics B: Atomic, Molecular and Optical Physics* **47,** 204030 (2014).

82. Kruchinin, S. Y., Krausz, F. & Yakovlev, V. S. "Colloquium: Strong-field phenomena in periodic systems". *Reviews of Modern Physics* **90,** 021002 (2 2018).

83. Vampa, G. *et al.* "All-Optical Reconstruction of Crystal Band Structure". *Physical Review Letters* **115,** 193603 (19 2015).

84. Lanin, A. A., Stepanov, E. A., Fedotov, A. B. & Zheltikov, A. M. "Mapping the electron band structure by intraband high-harmonic generation in solids". *Optica* **4,** 516–519 (2017).

85. Li, L. *et al.* "Determination of Electron Band Structure using Temporal Interferometry". *Physical Review Letters* **124,** 157403 (15 2020).

86. You, Y. S., Cunningham, E., Reis, D. A. & Ghimire, S. "Probing periodic potential of crystals via strong-field re-scattering". *Journal of Physics B: Atomic, Molecular and Optical Physics* **51,** 114002 (2018).

87. Hassan, M. T. *et al.* "Optical attosecond pulses and tracking the nonlinear response of bound electrons". *Nature* **530,** 66–70 (2016).

88. Von Hoegen, A., Mankowsky, R., Fechner, M., Först, M. & Cavalleri, A. "Probing the interatomic potential of solids with strong-field nonlinear phononics". *Nature* **555,** 79–82 (2018).

89. Lakhotia, H. *et al.* "Laser picoscopy of valence electrons in solids". *Nature* **583,** 55–59 (2020).

90. Garg, M. *et al.* "Multi-petahertz electronic metrology". *Nature* **538,** 359–363 (2016).

91. Langer, F. *et al.* "Lightwave-driven quasiparticle collisions on a subcycle timescale". *Nature* **533,** 225–229 (2016).

92. Mücke, O. D. "Isolated high-order harmonics pulse from two-color-driven Bloch oscillations in bulk semiconductors". *Physical Review B* **84,** 081202 (8 2011).

93. Higuchi, T., Stockman, M. I. & Hommelhoff, P. "Strong-Field Perspective on High-Harmonic Radiation from Bulk Solids". *Physical Review Letters* **113,** 213901 (21 2014).

94. Sivis, M. *et al.* "Tailored semiconductors for high-harmonic optoelectronics". *Science* **357,** 303–306 (2017).

95. Goulielmakis, E. *et al.* "Attosecond Control and Measurement: Lightwave Electronics". *Science* **317,** 769–775 (2007).

96. Schiffrin, A. *et al.* "Optical-field-induced current in dielectrics". *Nature* **493,** 70–74 (2013).

97. Krausz, F. & Stockman, M. I. "Attosecond metrology: from electron capture to future signal processing". *Nature Photonics* **8,** 205–213 (2014).

98. Mashiko, H., Oguri, K., Yamaguchi, T., Suda, A. & Gotoh, H. "Petahertz optical drive with wide-bandgap semiconductor". *Nature Physics* **12,** 741–745 (2016).

99. Sommer, A. *et al.* "Attosecond nonlinear polarization and light–matter energy transfer in solids". *Nature* **534,** 86–90 (2016).

100. Golde, D., Meier, T. & Koch, S. W. "High harmonics generated in semiconductor nanostructures by the coupled dynamics of optical inter- and intraband excitations". *Physical Review B* **77,** 075330 (7 2008).

101. Vampa, G. *et al.* "Theoretical Analysis of High-Harmonic Generation in Solids". *Physical Review Letters* **113,** 073901 (7 2014).

102. Vampa, G., McDonald, C. R., Orlando, G., Corkum, P. B. & Brabec, T. "Semiclassical analysis of high harmonic generation in bulk crystals". *Physical Review B* **91,** 064302 (6 2015).

103. Wu, M., Ghimire, S., Reis, D. A., Schafer, K. J. & Gaarde, M. B. "High-harmonic generation from Bloch electrons in solids". *Physical Review A* **91,** 043839 (4 2015).

104. Tamaya, T., Ishikawa, A., Ogawa, T. & Tanaka, K. "Diabatic Mechanisms of Higher-Order Harmonic Generation in Solid-State Materials under High-Intensity Electric Fields". *Physical Review Letters* **116,** 016601 (1 2016).

105. Ikemachi, T. *et al.* "Trajectory analysis of high-order-harmonic generation from periodic crystals". *Physical Review A* **95,** 043416 (4 2017).

106. Osika, E. N. *et al.* "Wannier-Bloch Approach to Localization in High-Harmonics Generation in Solids". *Physical Review X* **7,** 021017 (2 2017).

107. Tancogne-Dejean, N., Mücke, O. D., Kärtner, F. X. & Rubio, A. "Impact of the Electronic Band Structure in High-Harmonic Generation Spectra of Solids". *Physical Review Letters* **118,** 087403 (8 2017).

108. Schultze, M. *et al.* "Attosecond band-gap dynamics in silicon". *Science* **346,** 1348–1352 (2014).

109. Lucchini, M. *et al.* "Attosecond dynamical Franz-Keldysh effect in polycrystalline diamond". *Science* **353,** 916–919 (2016).

110. Moulet, A. *et al.* "Soft x-ray excitonics". *Science* **357,** 1134–1138 (2017).

111. Schlaepfer, F. *et al.* "Attosecond optical-field-enhanced carrier injection into the GaAs conduction band". *Nature Physics* **14,** 560–564 (2018).

112. Ghimire, S. & Reis, D. A. "High-harmonic generation from solids". *Nature Physics* **15,** 10–16 (2019).

113. Földi, P., Benedict, M. G. & Yakovlev, V. S. "The effect of dynamical Bloch oscillations on optical-field-induced current in a wide-gap dielectric". *New Journal of Physics* **15,** 063019 (2013).

114. McDonald, C. R., Vampa, G., Corkum, P. B. & Brabec, T. "Interband Bloch oscillation mechanism for high-harmonic generation in semiconductor crystals". *Physical Review A* **92,** 033845 (3 2015).

115. Liu, L., Zhao, J., Yuan, J. & Zhao, Z. "The role of Bloch oscillation in high-order harmonic generation from periodic structure(Invited review: Strong-field atomic and molecular physics)". *Chinese Physics B* **28,** 114205 (2019).

116. Leo, K., Bolívar, P., Brüggemann, F., Schwedler, R. & Köhler, K. "Observation of Bloch oscillations in a semiconductor superlattice". *Solid State Communications* **84,** 943–946 (1992).

117. Waschke, C. *et al.* "Coherent submillimeter-wave emission from Bloch oscillations in a semiconductor superlattice". *Physical Review Letters* **70,** 3319–3322 (21 1993).

118. Vampa, G. *et al.* "Linking high harmonics from gases and solids". *Nature* **522,** 462–464 (2015).

119. Schlaepfer, F. *et al.* "Attosecond optical-field-enhanced carrier injection into the GaAs conduction band". *Nature Physics* **14,** 560–564 (2018).

120. Vampa, G. & Brabec, T. "Merge of high harmonic generation from gases and solids and its implications for attosecond science". *Journal of Physics B: Atomic, Molecular and Optical Physics* **50,** 083001 (2017).

121. Wu, M., Browne, D. A., Schafer, K. J. & Gaarde, M. B. "Multilevel perspective on high-order harmonic generation in solids". *Physical Review A* **94,** 063403 (6 2016).

122. Hansen, K. K., Deffge, T. & Bauer, D. "High-order harmonic generation in solid slabs beyond the single-active-electron approximation". *Physical Review A* **96,** 053418 (5 2017).

123. Huttner, U., Kira, M. & Koch, S. W. "Ultrahigh Off-Resonant Field Effects in Semiconductors". *Laser & Photonics Reviews* **11,** 1700049 (2017).

124. Yu, C., Jiang, S. & Lu, R. "High order harmonic generation in solids: a review on recent numerical methods". *Advances in Physics: X* **4,** 1562982 (2019).

125. Ghimire, S. *et al.* "Generation and propagation of high-order harmonics in crystals". *Physical Review A* **85,** 043836 (4 2012).

126. Hawkins, P. G., Ivanov, M. Y. & Yakovlev, V. S. "Effect of multiple conduction bands on high-harmonic emission from dielectrics". *Physical Review A* **91,** 013405 (1 2015).

127. Lindberg, M. & Koch, S. W. "Effective Bloch equations for semiconductors". *Physical Review B* **38,** 3342–3350 (5 1988).

128. Runge, E. & Gross, E. K. U. "Density-Functional Theory for Time-Dependent Systems". *Physical Review Letters* **52,** 997–1000 (12 1984).

129. Tancogne-Dejean, N., Mücke, O. D., Kärtner, F. X. & Rubio, A. "Ellipticity dependence of high-harmonic generation in solids originating from coupled intraband and interband dynamics". *Nature Communications* **8,** 745 (2017).

130. Floss, I. *et al.* "Ab initio multiscale simulation of high-order harmonic generation in solids". *Physical Review A* **97,** 011401 (1 2018).

131. Peierls, R. "Zur Theorie des Diamagnetismus von Leitungselektronen". *Zeitschrift für Physik* **80,** 763–791 (1933).

132. Silva, R., Blinov, I. V., Rubtsov, A. N., Smirnova, O. & Ivanov, M. "High-harmonic spectroscopy of ultrafast many-body dynamics in strongly correlated systems". *Nature Photonics* **12,** 266–270 (2018).

133. Zhu, W., Fauseweh, B., Chacon, A. & Zhu, J.-X. "Ultrafast laser-driven many-body dynamics and Kondo coherence collapse". *Physical Review B* **103,** 224305 (22 2021).

134. Imai, S., Ono, A. & Ishihara, S. "High Harmonic Generation in a Correlated Electron System". *Physical Review Letters* **124,** 157404 (15 2020).

135. Murakami, Y., Takayoshi, S., Koga, A. & Werner, P. "High-harmonic generation in one-dimensional Mott insulators". *Physical Review B* **103,** 035110 (3 2021).

136. Murakami, Y. & Werner, P. "Nonequilibrium steady states of electric field driven Mott insulators". *Physical Review B* **98,** 075102 (7 2018).

137. Murakami, Y., Eckstein, M. & Werner, P. "High-Harmonic Generation in Mott Insulators". *Physical Review Letters* **121,** 057405 (5 2018).

138. Lysne, M., Murakami, Y. & Werner, P. "Signatures of bosonic excitations in high-harmonic spectra of Mott insulators". *Physical Review B* **101,** 195139 (19 2020).

139. Aoki, H. *et al.* "Nonequilibrium dynamical mean-field theory and its applications". *Reviews of Modern Physics* **86,** 779–837 (2 2014).

140. Tancogne-Dejean, N., Sentef, M. A. & Rubio, A. "Ultrafast Modification of Hubbard U in a Strongly Correlated Material: Ab initio High-Harmonic Generation in NiO". *Physical Review Letters* **121,** 097402 (9 2018).

141. White, S. R. & Feiguin, A. E. "Real-Time Evolution Using the Density Matrix Renormalization Group". *Physical Review Letters* **93,** 076401 (7 2004).

142. Vidal, G. "Classical Simulation of Infinite-Size Quantum Lattice Systems in One Spatial Dimension". *Physical Review Letters* **98,** 070201 (7 2007).

143. Fauseweh, B. & Zhu, J.-X. "Laser pulse driven control of charge and spin order in the two-dimensional Kondo lattice". *Physical Review B* **102,** 165128 (16 2020).

144. Jin, J.-Z. *et al.* "High-order harmonic generation from a two-dimensional band structure". *Physical Review A* **97,** 043420 (4 2018).

145. Tancogne-Dejean, N. & Rubio, A. "Atomic-like high-harmonic generation from two-dimensional materials". *Science Advances* **4** (2018).

146. Mrudul, M. S. & Dixit, G. "High-harmonic generation from monolayer and bilayer graphene". *Physical Review B* **103,** 094308 (9 2021).

147. Higuchi, T., Heide, C., Ullmann, K., Weber, H. B. & Hommelhoff, P. "Light-field-driven currents in graphene". *Nature* **550,** 224–228 (2017).

148. Limelette, P. *et al.* "Universality and Critical Behavior at the Mott Transition". *Science* **302,** 89–92 (2003).

149. Taguchi, Y., Matsumoto, T. & Tokura, Y. "Dielectric breakdown of one dimensional Mott insulators Sr_2CuO_3 and $SrCuO_2$". *Physical Review B* **62,** 7015–7018 (11 2000).

150. Okamoto, H. *et al.* "Photoinduced transition from Mott insulator to metal in the undoped cuprates Nd_2CuO_4 and La_2CuO_4". *Physical Review B* **83,** 125102 (12 2011).

151. Liu, M. *et al.* "Terahertz-field-induced insulator-to-metal transition in vanadium dioxide metamaterial". *Nature* **487,** 345–348 (2012).

152. Wall, S. *et al.* "Quantum interference between charge excitation paths in a solid-state Mott insulator". *Nature Physics* **7,** 114–118 (2011).

153. Zener, C. "Non-adiabatic crossing of energy levels". *Proceedings of the Royal Society of London A* **137,** 696–702 (1932).

154. Zener, C. "A theory of the electrical breakdown of solid dielectrics". *Proceedings of the Royal Society of London A* **145,** 523–529 (1934).

155. Oka, T., Arita, R. & Aoki, H. "Breakdown of a Mott Insulator: A Nonadiabatic Tunneling Mechanism". *Physical Review Letters* **91,** 066406 (6 2003).

156. Takahashi, A., Itoh, H. & Aihara, M. "Photoinduced insulator-metal transition in one-dimensional Mott insulators". *Physical Review B* **77,** 205105 (20 2008).

157. Lenarcic, Z. & Prelovsek, P. "Dielectric Breakdown in Spin-Polarized Mott Insulator". *Physical Review Letters* **108,** 196401 (19 2012).

158. Oka, T. & Aoki, H. "Ground-State Decay Rate for the Zener Breakdown in Band and Mott Insulators". *Physical Review Letters* **95,** 137601 (13 2005).

159. Oka, T. & Aoki, H. "Photoinduced Tomonaga-Luttinger-like liquid in a Mott insulator". *Physical Review B* **78,** 241104 (24 2008).

160. Kirino, S. & Ueda, K. "Nonequilibrium Current in the One Dimensional Hubbard Model at Half-Filling". *Journal of the Physical Society of Japan* **79,** 093710 (2010).

161. Oka, T. & Aoki, H. "Dielectric breakdown in a Mott insulator: Many-body Schwinger-Landau-Zener mechanism studied with a generalized Bethe ansatz". *Physical Review B* **81,** 033103 (3 2010).

162. Heidrich-Meisner, F. *et al.* "Nonequilibrium electronic transport in a one dimensional Mott insulator". *Physical Review B* **82,** 205110 (20 2010).

163. Eckstein, M., Oka, T. & Werner, P. "Dielectric Breakdown of Mott Insulators in Dynamical Mean-Field Theory". *Physical Review Letters* **105,** 146404 (14 2010).

164. Lee, W.-R. & Park, K. "Dielectric breakdown via emergent nonequilibrium steady states of the electric-field-driven Mott insulator". *Physical Review B* **89,** 205126 (20 2014).

165. Oka, T. "Nonlinear doublon production in a Mott insulator: Landau-Dykhne method applied to an integrable model". *Physical Review B* **86,** 075148 (7 2012).

166. Stafford, C. A. & Millis, A. J. "Scaling theory of the Mott-Hubbard metal-insulator transition in one dimension". *Physical Review B* **48,** 1409–1425 (3 1993).

167. Bajdich, M., Mitas, L., Wagner, L. K. & Schmidt, K. E. "Pfaffian pairing and backflow wavefunctions for electronic structure quantum Monte Carlo methods". *Physical Review B* **77,** 115112 (11 2008).

168. "mVMC - Open-Source Software for Many-Variable Variational Monte Carlo Method". *Computer Physics Communications* **235,** 447–462 (2019).

169. Gutzwiller, M. C. "Effect of Correlation on the Ferromagnetism of Transition Metals". *Physical Review Letters* **10,** 159–162 (5 1963).

170. Becca, F. & Sorella, S. "Quantum Monte Carlo Approaches for Correlated System" (Cambridge University Press, 2017).

171. Yokoyama, H. & Shiba, H. "Variational Monte-Carlo Studies of Hubbard Model. I". *Journal of the Physical Society of Japan* **56,** 1490–1506 (1987).

172. Capello, M., Becca, F., Fabrizio, M., Sorella, S. & Tosatti, E. "Variational Description of Mott Insulators". *Physical Review Letters* **94,** 026406 (2 2005).

173. Jastrow, R. "Many-Body Problem with Strong Forces". *Physical Review* **98,** 1479–1484 (5 1955).

174. Tahara, D. & Imada, M. "Variational Monte Carlo Method Combined with Quantum-Number Projection and Multi-Variable Optimization". *Journal of the Physical Society of Japan* **77,** 114701 (2008).

175. Ceperley, D., Chester, G. V. & Kalos, M. H. "Monte Carlo simulation of a many-fermion study". *Physical Review B* **16,** 3081–3099 (7 1977).

176. Metropolis, N., Rosenbluth, A. W., Rosenbluth, M. N., Teller, A. H. & Teller, E. "Equation of State Calculations by Fast Computing Machines". *The Journal of Chemical Physics* **21,** 1087–1092 (1953).

177. Sorella, S. "Generalized Lanczos algorithm for variational quantum Monte Carlo". *Physical Review B* **64,** 024512 (2 2001).

178. Sorella, S., Casula, M. & Rocca, D. "Weak binding between two aromatic rings: Feeling the van der Waals attraction by quantum Monte Carlo methods". *The Journal of Chemical Physics* **127,** 014105 (2007).

179. `https://github.com/issp-center-dev/mVMC`.

180. Haegeman, J., Osborne, T. J. & Verstraete, F. "Post-matrix product state methods: To tangent space and beyond". *Physical Review B* **88,** 075133 (7 2013).

181. McLachlan, A. "A variational solution of the time-dependent Schrodinger equation". *Molecular Physics* **8,** 39–44 (1964).

182. Takai, K., Ido, K., Misawa, T., Yamaji, Y. & Imada, M. "Finite-Temperature Variational Monte Carlo Method for Strongly Correlated Electron Systems". *Journal of the Physical Society of Japan* **85,** 034601 (2016).

183. Carleo, G., Becca, F., Schiro, M. & Fabrizio, M. "Localization and glassy dynamics of many-body quantum systems". *Scientific Reports* **2,** 243 (2012).

184. Carleo, G., Becca, F., Sanchez-Palencia, L., Sorella, S. & Fabrizio, M. "Light-cone effect and supersonic correlations in one- and two-dimensional bosonic superfluids". *Physical Review A* **89,** 031602 (3 2014).

185. Ido, K., Ohgoe, T. & Imada, M. "Time-dependent many-variable variational Monte Carlo method for nonequilibrium strongly correlated electron systems". *Physical Review B* **92,** 245106 (24 2015).

186. Carleo, G. & Troyer, M. "Solving the quantum many-body problem with artificial neural networks". *Science* **355,** 602–606 (2017).

187. Schmitt, M. & Heyl, M. "Quantum Many-Body Dynamics in Two Dimensions with Artificial Neural Networks". *Physical Review Letters* **125,** 100503 (10 2020).

188. Gutiérrez, I. L. & Mendl, C. B. "Real time evolution with neural-network quantum states". 2021. arXiv: `1912.08831 [cond-mat.dis-nn]`.

189. Fabiani, G. & Mentink, J. H. "Investigating ultrafast quantum magnetism with machine learning". *SciPost Physics* **7,** 4 (1 2019).

190. Ido, K., Ohgoe, T. & Imada, M. "Correlation-induced superconductivity dynamically stabilized and enhanced by laser irradiation". *Science Advances* **3** (2017).

191. Cevolani, L., Carleo, G. & Sanchez-Palencia, L. "Protected quasilocality in quantum systems with long-range interactions". *Physical Review A* **92,** 041603 (4 2015).

192. Sun, Q. *et al.* "PySCF: the Python-based simulations of chemistry framework". *WIREs Computational Molecular Science* **8,** e1340 (2018).

193. Fertitta, E. & Booth, G. H. "Energy-weighted density matrix embedding of open correlated chemical fragments". *The Journal of Chemical Physics* **151,** 014115 (2019).

194. Fertitta, E. & Booth, G. H. "Rigorous wave function embedding with dynamical fluctuations". *Physical Review B* **98,** 235132 (23 2018).

195. Sriluckshmy, P. V., Nusspickel, M., Fertitta, E. & Booth, G. H. "Fully algebraic and self-consistent effective dynamics in a static quantum embedding". *Physical Review B* **103,** 085131 (8 2021).

196. Leung, P. W., Liu, Z., Manousakis, E., Novotny, M. A. & Oppenheimer, P. E. "Density of states of the two-dimensional Hubbard model on a 4×4 lattice". *Physical Review B* **46,** 11779–11786 (18 1992).

197. Bulut, N., Scalapino, D. J. & White, S. R. "Electronic Properties of the Insulating Half-Filled Hubbard Model". *Physical Review Letters* **73,** 748–751 (5 1994).

198. Kohno, M. “Mott Transition in the Two-Dimensional Hubbard Model”. *Physical Review Letters* **108,** 076401 (7 2012).

199. Kohno, M. “Spectral properties near the Mott transition in the two-dimensional Hubbard model with next-nearest-neighbor hopping”. *Physical Review B* **90,** 035111 (3 2014).

200. Gabor, D. “Theory of communication. Part 1: The analysis of information”. *Journal of the Institution of Electrical Engineers* **93,** 429–441(12) (26 1946).

201. Chirilă, C. C., Dreissigacker, I., van der Zwan, E. V. & Lein, M. “Emission times in high-order harmonic generation”. *Physical Review A* **81,** 033412 (3 2010).

202. Torrence, C. & Compo, G. P. “A Practical Guide to Wavelet Analysis”. *Bulletin of the American Meteorological Society* **79** (1998).

203. `https://github.com/aaren/wavelets`.

204. Shalaby, M. & Hauri, C. P. “Demonstration of a low-frequency three-dimensional terahertz bullet with extreme brightness”. *Nature Communications* **6,** 5976 (2015).

205. Kovalev, S. *et al.* “Non-perturbative terahertz high-harmonic generation in the three-dimensional Dirac semimetal Cd_3As_2”. *Nature Communications* **11,** 2451 (2020).

206. Cheng, B. *et al.* “Efficient Terahertz Harmonic Generation with Coherent Acceleration of Electrons in the Dirac Semimetal Cd_3As_2”. *Physical Review Letters* **124,** 117402 (11 2020).

207. Tomita, N. & Nasu, K. “Quantum fluctuation effects on light absorption spectra of the one-dimensional extended Hubbard model”. *Physical Review B* **63,** 085107 (8 2001).

208. `https://github.com/issp-center-dev/HPhi`.

209. McClean, J. R., Parkhill, J. A. & Aspuru-Guzik, A. “Feynman’s clock, a new variational principle, and parallel-in-time quantum dynamics”. *Proceedings of the National Academy of Sciences* **110,** E3901–E3909 (2013).

210. Basov, D. N., Averitt, R. D. & Hsieh, D. "Towards properties on demand in quantum materials". *Nature Materials* **16,** 1077–1088 (2017).

211. Wang, C. & Liu, Y. "Ultrafast optical manipulation of magnetic order in ferromagnetic materials". *Nano Convergence* **7,** 35 (2020).

212. Serban, I., Werschnik, J. & Gross, E. K. U. "Optimal control of time-dependent targets". *Physical Review A* **71,** 053810 (5 2005).

213. Werschnik, J. & Gross, E. K. "Quantum optimal control theory". *Journal of Physics B: Atomic, Molecular and Optical Physics* **40,** R175–R211 (2007).

214. Doria, P., Calarco, T. & Montangero, S. "Optimal Control Technique for Many-Body Quantum Dynamics". *Physical Review Letters* **106,** 190501 (19 2011).

215. Kosloff, R., Hammerich, A. D. & Tannor, D. "Excitation without demolition: Radiative excitation of ground-surface vibration by impulsive stimulated Raman scattering with damage control". *Physical Review Letters* **69,** 2172–2175 (15 1992).

216. Magann, A., Ho, T.-S. & Rabitz, H. "Singularity-free quantum tracking control of molecular rotor orientation". *Physical Review A* **98,** 043429 (4 2018).

217. Campos, A. G., Bondar, D. I., Cabrera, R. & Rabitz, H. A. "How to Make Distinct Dynamical Systems Appear Spectrally Identical". *Physical Review Letters* **118,** 083201 (8 2017).

218. Elu, U. *et al.* "Seven-octave high-brightness and carrier-envelope-phase-stable light source". *Nature Photonics* **15,** 277–280. ISSN: 1749-4893 (2021).

219. Lesko, D. M. B. *et al.* "A six-octave optical frequency comb from a scalable few-cycle erbium fibre laser". *Nature Photonics* **15,** 281–286. ISSN: 1749-4893 (2021).

220. Koulouklidis, A. D. *et al.* "Observation of extremely efficient terahertz generation from mid-infrared two-color laser filaments". *Nature Communications* **11,** 292. ISSN: 2041-1723 (2020).

221. Jin, C., Wang, G., Wei, H., Le, A.-T. & Lin, C. D. "Waveforms for optimal sub-keV high-order harmonics with synthesized two- or three-colour laser fields". *Nature Communications* **5,** 4003 (2014).

222. Lara-Astiaso, M. *et al.* "Enhancing High-Order Harmonic Generation in Light Molecules by Using Chirped Pulses". *Physical Review Letters* **117,** 093003 (9 2016).

223. Liu, H. "Enhanced high-harmonic generation from an all-dielectric metasurface". *Nature Physics* **14,** 1006–1010 (2018).

224. Peng, D., Frolov, M. V., Pi, L.-W. & Starace, A. F. "Enhancing high-order harmonic generation by sculpting waveforms with chirp". *Physical Review A* **97,** 053414 (5 2018).

225. Rajpoot, R., Holkundkar, A. R. & Bandyopadhyay, J. N. "Controlling resonant enhancement in higher-order harmonic generation". 2021. arXiv: 2107.05196 [physics.atom-ph].